DIVERGENT ENVIRONMENTAL BEHAVIOUR OF IMIPENEM AND FLUOXETINE: STABILITY, INTERACTIONS, AND REMOVAL PROCESS

PRATISHTHA KHURANA

A DISSERTATION SUBMITTED
TO THE FACULTY OF GRADUATE STUDIES
IN PARTIAL FULFILLMENT OF THE REQUIREMENTS
FOR THE DEGREE OF
DOCTOR OF PHILOSOPHY

GRADUATE PROGRAM IN CIVIL ENGINEERING
YORK UNIVERSITY
TORONTO, ONTARIO

May 2026

ABSTRACT

The occurrence of pharmaceutical residues has long been recognized as a potential health concern; however, the fate of these pharmaceuticals has not been thoroughly investigated. In this regard, the present thesis aims to investigate the environmental behaviour of two model pharmaceuticals: Imipenem (IMP), an antibiotic, and Fluoxetine (FLX), an antidepressant, focusing on stability and metal interactions, and devising removal/degradation strategies where applicable.

The findings of the present dissertation indicate that the antibiotic IMP is photolabile and thermosensitive, undergoing rapid degradation under ambient light and temperature. The presence of dissolved organic matter (DOM) and Cu (II) further accelerate its degradation. The drug also exhibits potential to form Imipenem-metal complexes (IMP-Me), exhibiting increased antibacterial activity compared to IMP. Since the drug was observed to be labile, no degradation strategy was proposed.

In contrast to IMP, FLX resists natural attenuation, resulting in its persistence in aquatic environments and making its removal challenging. The present dissertation, thereby, investigates physically activated olive-stone-derived biochar for FLX removal. The optimized biochar demonstrated superior FLX adsorption, surpassing previously reported waste-derived biochar. To further improve practical implementation and achieve FLX degradation, an integration of biochar-based adsorption and UVC-based photocatalysis was employed. The proposed CuO-BC/UVC composite photocatalytic system achieved >95% FLX removal under 2 minutes of treatment. The synergistic CuO-BC/UVC system offers a practical, scalable, and safer alternative to more energy-intensive or chemically harsh oxidation processes.

Overall, the findings for both drugs represent the two extremes of emerging contaminants and highlight opposite ends of a decision framework. For IMP, intervention was not deemed necessary due to its chemically labile structure and natural attenuation; however, toxicity to bacteria persists both with and without transformation, indicating that risk is chemically dynamic and significant, despite rapid transformation. On the contrary, FLX is chemically stable, exhibits no metal complexation, remains bioavailable, and poses a risk for long-term exposure. This persistence,

coupled with chronic effects, makes the invention essential. With these contrasting case studies of IMP and FLX, this dissertation aims to establish that the decision to intervene should be guided by stability, interaction dynamics, and toxicity of the contaminant.

Keywords: Emerging contaminants, Environment, Fluoxetine, Imipenem, Metals, Toxicity, Wastewater

DECLARATION

This is to confirm that I, Pratishtha Khurana, working under the supervision of **Prof. Satinder Kaur Brar**, am responsible for the authenticity of the work presented in this doctoral dissertation "***Divergent Environmental Behaviour of Imipenem and Fluoxetine: Stability, Interactions, and Removal Process***". It is accepted that this is an original work and is being submitted in partial fulfillment of the requirements for Doctor of Philosophy (Ph.D.) Civil Engineering. To the best of my knowledge and belief, this report has not been previously presented to this university or any other institution.

Supervisor: Prof. Satinder Kaur Brar

Committee members: Prof. Derek Wilson and Prof. Stephanie Gora

Submitted by: Pratishtha Khurana (218373688)

May 2026

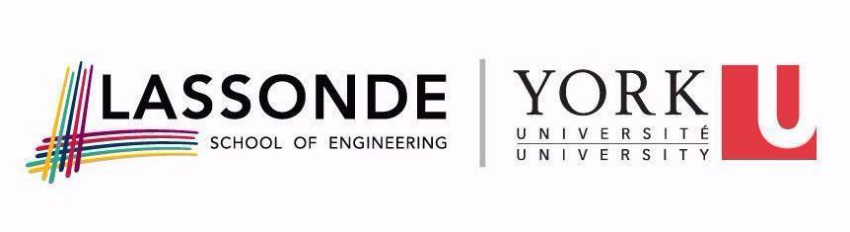

DEDICATION

TO MY PARENTS

For the values that built me

TO MY HUSBAND

For the strength that carried me

TO OUR CHILD TO COME

For the love that already fills our hearts

TO MY TEACHERS

For the lessons that transformed me

ACKNOWLEDGEMENTS

I take this opportunity to convey my sincere gratitude to my supervisor, **Prof. Satinder Kaur Brar**, for her invaluable suggestions, motivation, and insightful comments throughout the course of this research. Their insights, guidance, and expertise were instrumental in making this research productive and stimulating. I would also like to thank **Dr. Rama Pulicharla** and **Dr. Ratul Kumar Das,** who have been constant supporters, critics, and companions.

I am sincerely thankful to my committee members, **Prof. Derek Wilson**, Department of Chemistry and **Prof. Stephanie Gora**, Department of Civil Engineering, for their time, interest, kind evaluation and constructive criticism of my previous progress. I extend my thanks to my internal examiner, **Dr. Siu Ning (Sunny) Leung**, and my external examiner, **Dr. Rania Hamza**, for their time, effort, valuable comments, and careful evaluation of the thesis.

My sincere thanks to **York University,** the faculty and staff of Lassonde School of Engineering, and the **Natural Sciences and Engineering Research Council of Canada** (NSERC; Discovery grant 23451, strategic project grants) for academic and financial support. I am especially grateful to **Ms. Sindy Mahal and Ms. Yvonne Yim** for all her help, support, and academic and administrative guidance throughout.

I am thankful to the laboratory personnel and technicians for their assistance. I thank **Dr. Maxime Rossato**, York University, for their contributions to LC-MS (liquid chromatography-mass spectrometry) measurements and analysis, **Dr. Iraklii (Ira) Ebralidze**, Ontario Tech. University, for BET and SEM analysis. I extend my appreciation to my colleagues and friends for their constant queries and suggestions in weekly group meetings and elsewhere, for making this journey enjoyable and productive. My sincere thanks to **Dr. Gurpreet Kaur**, a very dear friend and an elder sister in spirit, for her unwavering support and encouragement.

Finally, my deepest gratitude goes to my family for their endless support throughout my life for all my choices and their love, which is a constant source of strength for everything I do. I am especially thankful to my husband for his endless support, patience, and strength during this time.

TABLE OF CONTENTS

ABSTRACT ii
DECLARATION iv
DEDICATION v
ACKNOWLEDGEMENTS vi
TABLE OF CONTENTS vii
LIST OF TABLES xii
LIST OF FIGURES xiii
LIST OF ABBREVIATIONS xvi
RESEARCH CONTRIBUTIONS xix
Chapter 1: Introduction 1
PART A: IMIPENEM: STABILITY, METAL INTERACTIONS, AND TOXICITY 6
Chapter 2: Review of Literature 7
2.1 Introduction 7
2.2 Fundamentals of antibiotic-metal complexation 8
2.2.1 Structural features of Antibiotics related to the complexation 9
2.2.2 Chemical properties of metals related to the complexation process 9
2.3 Introduction to Imipenem: Structure, Mechanism, and Environmental occurrence 11
2.3.1 Structure of IMP 11
2.3.2 Dosing, Metabolism and Pharmacokinetics 12
2.3.3 Antibacterial spectrum and Mechanism of action 13
2.3.4 Environmental occurrence and fate of IMP 13
2.3.5 Treatment technologies for IMP-polluted water 16
2.4 Knowledge Gaps 18
2.4.1 Limited studies on IMP fate and behaviour in wastewater 18
2.4.2 No studies of IMP-metal complexes 18
Chapter 3: Research Gaps, Objectives, and Originality 19
Chapter 4: Occurrence of Imipenem in natural water: Effect of dissolved organic matter and metals 21
Abstract 22
4.1 Introduction 23
4.2 Materials and Methods 24

4.2.1 Chemicals and Materials 24
4.2.2 Analytical methods 25
4.2.3 Stability assay 25
4.2.4 Effect of DOM and metals 26
4.2.5 Generation of hydroxyl radicals (OH•) in the Imipenem-copper system 26
4.3 Results and discussion 27
4.3.1 Stability assay 27
4.3.2 Effect of DOM and metals 30
4.4 Conclusion 37
Chapter 5: Imipenem-metal complexes: Computational analysis and toxicity studies with wastewater model microorganisms 39
Abstract 40
5.1 Introduction 41
5.2 Materials and methods 45
5.2.1 Chemicals and reagents 45
5.2.2 Wastewater collection and metal analysis 45
5.2.3 Potentiometric measurements 46
5.2.4 Bacterial strains and culture media 47
5.2.5 Minimum Inhibitory Concentrations (MIC) and growth inhibition assay 47
5.2.6 Computational details 48
5.3 Results and Discussions 49
5.3.1 Metal analysis (WW samples) 49
5.3.2 Structure optimization of Imipenem and Imipenem-metal complexes using software Gaussian 51
5.3.3 Potentiometric measurements for complexation of Imipenem and metals 54
5.3.4 Growth Inhibition Assay 55
5.4 Conclusions 59
PART B: FLUOXETINE: LITERATURE INSIGHTS AND TREATMENT STRATEGIES 61
Chapter 6: Review of Literature 62
Abstract 63
6.1 Introduction 64
6.2 Structural features of FLX and fluorocarbon chemistry 69
6.3 Environmental persistence and Fate of FLX 72

6.3.1 Hydrolysis and photolysis 72
6.3.2 Sorption and partition in Water/sediment systems 73
6.3.3 Microbial susceptibility and bioaccumulation potential 74
6.3.4 Interactions with co-existing pollutants and combined toxicity 75
6.4 Removal technology bottlenecks 78
6.4.1 Physical methods 78
6.4.1.1 Adsorption 78
6.4.1.2 Membrane technology 81
6.4.2 Chemical Technologies 81
6.4.2.1 Advanced Oxidation Processes (AOPs) 81
6.4.3 Biological Degradation 86
6.4.3.1 Phytoremediation (Microalgae) 86
6.4.3.2 Bacteria and bacterial consortia 90
6.4.3.3 Mycoremediation 91
6.5 Challenges and Future perspective 92
Chapter 7: Research Gap, Objective, and Originality 98
Chapter 8: High-Capacity Adsorption of Fluoxetine using Olive-Stone Derived Activated Biochar: Insights into Efficiency and Mechanism 99
Abstract 100
8.1 Introduction 101
8.2 Experimental 102
8.2.1 Materials and Methods 102
8.2.2 Biochar preparation and activation methods 103
8.2.3 Biochar characterization 103
8.2.4 Preliminary adsorption assays for biochar screening 103
8.2.5 Adsorption and kinetic studies 104
8.2.6 Regeneration and reusability 105
8.2.7 Adsorption mechanism 106
8.3 Results and Discussion 106
8.3.1 Biochar characterization and screening 106
8.3.2 Adsorption kinetics 109
8.3.3 Adsorption isotherm 115
8.3.4 Regeneration and reusability tests 117

8.3.5 Adsorption Mechanism 118
8.4 Conclusion 120
Chapter 9: Synergistic effect of CuO-biochar composite for efficient UVC photocatalytic treatment of Fluoxetine: Mechanism, Transformation products, and Toxicity assessment 123
Abstract 124
9.1 Introduction 125
9.2 Experimental 126
9.2.1 Materials and chemicals 126
9.2.2 Preparation and characterization of CO_2-activated olive stone biochar (BC) and CuO particles 127
9.2.3 Degradation of FLX and Mechanism of action 128
9.2.4 Identification of transformation products and ecotoxicity prediction 129
9.2.5 Matrix effects/ Degradation of FLX in simulated effluent 129
9.2.6 Catalyst reusability tests 129
9.2.7 Statistical analysis 130
9.3 Results and Discussion 130
9.3.1 Physicochemical characteristics of BC (CO_2-1000-30-600-1) and CuO 130
9.3.2 Adsorption behaviour of FLX on BC, CuO, and BC-CuO 132
9.3.3 Photolytic and photocatalytic degradation of FLX under UVC 136
9.3.4 Effect of water matrix: simulated effluent study 142
9.3.5 Transformation products, and their in-silico toxicity assessment 143
9.4 Conclusion 145
Chapter 10: Conclusions and Future Recommendations 147
10.1 Conclusions 147
10.2 A comparative review of Environmental Fate, Toxicity and Treatment implications: IMP vs FLX 149
10.3 Limitations of the study 151
10.4 Future Recommendations 152
Chapter 11: Bibliography 155
Appendices 182
Appendix A: Supplementary information for Chapter 4 183
Appendix B: Supplementary information for Chapter 5 194
Appendix C: Mechanism of action and Metabolites of FLX 205

Appendix D: Extraction and Detection of Fluoxetine from Wastewater and Wastewater sludge 208
Appendix E: Fluoxetine and metals: A Case of Complex Formation? 214
Appendix F: Supplementary Information for Chapter 8 221
Appendix G: Supplementary Information for Chapter 9 236

LIST OF TABLES

Table 2.1	Summary of IMP concentrations detected in wastewaters…….....	14
Table 2.2	Overview of degradation techniques employed for Imipenem (IMP)…….	17
Table 5.1	Summary of Imipenem concentrations detected in wastewater……...	43
Table 5.2	Electronic energy for different Imipenem-metal complexes from the computational study for different M: L ratios…….....	53
Table 5.3	Stoichiometric ratio and stability constants for different Imipenem-metal complexes from potentiometry…….....	55
Table 6.1	Summary of occurrence of FLX in wastewater and wastewater sludge.....	68
Table 6.2	Summary of interactions between FLX and other environmental co-pollutants……..	77
Table 6.3	Summary of removal of FLX by adsorption using different adsorbents in previous studies……	80
Table 6.4	Summary of FLX removal *via* Advanced Oxidation Processes (AOPs)……..	84
Table 6.5	Overview of FLX biodegradation performance in biological systems……	87
Table 6.6	Comparative assessment of FLX removal methods: Advantages and limitations…….	94
Table 8.1	Comparison of maximum adsorption capacities of FLX by different waste-derived adsorbents……	112
Table 8.2	Rate constants (k_1, k_2, and K_p) obtained for different initial concentrations of FLX by PFO, PSO, and Intraparticle diffusion kinetic model…….	115
Table 8.3	Langmuir and Freundlich isotherm model parameters of adsorption of FLX on biochar…….	116
Table 9.1	Rate constants (k_2) and adsorption capacities (q_e) for BC, CuO, and CuO + BC by PSO kinetic model …….	134
Table 9.2	Comparison of Fluoxetine (FLX) removal efficiency (%) at 2 and 20 minutes under different treatment conditions at initial concentrations of 25 and 50 mg/L…….	137
Table 9.3	Comparison of the photocatalytic response of several materials reported in literature for FLX degradation……	141

LIST OF FIGURES

Figure 2.1 Chemical structures for thienamycin and Imipenem (IMP)……. 12

Figure 4.1 Degradation kinetics of Imipenem (IMP) under three set of conditions: Set A (amber bottles, room temperature), Set B (clear glass Clear glass vials, room temperature), and Set C (Clear glass vials, refrigerated)…… 27

Figure 4.2 Time-dependent UV-visible spectra (λ= 280-400 nm) for IMP (a) 25 mg/L, (b) 125 mg/L, and (c) 250 mg/L stored in clear glass vials at room temperature. (d) shows normalized [0,1] UV-visible spectra for time-dependent spectrum of IMP (250 mg/L)…….. 29

Figure 4.3 (a.) UV-visible spectrum, and (b.) FTIR for Humic acid……. 30

Figure 4.4 Effect on the absorbance of (a.) 100 mg/L, and (b.) 50 mg/L of IMP at λ= 298 nm after exposure to humic acid (20 mg/L) in different volumetric ratios (2:1, 1:1, and 1:2, respectively)…… 31

Figure 4.5 UV-visible spectra of aqueous IMP solution and IMP spiked in wastewater at t = 0 and t = 5 (i.e., after 5 hours of natural solar exposure) ……33

Figure 4.6 UV-visible spectra for IMP-Cu-RNO system (IMP= 33, 165, 330 μM) (a-c); and rate of degradation of IMP in IMP-Cu (II) and IMP- Cu (II)- RNO system (d-f)……... 35

Figure 5.1 General structure of β-lactam antibiotics (a.) Cephalosporins, (b.) Penicillins, and (c.) Carbapenems; (d.) Monobactams. The β-lactam ring is shown in red……..41

Figure 5.2 Sampling points for wastewater and wastewater sludge collection from the Keswick Water Resource Recovery Facility (WRRF)……. 46

Figure 5.3 Concentrations of most abundant metals (Al, Ca, Cu, Fe, and Mg) in collected municipal wastewater (WW) and wastewater sludge samples. *(RS- Return activated sludge, TS- Thickened sludge, and liq- liquid fraction)…… 50

Figure 5.4 (a.) Optimized structure for IMP using DFT with the benchmarked B3LYP functional and 6-311 + G (2d, p) basis set (Electronic energy of -

1330.926349 Hartree and a dipole moment of 2.764476 Debye); (b.) charge delocalization and dipole moment in the optimized structure…….. 51

Figure 5.5 Toxicity studies of IMP and its metal complexes (1:1 and 1:2) in *Escherichia coli (E. coli)* ((a) and (b)); *Bacillus subtilis (B. subtilis)* and ((c) and (d)), respectively…… 57

Figure 6.1 Antidepressant consumption in OECD member countries (2020-2024)…….. 64

Figure 6.2 Statistics on antidepressant use in Canada and variations (2019-2023)…….... 65

Figure 6.3 Annual number of publications on FLX for 2000-2025. Data retrieved from Scopus using relevant keywords……...67

Figure 6.4 Substituent effects on the trifluoromethyl-benzyl group in FLX……. 70

Figure 8.1 SEM images of (i) Untreated biochar, (ii) Biochar loaded with 1 mg/L FLX, (iii) Biochar loaded with 25 mg/L FLX, and (iv) Biochar after desorption with MeOH for at magnification (A) 500x, (B) 5000 x. (C) shows EDS mapping for fluorine atom, inset shows EDS spectrum……108

Figure 8.2 (a.) Removal efficiency, and (b.) uptake (*qt*) of FLX by biochar 7 for FLX concentrations of 1, 5, 10, 25, and 50 mg/L for 0-120 minutes; (c). Removal efficiency, and (d.) uptake (*qt*) of FLX by biochar 7 and commercially available activated charcoal for FLX concentration of 50 mg/L for 0-120 minutes……..111

Figure 8.3 (a.) Removal efficiency, and (b.) uptake (*qt*) of FLX by biochar 7 for FLX concentrations of 25 mg/L for 0-120 minutes; (c.) Removal efficiency, and (d.) uptake (*qt*) of FLX by biochar 7 for FLX concentration of 50 mg/L for 0-120 minutes……113

Figure 8.4 Effect of (a) pH, (b) NaCl (ionic strength), and (c.) MeOH (organic solvent) on the adsorption of FLX (C0 25 mg/L) onto biochar……. 119

Figure 9.1 SEM images of pristine (a) BC and (b) CuO; and spent CuO + BC (c and d) 130

Figure 9.2 (a) XRD of synthesized CuO particles; Variation in (b) reflectance as a function of wavelength, (c) $[F(R)\ h\nu]^2$ and (d) $[F(R)\ h\nu]^{1/2}$ vs the photon energy (eV) for CuO and their extrapolation of the linear portion……... 132

Figure 9.3 Adsorption controls for FLX at initial concentrations of 25 and 50 mg/L shown as normalized concentration (C/C_0) in (a) and (c), respectively. (b) and (d) present the corresponding PSO kinetic model fits……133

Figure 9.4 Photocatalytic degradation of FLX using BC, CuO, and CuO-BC under UVC irradiation for initial FLX concentrations of (a) 25 mg/L, and (b) 50 mg/L; (c) in presence of scavengers ([FLX_0]= 25 mg/L), and (d) in simulated wastewater effluent ([FLX_0]= 25 mg/L) …….. 139

Figure 9.5 Proposed transformation products (TPs) for FLX after photocatalytic treatment with CuO-BC composite catalyst …….144

Figure 9.6 Predicted ecotoxicity indicators based on (a) acute values and (b) chronic values for FLX and its TPs generated during the proposed treatment (UVC-CuO/BC) ……145

LIST OF ABBREVIATIONS

AMC	Antibiotic-metal complex
AMR	Antimicrobial resistance
AOP	Advanced Oxidation Potential
APHA	American Public Health Association
BET	Brunauer-Emmett-Teller
BOD	Biochemical oxidation demand
CEC	Cation Exchange Capacity
CFU	Colony forming unit
cIAIs	Complicated intraabdominal infections
COD	Chemical oxidation demand
cUTI	Complicated urinary tract infections
DHP-1	Dehydropeptidase
ECOSAR	Ecological Structure Activity Relationship
EDA	Electron-donor-acceptor
EDC	1-Ethyl-3-(3-dimethylaminopropyl) carbodiimide
EDG	Electron Donating Group
EDS	Energy Dispersive X-Ray Spectroscopy
EWG	Electron Withdrawing Group
FLX	Fluoxetine
FTIR	Fourier Transform Infra-Red
HOMO	Highest occupied molecular orbital
ICP-OES	Inductively coupled plasma- Optical emission spectroscopy
IMP	Imipenem
IP	Intra-particle
ITC	Isothermal Titration Calorimetry
LC	Liquid chromatography
LC	Lethal Concentration
LOD	Limit of detection
LOQ	Limit of Quantification

LUMO	Lowest unoccupied molecular orbital
M: L	Metal to ligand stoichiometric ratio
MAE	Microwave Assisted Extraction
MBC	Minimal bactericidal concentrations
MES	2-(N-morpholino) ethane sulfonic acid
MIC	Minimal inhibitory concentrations
MS	Mass spectrometry
MS/MS	Tandem mass spectrometry
NF	Nanofiltration
NMR	Nuclear Magnetic Resonance
NOM	Natural organic matter
PA	Polyamide
PBP	Penicillin binding proteins
PEG	Polyethylene Glycol
PFO	Pseudo First Order
pH	Potential of hydrogen
pHzc	Point of zero charge
PMS	Peroxymonosulphate
PDS	Peroxydisulfate
PNEC	Predicted no-effect concentration
PS	Polystyrene
PSO	Pseudo Second Order
RAS	Return activated sludge
RO	Reverse Osmosis
SEM	Scanning Electron Microscopy
SPE	Solid phase extraction
SSRI	Selective Serotonin Reuptake Inhibitor
TGA	Thermogravimetric analysis
TS	Thickened sludge
TSB	Tryptic Soy Broth
UV-vis	UV-visible spectroscopy

WW	Wastewater
WRRF	Wastewater resource recovery facility
WWS	Wastewater sludge
WWTP	Wastewater treatment plant

RESEARCH CONTRIBUTIONS

LIST OF PUBLICATIONS OF THIS THESIS

1. **Khurana, P**., Pulicharla, R., Kaur Brar, S., 2021. Antibiotic-metal complexes in wastewaters: fate and treatment trajectory. **Environment International** 157, 106863. https://doi.org/10.1016/j.envint.2021.106863

2. **Khurana, P**., Pulicharla, R., Kaur Brar, S., 2022b. Analytical challenges of antibiotic-metal complexes in wastewaters: A mini-review. **Environmental Nanotechnology, Monitoring & Management** 18, 100747. https://doi.org/10.1016/j.enmm.2022.100747

3. **Khurana, P**., Pulicharla, R., Brar, S.K., 2023. Imipenem-metal complexes: Computational analysis and toxicity studies with wastewater model microorganisms. **Environmental Research** 117275. https://doi.org/10.1016/j.envres.2023.117275

4. **Khurana, P**., Pulicharla, R., Brar, S.K., 2024. Occurrence of Imipenem in natural water: Effect of dissolved organic matter and metals. **Science of The Total Environment** 957, 177846. https://doi.org/10.1016/j.scitotenv.2024.177846

5. **Khurana, P**., Kumar Das, R., Kaur Brar, S., 2025. From prescription to pollution: environmental behaviour and breakdown of fluoxetine. **Environmental Science: Water Research & Technology**. 11, 2825-2843. https://doi.org/10.1039/D5EW00636H

6. **Khurana, P**., Sran, S., Kumar Das, R., Sanchez-Silva, L., Kaur Brar, S., 2025. High-capacity adsorption of fluoxetine using olive-stone derived activated biochar: insights into efficiency and mechanism. **RSC Advances**, 15, 20330–20340. https://doi.org/10.1039/D5RA01258A

7. **Khurana, P**., Kumar Das, R., Kaur Brar, S., 2026. Synergistic effect of CuO-biochar composite for efficient UVC photocatalytic treatment of Fluoxetine: Mechanism, Transformation products, and Toxicity assessment. (Submitted)

LIST OF PUBLICATIONS OUT OF THIS THESIS

1. **Khurana, P**., Hasaneen, N., Pulicharla, R., Kaur, G., Brar, S.K., 2022a. Co-transport of PFCs in the environment- An interactive story. **Current Research in Green and Sustainable Chemistry** 5, 100302. https://doi.org/10.1016/j.crgsc.2022.100302

2. **Khurana, P**., Shu, X., Kaur, G., Pulicharla, R., Kumar, P., Brar, S.K., 2025a. Long chain perfluoro carboxylic acids in landfill leachate: Extraction, detection and biodegradation.

Journal of Environmental Management 373, 123518. https://doi.org/10.1016/j.jenvman.2024.123518

3. Nayebi, B., **Khurana, P**., Pulicharla, R., Karimpour, S., Kaur Brar, S., 2023. Preservation, storage, and sample preparation methods for freshwater microplastics – a comprehensive review. **Environmental Science: Advances** 2, 1060–1081. https://doi.org/10.1039/D3VA00043E

4. Chekili, M.; **Khurana, P.;** Etteieb, S.; Brar, S. K.; Blais, J.-F. Assessing Pharmaceuticals and Personal Care Products (PPCPs) and Their Environmental Risk in a Lake in North Quebec. **Case Studies in Chemical and Environmental Engineering** 2025, 12, 101295. https://doi.org/10.1016/j.cscee.2025.101295

5. Klanovicz, N.; **Khurana, P.**; Ramos, B.; Treichel, H.; Brar, S. K.; Teixeira, A. C. S. C. Efficient Degradation of Carbamazepine in Continuous and Batch Modes by Laccase-Photo-Fenton-Intensified Hybrid Treatment. **ACS EST Water** 2025, 5 (12), 7253–7266. https://doi.org/10.1021/acsestwater.5c00676

LIST OF CONFERENCES

1. **Khurana, P**., Pulicharla, R., Brar, S.K. (2024) Fate and Interactions of Imipenem in Wastewater: Assessing Stability and Environmental Impact. IWA World Water Day Congress and Exhibition, August 11-15, 2024, Toronto Metropolitan Centre, Toronto, Canada.

2. **Khurana, P**., Pulicharla, R., Brar, S.K. (2023). Antibiotic residues and metals: A deadly cocktail in wastewater. 58th Central Canadian Symposium on Water Quality Research (CAWQ), March 20-21, 2023, York University, Canada.

3. **Khurana, P**., Pulicharla, R., Brar, S.K. (2022). A comparative analysis of toxicity: Imipenem v/s Imipenem-metal complexes. 36th Eastern Canadian Symposium on Water Quality Research (CAWQ), November 4, 2022, Institut national de la recherche scientifique (INRS), Canada.

4. **Khurana, P.**, Pulicharla, R., Brar, S.K. (2021), Rapid and rugged analytical method for long chain perfluoro carboxylic acids (C9 and C10) in landfill leachate: Direct MS injection. Virtual Atlantic and Eastern Canadian Symposium on Water Quality Research (CAWQ), November 2-3, 2021, Canada.

5. **Khurana, P**., Pulicharla, R., Brar, S.K. (2021). Advances in analytical techniques: Unravelling antibiotic-metal complexes in wastewater. Eastern Analytical Symposium, November 15-17, 2021, NJ, USA.

LIST OF BOOK CHAPTERS

1. Hasaneen, N., **Khurana, P**., Pulicharla, R., Rezai, P., Brar, S.K., 2024. Nanomaterial-Based Sensors for Macrolide Sensing, in: Mohanta, D., Chakraborty, P. (Eds.), Nanoscale Matter and Principles for Sensing and Labeling Applications. Springer Nature, Singapore, pp. 513–535. https://doi.org/10.1007/978-981-99-7848-9_25

2. **Khurana, P**., Pulicharla, R., Brar, S.K., 2022. Chapter 16 - Modular drinking water systems: chemical treatment perspective, in: Kaur Brar, S., Kumar, P., Cuprys, A. (Eds.), Modular Treatment Approach for Drinking Water and Wastewater. Elsevier, pp. 281–302. https://doi.org/10.1016/B978-0-323-85421-4.00012-7

Chapter 1: Introduction

Emerging contaminants have garnered increasing attention from regulatory authorities worldwide, primarily because of their widespread detection in aquatic environments. Among these, human pharmaceuticals have been identified as a key concern and officially recognized by UNESCO as contaminants of emerging concern (CECs). Addressing their presence in the environment, including their detection and removal, has been included in the 2030 Agenda for Sustainable Development Goals by UNESCO [1,2]. Among these, antibiotics and antidepressants are of particular concern because of their unique modes of action and ecological implications, coupled with widespread consumption and frequent detection in the environment.

While antibiotics are a crucial component of modern medicine for the treatment and prevention of existing and 'new' clinical infections, the misuse, overuse, and inappropriate prescription of antibiotics directly contribute to an increase in the incidence of multi-drug resistant (MDR) infections. For instance, in Canada, from 2018 to 2023, the consumption of the 'Reserve' category antimicrobial increased by 52.3%, while total human antibiotic use decreased in all Canadian jurisdictions for 'Access' and 'Watch' antibiotics [3]. Similarly, the use of 'Reserve' antibiotics increased from <1% to 10% between 2014-2018, with an increase of more than 120% in the use of carbapenems alone [4]. Carbapenems are a class of antibiotics used to treat MDR infections, making them an important class for research. In this sense, Imipenem (IMP), which was the first carbapenem, was selected as a model antibiotic for the new class of antimicrobials. IMP is a broad-spectrum carbapenem antibiotic, commonly employed in combination therapies for MDR infections.

In addition to the antibiotic IMP, an antidepressant, Fluoxetine (FLX) was selected as the other model pharmaceutical. During the COVID-19 pandemic, the increased rates of incidence of psychiatric and mental disorders have led to an increase in the prescription rates and consumption of antidepressants globally. For instance, Canada has seen a 26% increase in the use of antidepressants from 2019 to 2023, with over 2.5 billion units (tablets/capsules) dispensed in 2023 [5]. Among all the antidepressants, FLX, a selective serotonin reuptake inhibitor, is the most commonly prescribed antidepressant globally for the treatment of depression, because of its tolerance, effectiveness, safety and prolonged half-life [6,7]. In the US in 2017, approximately 21

million prescriptions of FLX were filled, suggesting a relatively high level of consumption [8]. Owing to its ability to cross the blood-brain barrier (BBB) and human placenta due to its lipophilic nature, FLX poses a risk to all biomes [9]. The drug's uptake in fish has been reported to have consequences on growth and behaviour, reproductive axis, metabolism, accumulation, and gene expression [10–15]. This emerging pharmaceutical contaminant presents unique environmental challenges due to its resistance to natural degradation and its endocrine-disrupting potential, making its remediation an underexplored yet critical area of research.

Overall, both of these pharmaceuticals are significant in their own right and widely used and detected in aquatic environments, raising concerns about their environmental fate and impact. However, both these drugs exhibit widely varying behaviour based on their intrinsic chemical stability and interaction potential with metals, which play a crucial role in defining their behaviour in such environments and influencing the decision regarding the need for their intervention. It also helps determine if active removal strategies are required or if natural attenuation/transformation processes are sufficient for their management. In complex environments, interactions with metal ions can significantly influence the transformation, mobility, and toxicity of these parent drugs. Previous studies have reported that the co-occurrence of pharmaceutical residues and metals can facilitate the formation of pharmaceutical-metal complexes with altered bioactivity profiles and physicochemical properties, including solubility, photolysis, partition coefficient, and toxicity profiles [16–19]. It is speculated that the structural features of pharmaceutical residues allow them to act as organic ligands for metal complexation, and these metal complexes have higher persistence and toxicity than parent drugs due to electron delocalization and increased lipophilicity. However, minimal studies have been directed at the occurrence of metal complexes of these pharmaceutical residues. This knowledge gap limits the ability to prioritize these contaminants accurately and select suitable intervention measures in the treatment chain. In this regard, the present research analyses pharmaceutical-metal complexity for two model pharmaceuticals with contrasting behaviour: IMP, an antibiotic, and FLX, an antidepressant. Their occurrence in wastewater has frequently been reported; however, the potential of these pharmaceuticals to interact with co-existing metals has not been thoroughly investigated.

The objective of this thesis, therefore, is to investigate their environmental behaviour, focusing on their stability and metal interactions, and devising removal/degradation strategies where

applicable. The antibiotic served as a model compound for an unstable pharmaceutical, whereas FLX represents a structurally stable, persistent pharmaceutical that requires intervention. The selection of IMP and FLX is intended to represent two contrasting classes of pharmaceuticals with fundamentally different environmental stability, reactivity, and treatment requirements. In this dissertation, IMP served as a representative model of a relatively unstable and environmentally labile pharmaceutical, enabling assessment of whether intrinsic degradation and metal interactions may reduce the necessity for engineered treatment inventions. In contrast, FLX represents a structurally persistent pharmaceutical with no natural attenuation, thereby necessitating the development and evaluation of engineered removal strategies.

The thesis is divided into two parts: Part A, dedicated to IMP, and Part B, dedicated to FLX, respectively, with two research objectives each. Part A (Imipenem: Stability, Metal Interactions, and Toxicity) includes chapters 2 to 5, which are outlined as follows: Chapter 2 is the review of literature, which critically examines the existing literature for the antibiotic IMP and identifies the knowledge gaps that underpin this study. Chapter 3 introduces the research gaps, outlines the objectives (objectives 1 and 2) and states the originality of the study. Chapter 4 is devoted to the first objective of Part A of this dissertation and explores the effect of dissolved organic matter and metals on the occurrence and stability of IMP in aqueous solutions, while Chapter 5 continues to study the metal complexation of IMP and investigates their toxicity towards wastewater model bacterial species *E. coli* and *B. subtilis*. However, since the drug was found to be sensitive to light, temperature, and ambient conditions, a degradation technique was not deemed necessary and therefore, not developed for the antibiotic.

Following that, Part B (Fluoxetine: Literature insights and treatment strategies) includes chapters 6 to 9, drafted as: Chapter 6 provides a review of the literature for the structural features, environmental fate and persistence of the antidepressant FLX, and elaborates on the various removal techniques reported for FLX-polluted waters. Chapter 7 identifies the research gaps, discusses the objectives, and lists the originality of the study. Chapter 8 introduces olive-stone-derived activated biochar (BC) as a high-capacity adsorbent and a potent removal strategy for FLX, followed by Chapter 9, which proposes CuO-BC as a potential composite photocatalyst under UVC irradiation for the rapid degradation of FLX.

The findings of both parts are then followed by chapter 10, which presents conclusions, a comparative review of environmental fate, toxicity and treatment implications of both the pharmaceuticals, limitations of the present study and recommendations for future research. Both these pollutants possess distinct physicochemical properties that enabled the exploration of a diverse range of behaviours exhibited by pharmaceutical residues in the environment.

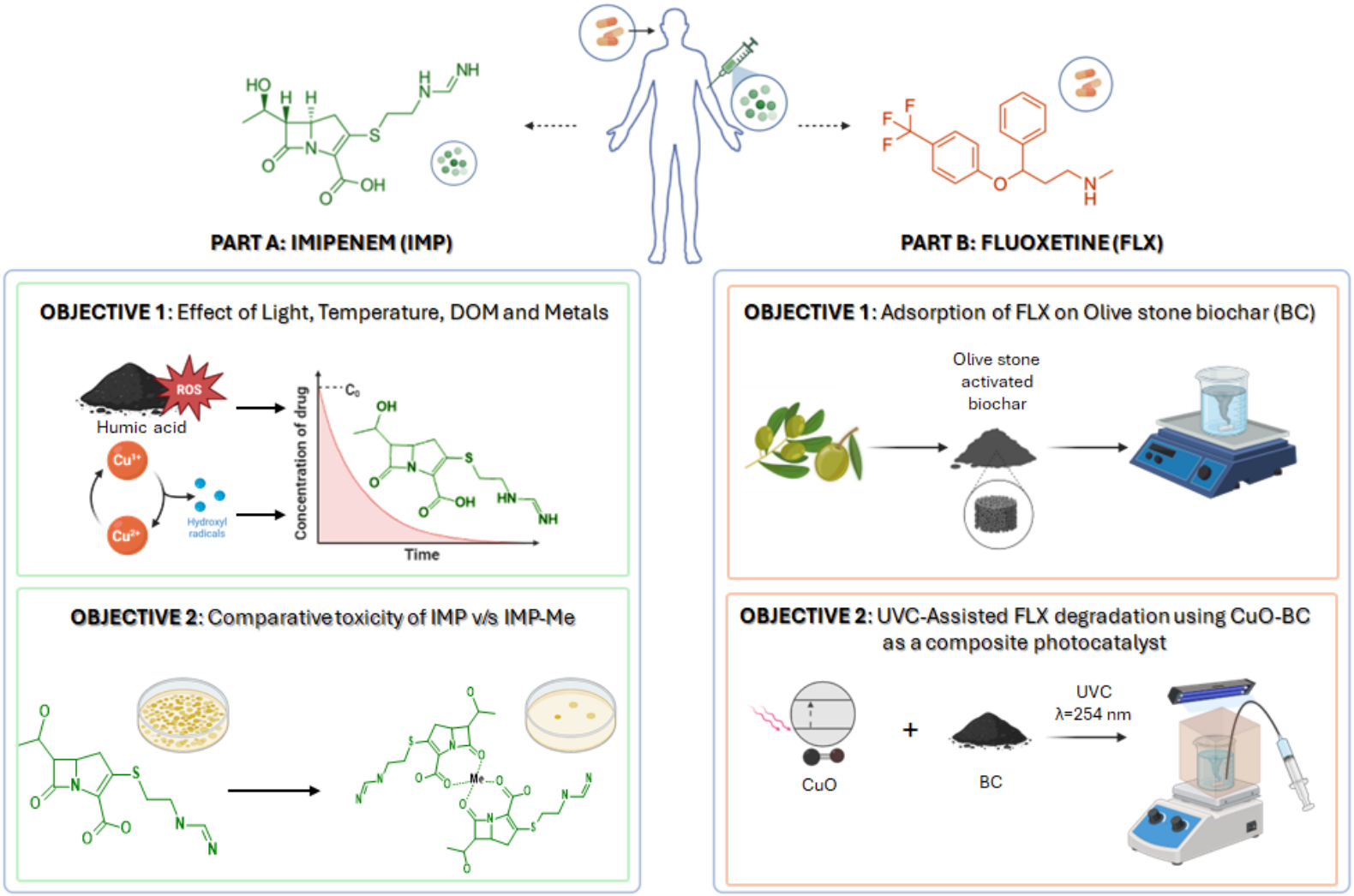

*IMP= Imipenem; FLX= Fluoxetine; DOM= Dissolved Organic Matter; IMP-Me= Imipenem-metal complexes; BC= Biochar; CuO= Cupric (II) Oxide

PART A: IMIPENEM: STABILITY, METAL INTERACTIONS, AND TOXICITY

Chapter 2: Review of Literature

(*Some of the content of this chapter is based on the Review article as communicated as a part of the present study: Khurana, P., Pulicharla, R., Kaur Brar, S., 2021. Antibiotic-metal complexes in wastewaters: fate and treatment trajectory. Environment International 157, 106863. https://doi.org/10.1016/j.envint.2021.106863)*

2.1 Introduction

The use of pharmaceuticals, including antibiotics, has greatly improved the lives of people across the globe. However, due to high prescription rates, improper disposal (expired/unused medication), incomplete utilization (not completing the antibiotic course) and low absorption (30-70%), these drugs are continuously released into different environmental compartments, either unchanged or in the form of active metabolites, including wastewater, surface and drinking water. This has long been acknowledged as a potential health concern due to the development and dissemination of antibiotic-resistant bacteria and genes, primarily due to prolonged exposure to residual antibiotics in environmental reservoirs [18,19].

Further, these antibiotic residues go through a vicious cycle of physical, chemical, and biological transformations or degradation once they are released into the environment, which may result in the generation of unknown intermediate by-products that might have unpredictable effects on ecosystems [20,21]. They can interact with co-existing pollutants, such as heavy metals, and exhibit changes in physicochemical properties due to metal complexation. The structural features of antibiotic molecules, such as hydroxyl, ether, carboxylic acid, carbonyl, enable them to chelate with several divalent and trivalent metal ions such as Cu (II), Co (II), Fe (II), Ca (II), Al (III), coexisting in the water matrix, and form stable coordination antibiotic-metal complexes (AMCs) with altered properties, including solubility, photolysis, partition coefficient, and toxicity profiles [18,19,22,23]. Metal complexation can also influence the natural degradation processes of antibiotics, for example, photo-degradation of tetracyclines is affected by metals (Mg^{2+}, Ca^{2+}), further increasing the risk of bioaccumulation due to prolonged exposure [24]. AMCs are more probable in wastewater matrices that are co-contaminated with antibiotics and heavy metals, such as pharmaceutical, hospital, livestock, poultry, municipal, and domestic wastewaters, and can induce

the selection and growth of antibiotic-resistant bacteria and genes, as reported in recent years [19,25,26].

Although there is a lack of information about the prevalence and concentrations of these contaminants in wastewater and sludge matrices, these complexes are studied to possess increased antibacterial properties than parent compounds. This can affect microbial communities in receiving environments, including activated sludge, and can adversely affect existing water treatment systems [19]. Further, due to electron delocalization during metal chelation, the lipophilicity of the antibiotic can increase, which facilitates the interactions of AMCs with the bacterial cell membrane [27]. However, the toxicity and activity against microorganisms depend on several factors, including the nature of metal ions and antibiotic, the chelate effect, and the charge of the complex[19,28].

Since they are more toxic than parent compounds, they may also affect microbial communities, like bacteria and fungi, which are an integral part of our ecosystem. Recent studies corroborate that the interaction between metals and antibiotics alters the behaviour of the complexes towards existing biological methods of water treatment [24,25,29]. In general, these complexes are toxic towards bacteria and might reduce bacterial communities present in activated sludge on longer exposure and adversely affect the existing biological water treatment systems [19]. Besides, these communities are inevitably under pressure, as long-term exposure to these diverse AMCs might result in the development of multi-resistant bacteria [19,30,31]. Therefore, this joint toxicity of antibiotics and metals, and formation of AMCs, is seen to be more severe than single toxicity and is, therefore, perceived as an emerging area of interest in environmental chemistry [32,33]. To the best of our knowledge, the formation of AMCs in complex environmental matrices, such as wastewaters, has been overlooked, and no attempt has been made for their detection, quantification, and characterization.

2.2 Fundamentals of antibiotic-metal complexation

This section presents a general overview of properties, which allow metal ions to bond well and produce stable adducts with antibiotics in real-time WWTPs (wastewater treatment plants).

2.2.1 Structural features of Antibiotics related to the complexation

Antibiotics contain several electron-rich functional groups which act as potential metal binding sites for AMC formation. For example, the ligand characteristics of Penicillins and Cephalosporins are due to the penam and cefem groups, i.e., β-lactam ring linked to thiazolidine, and dihydrothiazine, respectively [34]. They, along with their respective aliphatic side chains, bind to metal centers to form stable complexes comprising 5-membered ring structures. Likewise, the tetracyclines, too, contain various electron-donating groups, such as acetamides ($-CH_2CONH_2$) at C2, dimethylammonium ($-N(CH_3)_2$) at C4, and beta-diketone at C10-12, that allow metal linkage in different stoichiometries [22,35]. They act as a monodentate, or bidentate, or bridging ligand, depending upon the pH and the relative concentrations of metal ions and the ligands in the wastewater streams.

Treatment plants' working conditions, such as pH, often influence the ability of antibiotics to form metal complexes. The functional groups ionize and display dynamic conformations with varying pH of the medium. The pH variations of the medium further change the preference order of the donor sites for metal coordination and the efficiency of the binding. A pH-dependent study of tetracyclines and divalent metal ions by Carlotti et al. (2012) pointed out the effect of pH, which dominates over the metal ion concentration, to decide the stoichiometry of the complexes [22].

Besides the several ionizable chemical functional groups, the relative energies of HOMO (Highest Occupied Molecular Orbital) and LUMO (Lowest Unoccupied Molecular Orbital) (showed as E_{HOMO} and E_{LUMO}) also play a crucial role. The energy profiles of molecular orbitals measure the electron-donating and accepting tendencies and the nature of the complexation between these entities. For complexation between antibiotic ligands and metal centres, antibiotics should have higher E_{HOMO} to ensure an easy electron donation to the metal ions. A higher value of E_{HOMO}, such as that reported for chloramphenicol by Al-Khodir and Refat (2016), indicates an easy release of electrons and strong e-donation ability [36]. Lower E_{LUMO} signifies a good acceptance of electrons.

2.2.2 Chemical properties of metals related to the complexation process

a. Ionic radius, surface charge, and the charge density: A study by Demitras (1972) revealed that metal cation with higher charge density, i.e., smaller cationic radii with higher ionic charge

(high polarizing metals or hard Lewis's acid), results in a more stable complex. This is because small size, coupled with a high surface charge, favours closer proximity to the negatively charged organic ligands and results in a greater force of attraction. Also, the positive charge of the metal and the negative charge from the ligands get delocalized over the entire framework, reducing the polarity of the metals, and stabilizing the whole chelated system [37,38]. The analysis of the interaction of quinolones with metals showed higher complex formation constants with trivalent cations (Al^{3+}, Fe^{3+}) than bivalent alkaline earth metal cations (Mg^{2+}, Ca^{2+}, Ba^{2+}) [39].

Recent studies also reveal that transition metals form more stable and persistent complexes than alkaline earth metals due to their higher nuclear charge. For ions with the same ionic charge, the ionic radius is the measure of the strength of the metal-ligand bond. Park et al. (2000) determined that the stability of complexes formed by the drugs ofloxacin and norfloxacin with metal cations of the beryllium group follows the order: Mg^{2+}> Ca^{2+}> Ba^{2+}, owing to the increasing size of metal ions [40]. The metal radius also determines the binding site of the antibiotic, which otherwise contains multiple preferable functional groups for coordination.

b. Electronic interactions: Besides, the electronic factors also govern the stability of these antibiotic-metal complexes. To cite and strengthen this hypothesis, a comparison of complex formation constants by Park et al. (2000) revealed that Ni^{2+} and Co^{2+} form more stable coordination complexes with fluoroquinolones (ofloxacin and norfloxacin) than Zn^{2+} and Mn^{2+} [40]. For half and full-filled d orbitals of Mn^{2+} and Zn^{2+}, respectively, the interactions between the metal and antibiotic orbitals are limited, and the constant is determined only by weak ion-dipole interactions. Ni^{2+} and Co^{2+} have higher value of stability constants owing to additional inter-electronic interactions of the participating orbitals of the ligands and the d orbitals of the metal ions.

c. **Ionization potential and electronegativity**: Other than nuclear charge, the ease of formation and stability of AMCs further depends upon the type of interaction in the metal-ligand bonds [41,42]. The M-L bonds are typically stabilized by either electrostatic interactions or the covalent linkage between the two entities. It is a function of the ionization potential, the electron affinity of the metal, and the electronegativity difference between the metal and the donor atoms of the binding site [43]. The electronegativity difference of <1.7 units on the Pauling scale indicates covalent bond formation. The electrostatic interactions between partially ionized species depend inversely on the ionic radii. Metals with a larger radius have lower ionization and oxidation

potential, i.e., they tend to lose electrons and form complexes readily, and vice versa. In addition, Ghandour et al. (1992), by conducting potentiometric studies, suggested the dominance of stable covalent bond formation between tetracycline ligands in determining the transition metal stability constants [44]. Other factors, such as the chelate effect, the total charge of the complex, the nature of the ion neutralizing the ionic complex, nuclearity of the metal centre, and thermodynamic and kinetic factors of the complex, also determine the properties of AMCs.

2.3 Introduction to Imipenem: Structure, Mechanism, and Environmental occurrence

Imipenem (IMP) is a broad-spectrum, semisynthetic, carbapenem β-lactam antibiotic used extensively to treat endocarditis, respiratory tract (including pneumonia), urinary tract, abdominal, gynecological, blood, skin, bone, and joint infections. It was the first member of a relatively new class of antibiotics, Carbapenems (a class of β-lactam antibiotics), discovered in the 1970s. First marketed in Canada in 1987, IMP immediately attracted attention because of its broadest antibacterial spectrum of any antibiotic available then. It belongs to 'Reserve' category of antibiotics and is administered as combinational therapy (PRIMAXIN-IMP and Cilastatin; or RECARBRIO- IMP, Cilastatin and Relebactam) to treat moderate to severe bacterial infections and against infections caused by multidrug-resistant bacteria.

2.3.1 Structure of IMP

Imipenem (IMP), or N-formimidoyl thienamycin, is the amidine derivative of the parent compound thienamycin, isolated from the soil microorganism *Streptomyces cattleya* [45]. The chemical structures for both thienamycin and IMP are shown in Figure 2.1.

Naturally produced thienamycin exhibits potent, broad-spectrum antibacterial activity; however, its chemical instability- due to a highly reactive amino group- limited its therapeutic applicability [46]. Nevertheless, the structural backbone of thienamycin demonstrated exceptional resistance to most beta-lactamases, thereby serving as a foundation for the synthesis of IMP following structural modification. IMP was developed through a deliberate substitution of a formimidoyl group at the C-2 of the amino group, which conferred improved stability and enabled its formulation as a broad-spectrum antibacterial drug [45,47,48]. Unlike conventional β-lactams like penicillins and

cephalosporins, the trans configuration at the 5R and 6S in IMP (and all other carbapenems) enhances their resistance to β-lactamase hydrolysis [47].

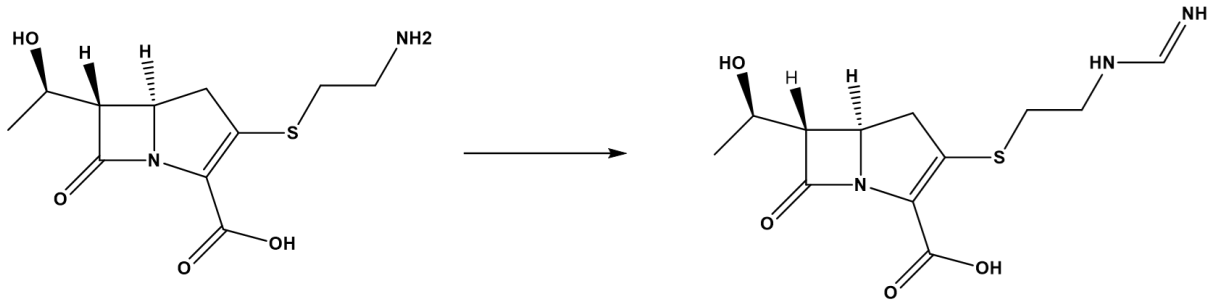

Thienamycin Imipenem (IMP)

Figure 2.1: Chemical structures for thienamycin and Imipenem (IMP)

The structure of the drug IMP is characterized by a fused beta-lactam and a five-membered pyrroline ring, with a N-formimidoyl substituent at the C-2 position. It features both carboxylic acid and primary amine in its structure, with reported pKa values of 3.2 and 9.9, respectively [49]. At circumeutral pH, IMP is expected to exist in its zwitterionic form, enhancing its solubility and membrane interactions. The low partition coefficient (log P~ -2.7 to -3.1) of the antibiotic indicates high hydrophilicity and poor lipid solubility. These properties suggest IMP's low sorption to sediments and high mobility in aquatic systems, which influence the environmental fate of the pharmaceutical residue.

2.3.2 Dosing, Metabolism and Pharmacokinetics

IMP is not effectively absorbed from the gastrointestinal tract. Rather, it is administered intravenously in a 1:1 ratio with Cilastatin in doses of either 500 mg or 1000 mg every 6 to 8 hours, depending on the severity of the infection [50]. Protein binding of IMP is low (13-21%), and the elimination half-life of IMP in normal renal function is about an hour [45,47]. The mean maximum plasma concentrations (C_{max}) at the end of infusion are 30-35 mg/L and 60-70 mg/L for the two dosing schemes [50 48]. When administered with Cilastatin, about ~70% of IMP is renally eliminated as the parent compound [47].

IMP is susceptible to rapid *in-vivo* degradation by enzyme dehydropeptidase (DHP-1), secreted by the proximal renal tubules of mammals. Briefly, the brush border dipeptidase hydrolytically cleaves the carbapenem nucleus, rendering the drug inactive [45]. To combat this, IMP is co-administered in a 1:1 ratio with Cilastatin and marketed under the brand name Primaxin (MSD) and Recarbrio. As a result, urinary recovery of intact IMP is about ~70%. Cilastatin is a specific and reversible DHP-1 inhibitor, and it prevents nephrotoxicity caused due to IMP administration. Further, Cilastatin has a similar pharmacokinetic profile as IMP, ensuring the same dosing schedule for both the compounds.

2.3.3 Antibacterial spectrum and Mechanism of action

The antibacterial spectrum of IMP is very broad and exceeds most of the currently available β-lactam antibiotics (Penicillins and Cephalosporins). IMP had the broadest in-vitro bacterial coverage at the time of its approval, encompassing gram-positive and gram-negative aerobes, such as *Serratia marcescens* and *Pseudomonas aeruginosa* and anaerobes such as *Bacteroides fragilis*, and was least affected by the inoculum size [45,47]. However, methicillin-resistant *Staphylococcus aureus* (MRSA), methicillin-resistant coagulase-negative staphylococci, *Streptococcus faecium*, *Pseudomonas cepacia*, and *Pseudomonas maltophilia* are some exceptions to this extensive antibacterial coverage [47]. For most organisms, minimal bactericidal concentrations (MBC) are close to the minimal inhibitory concentrations (MIC). Organisms with MIC $\leq$ 4 μg/mL are considered susceptible, organisms with 4 < MIC< 8 μg/L moderately susceptible, and organisms with MIC ≥8 μg/ml are considered resistant [45].

IMP is bactericidal and has a strong affinity toward penicillin-binding proteins (PBPs). IMP binds to PBPs, inhibits cell wall synthesis, and ultimately results in cell death. In addition, it was suggested that the molecule might easily pass the bacterial cell walls owing to its small size and zwitterionic state [45].

2.3.4 Environmental occurrence and fate of IMP

According to the AWaRe classification (Access, Watch, and Reserve) of antibiotics, IMP is an antibiotic reserved for hospital settings. That is, IMP is generally used to treat multidrug-resistant infections- infections that are resistant to other 'common' antibiotics. With the increase in

multidrug-resistant infections, their use is also growing steadily and is now starting to be detected in wastewater. Some of the recent studies are summarized in Table 2.1

Table 2. 1: Summary of IMP concentrations detected in wastewaters

Matrix	**Concentration**	**Method of detection**	**Year and Location**	**Ref.**
Tienam imipenem production facility	4.09-6.46 ng/L in influent; ND after MBR	HPLC-UV	2015 Taiwan	[51]
Hospital wastewater effluent (raw effluent)	14.42 µg/L	Solid Phase extraction (SPE) + LC-MS/MS	2017 Cluj County, Romania	[52]
Wastewater	198.4-4958.5 ng/L in influent 6.4-823.2 ng/L in effluent	SPE + LC-MS/MS	2017 Croatian secondary (sewage) WWTP, Zagreb	[53]
Municipal wastewater influent	10.80 µg/L	SPE + HPLC-UV	2017 Hamadan, Iran	32
Hospital wastewater	25.53 µg/L	SPE + HPLC-UV	2017 Hamadan, Iran	[55]
Pharmaceutical wastewater	0.012-7.242 ng/L in influent ND in effluent	UFLC-MS/MS	2024 India	[56]
Groundwater	0.018-3.251 ng/L	UFLC-MS/MS	2024 India	[56]
Hospital wastewater	3.12-110.37 ng/L	SPE + LC-MS/MS	2025 Poland	[57]

It is evident from these findings that reported concentrations for the antibiotic range from few ng/L to tens of µg/L, with LC-MS/MS and HPLC-UV being the most common detection methods. It is also noteworthy that effluent concentrations, where reported, usually exceed the predicted no-effect concentration (PNEC) (EUCAST database) of 125 ng/L for IMP, indicating a potential risk for antibiotic resistance selection in aquatic environments [53]. Residual IMP can exert a selective pressure on environmental bacteria, promoting the emergence and dissemination of carbapenem-resistant genes outside clinical settings.

However, despite its frequent detection, most studies have focused primarily on antibiotic resistance, while largely overlooking its environmental fate. Once released in wastewater, IMP may undergo physical, chemical, and biological transformations that influence its environmental occurrence, persistence, and potential toxicity. Understanding these transformation pathways is critical for assessing their long-term impact on the aquatic system.

Early pharmaceutical studies highlight that IMP is chemically labile and exhibits sensitivity to pH, temperature, oxygen, humidity, and solvent composition. For instance, Smith et al. (1989) investigated the degradation of IMP in aqueous solutions at acidic (citrate buffer; pH 4) and alkaline (borate buffer; pH 9-9.5) conditions. The study reported that the drug undergoes hydrolysis under both conditions. In weakly acidic media, IMP undergoes complex oligomerization by intermolecular attack of the carboxyl group on the beta-lactam ring, while in alkaline conditions, formimidoyl side chain attacks the beta-lactam ring, resulting in intermolecular products [58]. A similar study by Mendez et al. (1991) revealed that the degradation kinetics of IMP were significantly faster at acidic and alkaline pH, with maximum stability observed around neutral conditions (pH 6.4) [59]. A similar finding was reported by Swanson et al. [60].

More recent studies have also identified temperature, oxygen, concentration as potential factors that affect the half-life of the antibiotic [61–63]. Although most of the studies focus on solvents used for injections and extended infusions under controlled conditions for pH, ionic strength, and temperature, they provide important benchmarks for understanding influencing the degradation kinetics of IMP. The interplay of these parameters significantly affects the stability profile of IMP, which explains the variability in the reported stability results. This variability has also been observed for other carbapenems such as Ertapenem, Meropenem, and Doripenem [64–69]. However,

it is crucial to recognize that buffered laboratory systems may not fully replicate in real environmental matrices, where water quality fluctuates and interfering substances like natural organic matter (NOM) and metals can further influence degradation rates. The effect of NOM and metals remain unexplored for IMP, and yet a critical area of research.

2.3.5 Treatment technologies for IMP-polluted water

With increasing awareness of antibiotic residues as emerging contaminants, new and innovative degradation techniques, have been devised and applied for IMP, as summarized in Table 2.2. For instance, an integrated advanced oxidation-reduction process (AORP), using UVC/Fe^{2+}/H_2O_2, was employed in a batch mode to degrade IMP/Cilastatin antibiotic (ICA) from synthetic wastewater. The conditions to achieve maximum antibiotic removal (~100%) while minimizing energy consumption were optimized for 5-7.5 mg/L antibiotics in 18.9-33.86 minutes of reaction using 0.74-1.2 mM Fe^{2+} and 0.28-0.32 mM H_2O_2 at pH 3 (Godini et al., 2019). Further, the performance of different AORPs (UV alone, UV/Fe^{2+}, UV/ H_2O_2, and Fe^{2+}/ H_2O_2) (operated at an initial antibiotic concentration of 5 mg/L, reaction time of 40 min, 1.2 mM Fe^{2+}, 0.32 mM H_2O_2 and pH 3) showed antibiotic removal of 17%, 57%, 73%, and 70%, respectively. The study underlined that both oxidation (UV/ H_2O_2 and Fe^{2+}/H_2O_2) and reduction (UV/Fe^{2+}) play significant roles in the degradation of IMP, and simultaneous generation of oxidizing (OH•) and reducing agents (e^-) can improve degradation efficiency (Godini et al., 2019). Another piece of literature has reported that the drug undergoes fast hydrolysis at a pH of 4 or lower and thereby explored the potential of the Fenton process activated by zero-valent Iron (ZVI-Fenton) to degrade IMP in urban wastewater at a pH of 5 (Furia et al., 2021).

Other than AOPs, photochemical degradation under natural solar radiation and heterogenous photocatalysis, with TiO_2 as a catalyst, was studied to degrade carbapenem antibiotics, including IMP, from aqueous solutions (Cabrera-Reina et al., 2019; Reina et al., 2018). It was observed that about 88% of the antibiotic was photodegradable after 300 min of irradiation under natural solar light (for initial concentrations of 90.0224 mM (i.e. 7.12 mg/L) to 1.016 mM (i.e. 322.4 mg/L)) and ascertained that photodegradation had a significant contribution to the fate of this drug in natural aqueous matrices (Reina et al., 2018). However, another report by the same research group showed that, with TiO_2 as a catalyst, complete removal can be achieved with lower energy

consumption within 50 minutes of treatment (Cabrera-Reina et al., 2019). It is evident that adsorption-based methods have not been explored for the removal of IMP from aquatic environments, possibly because of its high hydrophilicity which can result in poor uptake and retention by the adsorbent media.

Table 2. 2: Overview of degradation techniques employed for Imipenem (IMP)

Degradation technique	**Dosage and Operating conditions**	**Removal Efficiency**	**Ref.**
Advanced Oxidation Reduction Process (AORP) [UVC/Fe^{2+}/H_2O_2]	5-7.5 mg/L IMP 0.74-1.2 mM Fe^{2+} and 0.28-0.32 mM H_2O_2 at pH 3	~100% (18.9-33.86)	[70]
Heterogeneous Fenton Oxidation (Zero Valent Iron (ZVI)- Fenton)	4 µmol/L (~1.20 mg/L) IMP, 100-200 µmol/L H_2O_2, 0.01-0.04 g/L ZVI, pH 5-7: in pure water	99%, 63%, and 57% for pH =5, 6, and 7, respectively, after 60 minutes	[71]
	10 µmol/L (~3.0 mg/L) IMP, 0.02-0.10 g L^{-1} ZVI; 100-400 µmol L^{-1} H_2O_2 added in three aliquots, pH 6: in wastewater	0-88% after 90 minutes	[71]
Photochemical degradation under natural solar radiation	90.0224 mM (i.e. 7.12 mg/L) to 1.016 mM (i.e. 322.4 mg/L)) IMP, Irradiance 28-50 W/m^2	88% in 300 minutes	[72]
Heterogenous photocatalysis	0.4 mg/L IMP, 50 mg/L TiO_2	~80% in 45minutes	[73]
Heterogenous photocatalysis	TiO2@Fe2O3/chitosan nanocomposite; 20 mg/L IMP, 150 W Xe lamp with 420 nm cutoff filter	~91.25% at pH 3 and 41.32% at pH 11 in 2 h	[74]

2.4 Knowledge Gaps

After a careful literature review, the following research gaps were identified:

2.4.1 Limited studies on IMP fate and behaviour in wastewater

Despite the drug's approval in the 1980s and continued use since then, there has been a limited exploration of its environmental occurrence. In addition, no studies have explored the fate and behaviour of IMP in an environmental context. Therefore, the knowledge gaps regarding the drug's stability, persistence, and fate in an aqueous environment, including the effect of environmental factors (pH, temperature, light) and interactions with co-existing entities and transformation, are significant.

With an increase in the consumption of last-resort antibiotics such as IMP and the accompanying spread of carbapenem resistance, it is crucial to investigate their environmental fate and behaviour [73,75,76]. As the drug is listed among the WHO's list of essential medicines, the loss of IMP's effectiveness against multi-drug resistant infections could make these infections untreatable [70].

2.4.2 No studies of IMP-metal complexes

Our research group has investigated the capacity of various antibiotic classes, namely tetracyclines (specifically chlortetracycline) and fluoroquinolones (specifically ciprofloxacin), to form complexes with metals [16,17,77]. In addition to this, other old classes of antibiotics such as macrolides (for example, azithromycin), have also been explored previously by other researchers [78,79]. Recent reports have also indicated the potential of β-lactam antibiotics to interact with co-existing metal ions and form AMCs, which are potentially more stable and toxic than the parent antibiotics [80–85].

However, to the best of our knowledge, no such studies were performed for newer classes of antibiotics, such as carbapenems or IMP, specifically. A few studies have reported IMP detection and quantification in wastewater matrices; however, Imipenem-metal complexes (IMP-Me) have not been studied.

This becomes crucial because the: (i) concentrations detected in environmental matrices are higher than the PNEC values, and (ii) presence of heteroatom functional groups that can facilitate metal coordination. A further analysis of comparative stability and toxicity of IMP and IMP-Me becomes crucial to determine their environmental persistence and ecological risks.

Chapter 3: Research Gaps, Objectives, and Originality

- **Research Gap 1**:

A significant knowledge gap regarding the stability profile of IMP in aqueous solutions, including the effects of environmental factors (temperature, light) and interactions with co-existing entities such as natural organic matter (NOM) and metals was identified. Some studies have shown that the β-lactam ring is susceptible to temperature, pH, presence of oxygen, moisture, and water (H^+ and OH^-) [58,62,63,86].

In addition, naturally occurring photosensitizers, such as dissolved organic matter (DOM), influence the behaviour of organic pollutants [87,88]. The DOM can generate photochemical intermediates, including singlet oxygen ($^1O_2$), excited triplet state of DOM (^{3}DOM*), and hydroxyl radicals (•OH), which contribute to the transformation and/or degradation of organic contaminants in real matrices [87,89]. However, this was not explored for carbapenems, including IMP.

Since investigating the photodegradation of these contaminants in environmental waters is essential to understand their fate and ecotoxicological risk assessment in environmental waters, effect of light, temperature, humic acid (as a model NOM), and metals was studied.

Objective 1: To study the stability profile of IMP under different conditions of light and temperature, and the effect of NOM.

In this regard, the present study: (i) examines the stability of IMP in aqueous solutions, (ii) explores its interactions with co-existing entities, such as metals and humic substances, and (iii) investigates its fate in environmental contexts.

- **Research Gap 2:**

The study of interactions of IMP with co-existing metal cations has not been explored, and to the best of our knowledge, no attempt has been made to detect and characterize AMCs in complex environmental matrices. It is primarily due to (i) the increased complexity of the matrices- parent antibiotics, transformed products, and their metal complexes with varying stoichiometries, stabilities, and combinations; and (ii) low concentrations of analytes. This limits the ability of many techniques to accurately and reproducibly measure these complexes. Thus, this project aims to analyse IMP-metal complexes and study their toxicity towards wastewater model microorganisms.

Objective 2: To investigate the formation and comparative toxicity of IMP-metal complexes

In this regard, the present work aims to investigate the interaction of the antibiotic with metals (Metals (M)= Mg (II), Ca (II), Fe (II), Cu (II), and Al (III)) and study the toxicity of IMP and its metal complexes towards wastewater model microorganisms. Two bacterial strains, *Bacillus subtilis (B. subtilis)* and *Escherichia coli (E. coli)*, were used as microbial models for gram-positive and gram-negative species.

Collectively, both these research gaps and objectives establish a framework to link environmental stability and metal-driven transformation of IMP with its resultant ecological toxicity, enabling assessment of whether intrinsic attenuation processes may reduce the need for engineered remediation.

Originality

The study is the first to comprehensively assess environmental fate of the antibiotic, Imipenem, by examining its photostability and interactions with natural organic matter and metals, while uniquely characterizing the formation and ecotoxicity of Imipenem-metal complexes.

Chapter 4: Occurrence of Imipenem in natural water: Effect of dissolved organic matter and metals

Pratishtha Khurana[a], Rama Pulicharla[a], Satinder Kaur Brar[a]*

[a] Department of Civil Engineering, Lassonde School of Engineering, York University, Toronto, Ontario, Canada

*Corresponding author: Satinder Kaur Brar; satinder.brar@lassonde.yorku.ca

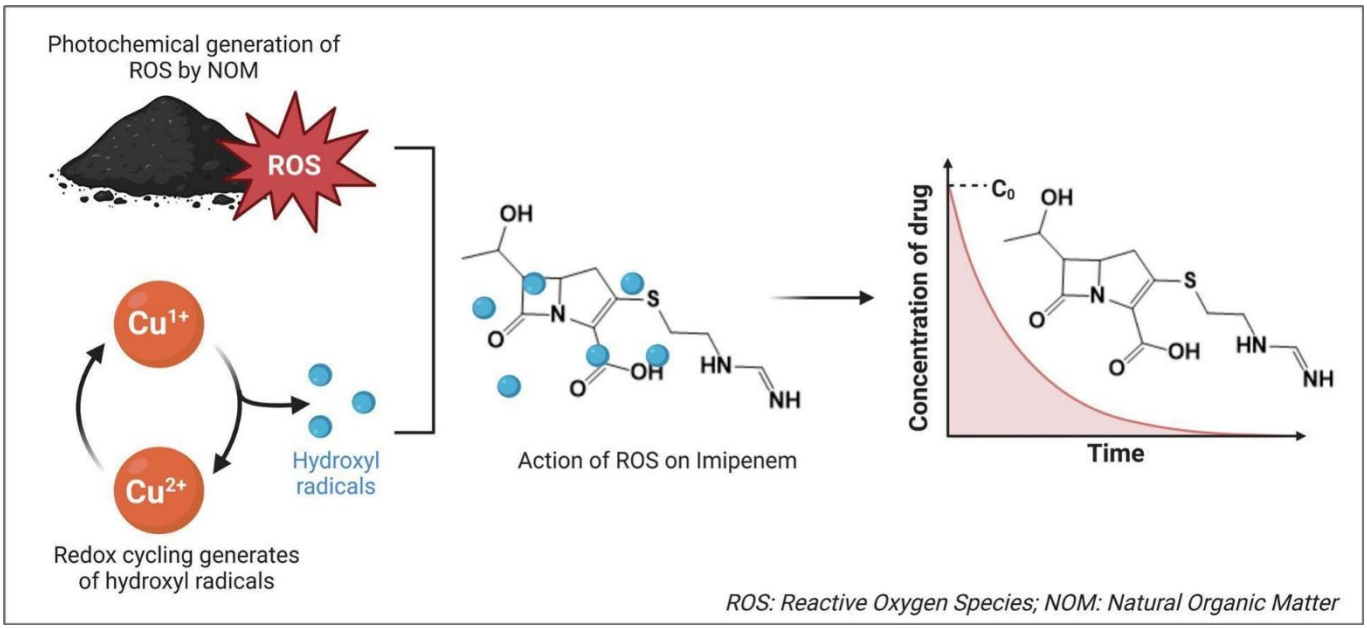

Science of The Total Environment, Volume 957, 2024, 177846;

DOI: https://doi.org/10.1016/j.scitotenv.2024.177846

Abstract

The occurrence of trace antibiotic residues in the environment poses a threat by promoting antibiotic resistance and spreading resistant genes. Recent studies show that these residues interact with metals, forming toxic and persistent antibiotic-metal complexes (AMCs). Investigating the photodegradation of these contaminants in environmental waters is essential to understand their fate and ecotoxicological risk assessment in environmental waters. In this sense, the present work delineates the fate of IMP, a carbapenem antibiotic, in the environmental matrix and studies its interactions with humic acid and metals. The study established that the drug was labile and underwent degradation under light and ambient temperatures. Further, analytical studies with dissolved organic matter (DOM), such as humic acids, established an accelerating effect on antibiotic degradation *via* indirect photochemical pathways. For instance, for a concentration of 100 mg/L IMP mixed with 20 mg/L HA in volumetric ratios of IMP: HA 1:2, 1:1, and 2:1, the final concentrations of IMP after 24 h were 26.11 mg/L (-73.89%), 34.44 mg/L (-65.56%), and 44.22 mg/L (55.78%), respectively. The higher the humic acid, the faster the degradation of IMP, thereby supporting the photochemical generation of reactive oxygen species (OH•) and subsequent oxidative degeneration of the drug. The interactions with metals, specifically copper, accelerated the degradation kinetics of the drug. The promotion effect was owed to the action of the OH• as the oxidizing agent. Based on the degradation products identified by LC-MS/MS, a scheme of the synergistic action of copper-redox coupling and IMP, resulting in the oxidative degradation of the drug, was proposed. Understanding the photochemical behaviour of antibiotics, and their behaviour in the presence of DOM and metal is vital for unravelling their fate and complexity in wastewater.

Keywords: Copper-redox coupling; Dissolved Organic matter (DOM); Hydroxyl radical; Imipenem; Photolysis; Wastewater

4.1 Introduction

The occurrence of antibiotics has long been identified as a potential threat due to the spread of antibiotic resistance (ABR) among bacteria, which can jeopardize the efficacy of antibiotics in future years. Incorrect disposal, high prescription rates, and leakage from the manufacturing sites contribute to the occurrence of antibiotics in environmental matrices, like wastewater, which serves as a significant contributor to the spreading of ABR. The concentrations of these antibiotic residues are usually trace, ranging from ng/L to µg/L, yet enough to favor the onset of resistance. In addition, the different unit operations of the wastewater treatment plant (WWTPs), particularly biological treatment, are poorly compatible with degrading bio-recalcitrant compounds, like antibiotics [71,90,91]. This, coupled with the inefficiency of disinfection to remove these resistant bacteria and genes, exacerbates the problem [71,92].

It is particularly damaging for the last-resort antibiotics and those reserved for hospital settings, such as carbapenems. The consumption of last-resort antibiotics, particularly Imipenem (IMP), has been on the rise across the globe and has been associated with the spread of carbapenem resistance [73,75,76]. Included on WHO's list of essential medicines, the loss of IMP's efficacy in treating multi-drug resistant infections will render it incurable for humankind [70]. In addition, the drug has also been studied previously to interact with metals to form antibiotic-metal complexes (AMCs), which have exhibited higher antimicrobial activity compared to the parent drug [93]. This raised concerns over the adverse effects it can bring to the environments receiving antibiotic and metal-laden wastewater.

To combat this, researchers have developed and employed various chemical and hybrid technologies aimed at removing antibiotic residues from wastewater. However, the presence of IMP as an environmental contaminant is a debate. Some studies have shown that the β-lactam ring is susceptible to temperature, pH, presence of oxygen, moisture, and water (H^+ and OH^-) [58,62,63,86]. The β-lactam ring is affected by the presence of OH^- and H^+ in water, that results in the opening of the ring due to amide bond rupturing [63]. The oxygen, on the other note, results in oxidative degradation of IMP [63]. In addition, kinetic studies of IMP (20 mg/mL) by [58] under varying pH conditions revealed decomposition of about 90% and 50% of the drug within 3 h at pH 4 and 9, respectively, and account for the decomposition of the drug at neutral pH range as well [58]. Meanwhile, others have aimed at degrading this antibiotic using advanced removal techniques like

Fenton-based advanced Oxidation processes (AOP), advanced oxidation-reduction process (AORP) using UVC/Fe^{2+}/H_2O_2, and photocatalysis with TiO_2, which seems conflicting [70–73]. Also, the concentration of the antibiotic considered for the degradation studies ranged from few mg/L to a few hundred mg/L, which is unrealistically high when compared to 0.005-25.53 µg/L IMP reported in real matrices like municipal wastewater influent, hospital effluent, pharmaceutical discharge stream [51–55].

In this sense, the present work delineates the fate of IMP, a last resort carbapenem antibiotic, in the environmental matrix and studies its interactions with humic acid and metals, which is less studied. For instance, naturally occurring photosensitizers, such as dissolved organic matter (DOM), influence the behaviour of organic pollutants [87,88]. The DOM can generate photochemical intermediates, including singlet oxygen ($^1O_2$), excited triplet state of DOM (^{3}DOM*), and hydroxyl radicals (•OH), which contribute to the transformation and/or degradation of organic contaminants in real matrices [87,89]. Similarly, co-existing metals can also alter the stability and behaviour of antibiotics in natural systems [19,22,23,93].

The research gaps regarding the drug's stability, persistence, and fate in an aqueous environment, including the effect of environmental factors (pH, temperature, light) and interactions with co-existing entities and transformation, are significant. In this regard, the present study: (i) examines the stability of IMP in aqueous solutions, (ii) explores its interactions with co-existing entities, such as metals and humic substances, and (iii) investigates its fate in environmental contexts. Subsequently, the manuscript delves into a critical discussion, providing insights into the existing literature on antibiotic treatment and the importance of implementing these techniques.

4.2 Materials and Methods

4.2.1 Chemicals and Materials

Imipenem (European Pharmacopoeia (EP) reference standard, $C_{12}H_{17}N_3O_4S$) was purchased from Millipore Sigma (Burlington, Ontario, Canada), and N, N-dimethyl-4-nitrosoaniline ($C_8H_{10}N_2O$, 98%) was purchased from Thermo Scientific Chemicals, Canada. Magnesium chloride tetrahydrate ($MgCl_2.4H_2O$) was obtained from Fisher bioreagents (Mississauga, Ontario, Canada).

Copper (II) chloride dihydrate ($CuCl_2.2H_2O$), Aluminum chloride hexahydrate ($AlCl_3.6H_2O$), and humic acid (>95 %; CAS 1415-93-6) were procured from Thermo Alfa Aesar (Canada).

4.2.2 Analytical methods

A UV-vis Genesys 50 spectrophotometer (Thermo Scientific, Canada) was used with 1.0 cm quartz cells for absorbance measurements in the wavelength range 280-400 nm. The wavelength of maximum absorbance, or λ_{max} was identified as 298 nm for the antibiotic.

For lower working concentrations (<25 mg/L), an accurate and robust method was developed for the detection and quantification of IMP using LC-MS, and the calibration standards were made right before the analysis. The liquid chromatography (LC) system (Waters M-class (UHPLC)) consisted of a degasser, a column thermostat, a binary pump, and an autosampler. The chromatographic separation was carried out with a Kinetex 2.6 µm XB-C18 100 Å, LC Column 50 x 0.3 mm, microflow column, maintained at 50 °C. The mobile phase consisted of a: (A) ultrapure water with 0.1 % v/v formic acid, and (B) Acetonitrile (MeCN) with 0.1 % v/v formic acid. A gradient was optimized as follows: 99% A and 1% B for 0-5 minutes, increasing gradually to 100% B at 5 minutes, followed by 99% A and 1% B at 6 minutes. The flow rate was 20 µL/min, and the injection volume was 5 µL. The mass spectrometry (MS) system consisted of an Sciex ZenoToF 7600 equipped with an electrospray ionization source (ESI), operated in positive ionization mode. The ion source parameters were optimized as follows: curtain gas 35 psi; CAD gas 7 psi; and spray voltage 5500 V.

4.2.3 Stability assay

The stability of the antibiotic IMP was studied using UV-visible spectroscopy under different conditions of light and temperature, considering a range of drug concentrations. The experimental conditions were categorized into Set A (light-protected in amber bottles, room temperature), Set B (clear glass vials, room temperature), and Set C (clear glass vials, refrigerated) for IMP, with concentrations varying from 25 mg/L to 250 mg/L. The sampling was done for 120 hours (5 days), and the samples were promptly analyzed using UV-vis spectroscopy. The initial concentration of the antibiotic was maintained high to (i) accurately record the degradation of the drug under exposed conditions, and (ii) precise quantification of the antibiotic with UV-visible spectroscopy.

However, the findings can be reliably extrapolated to environmental fate due to its intrinsic structural instability and sensitivity to hydrolysis, which drives rapid transformation and reactivity in aquatic systems.

4.2.4 Effect of DOM and metals

To observe the interaction between IMP and various metals, UV-vis spectra were recorded by mixing 500 µL (50 mg/L) of IMP with metal solution (Mg (II), Cu (II), and Al (III)) in 1:1 molar ratio (~84 µM each) in a quartz cuvette. Additionally, for lower concentrations of IMP (33 µM or 10 mg/L), LC-MS was utilized using the method described above. Similarly, for the effect of DOM, humic acid was used as a model. A stock solution of humic acid (20 mg/L) was prepared by dissolving the appropriate amount of humic acid in water, followed by homogenization in an end-to-end shaker overnight at room temperature. For this, 50 and 100 mg/L of IMP were added to 20 mg/L humic acid in volumetric ratios of 1:2, 1:1 and 2:1, and monitored for 24 h using the same protocol. The LC-MS spectra of humic acid and humic acid-IMP mixture is included in Appendix A.

Spiking tests with real secondary wastewater were also performed to understand the fate of the antibiotic, when subjected to natural solar radiation in a complex matrix, like wastewater. The grab samples were collected in June 2021 from the Keswick Water Resource Recovery Facility (WRRF), Ontario, Canada.

4.2.5 Generation of hydroxyl radicals (OH•) in the Imipenem-copper system

The production of hydroxyl radicals (OH•) was investigated using a spectrophotometric method previously reported elsewhere [94]. Briefly, UV-vis absorption spectroscopy, using N, N-Dimethyl-4-nitrosoaniline (RNO) as a probe, was utilized for the indirect yet selective estimation of OH radicals. RNO does not react with other reactive oxygen species (ROS), such as singlet oxygen ($^1O_2$), superoxide anions (O_2^-), or other peroxy compounds, making it an ideal probe for the estimation of hydroxyl radicals [95]. For this, three concentration sets of IMP and Cu (II) were mixed in a molar stoichiometric ratio of 1:2 (IMP= 33, 165, and 330 µM, i.e., 10, 50, and 100 mg/L, respectively), and absorbance measurement (λ=440 nm for RNO, and λ=298 nm for IMP) using

UV-vis Genesys 50 spectrophotometer for 24 hours [94,96]. A concentration of 5 nM of the RNO dye was used for all the experiments.

4.3 Results and discussion

4.3.1 Stability assay

The stability of IMP was studied using UV-visible spectroscopy under different conditions of light, temperature, and concentrations (25 to 250 mg/L), categorized into Set A (amber bottles (light-protected), room temperature), Set B (clear glass vials, room temperature), and Set C (clear glass vials, refrigerated (4 ±1 °C)) for 5 days. The results are summarized in Figure 4.1.

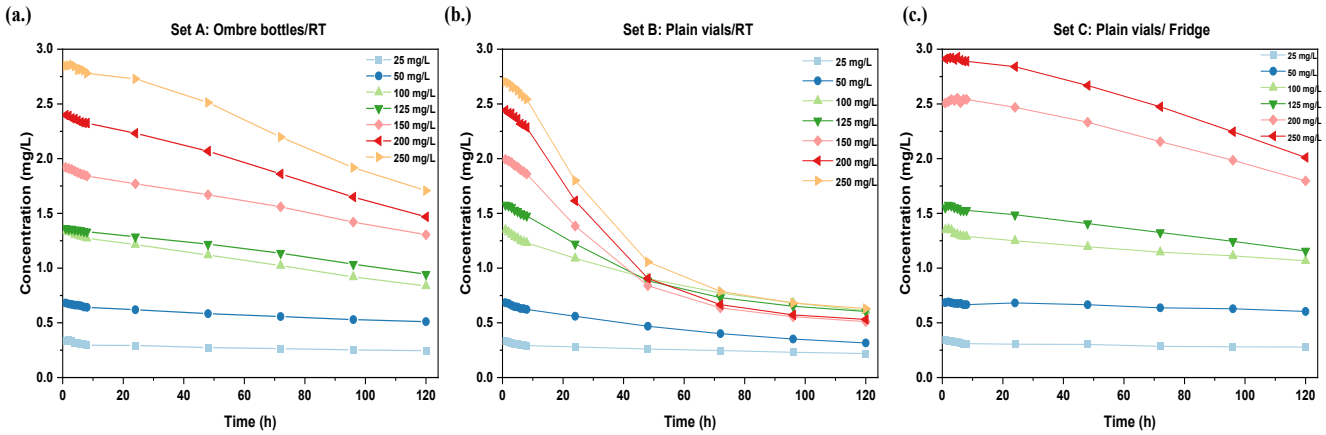

Figure 4.2: Degradation kinetics of Imipenem (IMP) under three set of conditions: Set A (amber bottles, room temperature), Set B (Clear glass vials, room temperature), and Set C (Clear glass vials, refrigerated).

As shown in Figure 4.1, the degradation of IMP is a function of - light, temperature, and concentration. Comparing Set A and Set B, when exposed to light at room temperature, the drug exhibited faster degradation. Further, Set C, which was refrigerated, showed slower degradation compared to room temperature storage (Set B). For instance, for 100 mg/L IMP, degradation % was observed to be about 9.33%, 19.33%, and 7.34% in sets A, B, and C, respectively, after 24 h.

From the results, it was evident that both light and temperature are defining factors for the stability of the drug IMP. This observation aligned well with common knowledge in pharmaceutical development and previous reports [97–99]. Moreover, when comparing the trend of degradation, it can be inferred that temperature has a greater influence on the stability of IMP, when compared to light. For example, for 100 mg/L IMP, about 16.49% of the drug degraded for set A (light-protected, Figure 4.1a) in 24 h, while the degradation was only about 11.42% for set C (temperature-protected, Figure 4.1c). The degradation was fastest for set B (Figure 4.1b), about 33.04% for the respective storage conditions. The rate constants after data fitting are included in Table A1 (Appendix A). The degradation kinetics for Set A and C follows zero-order kinetics, while that of set B exhibits both zero and first-order kinetics of degradation.

In addition to light and temperature, the trend of degradation was also found to depend on the antibiotic's concentration, as supported by the previous reports [58,61]. [61] evaluated the stability of IMP (5 and 10 mg/mL) at three temperatures (25 °C, 30 °C, and 40 °C) for up to 6 hours and established an association between the drug concentration, temperature, and the stability of the drug. Although the study was focused on solutions commonly employed for extended infusion, it showed that at these concentrations and temperatures, the drug was unstable and degraded rapidly. For instance, for 10 mg/mL, the drug was stable for less than an hour at temperatures of 30 and 40 °C. The study suggested that the stability of IMP decreased with increasing both- concentration and temperature, which lies in accordance with the results of the present study. From Figure 4.1, it is evident that higher concentrations degrade faster than the lower concentrations. For example, concentrations of 150-250 mg/L exhibited a faster rate of degradation than 100-125 mg/L, which further degraded faster than concentrations of 25-50 mg/L, as can be seen by the rate constants summarized in Table A1.

Further, a scan over the UV-vis range 280-400 nm revealed the emergence of dimer diketopiperazine (λ_{max} 360 nm; m/z 599) (Figure 4.2), a structure formed *via* intermolecular oligomerization of IMP. This is initiated by the biomolecular attack of the carboxyl group of one IMP on the β-lactam group of the second molecule [58,86]. Since the attack is intermolecular and the hydrolysis of both β-lactam and formimidoyl groups is pH-dependent, the decomposition rate of IMP is a function of both (i) pH, and (ii) IMP concentration. In addition, a rapid shift from 298 nm

to 288 nm is associated with ring opening, while imino isomers have been reported to have no characteristic UV peak [86].

In addition to pH, temperature, light, and concentration, presence of moisture, and oxygen also affects the stability profile of the drug. For instance, a recent study by [63] investigated the effect of oxygen, water, particle shape and size on the stability of IMP/Cilastatin mixture and proposed hydrolytic degradation of IMP, resulting in the formation of imipenemoic acid and its epimer. The study also confirmed that the stability of IMP was indeed related to the presence of free water content (moisture and humidity), in addition to pH and concentration.

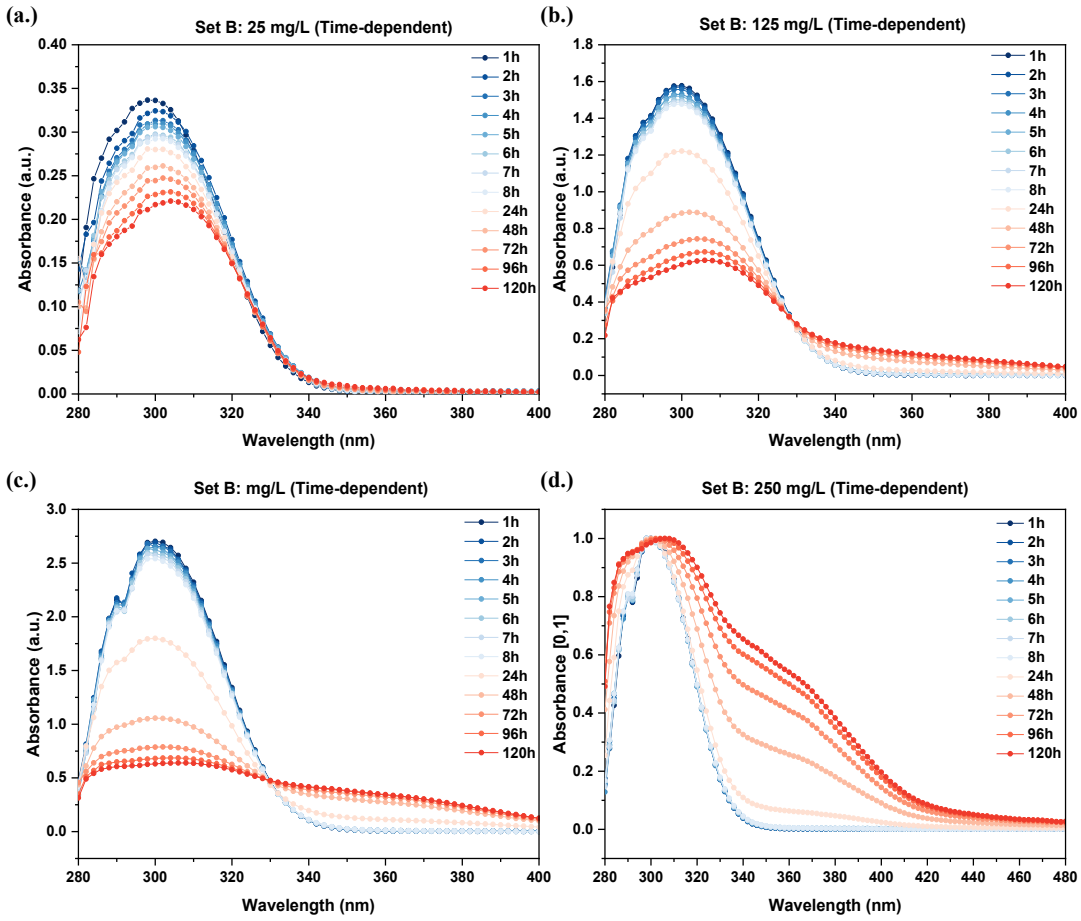

Figure 4.3: Time-dependent UV-visible spectra (λ= 280-400 nm) for IMP (a) 25 mg/L, (b) 125 mg/L, and (c) 250 mg/L stored in clear glass vials at room temperature. (d) shows normalized [0,1] UV-visible spectra for time-dependent spectrum of IMP (250 mg/L)

4.3.2 Effect of DOM and metals

The humic acid used in the study has been characterised with UV-visible and FT-IR spectroscopy. The UV-visible spectrum (Figure 4.3a) does not show a specific absorption, as also reported by previous studies [100,101]. The FTIR spectrum of humic acid, as shown in Figure 4.3b, confirms the previous report on the characterization of humic acids. Broad absorption signals centred at 3400 cm^{-1} is attributed to the -OH stretching vibration in -COOH, phenols, and alcohols [101,102]. The peaks around 1600 cm^{-1} are related to the stretching vibration of C=C in the benzene rings and -C=O of carbonyl or ketonic groups. The signals centred at 1385 cm^{-1} can be assigned to the symmetric bending vibrations of methyl functionality. The peaks around 1100 cm^{-1} indicate the symmetric stretching vibrations of the sulfonic acid groups. Humic acids show spectral features in the fingerprint region, unlike fulvic acids, which can be used to characterize the two naturally occurring organic acids. In the fingerprint regions peaks at 916, 800, and 470 cm^{-1} are attributed to aliphatic CH_2, out-of-plane stretching of CH binds in benzene, and vibration of the sulphur-containing group and Me-OH bond, respectively [102].

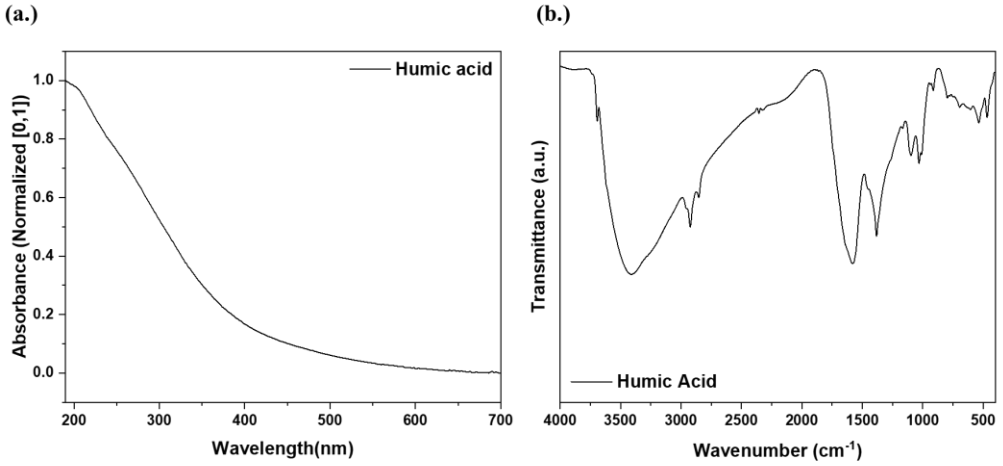

Figure 4.4: (a.) UV-visible spectrum, and (b.) FTIR for Humic acid

To understand the fate of the antibiotic in real wastewater, the effect of DOM (humic acid, HA) on the stability of the drug was studied. In the presence of HA, a dramatic decrease in absorbance of

IMP at λ= 298 nm was observed, as shown in the Figure 4.4. For instance, starting with a concentration of 100 mg/L IMP mixed with 20 mg/L HA in volumetric ratios of IMP: HA 1:2, 1:1, and 2:1, the final concentrations after 24 h were 26.11 mg/L (-73.89%), 34.44 mg/L (-65.56%), and 44.22 mg/L (55.78%), respectively. Similarly, for 50 mg/L IMP exposed to HA in volumetric ratios of IMP: HA 1:2, 1:1, and 2:1, a decrease of 90.07%, 86.56%, and 84.56% in IMP concentration was recorded, resulting in final concentrations of 9.93 mg/L, 13.44 mg/L, and 15.44 mg/L, respectively, after 24 h of exposure. As shown in Figure 4.4, the higher the humic acid, the faster the degradation of IMP.

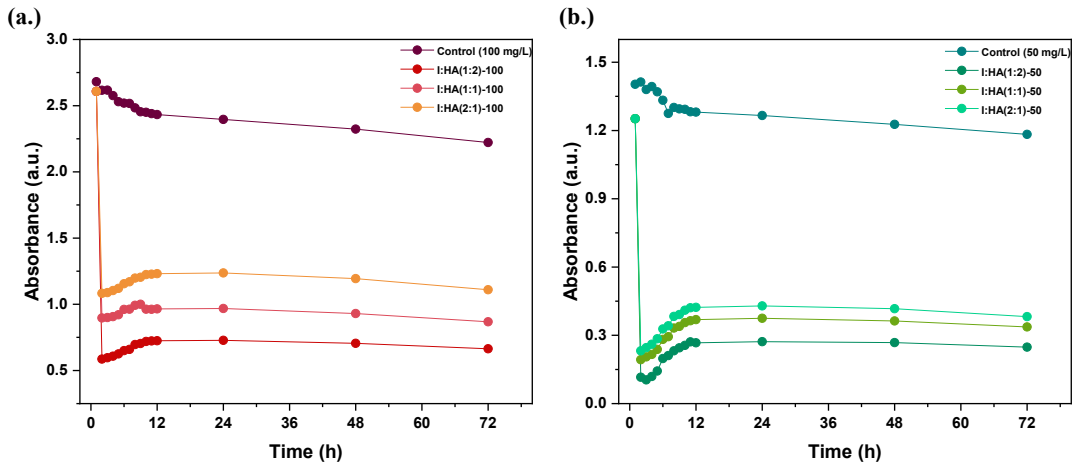

Figure 4.4: Effect on the absorbance of (a.) 100 mg/L, and (b.) 50 mg/L of Imipenem at λ= 298 nm after exposure to humic acid (20 mg/L) in different volumetric ratios (2:1, 1:1, and 1:2, respectively).

The presence of HA enhanced the photochemical removal of IMP, similar to what has been reported for antibiotics such as Ciprofloxacin [103]. A previous study by [103] observed about 90% removal of Ciprofloxacin (60 µM) in presence of 5 mg/L humic substances at pH 7 within 2 h of irradiation. This can be attributed to the photochemical generation of reactive oxygen species ($OH^{\bullet}$) and subsequent degradation of the drug, as studied by previous reports. As indicated previously, DOM can transform or degrade the pollutants of concern *via* indirect photochemical pathways by the photochemical generation of reactive oxygen species ($OH^{\bullet}$) and DOM in the

triplet state [72,104]. In addition, humic substances have also been studied to react *via* energy transfer processes with water constituents, including dissolved molecular oxygen and interact with substrates in photo-redox reactions [103,105,106].

Further, it is well known that humic acid is a complex organic structure, with both aromatic and aliphatic structures and heteroatoms N, O, and/or S. They are composed of functional groups including and not limited to phenols, carboxylic acid, enols, quinone, ether, amines [107]. Humic acids also contain metal oxides (such as Fe_2O_3) and aromatic groups (such as hydroquinone). These groups facilitate electron transfer between the participating groups, resulting in formation of free radicals [108]. It had been studied that the in presence of O_2 and UV-vis light, humic acid can produce $O_2^{\bullet-}$, H_2O_2, and finally OH• by Fenton reaction between H_2O_2 and Fe^{3+} [109]. As seen from the study, IMP is photosensitive. It undergoes degradation in the presence of light, as discussed in the manuscript. Further, the presence of natural photosensitizer, like humic acid, accelerates the photodegradation of IMP.

The LC-MS spectra of both humic acid and humic acid-IMP mixture have been displayed in Figure A1 in Appendix A. Since humic acid is a complex media, the transformation/degradation products were not identified in the present study. As free radical reactions are dynamic and continue until quenched, the transformation products are expected to vary with time. A recent study by Furia et. al (2021) attempted to identify some of the transformation products after Fenton's treatment. However, it must be noted that the free-radical degradation of organic pollutants, if not quenched, usually results in mineralization, i.e., CO_2 and H_2O [110].

Also, it is noteworthy that since there were no suspended particles in the reaction mixture, the possibility of adsorption of IMP on humic acids is minimized. However, this was not directly studied and cannot be ruled out as a possible factor in the observed decrease in concentration of IMP after exposure to humic acids.

Following humic substances, the effect of co-existing metals (Mg (II), Cu (II), and Al (III)) on the stability of the antibiotic was investigated using UV-visible spectroscopy and Mass spectrometry (MS). A significant shift in the maximum absorption wavelength (298, λ_{max} for IMP), the reduction in intensity and the broadening of peaks were observed for IMP-Cu, IMP-Mg, and IMP-Al mixtures, respectively, as shown in Figure 4.5a. These changes in UV spectra emphasize strong interactions between the antibiotic and the metal ions [111].

In addition to UV spectra, a reduction in signal intensity at m/z 300.1012 (IMP) was observed in direct MS injection for IMP-Al binary system (Figure A2). Further, the appearance of an additional peak at m/z 311.08595 for IMP-Mg binary system, attributed to $[Mg\ (IMP)_2]^{2+}$, corroborates the interactions of antibiotic and metal cations when present together (Figure A3). However, the time-resolved investigation of IMP with Cu (II) yielded unforeseen results.

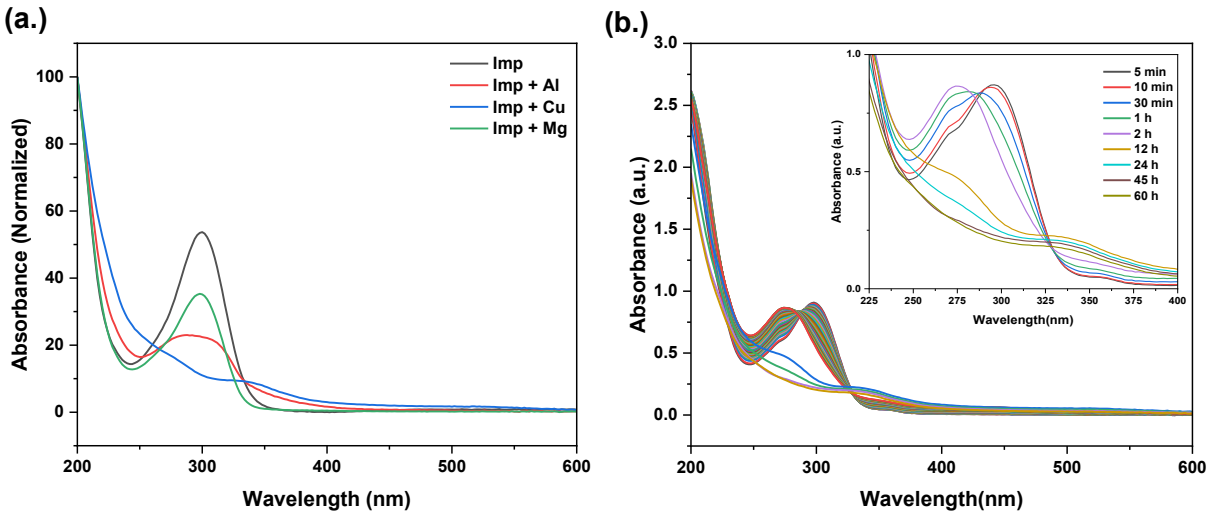

Figure 4.5: UV-vis spectra from 1:1 molar ratio of Imipenem with Al (III), Cu (II), Mg (II), and (b.) Time-resolved UV-vis spectra for IMP: Cu (II) system. Working concentrations of Imipenem and the metals: 25 mg/L.

When monitored over 24 h, UV-visible spectra (Figure 4.5b) showed a continuous shift in the peak from λ= 297 to 275 nm within 2 hours, along with the emergence of a new hump near λ= 337 nm. This shift in the peak position can be attributed to the evolving dynamics of the reaction and production of intermediate and/or transformation products. The MS spectra of the reaction mixture displayed a notable signal at m/z 316.096, corresponding to $[IMP\text{-}O\text{-}H^+]$, followed by a gradual decrease in the drug concentration (Figure A4-A6). This indicated oxidative degradation likely due to the *in-vivo* generation of reactive species. The redox cycling of copper has been extensively studied previously for its role in the *in-vivo* generation of reactive species and transformation of substrates [112–116]. These reactive oxygen species can initiate a cascade of reactions in complex

matrices like wastewater. However, not all substrates can initiate these chain reactions. Substrates that can reduce Cu (II) to Cu (I) are essential for the oxidation process catalyzed by copper, such as L-ascorbic acid (L-AA) [116].

Previous reports have shown that under an inert atmosphere, IMP undergoes non-oxidative decomposition within a neutral pH range (Smith et al., 1990). However, the decomposition process becomes much more complex in the presence of copper. The generation of OH• during the oxidation of IMP by oxygen, with copper as a catalyst, was investigated using RNO as a probe reagent. This organic dye selectively bleaches upon exposure to OH•, leading to a reduction in absorbance at 440 nm. As shown in Figure 4.6(a-c), for IMP-Cu-RNO system, increasing the concentration of IMP significantly affects the rate of the yellow colour bleaching of the dye RNO. For instance, when the concentration of IMP was increased from 33 µM (10 mg/L) to 165 µM (50 mg/L) and 330 µM (100 mg/L) in the presence of Cu (II) (66, 330, and 660 µM, respectively), the rate of disappearance of the strong absorption band at 440 nm, which is characteristic of the dye, increased. When a mixture of 660 µM Cu (II) and 330 µM of IMP was prepared with 5 nM RNO, the absorption band at 440 nm drastically reduced immediately after mixing, exhibiting over an 80% decrease in less than an hour of reaction. This reduction was followed by about 60% and 30% reduction for 165 µM and 33 µM IMP, respectively. It is also evident that copper alone has no bleaching activity for the dye (data not shown), confirming the synergistic effect of IMP and Cu (II)/Cu (I) in discolouring the dye RNO. This synergy can be explained by the oxidation of IMP to form [IMP-O-H^+] (m/z 316.096) and the reduction of Cu (II) to Cu (I), which induces the *in-situ* formation of H_2O_2. Copper, owing to its redox cycles of cuprous and cupric copper [Cu (I)/Cu (II)], can decompose the transient intermediate of H_2O_2 to produce OH radicals *via* a heterogenous Fenton-like reaction, responsible for significant bleaching of RNO (Figure A7) [116,117].

This decrease in the RNO absorption was also accompanied by a drop in absorption at 298 nm, which is characteristic of the antibiotic IMP. As Figure 4.6(d-f) illustrates, the decrease in the concentration of IMP is evident in the presence of copper, even in the absence of RNO, suggesting that Cu (II)/Cu (I) alone can oxidize IMP. In the absence of RNO, hydroxyl radicals formed can accelerate the oxidation of IMP, leading to its more rapid degradation compared to when RNO is present.

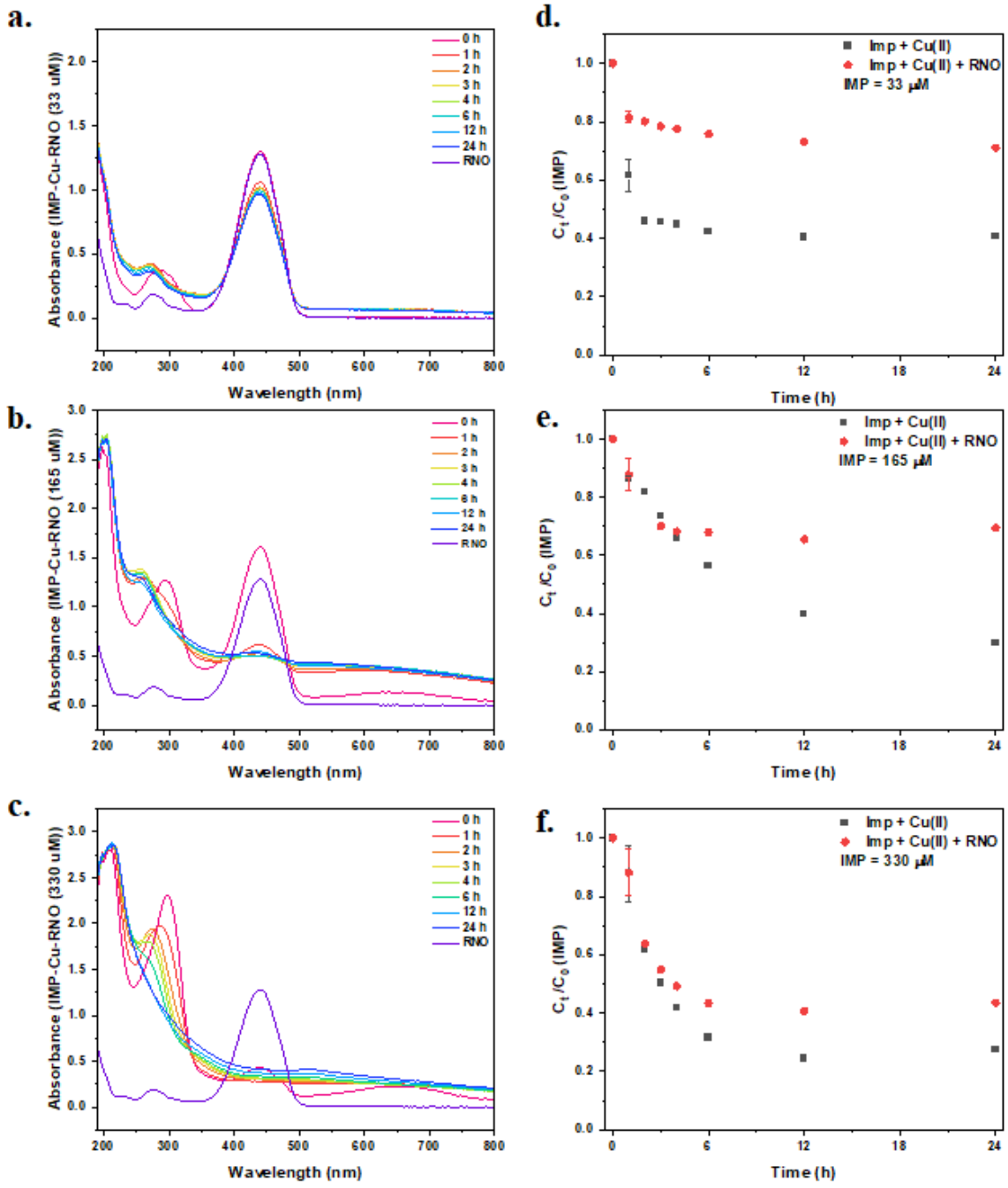

Figure 4.6: UV-visible spectra for IMP-Cu-RNO system (IMP= 33, 165, 330 μM) (a-c); and rate of degradation of IMP in IMP-Cu (II) and IMP- Cu (II)- RNO system (d-f).

Although the oxidation of antibiotics is due to OH• obtained from O_2, it is different from the conventional AOPs as it does not require any (i) additional dosage of oxidizers, such as H_2O_2, ozone, persulfate, and peroxymonosulphate, and (ii) pH adjustment.

Conventional AOPs, including UV alone, UV/Fe^{2+}, UV/H_2O_2, Fe^{2+}/H_2O_2, and UVC/Fe^{2+}/H_2O_2, have been employed to degrade IMP from wastewaters [70,72,73]. These studies underlined that both oxidation (UV/H_2O_2 and Fe^{2+}/H_2O_2) and reduction (UV/Fe^{2+}) play significant roles in the degradation of the antibiotic, and simultaneous generation of oxidizing (OH•) and reducing agents (e^-) can improve the degradation efficiency [70]. While the assertion that the degradation of IMP is due to the production of OH• and e^- holds; however, a pH of 3 seems unsound, considering the instability of the drug. Another piece of literature has reported that the drug undergoes fast hydrolysis at a pH of 4 or lower, which is conflicting [71]. Further, since the drug can auto-degrade rapidly in the presence of humic substance and Cu^{2+} without any pH adjustment or additional supplements, as reported in the present study, the addition of H_2O_2 and adjustment of pH to 3 seems unessential, which increases the chemical footprint and cost of the process to achieve degradation. Also, for techniques involving the addition of Fe^{2+} for wastewater remediation, pH adjustment after treatment becomes a crucial step. However, adjusting the pH before releasing the treated water results in the precipitation of ferric salts (Fe^{3+}), thereby leading to the production of sludge, making it unsuitable for real-time applications [118].

Other than AOPs, photochemical degradation under natural solar radiation and heterogenous photocatalysis, with TiO_2 as a catalyst, was studied to degrade carbapenem antibiotics, including IMP, from aqueous solutions [72,73]. However, the existing literature poses an intriguing question amidst its complexities. Since the drug undergoes rapid degradation under natural radiation and ambient temperatures, the authors would like to raise concerns about the need for this treatment. Further, the present study shows that the drug undergoes rapid degradation in the presence of humic acid (20 mg/L) and copper (66-660 μM) due to the generation of hydroxyl radicals. It was surprising to note that the antibiotic degraded in the presence of these entities, while there are recent research articles devising AOP-based treatment technologies to degrade IMP. With this susceptibility to auto degradation, the drug might never find its way to the effluent after treatment at the facilities.

Spiking tests with real secondary wastewater were also performed to understand the fate of the antibiotic, when subjected to natural solar radiation in a complex matrix, like wastewater and the results are shown in Figure A8. To identify the transformation products of IMP in wastewater on being subjected to natural solar radiation, MS spectra were recorded at zero hours (control; Figure A8b) and after 5 hours of exposure to natural solar radiation (Figure A8c). From recorded mass spectra, it is evident that the drug actively interacts with the coexisting entities, such as metals, and humic substances and exists as an adduct. The mass spectra MS reveals the presence of $[IMP\text{-}Na]^+$ at m/z 322.0824 (absolute intensity 1.34E6), and no free drug (m/z 300.1012) (as shown in Figure A8a) was observed even for the antibiotic spiked in wastewater at zero hours (Figure A8b). After 5 hours, the intensity of Na-adduct decreased (9.67E4), and other degradation products became predominant at m/z 102.1274 and 152.9525 (Figure A8c).

Considering these findings, one might question the necessity of devising new techniques for the photolabile antibiotics, including IMP's removal that potentially include the addition of other harmful chemicals and/or metal salts, which not only increases the cost of treatment but also the chemical footprint of the removal techniques [25,119–122]. This raises a critical enquiry into the direction of future research and the sustainable management of photosensitive pharmaceutical pollutants in aquatic systems.

4.4 Conclusion

The present study investigated the degradation kinetics of antibiotic IMP under various conditions of light, temperature, and concentration, as well as in the presence of humic substances and metals such as copper. The findings indicated that the drug is labile and undergoes ring opening, resulting in the formation of dimer diketopiperazine, laboratory conditions and ambient temperatures. Additionally, the presence of humic substances and copper accelerated the decomposition kinetics of the drug *via* free-radical pathways. Further, the study showed that the higher the humic acid, the faster the degradation of IMP. For instance, for 50 mg/L IMP exposed to HA in volumetric ratios of IMP: HA 1:2, 1:1, and 2:1, a decrease of 90.07%, 86.56%, and 84.56% in IMP concentration was recorded, resulting in final concentrations of 9.93 mg/L, 13.44 mg/L, and 15.44 mg/L, respectively, after 24 h of exposure. The study also corroborated the interactions of IMP with metal cations, such as copper. Copper, owing to its redox cycles of cuprous and cupric copper [Cu (I)/Cu (II)], can produce H_2O_2 and decompose generated H_2O_2 to produce OH radicals *via* a

heterogenous Fenton-like reaction, resulting in the oxidation of IMP to form [IMP-O-H+] (m/z 316.096), thereby accelerating the degradation kinetics. The study raises a question regarding the necessity of devising new techniques for labile drugs, such as IMP, which might never make their way to tertiary treatment of the treatment train.

The previous study established that the antibiotic is photo- and thermolabile, and the presence of humic acids and copper accelerates the decomposition kinetics of the drug. In addition to humic acid and copper, IMP also showed interaction with other metal cations.

For the next study, the formation of IMP-metal complexes was investigated using different analytical techniques, and their antibacterial activity, in comparison to the parent drug, was explored.

Chapter 5: Imipenem-metal complexes: Computational analysis and toxicity studies with wastewater model microorganisms

Pratishtha Khurana[a], Rama Pulicharla[a], Satinder Kaur Brar[a*]

[a]Department of Civil Engineering, Lassonde School of Engineering, York University, North York, Toronto, Ontario M3J 1P3, Canada

*Corresponding author: satinder.brar@lassonde.yorku.ca

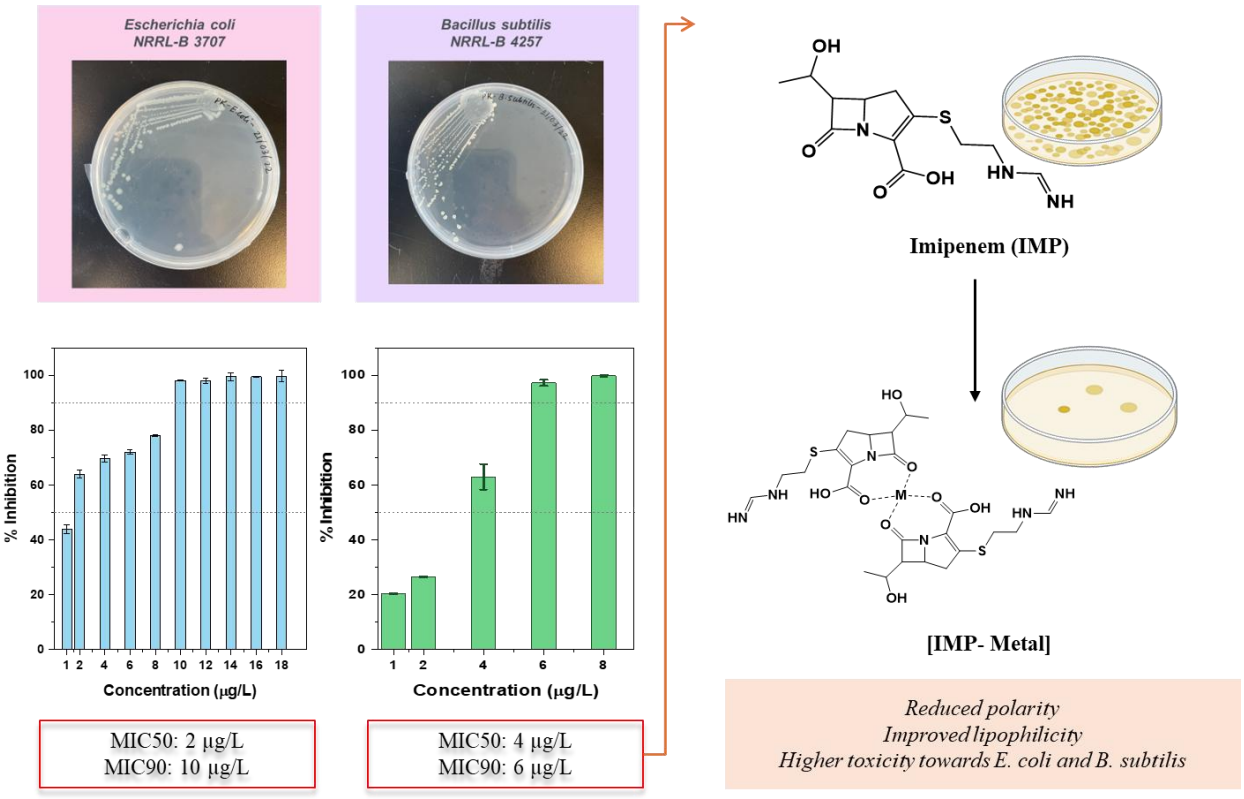

Environmental Research, Volume 239, Part 2, 2023, 117275

DOI: https://doi.org/10.1016/j.envres.2023.117275

Abstract

The occurrence of antibiotic residues in diverse water sources has long been acknowledged as a potential health concern due to the emergence and spread of antibiotic-resistant bacteria and genes. However, there have been limited studies into the presence of antibiotic-metal complexes (AMCs) in real-time wastewater matrices, and their impact on wastewater microbial communities. The present work, in this regard, investigated the stability of Imipenem-metal complexes (Me= Mg (II), Ca (II), Fe (II), Cu (II), and Al (III)) with computational studies, stoichiometry with potentiometric measurements, and their antibacterial activity towards wastewater model microorganisms- *Bacillus subtilis (B. subtilis)* and *Escherichia coli (E. Coli)* by Colony Forming Unit (CFU) method. The lower energy of Imipenem-metal complexes than the parent antibiotic-Imipenem (IMP), during energy optimization using density functional (DFT) methods, revealed that metal interactions of IMP stabilize the drug by minimising its energy. Further, CFU studies indicated that these complexes display higher antimicrobial activity than parent antibiotics. The electron delocalization over the entire chelated system (AMCs) reduces polarity and increases the lipophilicity of the complexes, thereby facilitating stronger interaction between AMCs and the bacterial cell membrane. Results indicate increased antibacterial activity of Imipenem-metal complexes for both *E. coli* and *B. subtilis*. The antibacterial activity, was however, more pronounced in *B. subtilis*, with >97% growth inhibition for metal complexes of IMP (at a Minimum Inhibitory Concentration of 20nM or 6ppb (i.e., MIC90)), for both the stoichiometric ratios (metal to ligand) ratios (M: L 1: 1 and 2: 1). All around, with increased stability and toxicity, AMCs are emerging as contaminants of concern and demand immediate attention to devise methods for their removal.

Keywords: Emerging contaminant; Imipenem; Imipenem-metal complexes; Toxicity, Antibacterial activity; Potentiometry.

5.1 Introduction

β-lactam antibiotics have consistently revolutionized the treatment of bacterial infections since the groundbreaking discovery and utilization of Penicillin antibiotics, which represents a significant milestone in modern chemotherapy. Since their original introduction, these antibiotics have undergone constant enhancements in various aspects, such as potency, the spectrum of antimicrobial activity, stability and safety profiles, and pharmacokinetics. Currently, there are four primary categories of β-lactams utilized in clinical practice: (1) Penicillins (β-lactam fused to a thiazolidine ring); (2) Cephalosporins (β-lactam fused to a dihydrothiazine); (3) Carbapenems (β-lactam fused to a pyrroline); and (4) Monobactams. Each class has been extensively modified, resulting in a wide range of synthetic derivatives. Their general structures are shown in Figure 5.1. The chemistry, mode of action and mechanism of resistance of these antibiotics have been extensively studied and comprehensively reviewed in recent review articles [50,123,124].

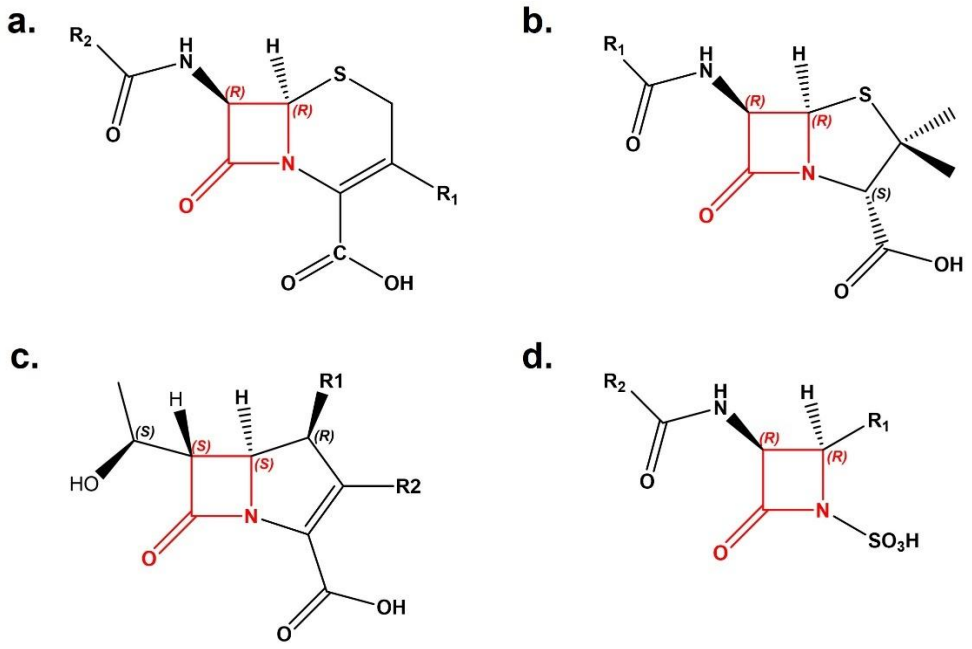

Figure 5.1: General structure of β-lactam antibiotics (a.) Cephalosporins, (b.) Penicillins, and (c.) Carbapenems; (d.) Monobactams. The β-lactam ring is shown in red.

Carbapenems are one of the newest and most important classes of β-lactam antibiotics. The term 'carbapenem' reflects the replacement of the sulphur, at position 1, in the thiazolidine ring with carbon in the characteristic 4:5 fused ring structure of conventional β-lactams (4-membered β-lactam ring fused to a C2-C3 unsaturated 5-membered ring) [50], as shown in Figure 5.1.

Carbapenems have a different stereochemistry, compared to other β-lactams Penicillins and cephalosporins. They possess a unique trans-α-1-hydroxyethyl (S-absolute stereochemistry) substituent at position 6, which differs from the cis configurations of the acylamino side chain found in conventional β-lactams (Cephalosporins and Penicillins) (Figure 5.1a and 5.1b, respectively). This structural feature provides intrinsic resistance to almost all β-lactamases, as noted in studies by Lyon (1985) and Zhanel et al. (2007) and confers a broad spectrum of antimicrobial activity against a variety of gram-positive and gram-negative pathogens [47,50].

The first carbapenem-imipenem (IMP), had the broadest in-vitro bacterial coverage at the time of its approval, encompassing gram-positive and gram-negative aerobes, such as Serratia marcescens and Pseudomonas aeruginosa and anaerobes such as Bacteroides fragilis, and was least affected by the inoculum size, leading to its prompt acceptance and widespread usage in healthcare settings [45,47]. In addition to its widespread acceptance, its high renal excretion rate (about 60-70% of IMP remains unchanged upon release into the environment), direct disposal of expired or unused antibiotics and leaks from manufacturing sites or pharma factories also increase the abundance of IMP in wastewater, as discussed in Table 5.1.

Although the information on the prescription of IMP and its occurrence in wastewater is limited, however, a comprehensive literature review reveals that within recent years, IMP has been detected in wastewater with concentrations ranging from ng/L to µg/L (as summarized in Table 5.1), indicating its presence in the environment. For instance, Shokoohi R. et al. (2017) reported IMP as one of the prevalent antibiotics in the municipal wastewater of Hamadan, Iran, with an inflowing concentration of 10.8 µg/L [54], and in-hospital effluents of Sina Hospital in Hamadan, Iran with a concentration of 25.53 µg/L [55]. Similarly, Szekers E. et al. (2017) reported the occurrence of IMP in hospital effluent, with a concentration of 14.42 µg/L [52]; which lies in the predicted order of IMP in hospital wastewaters [125].

Table 5.1: Summary of Imipenem concentrations detected in wastewater.

Matrix	Concentration (µg/L)	Location	Ref.
Hospital effluent	14.42	Cluj County, Romania	[52]
Wastewater influent	0.20 to 4.96	Croatian secondary (sewage) WWTP, Zagreb	[53]
Municipal wastewater influent	10.80	Hamadan, Iran	[54]
Hospital wastewater	25.53	Hamadan, Iran	[55]
Pharmaceutical factory discharge stream	0.005	Taiwan	[51]

A recent study by J. Hrenovic et al. (2017) has also revealed the occurrence of IMP in the influent and effluent of a Croatian secondary (sewage) WWTP, Zagreb, in concentrations ranging from 198.4 to 4958.5 and from 78.4 to 1137.9 ng/L, respectively [53]. From this data, it is evident that the detected concentrations are higher than the predicted no-effect concentration (PNEC) (EUCAST database) of 125 ng/L for IMP, and therefore, the selection of IMP-resistant strains in these environments is possible [53].

Based on the literature, metal complexes of organic ligands, such as antibiotics and their derivatives, have demonstrated higher antibacterial activity than the parent ligands and have been rightly explored for the development of new antibiotics and other biomedical applications like drug delivery [126–133]. Furthermore, compelling research indicates the existence of antibiotic-metal complexes (AMCs) in actual environmental samples like wastewater, primarily because of the concurrent presence of metals and antibiotic residues. A preliminary literature survey reveals the potential of β-lactam antibiotics to interact with co-existing metal ions and form antibiotic-metal complexes, or AMCs, which are potentially more stable and toxic than the parent antibiotics [80–85]. This, in general, is owed to the presence of heteroatom functional groups, such as hydroxyl, thioether, carboxylic acid, and carbonyl, that might be involved in coordination with metals. The antibiotic-metal complexes (AMCs) are studied to possess different behaviour for photolysis,

adsorption, toxicity, bioavailability, and solubitily, compared to parent antibiotics [18,39,134–137]. These complexes are, thereby, becoming a cause for concern due to their environmental persistence and toxicity [16,18,19,27]. These AMCs have also been previously investigated for their potential to trigger the proliferation of antibiotic-resistant bacteria and genes [25–27].

However, there is a lack of information about the prevalence and concentrations of the metal complexes of IMP in wastewater and sludge matrices and the consequences it may cause. This becomes crucial because the: (i) concentrations detected in environmental matrices are higher than the PNEC values, and (ii) possession of functional groups capable of metal chelation. That is, IMP can chelate with several divalent and trivalent metal ions coexisting in the water matrix and form Imipenem-metal complexes (IMP-Me), which has not been explored.

Our research has investigated the capacity of various antibiotic classes, namely tetracyclines (specifically chlortetracycline) and fluoroquinolones (specifically ciprofloxacin), to form complexes with metals. Additionally, we have assessed the stability and toxicity of these antibiotics, which belong to older antibiotic classes [16,17,77]. In addition to this, other old classes of antibiotics such as macrolides (for example, azithromycin), have also been explored previously by other researchers [78,79]. However, to the best of our knowledge, no such studies were performed for newer classes of antibiotics, such as carbapenems. IMP, the first carbapenem, is a broad-spectrum antibiotic, frequently prescribed for multi-drug-resistant infections *via* combinational therapies. Due to this high rate of consumption, IMP is frequently detected in wastewater and to the best of our knowledge, no such studies are reported for this antibiotic. Additionally, computational studies examining the structure, and stability of these complexes have not been extensively conducted in the environmental matrices. This is particularly important to understand their physicochemical properties and predict their toxicity and fate in real environments, including surface water, wastewater, and sediments.

In this regard, the present work aims to investigate the stability of IMP-metal complexes (Metals (M)= Mg (II), Ca (II), Fe (II), Cu (II), and Al (III)) by optimizing the ground state geometry of IMP and IMP-metal complexes with different M:L ratios using computational studies. The results from the computational studies are substantiated with (a.) potentiometry and (b.) the study of the toxicity of IMP and its metal complexes towards wastewater model microorganisms. Two bacterial strains, *Bacillus subtilis (B. subtilis)* and *Escherichia coli (E. coli)*, were used as microbial models for gram-positive and gram-negative species.

5.2 Materials and methods

5.2.1 Chemicals and reagents

Imipenem (European Pharmacopoeia (EP) reference standard, $C_{12}H_{17}N_3O_4S$) was purchased from Millipore Sigma (Burlington, Ontario, Canada). Magnesium chloride tetrahydrate ($MgCl_2.4H_2O$), and Sodium chloride (NaCl, 58.44 g/mol) were obtained from Fisher bioreagents (Mississauga, Ontario, Canada). Copper (II) chloride dihydrate ($CuCl_2.2H_2O$, 170.48 g/mol, 99%), Iron (II) chloride tetrahydrate ($FeCl_2.4H_2O$, 198.81 g/mol, 98%), and Aluminium chloride hexahydrate ($AlCl_3.6H_2O$, 241.43 g/mol) were procured from Alfa Aesar (Canada). Calcium chloride anhydrous ($CaCl_2$, >99%) was obtained from EMD chemicals (Canada).

For bacteria studies, both *Bacillus subtilis* (NRRL-B 4257) *(B. subtilis*) and *Escherichia coli* (NRRL-B 3707) (*E. coli*) were acquired from ARS Culture Collection (NRRL), and nutrient broth and agar were purchased from Hardy diagnostics, and BioShop Canada, respectively.

5.2.2 Wastewater collection and metal analysis

Wastewater samples were collected from the Keswick Water Resource Recovery Facility (WRRF), Ontario, Canada, which has an average flow of 18,000 m3/day and a peak flow of 64,000 m^3/day. The facility is in an extended aeration treatment plant equipped with tertiary ultrafiltration membranes and UV disinfection for the treatment of sanitary sewage and releases the treated effluent to Lake Simcoe. The grab samples were collected in June 2021 into prewashed containers from seven points of the treatment facility, namely influent after the screening, primary effluent, secondary effluent, membrane treated water, final effluent, return activated sludge (RAS) and the thickened sludge (TS), as shown in Figure 5.2. The collected wastewater (WW) and sludge samples were stored under dark conditions at 4 ±1 °C until used.

All the collected samples were prepared for the analysis of metals based on the work of Cuprys et al. (2021), with slight modifications [138]. Briefly, for sludge samples, the solid fraction was separated from the liquid fraction by centrifugation (2 X 5000 rpm, 20 min), frozen at -20 °C overnight, followed by freeze drying for 24 h.

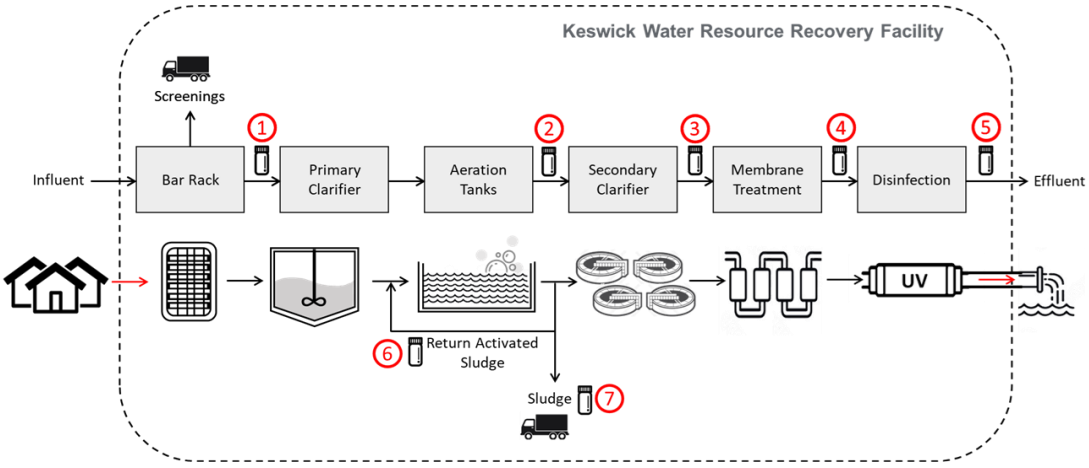

Figure 5.2: Sampling points for wastewater and wastewater sludge collection from the Keswick Water Resource Recovery Facility (WRRF)

All the samples (solid fraction, liquid fraction of the sludge and wastewater samples) were then subjected to acid digestion. About 0.5 g solid fraction (dry sludge) or liquid samples were placed in a 50 ml tube, and 1 ml nitric acid (HNO3) was added and left overnight. Subsequently, 3 mL of 1 mL HCl was added and put in the heating block (95 °C) for 2 hours. The samples were then cooled to room temperature, and milli-Q water was added to make up the volume to 50 mL. The prepared samples were then analyzed with ICP-OES (Inductively Coupled Plasma Optical Emission Spectroscopy). The results for the metal are summarized in Appendix B.

5.2.3 Potentiometric measurements

The stability constants and stoichiometric equilibrium for binding of IMP to selected metal ions including Mg (II), Ca (II), Fe (II), Cu (II), and Al (III) were studied with potentiometric titrations using JP Selecta pH meter pH-2005 with accumet pH probe. The experiments were conducted in MilliQ water having pH 6.0 ± 0.5 at room temperature [16]. The metal solutions of Mg (II), Ca (II), Fe (II), Cu (II), and Al (III) were gravimetrically prepared using their anhydrous chloride salts in water. Errors in metal ion concentrations were minimized by using fresh anhydrous salts and completely dissolving them in water. The ionic strength of the working metal solutions was adjusted to 0.1 mol/L using sodium chloride to minimize the potential shifts in pH upon ion binding. Before the experiments, 50 ppm (0.16703 mM) IMP was freshly prepared by diluting

stock IMP in 5 mL pH-adjusted water (pH ≈ 7). The choice of this concentration was guided by a thorough assessment of the sensitivity of the analytical instruments and experimental techniques employed to ensure robust resolution and reliable detection of transformation under controlled conditions. Finally, the stoichiometric coefficient and the stability constants were determined by the titration of IMP (50 ppm, 5 mL) in water, using metal solutions as titrant (100 ppm) in 0.1 mol/L NaCl. The metal solutions were added to the antibiotic solution in small aliquots (20 µL) and the titrations were continued as the IMP: metal ratio changed from 25: 1 to 0.2: 1 (or 1: 5). The changes in pH and potential were noted and plotted against IMP: metal ratio to get the stoichiometric ratio (m: n) for IMP-metal complexes, and the stability constants (K) were calculated using the following equation (5.1):

$$K = \frac{[M_m L_n]}{[M^m][L^n]} = \frac{x}{(a-mx)^m\,(b-nx)^n} \qquad \ldots\text{equation (5.1)}$$

where, a and b are the initial concentrations of metal (M) and ligand (L) (IMP, here), respectively, and x is the equilibrium concentration of $[M_m L_n]$. The results from the potentiometric studies are summarized in Table 3.

5.2.4 Bacterial strains and culture media

To investigate the antibacterial activity of the IMP-metal complexes, two bacterial strains, the gram-positive, rod-shaped bacterium *Bacillus subtilis* (NRRL-B 4257) (*B. subtilis*) and the gram-negative, rod-shaped bacterium *Escherichia coli* (NRRL-B 3707) (*E. coli*), were used as microbial models, owing to their abundance in environmental matrices and fast growth rate. Both bacteria were sub-cultured in nutrient broth and streaked on nutrient broth-agar plates, followed by incubation at 30 °C for 24 h. The prepared plates were preserved at 4 °C till further use.

5.2.5 Minimum Inhibitory Concentrations (MIC) and growth inhibition assay

For determining the MIC and performing a growth inhibition assay, the CFU method used previously by Pulicharla et al., 2015, was employed with slight modifications. Briefly, a single colony of *B. subtilis* and *E. coli* from nutrient broth-agar plates was used to inoculate a 50 mL

falcon tube containing 10 mL of sterilized nutrient broth. The tubes were incubated on a rotary shaker at 200 rpm and 30 °C for 24 h. The actively growing cells from these tubes were used as an inoculum for the toxicity studies. About 1% (v/v) (OD_{600} 1.0) from these tubes was used to inoculate 50 mL falcon tubes containing 10 mL sterilized nutrient broth. For further toxicity studies, these tubes were incubated under the same conditions as mentioned earlier (200 rpm, 30 °C for 12 h) and OD600 was recorded to determine the Minimum inhibitory concentration (MIC). MIC was confirmed in terms of colony-forming unit (CFU) on agar plates.

The appropriately diluted samples of both bacteria were plated on agar plates and incubated at 30 °C for 24 h to form fully developed colonies of both *E. coli* and *B. subtilis*. The colonies counted on the plates should be between 20 and 300, and each data point in the figure is an average of two plate counts for each set for % viability. The IMP concentration tested for toxicity was 1 to 20 µg/L for *B. subtilis* and 1 to 50 µg/L for *E. coli*. The study was performed in triplicates.

After the determination of MIC, the antibacterial activity of IMP and its metal complexes (M: L= 1: 1 and 2: 1) were compared for MIC90 using the same method, and the results are discussed in section 3.5. It is worth noting that metals have consistently been detected in higher concentrations than IMP residues in wastewater. Therefore, to simplify the experiment design, stoichiometric ratios of M: L 1:1 and 2:1 were employed for a streamlined investigation while maintaining a scientific framework.

5.2.6 Computational details

Since limited studies are reported towards the understanding of IMP-metal complexes, an attempt was made to obtain energy-optimized structures for IMP and IMP-metal complexes, for different possible stoichiometric ratios with Gaussian 16W computational package. Benchmarking studies were performed by the combination of various functional and basis sets. The ground state geometry optimization was carried out using density functional theory (DFT) with the benchmarked B3LYP functional and 6-311 + G (2d, p) basis set for IMP and different M:L ratios for IMP-metal complexes unless mentioned otherwise and the results are discussed in section 3.2.

At first, the optimized structure for IMP was obtained by minimizing energy using ground state, DFT, default spin (B3LYP) with basis set 6-311G+(2d, p) with charge zero and singlet spin. The effect of solvent was included through the Integral equation formalism (IEFPCM) model [139,140].

Following, based on the Mulliken charge distribution and availability of free lone pairs on heteroatoms N and O, four potential binding sites for metal coordination were predicted: carbonyl and carboxylic oxygen (O7 and O17) (1: 1 and 1: 2), carbonyl and carboxylic oxygen with hydroxyl oxygen (O10), nitrogen (N30), or thiol (S20), which were later compared for IMP-metal complexes (Me= Ca (II), Mg (II), Cu (II), and Al (III)). Since for Fe (II), SCF failed to converge, additional input of "SCF=Fermi" was used as an additional keyword to avoid SCF convergence difficulties by Fermi broadening, damping and level shifting and the results are summarized in Table 5.2.

The results from the computational studies were compared and substantiated with experimental studies, including potentiometric measurements and toxicity studies with wastewater model microorganisms. In addition, UV-vis spectroscopy (Genesys 50, Thermo Scientific) and LC-MS were also employed, and the results are included in figures S4-S9 in the Appendix A. The liquid chromatography (LC) system (Waters M-class (UHPLC)) consisted of a degasser, a column thermostat, a binary pump, and an autosampler. The chromatographic separation was carried out with a Kinetex 2.6 µm XB-C18 100 Å, LC Column 50 x 0.3 mm, microflow column, maintained at 50 °C. The mobile phase consisted of a (A) ultrapure water with 0.1 % v/v formic acid, and (B) Acetonitrile (MeCN) with 0.1 % v/v formic acid. A gradient was optimized as follows: 99% A and 1% B for 0-5 minutes, increasing gradually to 100% at 5 minutes, followed by 99% A and 1% B at 6 minutes. The flow rate was 20 µL/min, and the injection volume was 5 µL. The mass spectrometry (MS) system consisted of an Sciex ZenoToF 7600 equipped with an electrospray ionization source (ESI), operated in positive ionization mode. The ion source parameters were optimised as follows: curtain gas 35; CAD gas 7; and spray voltage 5500 V.

5.3 Results and Discussions

5.3.1 Metal analysis (WW samples)

Metal analysis by ICP-OES revealed a high abundance of Al, Ca, Cu, Fe, and Mg in both-wastewater and wastewater sludge samples. The concentrations of the five most abundant elements found in the collected wastewater and wastewater sludge samples, along with their limit of detection (LOD), are presented in Figure 5.3. The list of the tested metals and their concentrations have been provided in Tables B1 and B2. Aluminum (Al) ranged from 0.048 to 38.6 mg/L in

wastewater and between 33840 to 38840 mg/kg in sludge. Since the plant uses alum (double salt of aluminum) as a coagulant during primary treatment, high concentrations of Al in both wastewater and wastewater sludge are evident.

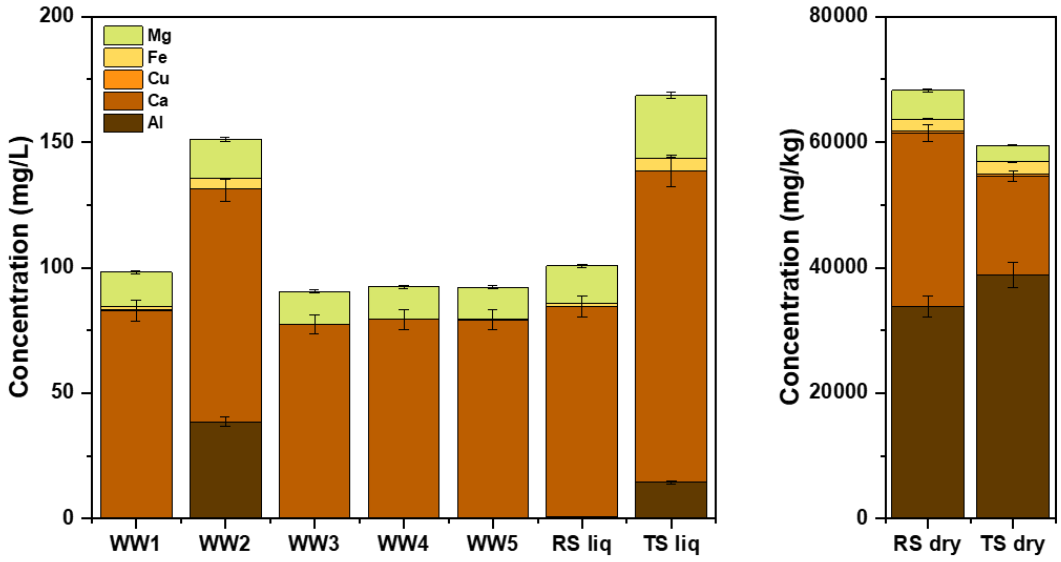

Figure 5.3: Concentrations of most abundant metals (Al, Ca, Cu, Fe, and Mg) in collected municipal wastewater (WW) and wastewater sludge samples. *(RS- Return activated sludge, TS- Thickened sludge, and liq- liquid fraction)

Other than aluminum, alkaline earth metals, Magnesium (Mg) and Calcium (Ca), and transition metals, Iron (Fe) and Copper (Cu), are the most abundant. Their low concentrations in wastewater effluent (Cu 0.018 mg/L and Fe 0.014 mg/L) and high concentrations in sludge (Cu 299-354 mg/kg and Fe 1895-1973 mg/kg) suggest that they were completely removed from the wastewater *via* adsorption onto sludge as mentioned previously by Cuprys et al., 2021. The values are also consistent with the previous reports. For instance, a metal analysis of municipal sewage sludge in South Africa revealed Cu concentrations in the range of 263.68 to 626.00 mg/kg of dry mass [141]. In another study by Morrison et al., the Cu was found to be in the range of 245 to 441 mg/kg, which lies well in accordance with the present analysis [142]. Similarly, heavy metal analysis in

municipal wastewater and wastewater sludge from WWTPs in South Africa revealed similar concentrations for Fe [143]. Based on these concentrations, Mg (II), Ca (II), Cu (II), Fe (II), and Al (III) ions were selected for further experiments.

5.3.2 Structure optimization of Imipenem and Imipenem-metal complexes using software Gaussian

The ground state geometry optimization of IMP using density functional theory (DFT) with the B3LYP functional and 6-311 + G (2d, p) basis set yielded structure (a), as shown in Figure 5.4. It was discovered that the optimized structure of IMP has electronic energy of -1330.926349 Hartree and a dipole moment of 2.764476 Debye. Figure 5.4 (b) shows the charge delocalization and dipole moment in the optimized structure of IMP obtained by minimizing energy, as obtained from the DFT study. The origin of the dipole moment vector is from the center of the electronic charge, and the atoms are symmetrically colour-coded to represent the Mulliken atomic charges, red being the most negatively charged and green the most positively charged atom.

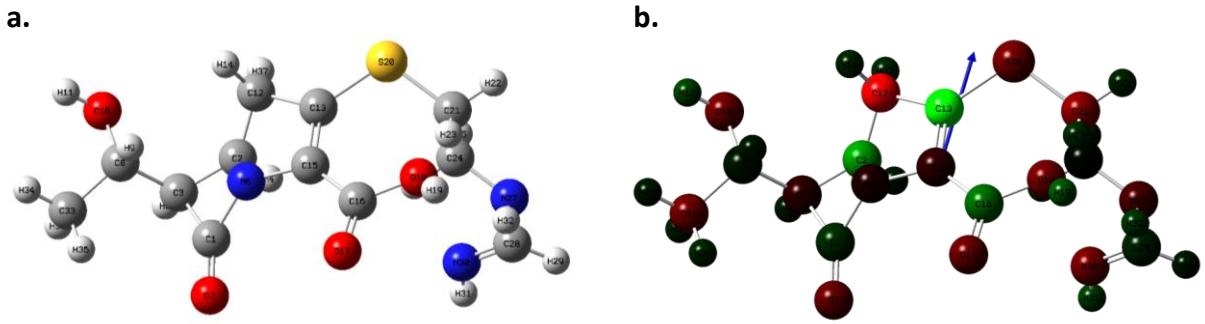

Figure 5.4: (a.) Optimized structure for IMP using DFT with the benchmarked B3LYP functional and 6-311 + G (2d, p) basis set (Electronic energy of -1330.926349 Hartree and a dipole moment of 2.764476 Debye); (b.) charge delocalization and dipole moment in the optimized structure. The atoms are color coded by charge (symmetrically) and represent Mullikan atomic charges; Red marking the most negatively charged and green the most positively charged atom. The origin of the dipole moment vector is from the center of the electronic charge.

After optimizing the structure of IMP, the structures for different IMP-metal complexes were optimized using the same functional and basis set, and the results for the structure optimization of IMP-metal (Me= Al (III), Mg (II), Cu (II), and Fe (II)) complexes are summarized in Table 5.2. The energy values in Table 5.2 reveal that, in general, IMP-metal complexes have lower electronic energy, and thereby higher stability than IMP. The higher the absolute energy, the more stable the structure is.

For example, for Mg- and Ca- complexes of IMP, the order for energy was observed to be (M: L): 1: 2 > 2: 1> 1:1; however, very little to no effect was observed for the three binding sites (a, b, and c), as shown in Table 5.2. Similarly, for Al (III), the order was found to be: 2: 3> 1: 2> 2: 1> 1: 1. It is noteworthy, since aluminum is trivalent, the ratio M: L 2: 3 was exclusively studied only for Al. Further, the order of electronic energy for Cu (II) and Fe (II)-IMP complexes varied in the M: L order: 1:2 ≈ 2:1 > 1:1, as shown in Table 5.2.

Based on these electronic energies, it is further evident from Table 5.2 that transition metals, Cu (II) and Fe (II) form more stable complexes than alkaline earth metals, Ca (II) and Mg (II), and trivalent Al (III) for any M: L ratio. This can be primarily owed to their higher nuclear charge. Electronic energies are important because they govern the distribution of electrons within the AMCs, which in turn affects the bonding interactions and overall stability. However, this is a theoretical study, and further experimental validation is required to confirm these findings and establish their environmental implications.

In addition to potentiometry, UV-visible spectroscopy was also utilised to corroborate the formation of these complexes qualitatively. Figure 4.5 shows the UV-vis spectra for the antibiotic IMP, and its metal complexes after 24 hours of equilibrium. The shift in wavelength of maximum absorption, $\lambda_{max\ (297\ nm)}$ for IMP-Cu, decreasing intensity and broadening of peaks for IMP-Mg and -Al, is indicative of the interactions between the parent antibiotics and the metal cations. The formation of IMP-Cu (II) complex was monitored for 24 h with UV-vis spectroscopy. A gradual peak shift from λ= 297 (λ_{max} for IMP) to 275 nm was observed and a new peak near λ= 337 nm was also observed.

Table 5.2: Electronic energy for different Imipenem-metal complexes from the computational study for different M: L ratios. (E_h : Electronic energy (Hartree), μ': Dipole moment (Debye))

Metal	Electronic Energy (Hartree)			
	1: 1*	**2: 3**	**1: 2**	**2: 1**
Mg (II)	-1530.97	-	-2861.96* -2861.66**	-1730.49[a] -1730.14[b] -1730.90[c]
Ca (II)	-2008.45	-	-3339.49* -3339.19**	-2685.47[a] -2865.55[b] -2686.03[c]
Al (III)	-1573.17	-4474.18	-2904.25*	-1815.22[a] -1815.31[b] -1815.73[c] -1815.74*
Cu (II)	-2971.41	-	-4302.36*	-4611.30[a, c] -4611.47[b]
Fe (II)	-2594.49	-	-3925.45*	-3782.30[a] -3855.42[c]

** Carboxylate and carbonyl Oxygen (O7-O17); ** carboxylate and carbonyl Oxygen and thiol (O7-O17 and S20)*

[a] carboxylate and carbonyl Oxygen and hydroxyl Oxygen (O7-O17 and O10); [b] carboxylate and carbonyl Oxygen and Carbon (O7-O17 and C12), carboxylate and carbonyl Oxygen and Nitrogen (O7-O17 and N30)

In addition to these techniques, LC-MS was also performed to compare the peak signal intensity of IMP in presence and absence of metal ions to ascertain its interaction with metal ions and complex formation. The overlapped chromatogram and MS-spectra are included in the Appendix B (Figures B1-B5). Figure B1 shows the overlapped chromatogram and mass spectra for IMP and its Mg- and Ca- complexes. The decrease in intensity of the parent peak at m/z 300.1013 $[Imp-H]^+$ in presence of the metals is indicative of its interaction and formation of these metal complexes. In addition to the reduction in signal intensity, additional peaks at m/z 319.0742 and 311.08595 are attributed to $[Ca\ (IMP)_2]^{2+}$ and $[Mg\ (IMP)_2]^{2+}$, respectively. Similarly, Figures B4 and B5 display the overlapped chromatogram for Fe (II), Cu (II), and Al (III)- IMP complexes, respectively.

5.3.3 Potentiometric measurements for complexation of Imipenem and metals

The pH of the IMP solution was found to be 7.2 and at this pH, IMP is expected to exist as a zwitterion, possessing both positive and negative charges (protonated nitrogen and deprotonated carboxylic group). Upon the addition of metal salt solutions, the pH started to decrease until it reached a constant value. The stoichiometric ratio and the complexation constants obtained from the study are summarized in Table 5.3.

Upon comparing the stability coefficients of the complexes, the stability of the complexes decreased in the order: Imp-Al > Imp-Ca ≈ Imp-Mg > Imp-Cu > Imp-Fe. It is evident, that the trivalent cation (Al (III)) showed a higher formation constant with IMP than bivalent alkaline earth metals (Mg (II) and Ca (II)) and transition metals (Cu (II) and Fe (II)), which can be attributed to its higher charge density (smaller cationic radius with higher ionic charge). High polarizing metals (or hard Lewis's acids) result in more stable complexes by favouring closer proximity of the metal ion to negatively charged ligands, resulting in a greater force of attraction, owing to its small size and high surface charge [27,39]. For bivalent metal ions, alkaline earth metals (Mg (II) and Ca (II)) ($K= 3.59 \times 10^2$) were observed to form more stable complexes with IMP, compared to transition metals Cu (II) and Fe (II) with stability constants 77.98 and 2.82, respectively.

Table 5.3: Stoichiometric ratio and stability constants for different Imipenem-metal complexes from potentiometry

Metal ion	Al (III)	Ca (II)	Mg (II)	Cu (II)	Fe (II)
M: L	2: 3	1: 2	1: 2	2: 1	2: 1
	$[Al_2 (IMP)_3]$	$[Ca (IMP)_2]$	$[Mg (IMP)_2]$	$[Cu_2 (IMP)]$	$[Fe_2 (IMP)]$
$K_{stability}$	2.88×10^4	3.59×10^2	3.59×10^2	77.98	2.82

Further, the molar ratio for IMP with Mg (II) and Ca (II) was found to be 1: 2; 2: 1 with Fe (II) and Cu (II); and 2: 3 for IMP with Al (III), as summarized in Table 5.3. It is likely that alkaline earth metals, such as Mg (II) and Ca (II), form a mononuclear complex, where the central metal is coordinated to two molecules of IMP, possibly *via* carboxylate and carbonyl oxygen. Similarly, transition metals, Fe (II) and Cu (II), form a binuclear complex, and trivalent Al (III) forms a complex where each aluminum ion is surrounded by six oxygen atoms from three IMP ligands. IMP ligands likely bridge the Al (III) ions to form a trinuclear complex with a central Al-O-Al core. The proposed structures are included in the Appendix B (Figure B6).

5.3.4 Growth Inhibition Assay

5.3.4.1 MIC

The MIC is the minimum concentration of the antibiotic that inhibits bacterial growth after overnight incubation (12 h). First, the growth kinetics of both bacteria was studied in the presence of varying concentrations of IMP. The IMP concentration tested for toxicity was 1 to 20 µg/L for *B. subtilis* and 1 to 50 µg/L for *E. coli*. Based on their CFU, the concentration range was narrowed down to 1-8 µg/L for *B. subtilis* and 1-18 µg/L for *E. coli*. To define the toxicity of IMP towards wastewater model microorganisms- MIC50 and MIC90 for both *B. subtilis* and *E. coli* were determined using CFU. For *B. subtilis*, MIC50 and MIC90 were found to be 4 µg/L and 6 µg/L (~20 nM), respectively (as shown in Figure B7). Similarly, for *E. coli*, MIC50 and MIC90 were observed to be 2 µg/L and 10 µg/L (~33.4 nM), respectively (as shown in Figure B8). The values

were confirmed with CFU on agar plates and were found to be higher than the predicted no-effect concentration (PNEC) (EUCAST database) of 125 ng/L for IMP [53].

5.3.4.2 Imipenem vs Imipenem-metal complexes

Gram-negative bacteria, such as E. coli, and gram-positive bacteria, such as *Bacillus subtilis*, differ in the composition of their cell wall structure and composition, which dictates their behaviour towards the uptake of antibiotic molecules and susceptibility towards them. Gram-negative bacteria have a bilayer, consisting of lipopolysaccharides in the outer layer and phospholipids in the inner layer, with periplasmic space in between the two layers [144]. The outer layer is an impermeable barrier that separates and protects the cell from the extracellular milieu. It also prevents the efficient uptake of molecules with large scaffolds. The gram-positive bacteria lack an outer lipid membrane but are surrounded by thick, mesh-like, layers of peptidoglycan. This difference in the cell composition rules their susceptibility towards contaminants, including antibiotics. Gram-negative bacteria exhibit greater resistance compared to gram-positive bacteria due to their unique structure [145]. For instance, the current study observed that 6 µg/L of IMP was sufficient to inhibit 90% of the growth in *Bacillus subtilis*, whereas a higher concentration (10 µg/L) was needed to achieve the same effect in *E. coli*.

However, despite the cell structure, some metals, such as magnesium, iron, and copper, are essential for several biological processes. This is why supplementing trace metal salts to the growth media facilitated bacterial growth for both *B. subtilis* and *E. coli*, and an increase in bacterial cell count was observed, as shown in Figure 5.5. Owing to their unique redox potentials, transition metals, such as iron and copper, also play a crucial role as metal cofactors. Here, both these metals facilitated bacterial growth as can be seen from the increase in bacterial cell count in 12 h, compared to the control. In this study, the addition of Cu (II) at concentrations of 33.4 nM and 66.8 nM resulted in a growth enhancement of approximately 50% and 150%, respectively, for *E. coli*. Similarly, supplementation with Fe (II) at concentrations of 33.4 nM and 66.8 nM led to a 150% and 200% increase in bacterial growth, respectively (Figures 4.11 (a-b)). They serve as components of proteins (metalloproteins, storage proteins, transcription factors) and as cofactors or structural elements for enzymes [146,147]. For instance, magnesium plays a vital role in maintaining the permeability and integrity of the bacterial cell membrane by stabilization of spheroplasts [148]. The cation is also required for the activity of enzymes, helps preserve the structure of ribosomes,

and plays an essential role in stabilizing the tertiary structure of tRNA, serves as a cofactor of many enzymes, and is also required for RNA polymerase. Similarly, calcium ions (Ca^{2+}) are needed for membrane transport channels and the activity of ATPases that provide energy functions [149]. Similarly, *B. subtilis* also showed significant effect on growth (>3-fold) when supplemented with 20 nM of these metals, as shown in Figure 5.5. This is because they perform essential roles-such as, copper is required for cofactor of enzymes and structural component of proteins; and iron is required for cytochromes and heme proteins, Fe/S cluster, Fe-oxoglutarate, and other non-heme proteins, as reported previously [150]. However, when concentrations of metal salts were increased from 20 nM to 40 nM, no significant change was observed, as shown in Figure 5.5. In *B. subtilis*, Mg^{2+} and Ca^{2+} confer rigidity to the bacterial cell membrane as well [151]. For instance, the growth of *Bacillus* was enhanced by the addition of magnesium salts, as depicted in Figures 5.5c and 5.5d.

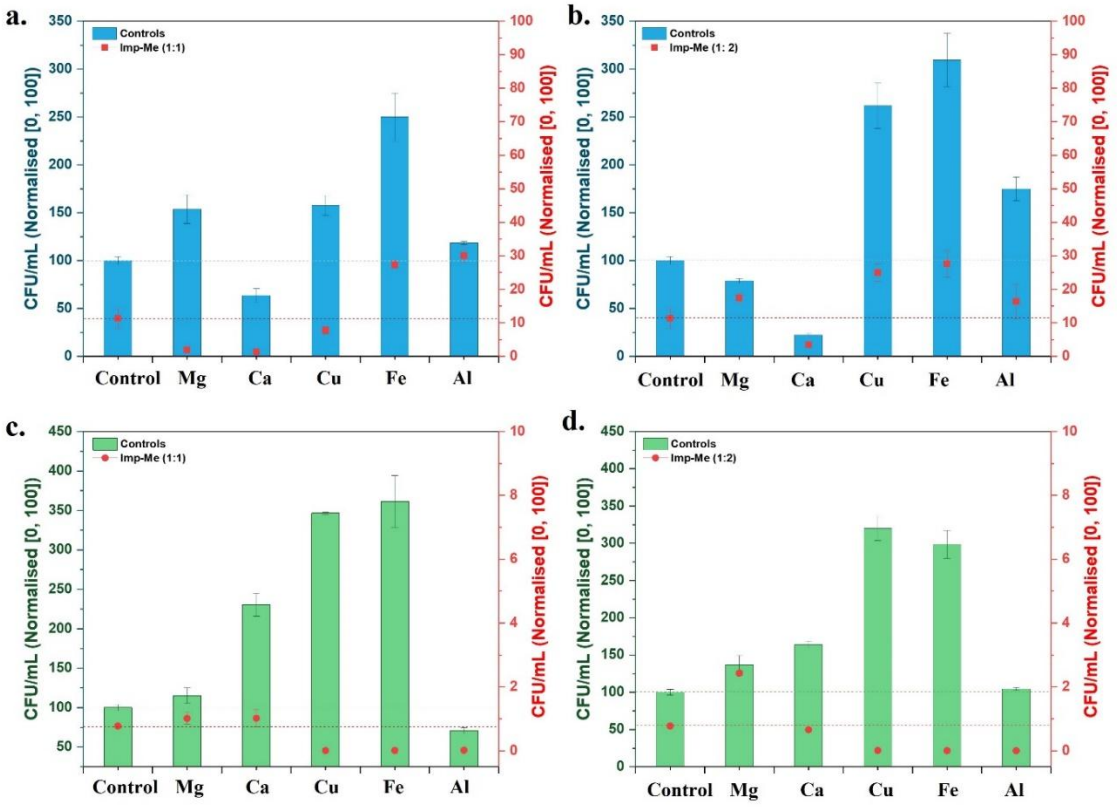

Figure 5.5: Toxicity studies of Imipenem and its metal complexes (1:1 and 1:2) in *Escherichia coli* (*E. coli*) ((a) and (b)); *Bacillus subtilis* (*B. subtilis*) and ((c) and (d)), respectively

Although aluminum belongs to the non-essential class of chemical elements, an increase in cell count was observed for both *E. coli* and *B. subtilis* when the media was supplemented with the metal salt. For instance, *B. subtilis* exhibited a higher rate of proliferation (+47.22%) with an increase in the concentration of Al (III) from 20 nM to 40 nM, as shown in Figures 5a and 5b. Similarly, for *E. coli*, the number of bacterial cells increased by 32.27% when metal concentration was increased from 33.4 nM to 66.4 nM (Figures 5.5 (c-d)). However, owing to its high association constants with diverse ligands, previous studies have reported the ability of aluminum to substitute magnesium and perform magnesium-dependent biochemical and regulatory functions to support bacterial growth, as observed here. To corroborate, the affinity of aluminum to ATP is almost 10^7 times that of magnesium, which means aluminum concentrations as low as nanomolar levels can replace millimolar concentrations of magnesium [152,153]. However, in biological systems, Al (III) may also bind to cell membrane phospholipids, affecting lipid-protein interactions and disrupting transport proteins [153]. They can also impact the enzymatic activity- either by binding to the enzyme or the enzyme substrate and affect metabolism within the bacterial cell [152].

However, both bacteria displayed different susceptibility against IMP and IMP-metal complexes. Being positively charged (+3), Aluminium preferentially interacts with oxygen-donor ligands or oxygen-containing functional groups in the ligands, such as phosphates and carboxylates, which being anionic, counter this charge [153]. On similar grounds, it also interacts with IMP in the medium to form Imp-Al complex [Al_2 $(IMP)_3$], as seen above, and displays higher antibacterial activity towards the studied model microorganisms, compared to the parent drug (as shown in Figure 5.5). This can be attributed to electron delocalization during this metal chelation- the lipophilicity of the antibiotic can increase, which facilitates the interactions and uptake of AMCs with the bacterial cell membrane [27] [16]. Further, their increased stability, as determined by the titration studies, together indicate their persistence and toxicity in the environmental matrices.

A similar trend was observed for all other metals as well, and it is evident from the findings that the IMP-metal complex displays higher antibacterial activity towards both gram-positive and gram-negative bacteria compared to IMP. The MIC90 of IMP (33.4 nM) for *E. coli*, ~98% inhibition was observed for Imp-Mg and Imp-Ca (1-1), >95% for Imp-Cu (1-1), compared to 90% inhibition in control. Similarly, for *B. subtilis*, >99% inhibition was observed for Imp-Me 1-1 (Me= Fe and Cu) for MIC90 (20 nM), as shown in Figure 5.5. These findings lie in good accordance with the results from the DFT studies. That is, lowering dipole moment, or increasing lipophilicity

by metal complexation of the antibiotic, displays higher antibacterial activity. Thereby, both studies substantiate each other.

This higher antibacterial activity of IMP-metal complexes compared to the parent antibiotic can be due to decreasing polarity (hydrophilicity) and an increase in lipophilicity because of electron delocalization, which can thereby facilitate the uptake and interaction of these molecules [19,27]. Further, metal ions can also interact with the bacterial cell membrane, leading to membrane destabilization and increased permeability- this increased permeability can lead to higher uptake of antibiotic molecules within the cell and increased toxicity.

While both these strains- *E. coli* and *B. subtilis* serve as representative model wastewater microorganisms for gram-negative and positive bacterial species, providing a standardized and widely accepted framework for comparative toxicity evaluation, they do not fully represent the complexity of the wastewater microbial communities. The results, thereby, should be interpreted as indicators of intrinsic antibacterial and metal-complexation-driven toxicity rather than direct predictions of community-level ecological impacts.

5.4 Conclusions

The binding affinity of IMP with metals Mg (II), Ca (II), Fe (II), Cu (II), and Al (III) follows the order: Al (III) > Ca (II) ≈ Mg (II) > Cu (II) > Fe (II), as determined by potentiometric titrations performed at pH 6.0 ± 0.2 at room temperature. The most stable stoichiometry (M: L) was observed to be 2: 3 for trivalent metal, (Al (III)); 1: 2 for alkaline earth metals Mg (II) and Ca (II); and 2: 1 for Cu (II) and Fe (II). The interaction of IMP and metals, and the formation of complexes were also studied by UV-vis spectroscopy and LC-MS. The peaks at m/z 319.0742 and 311.08595 are attributed to $[Ca(IMP)_2]^{2+}$ and $[Mg(IMP)_2]^{2+}$, respectively. Further, the metal complexes for IMP displayed higher antibacterial activity towards E. coli and B. subtilis, wastewater model microorganisms. For B. subtilis, MIC50 and MIC90 were found to be 4 µg/L and 6 µg/L (~20 nM), respectively. Similarly, for E. coli, MIC50 and MIC90 were observed to be 2 µg/L and 10 µg/L (~33.4 nM). For E. coli, ~98% inhibition was observed for Imp-Mg and Imp-Ca (1-1), >95% for Imp-Cu (1-1), compared to 90% inhibition in control (33.4 nM). Similarly, for B. subtilis, >99% inhibition was observed for Imp-Me 1-1 (Me= Fe and Cu) for MIC90 (20 nM). These findings lie in good accordance with the results from the DFT studies. DFT studies reveal that, in general, IMP-metal complexes have lower electronic energy, and thereby higher stability than IMP. For

instance, the electronic energy of IMP-Al (M: L= 2: 3) was determined to be -4474.18 Hartree, compared to -1330.93 Hartree of IMP alone. This higher stability, coupled with lower dipole moment or higher lipophilicity, facilitates higher uptake of IMP- metal complexes by bacterial community in environmental matrices, like wastewaters, thereby posing a threat to the existing wastewater treatment systems and triggers the rapid spread of antibiotic resistance.

PART B: FLUOXETINE: LITERATURE INSIGHTS AND TREATMENT STRATEGIES

Chapter 6: Review of Literature

From Prescription to Pollution: Environmental Behaviour and Breakdown of Fluoxetine

Pratishtha Khurana [a], Ratul Kumar Das [a], Satinder Kaur Bar [a*]

[a] Department of Civil Engineering, Lassonde School of Engineering, York University, Canada

*Corresponding author: Satinder Kaur Brar; email: satinder.brar@lassonde.yorku.ca

Graphical Abstract:

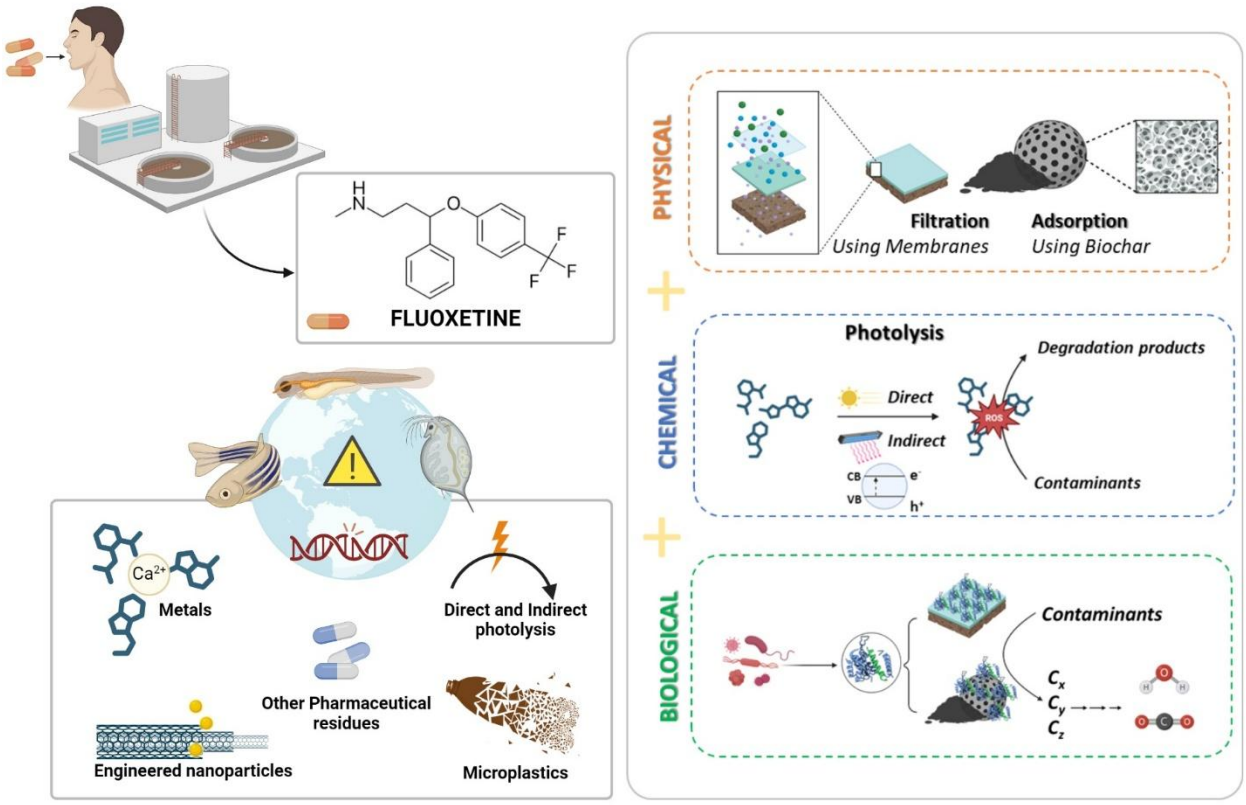

Environ. Sci.: Water Res. Technol., Volume 11, 2025, 2825-2843;

DOI: 10.1039/D5EW00636H

Abstract

Fluoxetine (FLX), a widely prescribed antidepressant and one of the most prevalent pharmaceuticals detected in the environment, has piqued significant interest recently due to its persistence and potential ecological effects. Despite its widespread detection, no comprehensive review currently exists that focuses specifically on FLX's environmental behaviour. As a polyfluorinated synthetic organic compound, FLX serves as an ideal model for understanding the broader challenges faced by fluorinated pharmaceuticals. This review presents a critical and integrative assessment of FLX, beginning with its molecular structure and role of the C-F bond in enhancing the chemical stability and recalcitrance. The review then explores its environmental fate, including its behaviour towards hydrolysis, photolysis, partitioning, susceptibility to microbial attack, potential for bioaccumulation, and interactions and joint toxicity with other co-existing pollutants. This is followed by a comprehensive and critical discussion of existing advanced removal techniques currently investigated for FLX removal and offers recommendations for future studies. Despite some promising approaches, challenges remain due to the inherent stability of the C-F bond, the toxicity of by-products, and the complexity of the matrix. This review also aims to highlight the need for environmental management of FLX, not only to mitigate its ecological footprint but also to offer broader insights into the class of polyfluorinated pharmaceuticals.

Keywords: Fluoxetine, Contaminant, PFAS, Biodegradation, Polyfluorinated compounds

6.1 Introduction

Fluoxetine (FLX), sold as Prozac®, belongs to the second generation of SSRI (Selective Serotonin Reuptake Inhibitor) class of antidepressants and is considered a breakthrough drug for depression. Following its discovery and FDA approval in 1987, FLX has become one of the most prescribed antidepressants globally [154]. This is primarily because of its safety, therapeutic efficiency for all genders and ages, and fewer adverse effects, withdrawal symptoms, and dropouts. It is considered a first line of treatment for mental disorders, including depression, anxiety, phobias, obsessive-compulsive disorders, and bulimia nervosa [154,155]. It acts on the central nervous system and inhibits the uptake of neurotransmitter serotonin (5-hydroxytryptamine or 5-HT) by the presynaptic neuron by blocking the serotonin transporters (or SERT) in the neural membrane. The mechanism of action of FLX and its metabolism in body is summarized in appendix C.

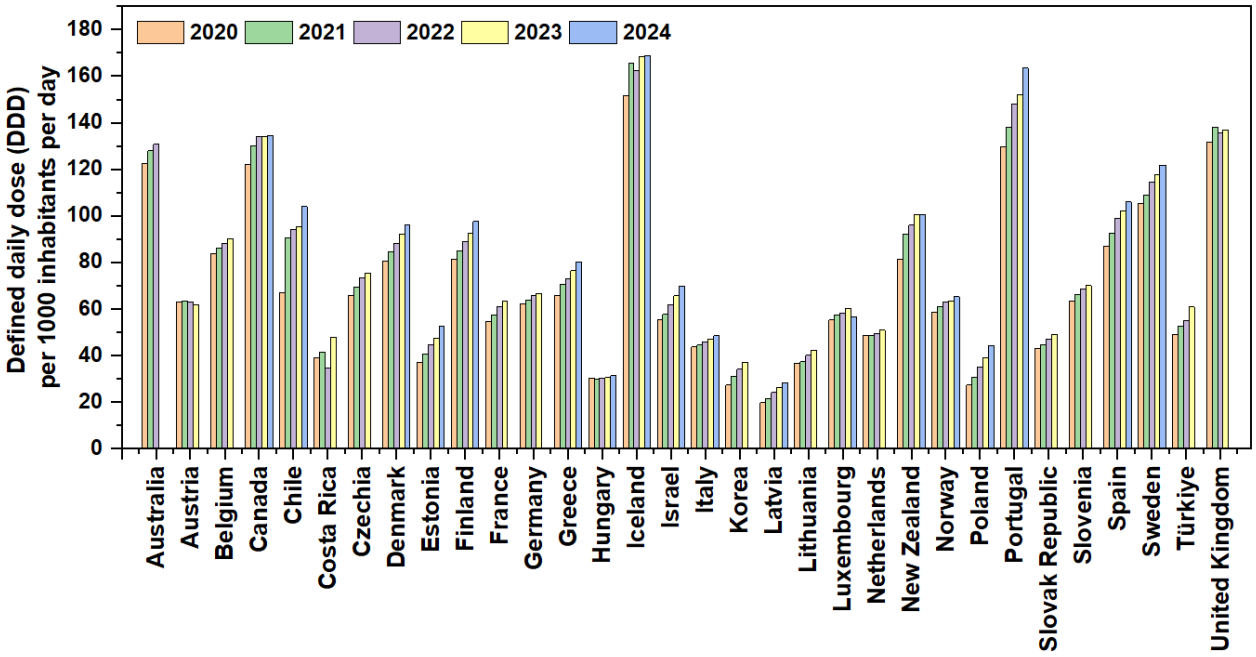

Figure 6.5: Antidepressant consumption in OECD member countries (2020-2024)

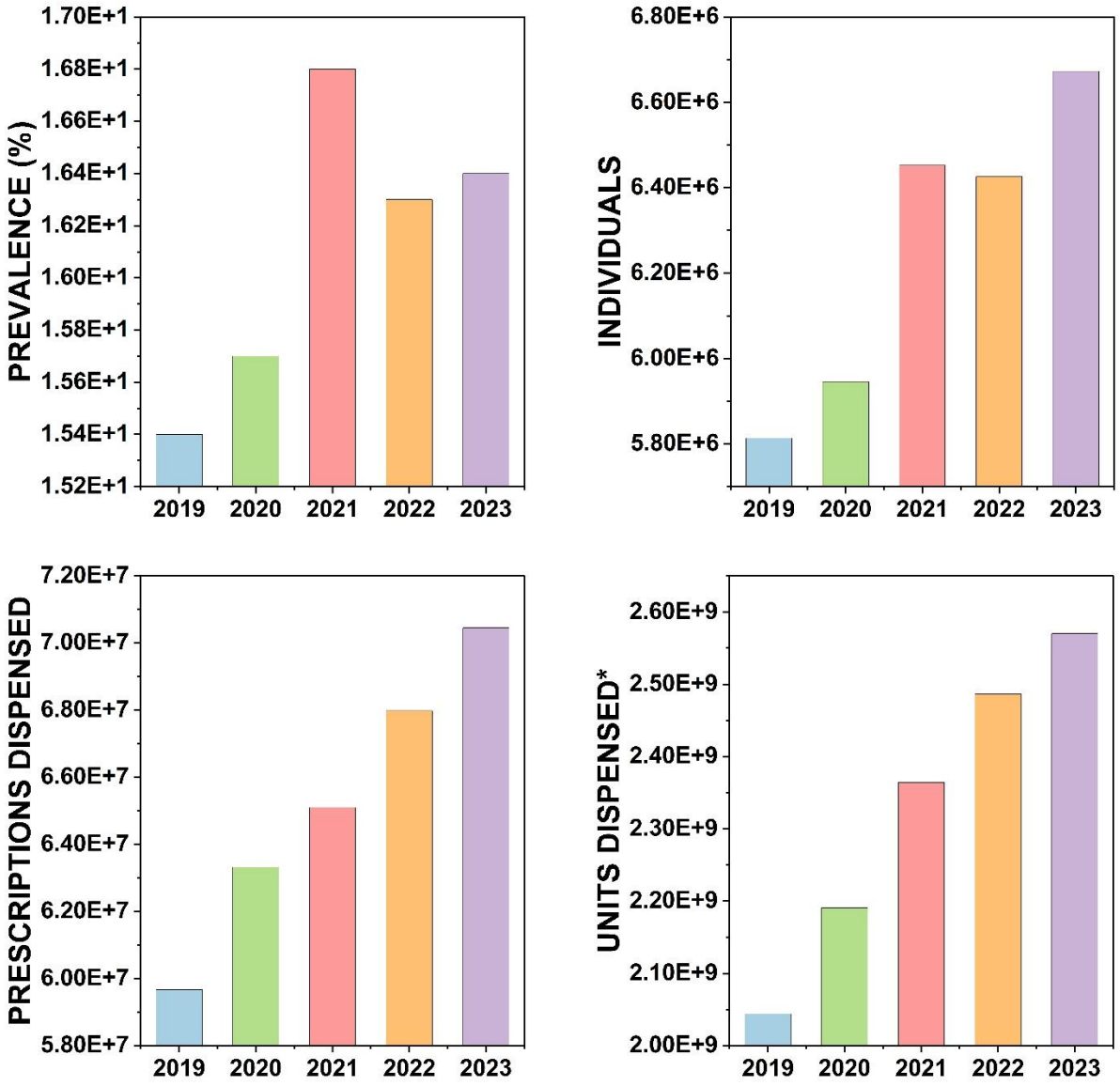

Figure 6.6: Statistics on antidepressant use in Canada and variations (2019-2023)

With increasing incidences of psychiatric and mental disorders, the prescription and consumption of FLX have increased over the years [156–160]. Figure 6.1 displays the most recent data by the OECD on antidepressant consumption (the USA was not a part of this study) [161]. However, as mentioned elsewhere, FLX was ranked 31 on the top 300 best-selling drugs in 2020, with 21.9 million prescriptions in the US in 2017. In 2019, 27.1 million prescriptions were filled for FLX, making it among the top 200 most prescribed drugs for the year at rank 20 [162]. Similarly, Canada has seen a 26% increase in the use of

antidepressants from 2019-2023 (as shown in Figure 6.2), with over 2.5 billion units (tablets/capsules) dispensed in 2023[5]. In addition to North America, the use of SSRIs has also been on the rise in Europe. For instance, prescription data from Denmark show a gradual increase from 42.32 to 48.24 defined daily doses (DDD) per 1000 inhabitants between 2020 and 2024 [163]. Similarly, data from Sweden and Spain indicate an increasing trend for FLX use for the same period, with DDD rising from 6.19 to 7.19, and from 7.06 to 8.08, respectively [163,164]. This increase in consumption is well reflected in the concentrations and frequency of its detection in environmental matrices, such as wastewater, wastewater sludge, and surface water, *via* domestic and hospital effluents, industrial leaks, and poor disposal practices, as summarized in Table 6.1. Among environmental matrices, the highest FLX concentrations have been reported for wastewater treatment plant (WWTP) influents (reaching up to ~ 3.2 µg/L), as it directly receives excreted drug residues from patients, and no chemical or biological methods of treatment have been applied to reduce their levels. In addition, the concentrations in Table 6.1 indicate highly variable removal efficiency for FLX during the wastewater treatment. For instance, an analysis of grab samples collected from a WWTP in the UK by Evans et al. (2015) revealed a ~49% efficiency, while another study by Piaga et al. (2019) in Portugal reported an efficiency of ~26% [165,166]. In some cases, a negative removal efficiency was also observed. For example, for Canadian hospital wastewater monitoring, a removal efficiency ranging between -171% and 40.2% was calculated based on the concentrations reported for the influent and effluent [167]. The negative values could indicate metabolite-back transformation, desorption, or sampling variability. Most of these samples are grab samples, which do not reflect the efficiency of WWTP correctly. Despite this, an inconsistent, often incomplete removal of FLX has been reported during wastewater treatment.

Due to its poor degradation along the treatment chain and its relatively high lipophilicity, FLX persists beyond the influent stage, resulting in frequent detection in wastewater sludge and effluent, which can further carry FLX to surface water. Its frequent detection, persistence and toxicity in these environmental matrices, instigate several concerns in aquatic and terrestrial ecosystems [165,167–170]. For instance, FLX uptake in fish has been reported to have consequences on growth and behaviour, reproductive axis, metabolism, accumulation, and gene expression[10–13]. Similarly, wild European starlings (also known as songbirds), after exposure to FLX (2.7 µg/day), displayed altered physiological and behavioural changes, such as higher aggression towards partners, poor courtship behaviour, and reduced female attractiveness [171]. The hydrophobic and lipophilic nature of FLX allows its adsorption on biological membranes, resulting in its uptake, and bioaccumulation. The lipophilic nature of the drug also allows it to readily distribute into cells, including central nervous systems in human body, and cross blood-brain barrier

(BBB) by passive lipophilic diffusion. This also poses a risk of neural disruptions by targeting serotonin pathways in non-target organisms, altered reproductive, growth, and physiological behaviours, including prey-predator dynamics, which can result in the disruption of food web [172–174]. Further, in regard to its environmental presence, previous reports have indicated that the drug is stable towards hydrolysis, photolysis, and facile microbial degradation, making them environmentally persistent [175–177]. This constant presence of FLX in both aqueous and solid matrices, along with its persistence and toxicity to non-target organisms, has rightly garnered attention recently. The number of publications addressing FLX in aquatic environments has increased markedly since, as shown in Figure 6.3, reflecting growing recognition of its importance, although significant research gaps remain in its treatment approaches. The drug has been identified as an emerging contaminant and demands immediate attention concerning its monitoring and degradation strategies.

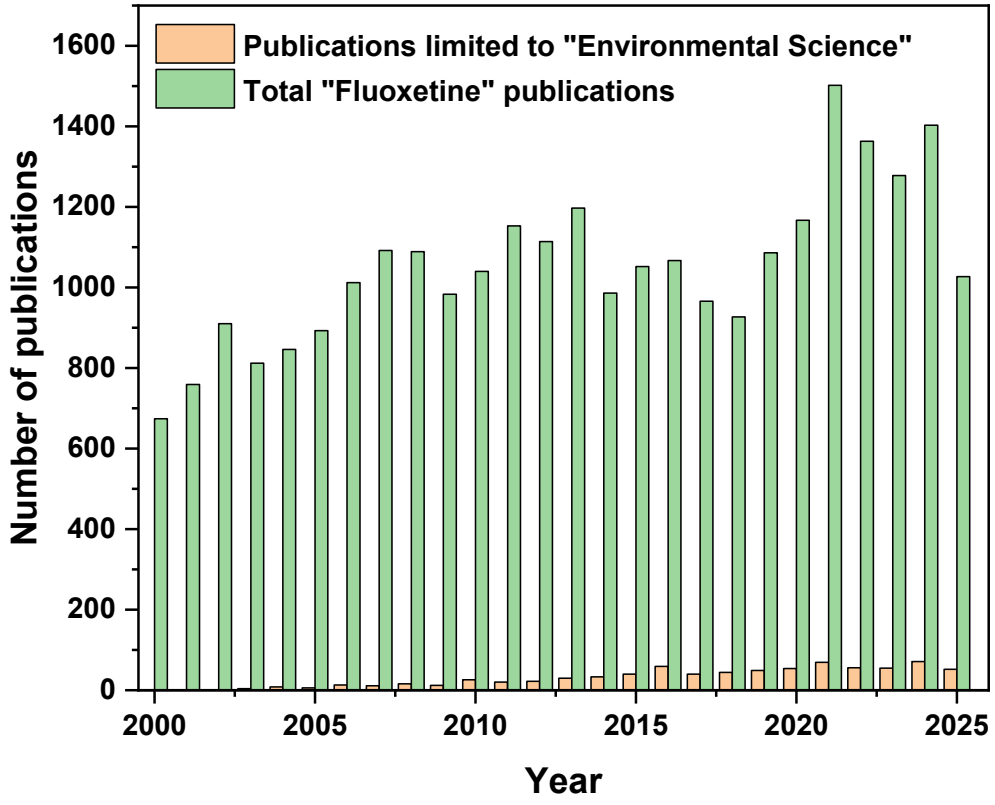

Figure 6.7: Annual number of publications on FLX for 2000-2025. Data retrieved from Scopus using relevant keywords.

(*Search strings used: (TITLE-ABS-KEY (Fluoxetine) AND TITLE-ABS-KEY (wastewater OR aquatic OR river OR environment OR effluent OR lake) for studies limited to Environmental Science. For total FLX publications: (TITLE-ABS-KEY (Fluoxetine))).

Table 6.1: Summary of occurrence of FLX in wastewater and wastewater sludge

Year	Matrix	Location	Concentration of FLX (ng/L)	Detection Method	Ref.
2010	Raw influent	Douro River estuary (Portugal)	0.80-3.20 µg/L	HPLC-DAD	[178]
2011	Hydro matrix	Scotland (WWTPs)	<10	LC-MS	[179]
2012	Raw influent Final effluent	5 STPs in Canada	9-26	LC-MS	[180]
2012	Effluent	Waterloo, Canada	5	LC-MS	[11]
2012	-	Italy	55-190 10-63	-	[181]
2013	Influent Effluent	UK	4.9-175.9 5.6-44.9	-	[182]
2015	Influent Effluent	UK WWTP	51 ± 4.3 26	LC-MS	[165]
2017	Influent Effluent	UK	36-436.5 33-66.5	-	[183]
2019	Influent Effluent	WWTPs in Portugal	78 57.5	LC-MS/MS	[166]
2019	Influent Effluent	Spain	77-207 63-72	LC-MS/MS	[184]
2019	Raw influent	4 WTPs in Belgium	7.5-70	RPLC-MS/MS	[168]
2020	Raw influent	WWTP London, UK	50-58	LC-MS/MS	[185]
2022	Influent Effluent	Hospital Wastewater, Canada	3.51 2.1-9.5	LC-MS/MS	[167]
Year	**Matrix**	**Location**	**Concentration of FLX (ng/g)**	**Detection Method**	**Ref.**
2011	Treated Sludge and sediments	WWTP, Scotland	<10	LC-MS	[170]
2012	Treated Sludge	WWTP, Sweden	144 ± 45	HF-LPME	[186]
2012	Primary sludge Secondary sludge Biosolids	STP, Canada	339 94 74	LC-MS	[180]
2015	Digested sludge	STP, Canada	85.6 ± 9.4	LC-MS	[165]
2019	Sewage sludge	STP, Brazil	90	LC-MS/MS	[169]

Various researchers have investigated physical and chemical methods to tackle FLX-polluted waters; however, no method currently identified is sustainable, promising, and effective for potentially retrofitting current wastewater treatment plant (WWTP) treatment chains. In order to overcome these challenges and present a low-energy, green, and economically feasible approach, several attempts have been made recently to degrade the recalcitrant FLX biologically. However, owing to the drug's low biodegradability, biodegradation attempts with microalgae, fungi, and bacteria (isolated and consortia), have displayed subpar results [187–190]. Previous reports have suggested that the current knowledge of bioremediation systems cannot handle polyfluorinated compounds due to evolutionary constraints [191–193]. While C-F bond cleaving enzymes are not rare, microbial intolerance to high concentrations of intracellular fluoride ion poses this limitation. Intracellular fluoride can deactivate enzymes, mimic phosphate in harmful ways, and disrupts cell's energy balance by collapsing the proton gradient across membranes. Due to this, very low concentrations of intracellular fluoride, as little as 70 μM, are reported to be toxic to prokaryotic cells and can result in cell death [193,194]. So, if a cell can defluorinate, it will generate fluoride ions, thereby causing cell death and putting a constraint on both microbial degradation and evolution. The same principle also makes the enrichment culturing an 'unpromising' method [193]. It is irrefutable that the efficiency of the employed removal technique depends on the structure of the pollutant, and its fate in the environment provides more insight into its behaviour and breakdown profile. In this regard, the present review aims to (i) delineate the structural features of FLX, including fluorocarbon chemistry, that renders it persistent in the environment, (ii) elaborate on fate of the drug in the environment, and (iii) comprehensively and critically discuss the existing removal methods for FLX, identify the challenges, and present prospects in the research area.

6.2 Structural features of FLX and fluorocarbon chemistry

The molecular structure of FLX contains two aromatic rings, one phenyl ring and one trifluoromethyl-substituted phenyl ring, connected by a substituted methoxy group (Figure 6.4). The aliphatic side chains comprise a secondary amine functionality and a chiral carbon (giving rise to (R) and (S)- enantiomers of FLX). Although the two enantiomers have similar efficiency in blocking serotonin reuptake, their metabolism, half-life, renal clearance from the human body, and environmental behaviour vary slightly [195,196]. For instance, the clearance and half-life of R-FLX are four times greater than those of S-FLX, as reported elsewhere [196]. Given its slower clearance and longer half-life, R-FLX is expected to be excreted and consequently released into the environment in greater quantities than the S-enantiomer. In addition,

the stereoselective biodegradation in WWTPs often favours the transformation of S-FLX, leading to further enrichment of the more persistent and ecotoxicologically more relevant R-FLX in effluents [195]. However, at least one study has demonstrated preferential degradation of R-FLX under specific microbial conditions, indicating that enantioselective outcomes may vary with the microbial community and operational context [197].

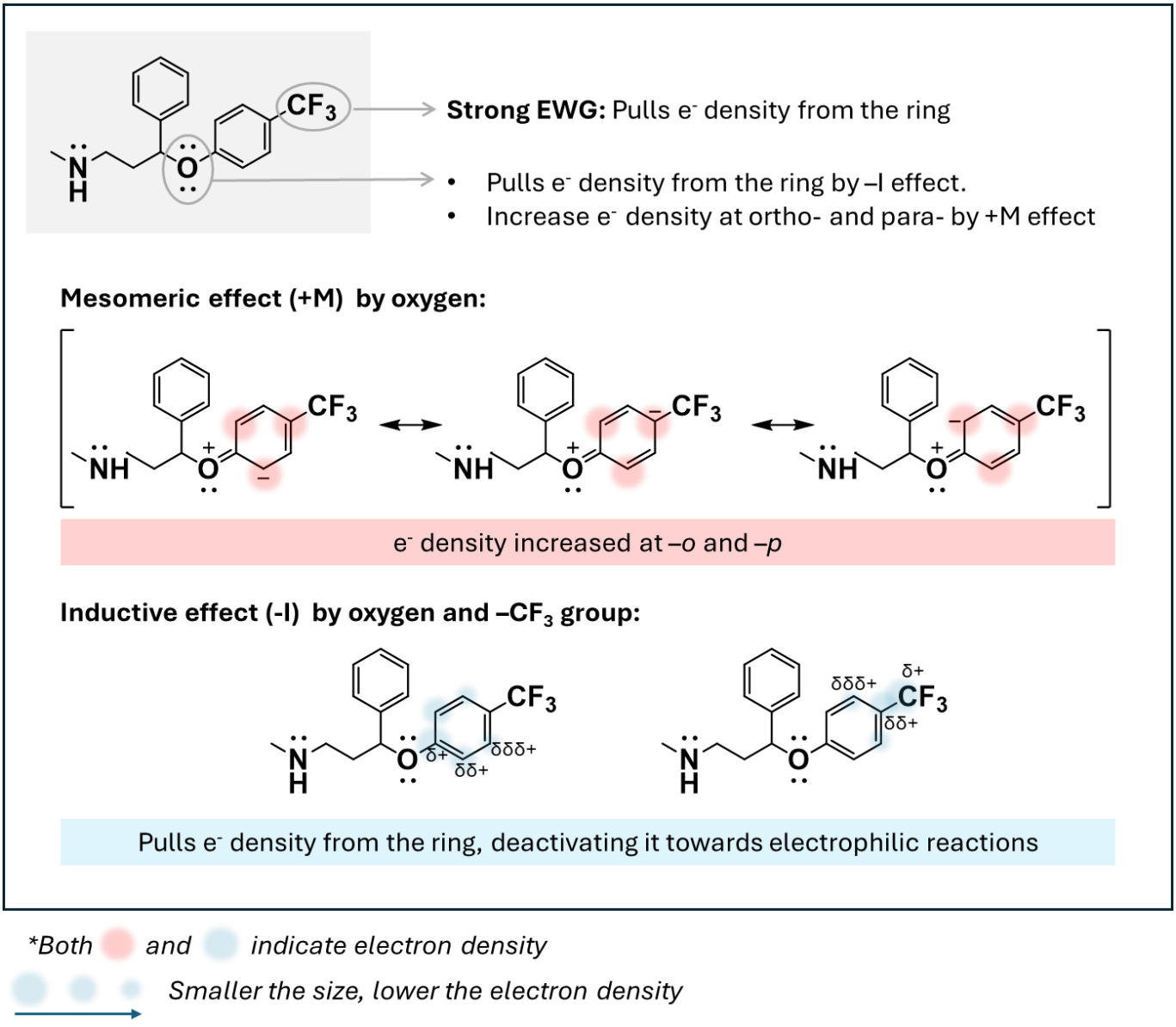

Figure 6.4: Substituent effects on the trifluoromethyl-benzyl group in FLX

The structural features of FLX hinder facile microbial degradation and define its environmental persistence. To begin with, the presence of the secondary amine group (pKa~ 9.8-10.3) indicates that FLX is a weak base and exists predominantly in its protonated or ionized form at circumneutral pH [187,198]. This not only improves the solubility of the drug at environmental pH but also stabilizes it against the nucleophilic attack.

Also, it is evident from the structure that the nitrogen heteroatom, which acts as an electron donor or Lewis base, is spatially well separated from the aromatic rings, suggesting that it does not significantly affect the π-electron delocalization of the rings [199]. The aromatic rings make the drug more hydrophobic and confers high affinity for sorption, thereby limiting its bioavailability. Further, the presence of an oxygen atom (in the phenoxy group, or ether linkage) and -CF_3 substitution at the para position introduces some interesting effects. To begin with, fluorine has the highest electronegativity of all elements, and having three fluorine atoms attached to a single carbon unit makes the -CF_3 a strong electron-withdrawing group (EWG). The Fluorine atoms tend to pull electron density from the adjacent C, and the aromatic ring. This strong -I (negative inductive effect) of the trifluoromethyl group makes the ring less nucleophilic, thereby deactivating it towards electrophilic aromatic substitution reactions (EASR). This reduces the susceptibility of the drug to oxidative metabolism and confers metabolic stability in the environment. This also means that FLX is resistant to environmental breakdown processes, like those mediated by sunlight and radicals, in addition to microbes, as they proceed *via* electrophilic attack on the aromatic ring. This resistance keeps the aromatic rings intact, and FLX persists in the environment with long half-lives.

In addition, oxygen, being electronegative, exhibits a -I effect, while also exerting a positive mesomeric effect (+M) *via* resonance. This means that oxygen tends to pull the electron density through the σ bond *via* an inductive component, while donating a pair of electrons into the π system (resonance) (Figure 6.3). Generally, for oxygen directly attached to an aromatic ring, the +M effect is stronger than the -I effect, which suggests that oxygen increases the electron density at the ortho and para positions of the ring, making it more reactive towards EASR. However, the -I of the CF_3 substituent at the para position often dominates the +M of the oxygen atom and, overall, deactivates the ring by making it electron deficient. This indicates low reactivity of the aromatic ring and greater chemical stability of the drug. The presence of ether also makes it relatively resistant to hydrolysis at ambient conditions that further limit microbial cleavage.

It is noteworthy that the molecular structure of FLX possesses 3 C-F bonds, which is known to have the highest bond dissociation energy (BDE) among all C-X bonds. To strengthen, the BDE of C-F bond is expected to be ranging between 105-130 kcal/mol (i.e., 4.53-5.59 eV), compared to 81 kcal/mol for C-Cl and 46 kcal/mol for C-Br bonds [200]. As mentioned elsewhere, the C-F bond in trifluoromethyl (CF_3H) has a BDE of 114.6 kcal/mol [201]. In FLX, the proton in the trifluoromethyl group has been substituted by an aromatic ring (phenyl), which stabilizes the structure by inductive and resonance effects, thereby increasing the BDE of C-F in aromatic structures, and supporting the high chemical stability of FLX under environmental and treatment conditions.

Owing to these highly stable fluorinated bonds, FLX has been identified as a per- and poly- fluoroalkyl substance (PFAS), commonly referred to as 'forever chemical', in line with OECD guidelines [191]. Overall, this lipophilic and stable chemical structure of FLX contributes to its environmental persistence, underscoring the need to understand its fate in real systems.

6.3 Environmental persistence and Fate of FLX

Once released into wastewater, the pharmaceutical residues can undergo physical, chemical, and biological transformations, determining their fate in the environment. Understanding the fate of the analyte is crucial for determining its behaviour and toxicity, and aids in devising suitable degradation methods for the same. This section, in this regard, outlines different courses, such as hydrolysis, photolysis, sorption and partition, microbial susceptibility, interactions with co-existing pollutants, and their single and combined toxicity, which could influence the occurrence, persistence, and toxicity of FLX. It is, however, important to note that in the 'real' world, these do not operate in isolation but work in integration to define the environmental behaviour of any pollutant, including FLX. The different courses highlighted in this section aim to summarize existing literature and provide a fundamental understanding of how these processes influence FLX fate and transformation in environmental matrices with a water-sediment-biota continuum.

6.3.1 Hydrolysis and photolysis

To understand the fate of the antidepressant FLX, Lam et al. (2005) investigated the direct and indirect photolysis of the drug in simulated sunlit waters (~300-800 nm) under pH 6, 8 and 10. An aqueous solution of FLX (10 μM) (pH 8) was observed to be susceptible to direct photolysis with a half-life of 7 ± 1 days (55.2 ± 3.6 h) with a pseudo-first-order rate constant of 0.0126 ± 0.001 h^{-1}. Negligible degradation in controls stored in the dark confirms the contribution of only base-catalyzed direct

photolysis (<5%) and no effect of thermal or hydrolytic degradation of the drug [202]. The thermal stability of the drug at pH>2.5, with ≥95% of initial FLX for 8 weeks at temperatures of 5 and 30 °C, was also reported previously by Peterson et al. (1994) [175].

Although the study by Lam et al. (2005) did not provide degradation rates for pH 6 and 10, degradation is expected to be faster at alkaline pH (pH 10) due to the prevalence of more neutral/anionic species that are more photoreactive, compared to slightly acidic pH. However, this must be viewed as a comparative trend, and it must be noted that FLX has demonstrated stability towards base, heat, humidity, and oxidative conditions and displayed degradation only under highly acidic conditions (pH <1), which is not environmentally relevant [203] [204]. Another study by Kwon and Armbrust (2006) conducted laboratory-scale studies to investigate the persistence of FLX in aquatic systems, including aqueous solution (buffered solution pH 7, synthetic humic water, and lake water), water/sediment systems and activated sludge media. The study reported that the drug was hydrolytically and photolytically stable for a period of 30 days [176]. Similarly, a more recent study by [177] observed low photolysis rates for the degradation of FLX and FLX-SO_4 by hydrolysis in pure water and natural pH and under simulated sunlight.

Also, it must be noted that hydrolysis and photolysis frequently overlap in aquatic environments, as hydrolytic reactions may occur under irradiation and photolytic pathways are typically studied in aqueous systems; these processes should not be considered entirely isolated, particularly in the environmental context.

6.3.2 Sorption and partition in Water/sediment systems

The physicochemical properties of FLX allow for the prediction of its environmental fate, including biodegradability and partition in water/sediment systems. For instance, the octanol-water partition coefficient, or hydrophobic descriptor, represented by log K_{ow}, defines its uptake in biological wastewater treatment processes. A log K_{ow} < 2.5 indicates low sorption potential, 2.5 < log Kow < 4 indicates medium sorption potential, while log K_{ow} > 4 indicates high sorption potential [187,205]. Additionally, the solid-water distribution coefficient (K_d) is defined as the partition of a compound between the sludge and the water phase at equilibrium. For compounds with K_d > 300 L/kg (i.e. log K_d > 2.48), sorption onto sludge is considered significant [206]. However, factors such as functional groups, their speciation with pH, organic matter, cation exchange capacity, ions, and clay also play crucial roles [207,208].

FLX has a log K_d = 2.76-3.78 (log K_d > 2.7) and log K_{ow} > 4 at circumneutral pH (pH 6-8), which indicates that the drug is lipophilic and predicts its high adsorption potential [187,188,209]. This suggests that

FLX tends to adsorb onto solids, indicating its elimination by activated sludge processes (ASP) during the treatment train at WWTPs. The study by Kwon and Armbrust (2006) also revealed that FLX rapidly partitions in water/sediment systems, with adsorption to sediments, and this distribution is unaffected by light: dark cycles [176]. Although this partitioning to sediments and natural organic matter (NOM), *via* adsorption or complexation, and salinity does not affect the concentration of FLX, it alters the bioavailability of the drug and uptake by organisms[210]. Recent studies have shown that (i) FLX is stable in soil for up to 270 days, which is sufficiently long period for plant uptake, if any, and (ii) the presence of FLX in soil significantly affects both- pH of the soil and internal pH of earthworm *Eisenia fetida*, which are the key terrestrial invertebrates [211,212].

It is worth mentioning that although there is a significant knowledge gap concerning the fate of FLX in soil systems, it is known that organic matter in the soil, and so the soil types, influences the sorption and bioavailability of FLX; however, it does not influence the stability and persistence of the drug residues [211,212]. Long-term stability of FLX in soil coupled with the land application of FLX-containing sludge and biosolids as fertilizer into the soil can provide a route of entry for the drug to the soil and agricultural fields. A previously reported preliminary study has reported the uptake of FLX into Brassicaceae tissues (cauliflower stems and leaves); however, more studies are required, especially for crops commonly grown on sewage-sludge amended soils, such as corn, potato, lettuce, and cabbage [213].

It has also been reported that nucleophilic -NH of FLX reacts with electrophilic chlorine of hypochlorite during chlorination to rapidly (<2 minutes) form N-chloramine [214]. It is noteworthy that the presence of amine-containing organics, such as FLX, creates a high 'chlorine demand' but results in lower disinfection efficiency. The release of N-chloramines is also concerning because of (i) increased hydrophobicity and (ii) acts as an active chlorine carrier. At neutral conditions, FLX exists in protonated form. However, the replacement of H by Cl makes it neutral or unprotonated, making it more hydrophobic than the parent FLX. This increased hydrophobicity can result in a greater tendency to adsorb on organic surfaces such as sediment, soil, and biological membranes [214,215]. The N-chlorofluoxetine can also serve as a carrier for 'active chlorine' and transfer its chlorine to other reductants or assimilation in biological cells post uptake[214].

6.3.3 Microbial susceptibility and bioaccumulation potential

The K_{biol} for FLX ranges from 0.03 to 9.0, demonstrating poor to significant biodegradability, depending heavily upon conditions [187]; the antidepressant was found to be resistant to microbial degradation in

WWTPs [176,216]. Ultrasonication has been explored as a pretreatment to improve the biodegradability of FLX [216].

In addition to microbial persistence, FLX has been studied to accumulate in aquatic organisms and transfer *via* the food chain, exhibiting the potential to bioaccumulate and bio-magnify at all trophic levels [217–219]. For instance, after exposure to 75 ng/L FLX for 15 days, mussel *M. galloprovincialis* showed signs of accumulation of both FLX and norfluoxetine, increasing from 2.53 and 3.06 ng/g dry weight on day 3 to 9.31 and 11.65 ng/g on day 15, respectively [220]. The SSRI has also been studied to accumulate in *Spirostomum ambiguum*, ciliated protozoa commonly found in activated sludge in WWTPs and surface waters [215]. Since protozoa have a critical role in controlling bacterial populations and dynamics, promoting floc formation, and improving sludge settling, FLX accumulation in them can potentially (i) affect their mobility and growth, (ii) cause a shift in bacterial communities, (iii) impair sludge settleability, affecting nutrient removal and WWTP performance. Although previous studies have reported consequences on growth and behaviour, reproductive axis, metabolism, accumulation, and gene expression due to accumulation of FLX in the brain, liver, and muscles of zebrafish (Danio rerio) and goldfish (*Carassius auratus*), reports on the accumulation of FLX in protozoa and its potential effects are lacking [10,12,155,13,210]. .

6.3.4 Interactions with co-existing pollutants and combined toxicity

Owing to its structural features and physicochemical parameters, FLX can interact with co-existing pollutants and has been the center of a few studies, as summarized in Table 6.2. The drug has been studied to interact, directly or indirectly, with organic matters such as co-existing pharmaceutical residues, microplastics, and inorganic entities like metals and engineered nanomaterials [221–225]. For instance, the co-occurrence of FLX and Sertraline (SER) has been studied to affect the growth, photosynthetic activity, and antioxidant system of the microalga *Chlorella pyrenoidosa*. Although both FLX and SER strongly inhibit microalgal growth, with 96-hour EC50 values of 493 and 61.1 µg/L, respectively. However, the combined effect is additive and causes more significant photosynthetic damage and oxidative stress than either compound alone. The microalgae *C. pyrenoidosa* can efficiently remove FLX by biodegradation and SER by both biodegradation and bioaccumulation, but their co-existence lowers the biodegradation rate and subsequent removal for both drugs [225]. A similar effect on the antioxidant system and inhibition of Ca (II)-ATPase was observed in Daphnia magna on simultaneous sub-chronic (7 days) and acute exposure (48 h) to FLX and Zn (II) [221]. The presence of FLX has also been reported to affect the

functioning of intracellular Ca (II) channels in cells, thereby inhibiting respiratory chain and disrupting ATP production [226–228].

Likewise, the co-existence of FLX and ketoprofen, an analgesic, induces greater disruptions in nitrogen and phosphorus cycles and micro-eukaryotic communities, including physicochemical and biological variations, compared to either pharmaceutical alone [223]. This can be partially owed to its potential to influence the antibacterial activity of several co-occurring antibiotics against both standard and multi-drug-resistant strains [222,229]. For instance, FLX is effective against gram-positive bacteria, with limited activity against gram-negative bacteria. Although it does not interfere with the antibacterial activity of antibiotics directly; however, it interferes with the bacterial resistance mechanism, such as inhibition of efflux pumps, to exhibit both antagonistic and synergistic effects [222]. It can also alter the behaviour of *Asellus aquaticus*, a benthic micro invertebrate and a decomposer, resulting in a slower rate of microbial decomposition of plant remains near the sediment [224].

A recent study by Yan et al. (2019) highlighted the increased FLX uptake and accumulation in fish in the presence of multi-walled carbon nanotubes (MWCNTs) [210]. Similar results were observed with mussels (*Mytilus galloprovincialis*) [220]. It is considered that the occurrence of nanomaterials, like MWCNTs, serves as an adsorbent for FLX, forms an adduct, increases the uptake, and promotes the accumulation in aquatic organisms [210].

All these studies highlight that combined exposure of FLX with other pollutants may instigate harmful impacts on ecosystem levels, including aquatic microcosms and bacterial communities. This has encouraged the researchers to devise effective removal techniques for FLX from aqueous matrices, including physical, chemical, and biological degradation, as discussed in the next section.

Table 6.2: Summary of interactions between FLX and other environmental co-pollutants

Co-pollutant/ Condition	Interaction Nature	Observed effects	Environmental relevance	Ref.
Sertraline	Additive	- FLX with sertraline showed additive toxicity to microalgal growth - Damaged antioxidant systems and photosynthesis	- Presence of SSRIs can affect microalgae-based bioremediation	[225]
Ketoprofen	Additive	- Induced greater disruptions in nitrogen and phosphorus cycles - Reduced D. magna brood rate, inhibited Lemna growth - Changed the composition of micro-eukaryotic communities	- Can affect ecosystem communities and their functional processes - May affect ecological risk estimations due to over/underestimation	[223]
Microplastics (polystyrene)	Synergistic	- Disruption of gene expression and oxidative pathways - Increased malformations, morality, and delayed embryonic development - Microplastics enhance FLX toxicity and tissue accumulation	- Interfere with fundamental biological processes, cause direct and indirect toxic effects	[230]
Microplastics (polystyrene)	Mixed	- Microplastics reduced trophic transfer of FLX along food chain and mitigated the neurotransmission biotoxicity in fish induced by FLX - Enhanced oxidative stress, apoptosis, immune responses in zebra fish	- Carrier effects of microplastics can affect trophic transfer of FLX and biotoxicity in environmental matrices - Relevant in matrices containing both the entities	[231]
Microplastics (polystyrene)	Complex	- Combination of FLX and microplastics influence phytoplankton biomass, zooplankton abundance, and microbial decomposition rate of plants	- Microplastics can reshape dose-response outcomes for FLX at ecosystem levels	[224]
Azoles	Synergistic	- Combination of FLX with fluconazole dimmish the virulence of C. albicans by downregulation of gene expression and weakening of extracellular phospholipase activity	- FLX in presence of azoles can be used as a potential therapeutic strategy against resistant C. albicans infections	[232]
Zinc (Zn^{2+})	Antagonistic	Reduced FLX toxicity on D. magna, along with antioxidant suppression and Ca(II)-ATPase- inhibition	Oxidative stress	[221]
Carbon nanotubes (MWCNTs)	Synergistic	- MWCNTs play as ‘carrier’, increasing bioavailability, uptake and accumulation in fish - NOM alleviated, and salinity reversed the carrier effect of MWCNTs	NOM and salinity affect the interactions between FLX and engineered nanostructures; can cause uncertainty in risk assessment of FLX	[210]

6.4 Removal technology bottlenecks

6.4.1 Physical methods

6.4.1.1 Adsorption

The physicochemical properties of FLX indicate its high tendency for surface adsorption, and this capacity has been utilized to remove FLX from aqueous solutions *via* adsorption. Various adsorbents, including but not limited to commercial adsorbents, biosorbents, and metal-based nanoparticles, have been employed for this purpose, as summarized in Table 6.3.

(i) Waste-derived adsorbents: The principles of waste valorization, zero-waste and circular economy have promoted the utilization of waste, such as lignocellulosic and agri-food waste, to prepare high-capacity adsorbents to combat pharmaceutical pollution. For instance, Silva et al. (2020) utilized spent coffee grounds, pine bark and cork waste to produce biosorbents with maximum adsorption capacity between 4.74 mg/g and 14.31 mg/g [233]. Nkana et al. (2024) prepared a series of adsorbents using different ratios of polyethylene glycol (PEG 2000) and carboxymethyl chitosan derivatives (O-CMCs and N, O-CMCs; 0.03 g/mL) (denoted as PHB1, PHB2, PHB3, PHB4, and PHB5, with surface area 19.84, 29.81, 37.50, 3.69, and 25.93 m^2/g, respectively), and used them to remove FLX *via* physisorption. The maximum absorption capacity observed for the materials ranged from 90.6 to 112.6 mg/g [234]. Similarly, adsorbents prepared by chemical activation of primary paper sludge with KOH, NaOH, and $ZnCl_2$, followed by pyrolysis (PS800-10KOH, PS800-10NaOH, and PS800-10$ZnCl_2$) achieved a maximum adsorption capacity of 191.6 ± 4.8, 136.6 ± 9.6, and 28.4 ± 0.3 mg/g, respectively. [235]

The naturally occurring fibres, such as xylan, pectin, and lignin, have also been exploited to produce efficient adsorbents. For instance, Farghal et al. (2023) used xylan and pectin-coated activated-carbon-based magnetite adsorbents to remove FLX. These nanocomposites-Xylan/AC/Magnetite (XCM) and Pectin/AC/Magnetite (PCM) displayed adsorption capacities of 90.9 mg/g and 114.9 mg/g, respectively. The xylan and pectin-modified nanocomposites displayed enhanced regeneration, reusability, and stability compared to AC/magnetite (CM) nanocomposite [236]. Similarly, Camiré et al. (2020) transformed lignin into anionic nanofibrous adsorbents *via* electrospinning, using poly(vinyl alcohol) (PVA) as a co-polymer. Nanofibers containing different rations of lignin and PVA were prepared, and the nanofibers with a lignin: PVA ratio of 50:50 exhibited the best performance, with a maximum adsorption capacity of 29 mg/g [237].

A study by Fernandes et al. (2019), on another note, utilized agri-food waste to produce twelve biochars and explored their potential to absorb and remove FLX. The biochar prepared by pyrolysis of eucalyptus proved to be the most promising, with a surface area of 335 m^2/g and an adsorption capacity of 6.41 mg/g [238].

(i) Inorganic adsorbents: Both waste-derived mineral-based and synthetic metal-based adsorbents have been employed for FLX removal from aqueous solutions. For example, Piccirillo et al. (2017) prepared biphasic apatite-carbon bone-char from cod fish bones by pyrolysis at different temperatures (200, 400, 600, 700, 800, 900, and 1000 °C) and used it to remove 60% of FLX from an initial concentration of 200 mg/L in aqueous solutions [239].

On the other hand, Narayanan et al. (2021) synthesized and utilized mesoporous ferrite nanoparticles of $RuFeO_3$ (80-100 nm) and $CeFeO_3$ (20-30 nm) for effective FLX removal (>99% for initial FLX concentrations of 20 mg/L), with maximum adsorption capacities of 683.5 mg/g and 729.6 mg/g, respectively [199]. A nanocomposite of ternary ZnCoAl layered double hydroxide, supported on activated carbon (LAC), was recently synthesized and used for FLX removal by Mahgoub et al. (2024), thereby reaching a maximum adsorption capacity of 450.92 mg/g for FLX concentration of 50 µg/mL. However, this adsorption capacity was achieved at pH 10, which is unsuitable for environmental applications [240].

(ii) Commercial adsorbents: A few studies have also investigated the potential of commercially available adsorbents for FLX removal, which have been summarized here for reference. A recent study by Silva et al. (2020) reported the adsorption capacity ranging between 21.86 mg/g - 233.5 mg/g for commercial adsorbents- granular activated carbon (GAC), zeolite 13X and zeolite 4A [233]. Similarly, a report by Escudero-Curiel et al. (2021) utilized low-cost commercial biochar, with an adsorption capacity of 6.57 mg/g, to remove FLX *via* adsorption at room temperature and pH 7.1 [241]. Another study by the same authors employed commercial carbon aerogel (NANOLIT 3D monolith NQ40 honeycomb premium (CO_2 activated); specific surface area of 790 m^2/g) as a high-capacity adsorbent to remove high concentrations of FLX *via* chemisorption, with an adsorption capacity of 125.24 mg/g at pH 7-7.5 [242]. However, after regeneration with Fenton's process, about 87% of the surface area was lost due to the collapse of the pores, which might not be well-suited for biochar removing FLX *via* pore-filling [242]. For biochar operating by other forces such as electrostatic, hydrophobic-hydrophobic, or π-π interactions, solvent desorption and thermal methods of regeneration have been reported to be effective [236,238,243].

Table 6.3: Summary of removal of FLX by adsorption using different adsorbents in previous studies

	q_{max} (mg. g^{-1})	pH	Initial concentration (mg/L)	Temperature (°C)	Ref.
Commercial adsorbents					
Activated carbon PBFG4	96.2	-	10	25	[235]
Granular activated carbon (GAC)	233.5	9	5	25	[233]
NQ40	125.24	7-7.5	1000	-	[242]
Biosorbents					
PS800–10KOH	191.6	-	10	25	[235]
PS800–10NaOH	136.6	-	10	25	[235]
PS800–10$ZnCl_2$	28.4	-	10	25	[235]
Fish bone char	55.87	-	100	-	[239]
Eucalyptus Biochar	6.41	6.5	20	RT	[238]
Nanofiber AL: PVA 50:50	29	-	50	-	[237]
Biochar	-	7.1	50	RT	[241]
Nanocomposite XCM	90.9	7.35	25	28	[236]
Nanocomposite PCM	114.9	7.35	25	28	[236]
Alperujo hydrochar	4.63, 5.95	6.4	30	RT	[244]
PHB4 (PEG/ O-CMCs, 3:3)	112.6	8.5	50	30	[234]
PHB5(PEG/N, O-CMCs 0:3)	109.3	8.5	50	30	[234]
Modified Pine bark	0.652	-	5	25	[243]
Synthetic adsorbents					
$RuFeO_3$ nanoparticles $CeFeO_3$ nanoparticles	683.5 729.6	7	-	25	[199]

6.4.1.2 Membrane technology

Membrane processes have gained immense attention recently, both as a method of separation and remediation technique of pharmaceutical wastewater. Membranes of varying pore size, retention characteristics, composition and membrane material, and configuration (hollow fibre, flat sheet, tubular) have been employed recently. However, the technique has not been explored for FLX removal, and only three studies have been reported.

Dalbosco et al. (2023) observed a FLX removal efficiency of 50-60% and >98% for polymeric nanofiltration (NF) and reverse osmosis (RO) membranes, respectively [245]. These commercial membranes comprised a polyamide (PA) layer on a polysulfone (PS) support for mechanical strength. The NF membrane was operated at 600 kPa, and the permeate flux decreased from 41 to 34 L/m^2 h after 1 h of operation when FLX concentrations were increased from 1 to 50 mg/L. Similarly, RO membranes displayed a high dependence on operating pressure and FLX concentrations. The RO membrane achieved a permeability of about 29 L/m^2 h with a rejection efficiency of 98.8% for an FLX concentration of 20 mg/L at a pressure of 1500 kPa, which makes it highly energy intensive [245].

In another study, Rad et al. (2024) prepared Ti-based MOF-modified electrospun PS/PEG nanofiber membranes (PSf/PEG/NH_2-MIL-125(Ti)) to achieve maximum flux and removal efficiency of 148.3 L/m^2 h and 84.5% at pH 8 and loading of 1.5% w/w in continuous mode and a maximum adsorption capacity of 21.6 mg/g for FLX concentration of 2 mg/L in batch mode [246]. It is also worth mentioning that membrane technology is a separation technique, and when applied to treat FLX-contaminated wastewater, it produces a secondary stream loaded with the pollutant, thereby underlining the need for complementary degradation technologies.

6.4.2 Chemical Technologies

6.4.2.1 Advanced Oxidation Processes (AOPs)

Reports on the degradation of micropollutants, including FLX, by ozonation and heterogenous photocatalysis are not scarce (Table 6.4) [247,247–252]. FLX is susceptible to the action of both oxidizing (•OH) and reducing agents (e^-_{aq}) [253,254]. They have been increasingly explored and reported to be highly efficient in removing contaminants by cyclo-addition and electrophilic reactions.

Ozone is an electrophile and can attack the secondary amine group in the FLX structure to aid its degradation *via* oxidation [255]. Hydroxylation, demethylation, carbonylation, and cleavage of benzene rings also contribute to the degradation of FLX *via* radical pathways [256,257]. As reported by Yu et al.

(2015), FLX is photo-susceptible and can be effectively degraded by direct UVC photolysis (254 nm), with ~30% degradation observed at a UVC dose of 100 mJ/cm^2 in the absence of H_2O_2. The addition of H_2O_2 (3-6 mg/L) did not result in a significant increase in FLX degradation, suggesting that indirect photolysis, or •OH-mediated oxidation, plays a minor role [258]. Nevertheless, various photosensitizers, including but not limited to ozone, hydrogen peroxide, and photocatalysts, have been recently investigated and reported to improve FLX degradation under UV irradiation [249,252,255,259].

Chemical oxidation of FLX using sulphate-radicals (SO_4^-) *via* peroxymonosulphate (PMS), peroxydisulphate (PDS), or sulphite (S(IV)) activation has also shown promising results in previously reported studies [241,256]. For instance, Escudero-Curiel et al. (2021) reported almost complete FLX removal under 5 minutes of treatment with PMS/Fe(II) and PMS/Fe(II)/Citric acid (CA) systems for different molar ratios. Although, the removal efficiency of FLX (50 mg/L) was directly influenced by doses of PMS and Fe(II), as well as the presence of CA, and demanded a high molar ratio of chemical reagents [241]. A comparison of FeO/S(IV), FeO/PDS and FeO/PMS under the same conditions for FLX degradation, as reported by Chen (2022), showed removal efficiencies of 84.4, 56.4, and 30.7%, respectively, in 17.5 minutes. Both PMS and PDS have a high oxidizing capacity, and the possibility of surface passivation of FeO, resulting in lower removal of FLX, could not be eliminated [256]. Also, despite the high removal efficiency of the FeO/S (IV) system in eliminating FLX at neutral conditions, the system could not degrade the pollutant satisfactorily (14.4% at pH 7) in real water because of the inhibitory effects of Cl^-, HCO_3^-, and NOM. For instance, with an increase in concentration of Cl- from 0 to 8 mM, the FLX removal efficiency decreased from 84.4% to 32.9%. Similarly, in the presence of 4 mg/L fulvic acid (used as a model NOM), FLX removal efficiency reduced by 61.1%. Both Cl^- and NOM quench the free radicals, thereby inhibiting the degradation pathways, while bicarbonate, *via* the buffering effect, results in slow dissolution of Fe(II) and, thus, slower degradation. Under circumneutral pH, iron can also precipitate as hydroxides, thereby retarding the S(IV) activation [256]. Also, despite the agent, AOPs necessitate the optimization of parameters to obtain desired results, which is not feasible in a dynamic setting such as wastewater.

Several nano-photocatalysts have also been fabricated, which have demonstrated improved degradation for FLX in real wastewater systems. For instance, application of a hybrid heterojunction photocatalyst (Fe_3O_4-$BiVO_4$/$Cr_2V_4O_{13}$ (FBC)) removed >99% FLX under 60 minutes of exposure to visible and solar radiation by the action of $^{\bullet}OH$ and $^{\bullet}O_2^-$ [260]. Another study by Liu et al. (2025) employed a molecularly imprinted photocatalyst (MI-BiOCl) and removed 99.3% FLX (C_0 20 mg/L) from municipal wastewater

in 150 minutes[252]. In another study, catalytic ozonation using nano-gamma-alumina catalyst degraded 96.14% of 28.56 mg/L FLX in 30 minutes of reaction using 30 mg/L ozone and 1 g/L catalyst [261].

Similarly, Fotiou et al. (2024) investigated the removal of FLX (C_0 5 mg/L) using TiO_2 P25 and g-C_3N_4 photocatalysts from both ultrapure water (lab scale) and real secondary treated hospital wastewater (HWW) (pilot scale)[249]. It should be noted that although a much lower concentration of FLX was used in HWW (250 ng/L) compared to ultrapure water (5 mg/L), the degradation proceeded at a lower rate in HWW, with a $t_{1/2}$ of 34 min vs 18 min in ultrapure water. This is primarily due to the complexity of the HWW, which contains dissolved organic and inorganic ions capable of scavenging the ROS and attenuating UV radiation. Overall, it is evident that inhibitory effects of Cl^-, HCO_3^-, NOM, surface passivation, and pH dependency limit the use of AOPs in real systems. Therefore, further studies are necessary to understand the effect of real wastewater on the efficiency of AOPs and to enhance their applicability to WWTPs, without compromising the overall WWTP performance and nutrient removal.

It is also noteworthy that these AOPs can result in more toxic byproducts, resulting in obstinate toxicity and limiting the application. Typically, toxicity has been reported to increase in the beginning due to the formation of free radicals, and then decrease with continued AOPs, which does not necessarily imply reduced toxicity. AOPs produce hydroxylated and dealkylated intermediates and transformation products, which often exhibit different environmental persistence, bioavailability, and toxicity [250,257,262]. For instance, the demethylated product of FLX, Norfluoxetine (NFLX) has a longer half-life and higher bioaccumulation potential than the parent compound itself. In addition to dealkylation, the formation of smaller molecular products with functionalities, such as aldehydes, also contribute to the toxicity of the transformation products at the end of AOPs [257]. As reported, 'high degradation efficiency' of AOPs, which generally means the removal of parent compound only, does not necessarily imply reduced toxicity; therefore, future studies should include toxicity analysis of intermediate and transformation products formed by AOPs rather than reporting parent compound removal.

Table 6.4: Summary of FLX removal *via* Advanced Oxidation Processes (AOPs)

AOP Method	Dosage and Operating conditions	Removal Efficiency	Insights/ Comments	Ref.
Ozone/H_2O_2	30 mg/L ozone, 0.02 mM H_2O_2, 20 minutes, 50 mg/L FLX	86.14% removal		[247] [259]
Ozonation and Ozone/Activated carbon	1 mM FLX, 2 g of activated carbon, 20 g N/m^3 O_3, flow rate 0.06 Nm^3/h; pH 3-9	~100% removal within 20 minutes (pH 7 and 9)	- Degradation slower under acidic conditions - FLX highly reactive with HO• but not with O_3 – Indirect oxidation primary route.	[248]
Catalytic ozonation with Nano-γ-alumina catalyst	30 mg/L ozone, 1 g/L catalyst	96.14% of 28.56 mg/L FLX in 30 minutes		[261]
Photocatalysis with TiO_2 P25 and g-C_3N_4 photocatalysts	Ultrapure water (lab); 5 mg/L FLX, 100 mg/L catalyst; I = 500 W/m^2	~100% in 120 minutes using TiO_2 ($t_{1/2}$ =18 minutes) ~91% removal using g-C_3N_4 ($t_{1/2}$ =69 minutes)	- Half life of 87 minutes was calculated for FLX under simulated solar radiation (I = 500 W/m^2) - TiO_2 found superior to g-C_3N_4	[249]
	Real secondary hospital wastewater (pilot scale); 5 mg/L FLX, 100 mg/L catalyst; I = 500 W/m^2	~100% in 120 minutes using TiO_2 ($t_{1/2}$ =34 minutes) ~90% removal using g-C_3N_4 ($t_{1/2}$ =65 minutes)		
Photocatalysis with hybrid heterojunction photocatalyst (Fe_3O_4-$BiVO_4$/$Cr_2V_4O_{13}$ (FBC)	10 mg/L FLX, 30 mg catalyst, 500 W Xe lamp (280 mW cm^2)	~99.2% removal in 60 minutes	- •OH and $•O_2^-$ identified as dominant species - Charge transfer mediated by Fe_3O_4	[260]

Photocatalysis with Molecularly imprinted catalyst (MI-BiOCl)	Municipal wastewater, 20 mg/L FLX, 20 mg (in V= 50 mL) catalyst; simulated solar irradiation (500 W)	99.3% removal in 150 minutes		[252]
Catalytic ozonation	0.11 mM FLX, 60 minutes, pH 11, 0.050 g/L TiO_2	UV/TiO_2 : ~100% removal in 60 minutes with 50% mineralization $UV/O_3/H_2O_2$: ~100% in 10 minutes, ~97% mineralization	- Strong pH dependence on adsorption of FLX on TiO_2 - Photolysis of FLX only under alkaline conditions - Peroxide enhances the removal of dissolved organic carbon	[250]
FeO/Sulphite (S(IV)) FeO/PMS FeO/PDS		84.4% 56.4% 30.7% in 17.5 minutes	- Surface passivation of FeO with operation results in lower removal	[256]
	Real wastewater	14.4%	- Inhibitory effects of Cl^-, HCO_3^-, and NOM	
PMS/ Fe(II) (with and without citric acid)	50 mg/L FLX	~100% in 5 minutes	- Removal efficiency directly influenced by doses of PMS, Fe(II), and citric acid	[241]
Electrogenerated peroxide (AO-H_2O_2) Electro-Fenton (EF) Photoelectron-Fenton (PEF)	BDD anode for PEF	94% in 300 minutes	- In-situ generation of hydroxy radicals' results in FLX oxidation	[263]
Heterogenous EF with FeS_2/C nano-catalyst	IrO_2/air diffusion cell 50 mA with 0.4 g/L catalyst	~100% in 60 minutes		[264]

6.4.2.2 Electrochemical methods

Some researchers have coupled AOPs with electrochemical methods to degrade FLX. For instance, Salazar et al. (2017) explored the potential of electrochemical methods (electrogenerated peroxide (AO-H_2O_2), electro-Fenton (EF) and photoelectron-Fenton (PEF)) to degrade fluorinated antidepressant FLX [263]. The drug was oxidized, owing to the generation of hydroxy radicals by in-situ peroxide production and Fenton's reaction, coupled with the photolytic action of UVA radiation. PEF with boron-doped-diamond (BDD) anode was observed to be the most effective process, with 94% mineralization in 300 minutes [263]. Another study by Ye et al. (2020) studied the heterogeneous EF treatment for FLX degradation in spiked wastewater using FeS_2/C nano-catalyst. EF treatment with an IrO_2/air diffusion cell ensured complete removal and mineralization of the drug (150 mL of 0.049 mM) at near neutral pH in 60 min at 50 mA with 0.4 g/L catalyst dose [264]. The electrochemical oxidation has also been coupled with adsorption to present a commercial solution, Nyex Rosalox, to FLX-contamination with impressive ~92% removal efficiency for FLX (from 0.06 µg/L to 0.0046 µg/L) [265]. Although very effective, these techniques can only be adapted to small-scale facilities, community-level water treatment systems, or modular installations, as a stand-alone or as a hybrid technology. High energy demand and matrix complexity (including but not limited to competition for electrons, fouling electrode surface, and lower selectivity) hinder their application in rugged, high-volume settings such as WWTPs.

6.4.3 Biological Degradation

6.4.3.1 Phytoremediation (Microalgae)

Microalgae-mediated remediation, or phytoremediation, is an environmentally friendly, sustainable, and cost-effective approach for remediating pharmaceutical-contaminated water. This carbon-fixation-based, sunlight-driven approach primarily removes pollutants by abiotic (hydrolysis and photolysis) and biotic processes (bio-adsorption, bioaccumulation, and biodegradation).

Previous studies have shown that positively charged pharmaceuticals (or pK_a >7) and higher lipophilicity (higher log K_{ow}) exhibit enhanced elimination due to their adsorption on the negatively charged surface of microalgae and their ability to penetrate the cell membrane [266–269]. With an acid dissociation constant of 9.80, FLX partially exists as a cationic species in the circumneutral pH (pH 6.5-8.5) environmental wastewater and surface waters. In addition, high lipophilicity (log K_{ow} of 4.10) renders it adept at biosorption and accumulation.

Table 6.5: Overview of FLX biodegradation performance in biological systems

Biodegradation Strategy	Organism/ System	Conditions	Removal Efficiency	By-products/ Insights	Ref.
Microalgae	*Chlorella pyrenoidosa*	25 °C, 12:12 h light-dark period	100 - 41.2% for [C_0] = 10-1000 µg/L in 4-10 days	- Growth inhibition by FLX - Uptake and transformation of FLX by demethylation, O-dealkylation, hydroxylation, and N-acylation	[268]
	Chlorella vulgaris (living and non-living)	RT, real wastewater. Biomass centrifuged, frozen, and free-dried	Maximum capacity 1.9 ± 0.1 mg/g and 1.6 ± 0.2 mg/g for living and non-living microalgae, respectively	- Significant contribution from adsorption by algae - Simultaneous removal of nutrients	[270]
Bacteria	*B. subtilis, C. testosteroni, P. aeruginosa, P. knackmussii*, and *P. putida*	Aerobic, 30 °C for 72 h, Mineral Salt Media (MSM) with FLX as only carbon source	-	- FLX hydrolysed to form 4-(trifluoromethyl) phenol (TFMP) and 3-(methylamino)-1-phenylpropan-1-ol, which is further catabolized *via* meta-cleavage to produce trifluoroacetate and fluoride ion	[271]
	Autochthonous aerobic community from a WWTP	Aerobic sludge (10% w/v) used as inoculum, real wastewater, RT, 6 days (144 h)	~60%, 85%, and ≈89% of degradation after 48, 72, and 144 h, respectively (at 20 mg/L FLX)	- P. putida, Enterobacter ludwigii, Pseudomonas nitirireducens, Alacaligenes faecalis, P. aeruginosa and P. nitroreducens	[189]

				could grow with FLX as sole carbon source - P. nitroreducens showed highes removal of 55% of 20 mg/L FLX after 24 hours.	
	SRB consortia from WWTP's lagoon system (anaerobic pond)	SRB consortia (10% v/v) used as inoculum; 20, 50, and 100 mg/L of FLX in presence of sulphate	28-69% removal for 20 mg/L FLX after 5-31 days 66% removal for 50 mg/L FLX after 31 days in sulfate reducing conditions	- Initial enrichments were performed without the drug and in the presence of 5, 10 and 20 mg/L of FLX - Observed a shift in bacterial community after addition of FLX (20 mg/L and 50 mg/L)	[190]
	Micrococcus yunnanensis strain (isolated from autochthonous marine organisms)	28 °C at 150 rpm in dark for 21 days in Synthetic media (MSM)	82.1% of 16 mg/L FLX mainly by adsorption; biodegradation also occurred. - 504 hours (21 days)	-	[188]
	Labrys portucalensis F11	Aerobic, 25 °C, 30 days, 0.6-2.8 mg/L FLX as sole carbon; 1.2-27.5 mg/L FLX when supplied with acetate	Sole C source: up to 97% (R) and 80% S in 55 days With acetate: Complete removal up to 21 μM; ≥ 81% at 49-89 μM in 55	- Observed stereoselective degradation (degradation of R more than S-enantiomer)	[272]

			days		
Algae + Bacteria	Algal-bacteria pond	Pilot scale, Continuous mode (6 days HRT)	66% removal	- Contribution from photo-oxidation, biodegradation, adsorption, not accounted	[273]
Fungi	*Pleurotus ostreatus* colonized lignocellulosic matrix	Batch and continuous studies with 600 and 750 µg/L FLX, resp.	Batch: ~83% Column: 70%	- Combined effect of biosorption (44.7%) and enzymatic activity (19.6%)	[274]
	White-rot fungi (*Bjerkandera sp. R1, Bjerkandera adusta, Phanerochaete chrysosporium*)	30 °C, 14 days Modified Kirk Medium, 1 mg/L FLX	Partial degradation (23-46%)		[275]

A few researchers have investigated the potential of microalgae in free and immobilized conditions in the removal of FLX. A recent study assessed the ecotoxicological effects of FLX (10-1000 µg/L) and its subsequent removal by a typical freshwater microalga *Chlorella pyrenoidosa* for 10 days. The study revealed that the presence of FLX at a concentration of ≥50 ug/L inhibited the growth of *C. pyrenoidosa* and can be considered as 'very toxic' to the studied microalgae based on the EU-Directive 93/67/EEC (EC_{50} 72h or longer) [268]. Similarly, FLX shows high toxicity to *Pseudokirchneriella subcapitata* and *Skeletonema marinoi* with 72 h EC_{50} values of 0.2 and 0.043 mg/L, respectively [276]. However, *C. pyrenoidosa* was able to recover its growth, along with photosynthetic and antioxidant functions, after exposure to FLX toxicity, with a removal efficiency of 100%, 97%, 77.4%, 58.6% and 41.2% for initial FLX concentrations of 10, 50, 200, 500, and 1000 µg/L, respectively.

After 10 days of exposure, biodegradation was found to be the primary factor in removing FLX, accounting for 88.2-92.8% of the total removal. In contrast, bioaccumulation and biosorption contributed negligibly towards the removal, with ND-5.33% and 0.38-1.90%, respectively. The greater contribution of biodegradation also suggests that FLX absorbed by the microalgae was rapidly metabolized, leading to the release of transformation products (demethylation, O-dealkylation, hydroxylation, N-acylation) into the medium. While a similar study with *Chlorella vulgaris* by Silva indicated biosorption as a leading contributor to the removal of FLX by the microalgae, followed by bioaccumulation and biodegradation in living algal medium. The maximum monolayer capacity (q_{mL}) for living *C. vulgaris* (pH_{ZC} 7.0) was only slightly better (1.9 ± 0.1 mg/L) than the dead biomass (pH_{ZC} 5.8) (1.6 ± 0.2 mg/g) [270].

6.4.3.2 Bacteria and bacterial consortia

Many advances have been made recently to tackle pharmaceutical pollution using bacterial consortia, such as those found in municipal wastewater, sludge, leachate, or bacterial strains isolated from these contaminated and complex matrices. These autochthonous bacterial communities often develop tolerance to these pollutants and release enzymes under stress that can facilitate their biodegradation. Some of the recent studies have been summarized in Table 6.5. For instance, a previous study by Khan and Murphy (2021) demonstrated the ability of common environmental bacteria, such as *B. subtilis, Comamonas testosteroni, P. aeruginosa, P. knackmussii,* and *P. putida*, to grow in present of FLX and use it as a sole carbon and energy source. Of these, *C. testosteroni* and *P. knackmussii* B-13 grew the best with 55% and 70% of glucose growth, respectively, whereas *E. coli* grew the least [271]. It was also proposed that the drug first undergoes hydrolysis to yield 4-(trifluoromethyl) phenol (TFMP) and 3-(methylamino)-1-

phenylpropan-1-ol, which is further catabolized *via* meta-cleavage to produce trifluoroacetate and fluoride ion [271]. However, the final product, trifluoroacetate, is both toxic and recalcitrant.

Further, in a recent study, Luz Palma et al. (2021) could degrade >50% and ~89% of the 20 mg/L drug after 48 h and 144 h (6 days), respectively, using autochthonous bacteria from municipal wastewater and aerobic sludge as an inoculum. The study further isolated six bacterial strains- *Pseudomonas putida, Enterobacter ludwigii, P. nitirireducens, Alacaligenes faecalis, P. aeruginosa* and *P. nitroreducens*, out of which *P. nitroreducens* showed the highest removal of 55 ± 1% of 20 mg/L FLX after 24 h [189]. The maximum removal efficiency of 69% and 66% were observed by anaerobic sludge as inoculum for FLX concentrations of 20 and 50 mg/L, respectively [190]. The same authors also reported the removal of 82.1 ± 0.9% of 16 mg/L FLX after 504 h (i.e., 21 days) utilizing isolated strains from marine organisms: *Micrococcus yunnanensis* strain TJPT4 from *Hymedesmia versicolor* and *Filograna implexa* [188]. However, both biosorption and biodegradation contributed to the drug's removal. The efficiency of the process was reported to be 82% with a rate of 0.0538 d^{-1} (R^2 = 0.9562) and $t_{1/2}$ of 13 days, while adsorption assay with 10% inactivated inoculum presented a removal efficiency of 81 ± 8% after 504 h, corresponding to rate of 0.0625 d^{-1} and $t_{1/2}$ of 11 days (R^2 = 0.9689). The biosorption of FLX onto inactivated inoculum followed a pseudo-second order kinetics with R^2 of 0.9954, equilibrium sorption capacity (K) of 0.048 ± 0.001 g/mg. days, and experimental sorption capacity of equilibrium ($q_{eq, exp}$) of 13.2 ± 0.6 mg/g [188]. Other studies have reported similar findings, showing that sorption significantly contributes to FLX removal [187,273].

Since FLX is chiral with one chiral-carbon, certain bacteria perform enantioselective biodegradation. For instance, a study by Moreira et al. (2014) used a bacterial strain, *Labrys portucalensis* F11, isolated from an industrially contaminated site to degrade 100%, 80%, and 67% of S-FLX; 100%, 97% and 89% of R-FLX at initial racemic-FLX concentrations varying from 2, 4, and 9 µM (i.e., 0.6, 1.2, and 2.8 mg/L), respectively, after 30 days of treatment. The presence of supplementary organic carbon sources, such as acetate, can further aid FLX biodegradation by achieving higher removal efficiency in a shorter period [272]. The study surely reported high removal for FLX; however, the rate of removal is excessively slow-paced for application in fast, dynamic, and large-scale WWTPs.

6.4.3.3 Mycoremediation

In addition to microalgae and bacteria, fungal-based solutions have shown promising potential in removing wastewater organic contaminants, and their application for wastewater remediation has been

extensively reviewed recently [277–279]. However, only two reports have employed fungal-based degradation methods for FLX removal, and that too with low rates of FLX removal by biodegradation. For example, a report by Rodarte-Morales et al. (2011) studied the degradation of the antidepressant (1 mg/L) by three white-rot fungi: *Bjerkandera adjusta*, *Phanerochaeta chrysosporium*, and an anamorph of *Bjerkandera sp.* R1, and observed poor drug removal in all the cases (maximum 46% by anamorph of *Bjerkandera sp.* R1) [275]. This could be owed to the concentration of FLX used for the study.

In another study conducted by Silva et al. (2022), mushroom substrate (CMS) colonized by *Pleurotus ostreatus* and its crude enzyme extracts, specifically laccase, were used to remove 600 µg/L of FLX from aqueous solutions, thereby achieving a removal efficiency of >83.1% and 19.6% in 10 minutes, respectively [274]. Although the authors reported a synergistic contribution of biosorption onto CMS and enzymatic degradation in the degradation of the contaminant, the contribution of biosorption was much greater than biodegradation. The oxidative catabolism of extracellular lignin-modifying enzymes (LMEs), such as laccase, depends highly on the structure of the substrate. It is acknowledged that the presence of EWGs, such as amide, halogen, carboxylic, and nitro, makes the molecule less susceptible to enzymatic oxidation by generating electron deficiency, whereas electron-donating groups (EDGs), like amines, hydroxyl, alkyl, among others, makes the substrate more prone to the electrophilic attack of enzymes, thereby exhibiting good removal efficiency. FLX, despite having methyl, ether, and secondary amines (EDGs), the presence of trifluoromethyl EWG hinders the laccase-based degradation [274]. A more recent article suggests that the role of laccase may be limited to acting as an adsorbent rather than a degrader, particularly in the removal of perfluorinated compounds [193,280].

6.5 Challenges and Future perspective

As discussed in previous sections, removal of FLX *via* physical, chemical, and biological systems has been extensively studied. However, after careful review, it is clear that these techniques have significant disadvantages (Table 6.6). Physical removal methods are based on adsorption and only work to remove the pollutant without degrading it. The disposal of generated secondary waste material, saturated with contaminants, is another challenge. Chemical treatment, such as Advanced Oxidation Processes (AOPs) and electrochemical methods, has a high chemical and carbon footprint and requires the optimization of influencing parameters, limiting its application in real wastewater systems. These methods generally require high energy input, chemical requirements, and/or extreme operating conditions. Further, the presence of organic matter, nitrates, phosphate, and bicarbonates affects the action of free radical [241,256,257]. Although FLX is classified as a PFAS, its structure differs from that of a long-chain PFAS, such as PFOA.

The structure of conventional PFAS consists of a fully fluorinated carbon chain, whereas FLX contains aromatic rings with one trifluoromethyl group. PFOA is extremely stable and resistant to most conventional chemical, biological, and photolytic degradation, with its removal dominated by physical separation methods. In contrast, FLX is stable in water and wastewater and resistant to biological methods but can be partially degraded by AOPs and removed by adsorbent-based strategies. However, newer technologies currently being explored for PFAS can inform approaches for FLX treatment. Some recently published reviews have also discussed the possibility of using mechanochemical degradation, sonolysis, gamma ray irradiation, electron beam (eBeam), sub- and supercritical treatment, vapor energy generator (VEG), and plasma for the degradation of PFAS, in addition to bioremediation and advanced oxidation/reduction processes [281,282]. However, research in the area has been lacking so far for FLX, and scalability and efficiency for real environmental samples remains a challenge. The current investigations for high-energy techniques, such as eBeam, gamma-ray, and plasma, are limited to a very small scale (< 1 L) and their implementation is expected to incur very high costs and energy, with challenging scale-up. Some of these advanced methods also require extreme working conditions, and optimization of all working parameters, which is practically not suitable for application in WWTPs. More research is needed to develop a treatment process that could effectively remove and degrade FLX (and other PFAS) at a reduced cost and under practical field conditions.

Although bioremediation is generally inexpensive and reliable means to degrade low concentrations of distributed pollutants, it is not currently practical for polyfluorinated compounds, including FLX, given the present level of scientific understanding.

Table 6.6: Comparative assessment of FLX removal methods: Advantages and limitations

Treatment Technology	**Advantages**	**Limitations**
Adsorption (e.g., biochar, GAC, nanoparticles)	- Simple and cost effective - Scalable - Effective for low/trace concentrations - No toxic by-products	- Limited desorption/regeneration strategies - Competitive adsorption with co-contaminants
Membrane filtration (e.g., NF, RO)	- No chemical transformation	- Energy and cost intensive - Membrane fouling - Concentrate disposal issue
Advanced Oxidation Processes (AOP) (e.g., UV/H_2O_2, Fenton, O_3, photocatalysis)	- High removal efficiency - Capable of mineralization of FLX - Fast and effective for micropollutants - Reusable catalysts - No sludge production	- Matrix effects - Optimization of all working parameters (dose, time, pH) - pH-sensitive performance - High energy/chemical costs - Toxic intermediate and/or by-products
Electrochemical oxidation	- Selective and tunable - High removal efficiency	- Electrode fouling - Optimization of parameters (pH, electrode distance, current, electrode material, electrolyte) - Limited full-scale studies
Biological treatment	- Low cost - Can be integrated with any physical-chemical treatment technology - Environmentally friendly and sustainable	- Low removal efficiency for FLX - Sorption to sludge

The biodegradation of FLX may appear promising based on the studies summarized in the previous section; however, a deeper analysis of the results reveals that: (i) there is a noticeable gap in enzyme-based solutions for FLX degradation, (ii) adsorption and absorption play crucial roles in the removal of FLX from biological systems, and (iii) these processes are time intensive. Most of the studies have shown that even under enriched consortia, the half-life of FLX varies from several days to weeks, while retention time in WWTPs is usually around a few hours to 1 day. It must also be noted that most of these studies were conducted at FLX concentrations significantly higher than those typically found in the environment (Table 6.1). At such elevated concentrations, the drug can act as a stressor, eliciting stress-induced responses from the microbial and micro-algal- systems. In contrast, in real systems, where the concentrations are much lower (ranging from ppt to a few ppb), these responses are neither expected nor observed. Moreover, the presence of easily degradable carbon sources in wastewater, like glucose and acetate, can compete with FLX for microbial activity, reducing the FLX biodegradation, even if the microbes are capable of degrading it.

Nevertheless, the drug continues to be detected in final effluent and sludge, despite undergoing biological treatment in WWTP and prolonged sludge retention times, respectively. It would, therefore, be correct to say that FLX recalcitrance is not a function of the sludge retention time (SRT) of municipal WWTPs, but its resistance to microbial transformation and low biodegradability. This raises concerns regarding the pseudo-persistence of FLX and its potential acute and chronic effects across ecosystems. Despite extensive research, effective, safe, and sustainable methods of removal for perfluorinated compounds, including FLX, remain lacking.

Previous reviews have suggested three main constraints, that limit biodegradation of polyfluorinated organic compounds: rarity of natural fluorine, low tolerance of microbes to intracellular fluoride, and fluorine chemistry that makes these compounds stable. There are only a few naturally occurring organo-monofluorinated compounds, such as fluoroacetone, fluorocitric acid, fluorothreonine, in contrast to over a million synthetic commercial polyfluorinated compounds introduced in that last few decades. This surge has put microbes at an ‘evolutionary disadvantage’. Some studies indicate that C-F bonds are stable and ‘harder’ to enzymatically cleave than other C-X bonds, while others claim that C-F bond can be cleaved, but it is the toxicity of fluoride that poses the constraint. Microbes have acquired the ability to tolerate high concentrations of extracellular fluoride by expelling the anion out of the cells using membrane export proteins. However, the cleavage of C-F bond generates a much higher concentration of intracellular fluoride, which is toxic and makes them non-viable. That means, if the microbe has the potential to cleave a C-F bond, it will toxify itself and die, thereby extinguishing the idea of evolutionary

innovation[193]. This leaves the knowledge gap in the remediation of organofluorinated compounds unfilled.

Recent review articles suggest addressing this gap by developing 'fluorophiles' and engineering or identifying novel defluorinating enzymes using machine learning tools, adaptive laboratory evolution, and rational enzyme design. Meanwhile, further research is needed to validate these approaches experimentally and assess their feasibility in real environmental contexts.

As natural evolutionary processes continue to adapt and refine microbial capabilities to tackle polyfluorinated organic compounds, it is important that we persist in our efforts. Given current resources, a compelling path forward lies in employing hybrid techniques combining physical, chemical, and biological strategies as a treatment chain. To begin with, the strong tendency of polyfluorinated pharmaceuticals, FLX and NFLX, to adsorb can be exploited, which not only concentrates these widely distributed pollutants for further treatment but also lowers the energy demand of the entire process. For this, carbon-based adsorbents, such as activated carbon and biochar, ion-exchange resins, and synthetic porous carriers, can provide effective and sustainable solutions. The spent adsorbent used for physical removal can then be subjected to degradation *via* electrochemical, AOPs, or thermal methods. They are effective in treating FLX-concentrated, small-volume streams and will ensure no legacy problems by degradation rather than mere physical removal. A commercial solution, Nyex Rosalox, as mentioned earlier, has combined electrochemical oxidation with adsorption for effective removal of FLX. However, toxic byproducts can form, which may need further treatment before environmental release. This highlights the need for combining chemical degradation with biological treatment, where the former fragments aromatic structures and the latter mineralize the biodegradable residuals and intermediates. This also reduces total organic carbon (TOC) and toxicity and offers sustainability to the treatment chain. Catalytic ozonation, Electro-Fenton, and UVC/Solar irradiation, coupled with a moving bed biofilm reactor (MBBR) or biofilters, can be seen as a promising solution to FLX-contamination.

In some cases, two methods can be combined to reduce the steps in the treatment chain, thereby improving efficiency and reducing operational complexity. For instance, immobilization of the photocatalyst on porous carriers with UVC/solar irradiation can be directly followed by biological systems. Another example includes coupling of AOPs with biological activated carbon (BAC), combining biological (MBBR or biofilters) and physical methods. Such integrative technologies can enhance treatment efficiency and overcome the limitations of a single technique. While this can enhance treatment performance, the environmental footprint, sustainability, and resource efficiency must be

evaluated using life cycle assessment (LCA). Future studies must quantify energy use, emissions, and potential secondary pollution across single and hybrid treatment stages to inform sustainable research in the area.

Beyond these hybrid approaches, source control and regulatory frameworks can also play a crucial role in mitigating FLX pollution. With the development of greener FLX analogues or the use of safer, more biodegradable FLX alternatives, environmental burden could potentially be controlled at the source. Further, by pairing scientific advances and 'control at source' strategies with thoughtful and practical policies, such as setting up discharge standards, monitoring guidelines, and ensuring compliance, sustainable pharmaceutical management can be achieved.

Chapter 7: Research Gap, Objective, and Originality

Research Gap

Despite existing studies, the removal of FLX remains a challenge. Physical, chemical, and biological methods alone are insufficient for its removal. The chemical footprint, high cost of chemicals, and toxic transformation products make chemical degradation methods less favorable. While bioremediation, which is generally an inexpensive and reliable means to degrade low concentrations of distributed pollutants, is not currently practical for FLX. Also, as indicated by literature review, adsorption based physical removal methods are effective at removing FLX but do not degrade the contaminant.

To combat FLX-pollution, a new hybrid physicochemical removal method has been proposed by combining adsorption with UVC-mediated transformation of the contaminant using CuO-biochar (BC) mixture as a composite photocatalyst.

Objective and Sub-objectives: To develop and evaluate effective treatment strategies for the removal of FLX using olive-stone-derived physically activated biochar and a CuO-assisted system under UVC irradiation.

- **Sub-objective 1**: To explore the specific application and integration of physically activated biochar derived from olive stone- an agro-industrial waste- for the targeted removal of FLX
- **Sub-objective 2**: To investigate the potential of CuO-biochar mixture as a composite photocatalyst for efficient UVC photocatalytic treatment of FLX

These objectives collectively aim to develop and evaluate an effective treatment strategy for FLX, reflecting its persistent nature and limited potential for natural attenuation.

Originality

The novelty of this work lies in developing a rapid and sustainable FLX treatment approach using agro-waste-derived biochar and a simple CuO-biochar system, achieving removal within 2 minutes of treatment, while supporting circular economy principles and avoiding complex synthesis.

Chapter 8: High-Capacity Adsorption of Fluoxetine using Olive-Stone Derived Activated Biochar: Insights into Efficiency and Mechanism

Pratishtha Khurana[a], Samreen Sran[b], Ratul Kumar Das[a], Luz Sanchez-Silva[c], Satinder Kaur Brar[a]*

[a]Department of Civil Engineering, Lassonde School of Engineering, York University, Ontario, Canada

[b]Department of Biology, York University, Ontario, Canada

[c]Department of Chemical Engineering, University of Castilla-La Mancha, Spain

*Corresponding author: Satinder Kaur Brar; email: satinder.brar@lassonde.yorku.ca

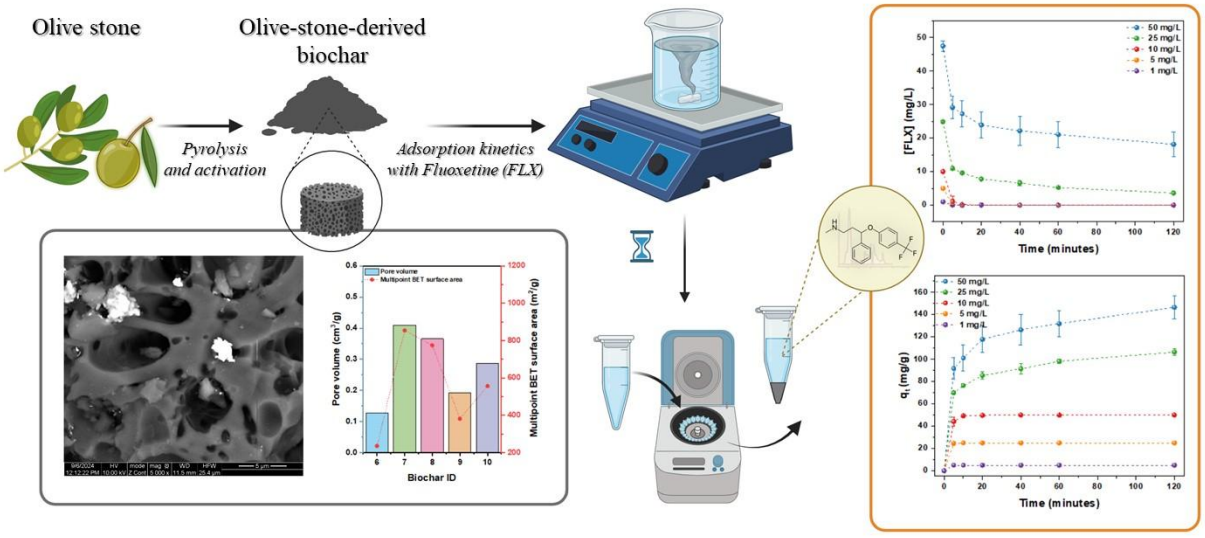

RSC Advances, Volume 15, 2025, 20330-20340;

DOI: https://doi.org/10.1039/D5RA01258A

Abstract

The increasing incidences of mood, anxiety, and panic disorders have made fluoxetine (FLX), known for its safety and therapeutic efficiency, one of the most widely prescribed antidepressants globally. However, due to its resistance to natural photolysis and hydrolysis, coupled with the potential to cause endocrine disruption, FLX has become an emerging contaminant, requiring urgent attention for removal. In this context, the present study explores the specific application and integration of physically activated biochar derived from olive stone-an agro-industrial waste-for the targeted removal of FLX. By optimizing activation parameters (CO_2-1000-30-600-1), this study demonstrates the ability to achieve superior adsorption capacities for FLX, which surpass the adsorption capacity of previously reported waste-derived biochar used for FLX removal. The maximum adsorption capacity for the biochar ranged from 4.82 ± 0.04 to 146.45 ± 10.55 mg g^{-1} for initial FLX concentrations of 1 to 50 mg L^{-1}, respectively, for a biochar dose of 0.2 g L^{-1}. Furthermore, the adsorption kinetics data revealed that the biochar–FLX interaction followed the Langmuir adsorption isotherm and a pseudo-second-order kinetic model, indicating irreversible adsorption of FLX onto the homogenous surface of the biochar. Non-electrostatic and non-hydrophobic interactions, such as hydrogen bonding, pore filling, and π–π EDA forces, were identified as the primary interactions facilitating FLX adsorption onto the biochar. This study, therefore, presents a novel approach addressing the dual objectives of environmental remediation and zero-waste principles, contributing significantly to advancing sustainable solutions for emerging contaminants.

Keywords: Olive-stone biochar, Fluoxetine, Adsorption, Kinetic models, Adsorption isotherms, Desorption

8.1 Introduction

The alarming rates of incidences of psychiatric and mental disorders have led to an increase in the prescription rates and consumption of antidepressants globally. According to a recent report, the defined daily doses (DDD) of anti-depressants per 1000 inhabitants has seen an increase from 13.20 in 2008 to 19.76 in 2018 globally [283]. Fluoxetine (FLX), an anti-depressant from the class of selective serotonin reuptake inhibitors, is the most commonly prescribed anti-depressant globally for the treatment of depression, because of its tolerance, effectiveness, safety and prolonged half-life [6,7]. In the US in 2017, approximately 21 million prescriptions of FLX were filled, suggesting a relatively high level of consumption [8]. However, due to its incomplete metabolism in humans by cytochrome P450 enzymes, whereby 2.5% of the administered dose is excreted unaltered *via* urine, it gets discharged into wastewater [284].

Due to its resistance to degradation and hydrolysis, and subsequent incomplete removal by WWTPs, has led to its frequent detection in waterbodies across the globe in concentrations ranging between 0.012 to 1.4 mg/L, causing defects in the behavioural, developmental and reproductive patterns of many aquatic organisms [10,285,286]. Despite its low concentration, FLX poses a risk to all biomes owing to its ability to cross blood-brain-barrier (BBB) and human placenta due to its lipophilic nature [9]. The drug's uptake in fish has been reported to have consequences on growth and behaviour, reproductive axis, metabolism, accumulation, and gene expression [10–15].

With a log K_d = 2.76-3.78 (log Kd > 2.7) and log K_{ow} > 4, adsorption appears as a robust, effective, and efficient tertiary method to enhance its removal and limit its exposure in environment [187,190,287]. Furthermore, with increasing emphasis on principles such as zero waste and circular economy, the production of waste-derived bio-adsorbents and their application in remediating FLX-polluted waters have been extensively researched [233,238,243]. However, their low adsorption capacities have proven insufficient. For instance, biosorbents derived from agri-food waste have shown a maximum adsorption capacity of 6.41 mg/g, as reported for biochar obtained from eucalyptus when tested with FLX_0 of 20 mg/L [238]. A similar study by Silva et al., (2020) investigated the maximum adsorption capacities of waste-based biosorbents derived from cork waste, spent coffee grounds, and pine bark for FLX_0 5 mg/L, which ranged between 4.74 mg/g - 14.31 mg/g [233]. In this regard, the present study explores the application of physically activated biochar derived from

olive stone for the removal of FLX. While the valorization of olive oil production residues, such as olive stones, has been explored to some extent, their specific application in biochar production and other sustainable materials remains an emerging area of research [288]. The novelty of this study lies in the use of these residues combined with physical activation (using CO_2 and steam) to create biochar for environmental remediation. This innovative approach not only highlights the potential of olive oil production residues but also introduces a sustainable alternative to chemical activation methods. The physical activation method, using CO_2 and steam, offers several advantages over chemical activation. It is more sustainable and environmentally friendly, as it does not require aggressive chemicals, thus reducing toxic byproducts and minimizing environmental impact. Additionally, it produces fewer hazardous waste materials, making it more compatible with circular economy principles [288,289]. The process also allows for precise control over biochar properties, such as surface area and porosity, which is crucial for its application in environmental remediation. Furthermore, physical activation can be more adaptable to various types of biomasses, more energy-efficient in certain cases, and better suited to comply with stringent environmental regulations, making it a versatile and cost-effective approach [288]. The novelty of this activation method, alongside its environmental benefits, further strengthens the innovative nature of this study.

The present study, thereby, demonstrates specific application and integration of physically activated biochar derived from olive stone, an agro-industrial waste, for the targeted removal of FLX. This emerging pharmaceutical contaminant presents unique environmental challenges due to its resistance to natural degradation and its endocrine-disrupting potential, making its remediation an underexplored yet critical area of research.

8.2 Experimental

8.2.1 Materials and Methods

Fluoxetine hydrochloride (FLX, >98%) was purchased from Sigma Aldrich (Toronto, Canada). An appropriate amount of the salt was dissolved in water to prepare the stock solution of FLX, which was stored in a dark glass vial at 4 °C until use. The olive stone waste was kindly received from an oil mill in Toledo, Spain (Aceites Garcia de la Cruz. It is worth mentioning that the olive stone was milled to obtain a particle size of 2-4 mm for pyrolysis and activation without any drying.

8.2.2 Biochar preparation and activation methods

Biochar was prepared by a single-step physical activation process, using olive stone as a low-carbon precursor and steam or carbon dioxide as the activation agents in a bench-scale high-pressure thermobalance (Linsesis STA HP/2 HP-TGA DSC). The biomass was carbonized by heating it to 600 °C at a heating rate of 10 °C/min, and resting for 60 minutes, under N_2 (300 NmL/min). The carbonized material was then subjected to physical activation using steam or CO_2 under different operating conditions for temperature (700-1000 °C) at a heating rate of 20 °C/min under N_2 atmosphere, pressure, holing time (30-60 min), and flow rate (CO_2: 300-600 NmL/min; Steam: 0.07-0.3 NmL/min), as summarized in Table 8.1.

Before use, the biochar samples were lightly crushed using a stainless-steel mortar pestle set and passed through metal sieves to obtain a fine powder (25-63 μm) and stored at room temperature until use.

8.2.3 Biochar characterization

The prepared biochar samples were characterized for their surface area and porosity (Brunauer-Emmett-teller (BET)), elemental content (CHNS analyzer), zeta potential, and cation exchange capacity (CEC). The selected biochar (biochar 7, CO_2-1000-30-600-1) was also characterized by FTIR for surface functional groups, point of zero charge (pHzc) to understand the conformational changes with varying pH. Morphological features of the biochar were observed *via* imaging with Scanning Electron Microscope (SEM). The sample preparation methods for all the techniques are outlined in Text 1 of Appendix F.

8.2.4 Preliminary adsorption assays for biochar screening

For screening the biochar, preliminary adsorption experiments were performed with 5 mg of respective biochar in 10 mL of FLX solution (0.5 to 50 mg/L) at room temperature. The initial FLX concentration was deliberately maintained high to (i) ensure accurate quantification of the drug and (ii) sought the saturation limit of the biochar. The samples were equilibrated for 24 hours on an end-to-end shaker, followed by centrifugation (Sorvall ST 16, Thermo Fisher Scientific, USA). The resulting supernatant was then analyzed for FLX using LC-MS. The LCMS system is

comprised of Waters M-class UHPLC and a Sciex ZenoToF 7600. The chromatographic separation was achieved with Kinetex 2.6 µm XB-C18 100 Å, 50 X 0.3 mm column, maintained at a temperature of 50 °C, using gradient mobile phase (ultrapure water with 0.1% v/v formic acid to Acetonitrile with 0.1% v/v formic acid). The other parameters were maintained as: positive ionization mode, flow rate 20 µL/min, injection volume 5 µL, curtain gas 35 psi, CAD gas 7 psi, and spray voltage of 5500 V.

The samples were analyzed in duplicates, and the removal percentage was calculated as:

$$\text{Removal (\%)} = \frac{C_0 - C_t}{C_0} \text{ X } 100 \qquad \ldots \text{ equation (8.1)}$$

where C_0 and C_t represent FLX concentrations (mg/L) at time 0 (initial) and t (24 h, here). Based on the preliminary screening, one biochar activated with steam, and one activated with CO_2 were selected for further evaluation using secondary screening method.

For the successive screening, the selected steam- and CO_2- activated biochar (10 mg/50 mL) was used to perform FLX removal kinetics with an initial concentration of 50 mg/L. The percentage of FLX removal was determined using equation (1). The biochar with faster kinetics was selected for the rest of the study.

8.2.5 Adsorption and kinetic studies

Adsorption studies were performed by adding the selected biochar to 50 mL FLX aqueous solution at room temperature with continuous stirring at 400 rpm for 2 hours. The effect of (i) initial dose of FLX (1, 5, 10, 25, and 50 mg/L); (ii) time (0, 5, 10, 20, 40, 60, and 120 minutes); and (iii) dose of biochar (10 and 20 mg for FLX 25 and 50 mg/L) were investigated. Commercial activated bamboo charcoal powder was used as a reference. The samples were regularly collected and analyzed in triplicates for residual FLX using UV-visible spectroscopy (λ_{max} 226 nm) and LC-MS for lower concentrations (<5 mg/L) after centrifugation to remove the adsorbent.

The adsorption capacity (q_t (mg/g)) was calculated using the equation (9.2):

$$q_t = (C_0 - C_t)\, X\, \frac{V}{m} \qquad \ldots \text{equation (8.2)}$$

Where m (g) is the mass of the biochar used, and V (L) is the volume of the solution.

Subsequently, to understand the kinetics and the behaviour of adsorption, the experimental data was fit to different adsorption isotherm models (Langmuir and Freundlich) and kinetic models (Pseudo-first order (PFO), Pseudo-second order (PSO), and Intra-particle diffusion (IP)), as described in Text 2 in the Appendix F.

While the environmental concentration of FLX usually ranges from a few ng/L to µg/L, high concentrations were used to construct complete adsorption isotherms and evaluate adsorption capacity over a broad loading range, which is an essential parameter to compare its performance with reported biochar systems. These high concentrations are routinely employed to determine maximum adsorption capacity, surface saturation, and performance for scale-up applications.

8.2.6 Regeneration and reusability

In order to investigate the regeneration and reusability of the spent biochar, solvent desorption assays were performed by change in solvent strength. For this, the residues from equilibrium adsorption experiments (25 mg/L FLX) were recovered by centrifugation and overnight drying at 45 °C. To evaluate the desorption, the 2 mg of spent biosorbent was then mixed with 5 mL of different extraction solvents (i) water, (ii) MeOH, (iii) MeOH (pH adjusted to 2 using 0.1 M HCl), and (iv) 50% ACN in water, under end-to-end shaking for 24 hours at room temperature. This was followed by centrifugation and determination of desorbed FLX in the supernatant using UV-visible spectroscopy and LC-MS method. The desorption efficiency was calculated using equation (8.3)

$$\text{Desorption effeciency} = \frac{\text{C X V}}{\text{q X m}} \text{ X } 100\% \qquad \ldots \text{ equation (8.3)}$$

where C (mg/L) is the desorbed FLX concentration. The spent biochar was regenerated by lyophilization.

In addition to solvent desorption, an advanced regeneration method combining Fenton's oxidation with ultrasonication (Ferro-sonication; Fe-UlS), as mentioned elsewhere, was also investigated [290]. For this, the spent biochar was suspended in 10 mL milliQ, to which 1:1 %v/v Fenton's reagent (0.05 M $FeSO_4$ and H_2O_2) was added, and acidic pH (2.5) was adjusted using H_2SO_4. The solution was then sonicated at 40 kHz for 30 minutes, followed by centrifugation, washing with water, and

lyophilization to obtain the regenerated biochar. The regenerated biochar (both solvent and Fe-UlS) was analysed for residual FLX by using Thermogravimetric Analyser (TGA) (Discovery TGA55, TA instruments, USA) at a heating rate of 10 °C/ min for a temperature range of RT (~20 °C) to 500 °C.

8.2.7 Adsorption mechanism

To determine the adsorption mechanism and investigate the contribution of electrostatic and hydrophobic interactions in facilitating the adsorption of FLX on the surface of biochar, the effect of pH (3-11), NaCl (0.01, 0.1, and 0.5 M) and MeOH (2.5, 5, and 10% v/v) on the adsorption capacity of biochar was investigated for $[FLX]_0$ 25 mg/L. The samples were collected at regular intervals (0, 5, 10, 20, 40, 60, and 120 minutes) and analyzed for residual FLX using UV-visible spectroscopy (λ_{max} 226 nm). ANOVA was used to determine their statistical significance with a *p*-value of 0.05 as the level of significance.

8.3 Results and Discussion

8.3.1 Biochar characterization and screening

BET technique, CHNS analysis, and CEC, as summarized in Table F2, were used to characterize the biochar samples for their surface area and pore size distribution. The results indicated that the biochar 3 (H_2O-900-30-0.15-1) had the largest surface area (1015 m^2/g) followed by biochar 4 (836 m^2/g, H_2O-900-30-0.07-1) ~ biochar 2 (828 m^2/g, H_2O-800-60-0.3-1), and biochar 5 (678 m^2/g, H_2O-800-60-0.15-1). Biochar 1 (449 m^2/g, H_2O-700-60-0.3-1) had the lowest surface area, as recorded by the surface area analysis. It is evident, both- here and from previous reports, that the surface area increases with the increasing activation temperature because of the removal of carbon atoms from the surface [289]. This can also be rationalized with the carbon content of steam-activated biochar, which follows the order biochar 3 (%C 69.6, 900 °C)> biochar 4 (%C 73.5, 900 °C)> biochar 2 (%C 76.1, 800 °C) ~ biochar 5 (%C 874.5, 800 °C)> biochar 1 (%C 83.5, 700 °C). Overall, the total carbon content in all biochar samples ranged from 63.3% to 83.5%, i.e., medium carbon content, as previously described by Lehmann et al. [291]. Correspondingly, the % oxygen for all the biochar samples varied from 13.94% to 32.83%.

Similarly, for CO_2 activation, the biochar followed the order: biochar 7 (855 m^2/g) > biochar 8 (775 m^2/g) >biochar 10 (557 m^2/g) >biochar 9 (382 m^2/g) > biochar 6 (236 m^2/g) for surface area. In general, surface area increases with rising activation temperature from and improving flow rate from 300 to 600 mL/min and decreases with time, as seen in Table F2. Additionally, the zeta potential of physically activated biochar (1-10) was close to 0 mV (data not shown), which indicates the presence of both positive and negative charges, and rapid coagulation or aggregation of the particles in the solution.

Adsorption experiments were performed to screen for the selected biochar. Batch adsorption assays were performed at room temperature for 24 hours, and the results are shown in Figure F1. As seen in Figure F1a, steam-activated biochar removed a significant portion of the drug, except biochar 1, where the activity drastically reduced when the FLX concentration gradually increased from 0.5 to 50 mg/L. Biochar 4 performed unfailingly throughout the drug concentration and was selected for the rest of the study. Similarly for the CO_2-activated biochar set, as the concentration of FLX increased from 0.5 to 50 mg/L, a significant reduction in % adsorption of FLX was seen for biochar 6 (from 94.99 ± 4.59 to 22.64 ± 0.09) and 9 (from 96.37 ± 3.46 to 31.55 ± 0.67), while gradual decrease was seen in the reactivity of biochar 8 and 10, where % removal of FLX decreased from 99.87 ± 3.48 and 99.81 ± 0.10 to 76.81 ± 4.97 and 76.48 ± 23.01, respectively (Figure F1b). For biochar 7, only a slight change in activity was seen (from 99.25 ± 0.73% to 92.20 ± 3.92%) and thus selected for the rest of the experiments.

Therefore, based on the results of the batch adsorption studies, steam-activated biochar 4 and CO_2-activated biochar 7 were selected for the next set of the experiments. To select one of the two biochar, the adsorption kinetics for removal of FLX was performed with 50 mL 50 mg/L FLX with 10 mg biochar 4 and biochar 7. As shown in Figure F2 CO_2- activated biochar 7 demonstrated a faster removal than steam-activated biochar 4, with residual FLX concentrations of 7.142 ± 2.48 mg/L and 16.515 ± 1.67 mg/L, respectively, after 1 h of contact. Thereby, biochar 7 was selected for the rest of the study. The pHzc of the selected biochar 7 was observed to be about 7, as shown in Figure F2b. Also, the obtained FTIR spectra (Figure F2c) for the biochar indicated the presence of O-rich functional groups including carbonyl, carboxylic, and alcohols (Table F3) [238].

The SEM analyses of the untreated, pristine biochar 7 (CO_2-1000-30-600-1) revealed a rough texture, heterogeneous surface, irregular granular morphology, and highly porous matrix with

interconnected pores (Figure 8.1A (i); magnification 200x). The grain size and high porosity could be attributed to the high pyrolysis temperature and CO_2-activation. When pyrolyzed at 1000 °C, the carbon tends to become crystalline and larger in grain size, as observed previously [239]. The magnified image (5000x, Figure 8.1B(i)) displays the porous structure network of interconnected micropores with variable pore size distribution. Furthermore, the pore size distribution of the selected biochar 7, as determined using BET, predominantly indicates the presence of only micropores (< 2 nm) (Figure F3).

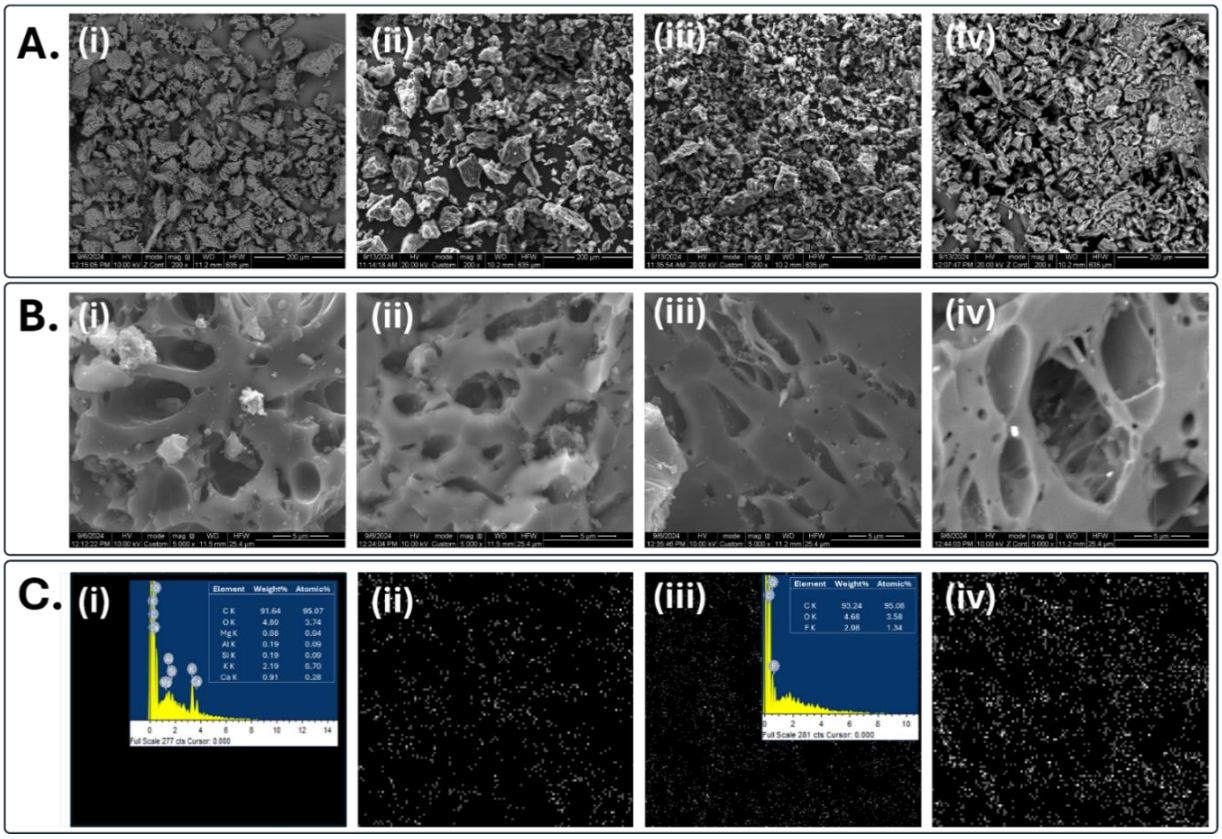

Figure 8.1: SEM images of (i) Untreated biochar, (ii) Biochar loaded with 1 mg/L FLX, (iii) Biochar loaded with 25 mg/L FLX, and (iv) Biochar after desorption with MeOH for at magnification (A) 500x, (B) 5000 x. (C) shows EDS mapping for fluorine atom, inset shows EDS spectrum.

8.3.2 Adsorption kinetics

The kinetic assays of FLX (1, 5, 10, 25, and 50 mg/L) with olive-stone derived CO_2-activated biochar 7, as shown in Figure 8.2 (a), indicate that FLX removal occurs rapidly in the first 5 minutes of contact. For lower initial concentrations of FLX (1 and 5 mg/L), equilibrium was attained within 5 minutes with 100% removal of FLX. For 10 mg/L FLX, equilibrium and 100% removal were achieved within 10 minutes of the assay. Further, as can be seen in Figure 8.2 (a), for higher concentrations (25 and 50 mg/L FLX), the minimum time required to attain equilibrium was <20 minutes, as reported previously [238,239,241]. The performed kinetic studies show that after 2 h of exposure, the amount of FLX adsorbed on the surface of biochar ranged from 4.82 ± 0.04 mg/g to 146.45 ± 10.55 mg/g, for initial FLX concentrations of 1 mg/L to 50 mg/L, respectively (Figure 8.2 (b)). While commercial bamboo activated charcoal, which was used as a reference, exhibited maximum adsorption capacity of 9.85 ± 4.83 mg/g and a removal efficiency of 4.09 ± 2.07% after 2 h of contact with 50 mg/L FLX (Figure 8.2 (a-b)). The uptake of FLX can also be traced by EDS mapping of F, as shown in Figure 8.1C (iii). For the biochar saturated with 25 mg/L, EDS mapping shows 2.08 wt% or 1.34 atomic% in the mapped area. However, no morphological changes were observed for the biochar.

The uptake potential of the prepared olive-stone biochar (146.45 ± 10.55 mg/g within 2 h for [C_0] = 50 mg/L FLX) surpasses the adsorption capacity of previously reported waste-derived biochar used for FLX removal. Some of these recent studies are summarised in Table 8.1 for comparison. For instance, a study by Fernandes (2019) reported the attainment of equilibrium of agri-food waste derived biosorbents after 15 minutes of the assay, with a maximum adsorption capacity of 6.41 mg/g for biochar obtained from eucalyptus for FLX_0 20 mg/L, while olive-stone biochar achieved a q_{max} of 106.32 ± 2.73 mg/g (>16 fold increase) [238]. Similarly, a recent study by Escudero-Curiel et al., (2023) utilised nitrogen-doped alperujo derived hydrochars to remove FLX with q_{max} of 111.63 mg/g urea-modified hydrochar, while polyethyleneimine-modified adsorbent achieved a q_{max} of 29.31 mg/g for FLX [244]. Silva et al., (2020) investigated the maximum adsorption capacities of waste-based biosorbents derived from cork waste, spent coffee grounds, and pine bark for FLX_0 5 mg/L, which ranged between 4.74 mg/g - 14.31 mg/g [233]; whereas, the present study achieves a q_{max} of 25 mg/g for FLX_0 5 mg/L. In addition to agri-food waste, xylan, pectin, and lignin were also explored for their potential to removal FLX from aqueous solutions. For instance, Farghal et al., (2023) studied the ability of xylan and pectin coated activated-carbon

(XCM and PCM) based magnetite adsorbents to adsorb FLX and achieved a maximum adsorption capacity of 90.9 mg/g and 114.9 mg/g, respectively [236]. A similar study with lignin-derived anionic nanofibers demonstrated a capacity of 29 mg/g [237]. It is worth mentioning that the olive-stone derived CO_2-activated biochar performed better for FLX removal than some of the previously reported commercial adsorbents. For example, commercial carbon aerogel (NANOLIT 3D monolith NQ40 honeycomb premium (CO_2 activated), with a specific surface area of 790 m^2/g, obtained an adsorption capacity of 125.24 mg/g at pH 7-7.5 [242]. Similarly, an adsorption capacity of 96.2 mg/g was observed for commercial activated carbon PBFG4 in a study by [235]. Therefore, CO_2- activated biochar (CO_2-1000-30-600-1) used in the present study demonstrates the ability to achieve superior adsorption capacities for FLX. Further, FLX removal combined with the valorization of agricultural residues, represents a novel approach that addresses the dual objectives of environmental remediation and zero-waste principles. We believe this integration fills an important research gap and contributes to advancing sustainable solutions for emerging contaminants.

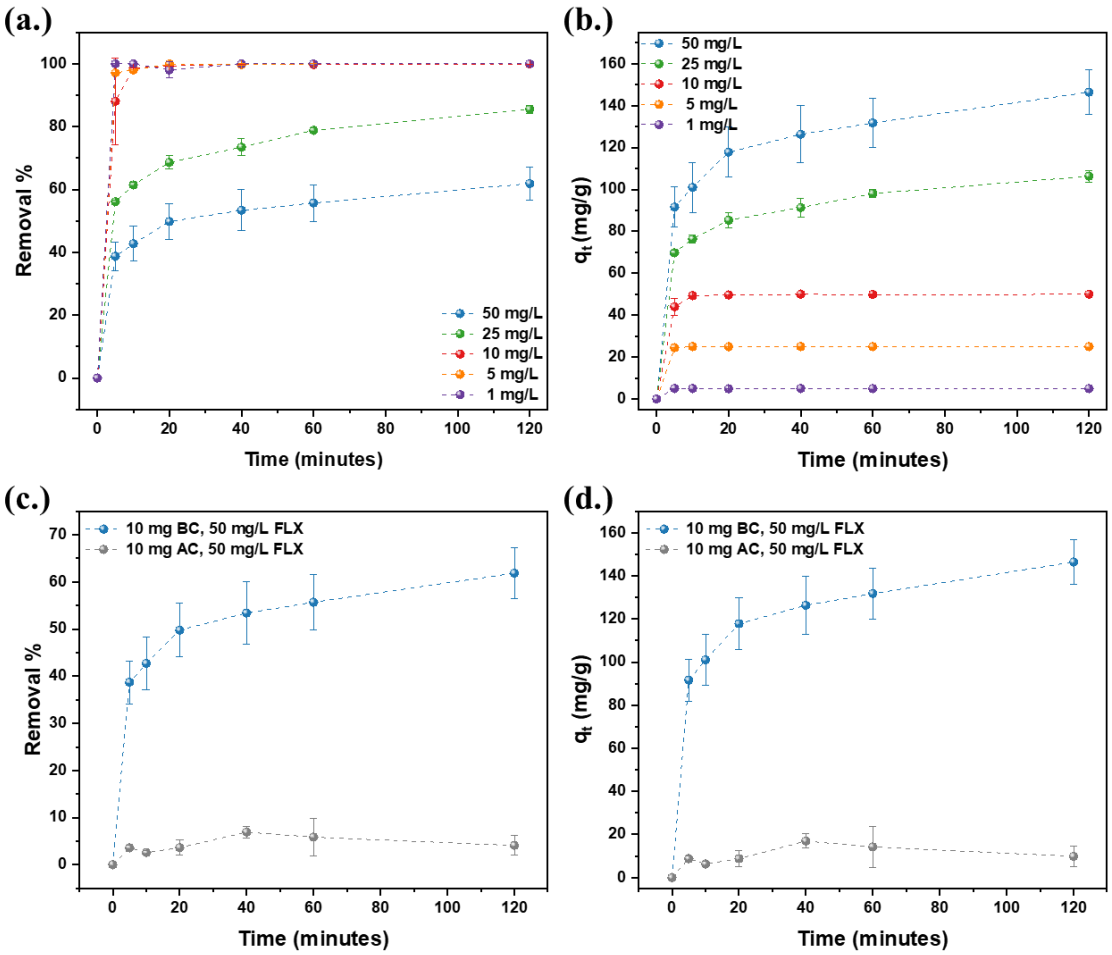

Figure 8.2: (a.) Removal efficiency, and (b.) uptake (q_t) of FLX by biochar 7 for FLX concentrations of 1, 5, 10, 25, and 50 mg/L for 0-120 minutes; (c). Removal efficiency, and (d.) uptake (q_t) of FLX by biochar 7 and commercially available activated charcoal for FLX concentration of 50 mg/L for 0-120 minutes

Table 8.1: Comparison of maximum adsorption capacities of FLX by different waste-derived adsorbents

Waste-Derived Biosorbent	**q_{max} (mg. g^{-1})**	**pH**	**Initial concentration (mg/L)**	**Temperature (°C)**	**Ref.**
Eucalyptus Biochar	6.41	6.5	20	RT	Fernandes et al., 2019
Alperujo Biochar	4.63, 5.95	6.4	30	RT	Escudero-Curiel et al., 2023
Nitrogen – Doped Alperujo Biochar	16.09, 111.63	6.4	30	RT	Escudero-Curiel et al., 2023
Fish bone char	55.87	---	100	---	Piccirillo et al., 2017
Spent coffee ground	14.31	9	5	RT	Silva et al., 2020
Pine bark	6.53	9	5	RT	Silva et al., 2020
Cork waste	4.74	9	5	RT	Silva et al., 2020
Nanofiber AL: PVA 50:50	29	---	50	---	Camiré et al., 2020
Nanocomposite XCM	90.9	7.35	25	28	Farghal et al., 2023
Nanocomposite PCM	114.9	7.35	25	28	Farghal et al., 2023
Pine-bark biosorbents	0.652	-	5	25	Lago et al., 2024
Olive-stone Biochar	4.82 - 146.45	6-7	1 - 50	RT	This study

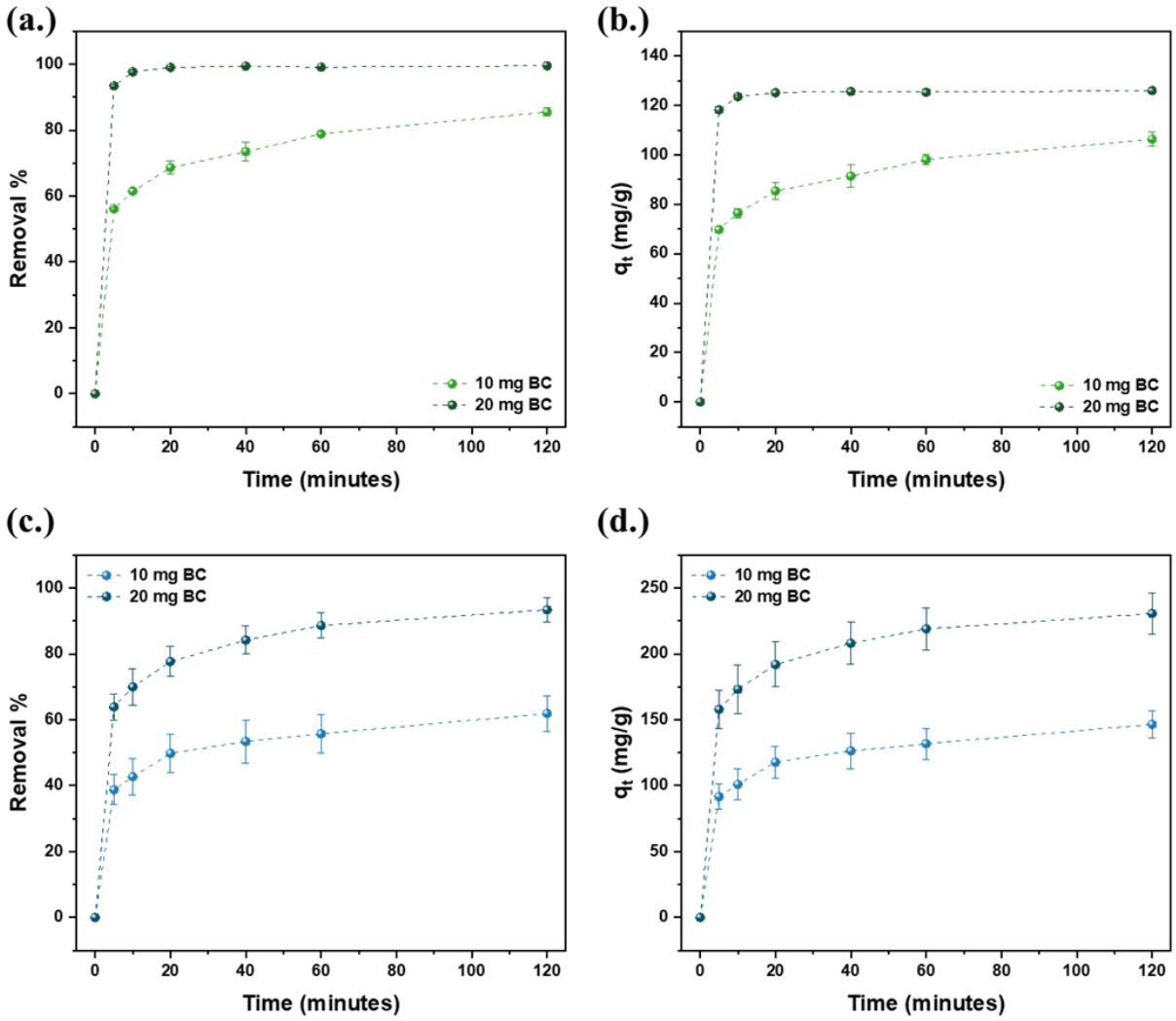

Figure 8.3: (a.) Removal efficiency, and (b.) uptake (q_t) of FLX by biochar 7 for FLX concentrations of 25 mg/L for 0-120 minutes; (c.) Removal efficiency, and (d.) uptake (q_t) of FLX by biochar 7 for FLX concentration of 50 mg/L for 0-120 minutes.

A higher adsorbent dose of 20 mg/50 mL was also studied for initial FLX concentrations of 25 and 50 mg/L, as shown in Figure 8.3. For initial FLX concentration 25 mg/L, biochar dose of 10 mg removed 85.49 ± 1.22% FLX with maximum uptake capacity of 106.32 ± 2.73 mg/g, while adsorbent dose 20 mg could remove 99.10 ± 0.18% of FLX with adsorption capacity of 125.27 ± 0.90 mg/g (Figure 8.3 (a-b)). Similarly, for 50 mg/L FLX, 10 mg of olive-stone derived biochar had a removal efficiency of 61.87 ± 5.39 and an uptake of 146.45 ± 10.55 mg/g, while 20 mg of

biochar removed 93.35 ± 3.62% FLX with q_t of 230.56 ± 15.48 mg/g (Figure 8.3 (c-d)). This is markedly better than other reported agri-food waste derived adsorbents and comparable to the maximum adsorption capacities of commercial adsorbents explored by Silva et al., (2020), which ranged between 21.86 mg/g - 233.50 mg/g [233].

To further understand the kinetics of the adsorption, the experimental data was fit into the PFO, PSO, and IP models (Figure F4). The model parameters as obtained are shown in Table 8.2. A comparative analysis of the model parameters reveals that the correlation coefficient of the PSO rate equation is higher than that of the PFO kinetics equation, thereby suggesting that the adsorption of FLX onto biochar follows PSO kinetics. Since high-fitting correlations to PFO and PSO have often been related to physisorption and chemisorption, respectively; the adsorption of FLX in the present study indicates chemisorption. However, physicochemical properties of both adsorbate and adsorbent, activation energy, and thermodynamic parameters, as mentioned elsewhere, play a crucial role in the adsorption mechanism [234].

Also, it is noteworthy that both the kinetic models- PSO and PFO, exclude mass transfer considerations. Since the olive-stone-derived biochar is highly porous with internal pores accessible to FLX and the media, consideration of mass transfer, and external and internal diffusion becomes important. Thereby, to determine diffusion and rate limiting step during adsorption, the experimental data was fit to IP diffusion model.

The model parameters- C (mg/g) and rate constant (K_p), as determined from the intercept and slope of the linear plot of q_t *vs* $\sqrt{t}$ (Figure F4c), respectively, are shown in Table 8.2. Since the plot does not pass through origin, the intraparticle diffusion model plot, demonstrates that there are more than one rate-limiting steps for the adsorption of FLX onto the surface of biochar. The plot can be divided into two zones- zone I, and zone II, with different slopes. In zone I, the slope is steeper, indicating the adsorption of FLX molecules onto the macropores of the biochar and the existence of diffusion film [242]. While zone II is associated with the diffusion of FLX into the microporous structure of biochar. Further, the greater the value of the y-intercept, the more is the intraparticle diffusion [242,292]. Since the y-intercept (i.e., C (mg/g)) is greater in zone II compared to zone I, the process is driven by intra-particle diffusion.

For lower initial FLX concentrations of (1 and 5 mg/L), the plateau in both zone I and zone II indicate that the system has reached equilibrium. For a concentration of 10 mg/L, zone I suggests the simultaneous occurrence of both film and intra-particle diffusion, while zone II represents

equilibrium. Similarly, for higher concentrations (25 and 50 mg/L), both zone I and zone II indicate a concurrent occurrence of film and intra-particle diffusion, as mentioned previously [242,293]. As the initial concentration of FLX increases from 1 to 50 mg/L, the value for the boundary thickness (C) also increases. Larger the intercept, more the boundary layer effect. Also, as shown in Table 8.2, the value of K_p also increases with increasing initial concentration of FLX, indicating a direct correlation between FLX concentration and the intra-particle diffusion [199,294].

Table 8.2: Rate constants (k_1, k_2, and K_p) obtained for different initial concentrations of FLX by PFO, PSO, and Intraparticle diffusion kinetic model

	PFO			**PSO**			**IP (Zone I)**			**IP (Zone II)**		
FLX (mg/L)	**q_e (mg/g)**	**k_1 (min^{-1})**	**R^2**	**q_e (mg/g)**	**k_2 (g/mg. min)**	**R^2**	**C (mg/g)**	**k_p (mg/g min)**	**R^2**	**C (mg/g)**	**k_p (mg/g min)**	**R^2**
50	65.366	0.031	0.662	141.844	0.002	0.994	65.092	11.686	0.992	98.059	4.408	0.997
25	75.944	0.050	0.648	102.459	0.004	0.994	54.065	7.031	0.999	75.232	2.869	0.940
10	49.402	0.168	0.785	49.652	0.061	1.000	38.102	2.301	0.997	49.057	0.037	0.999
5	24.532	0.130	0.584	24.704	2.128	1.000	24.603	0.009	0.990	24.287	0.065	1.000
1	4.759	0.121	0.516	4.751	1.064	1.000	4.268	0.099	0.879	4.757	-0.004	0.757

8.3.3 Adsorption isotherm

To understand the adsorption behaviour and predict the nature of adsorption mechanisms, the experimental data was fit into the Langmuir and Freundlich isotherm models (Figure F5). The fitting coefficients and statistical parameters for both models are summarised in Table 3. These parameters show that both the isotherm model fit the experimental data with good regression

coefficients. From a comparative analysis of model parameters, it is evident that Langmuir isotherm model was the better fit for the obtained data, with higher values for linear regression coefficients (R^2 >0.98). As the experimental data aligns best with Langmuir isotherm, the separation factor, R_L, can be appropriately determined using equation (9.4) [199,295].

$$R_L = \frac{1}{1+ b\, C_0} \quad \text{… equation (8.4)}$$

where C_0 is the initial concentration of FLX. It is a dimensionless equilibrium parameter to understand the feasibility of the adsorption behaviour of FLX onto the adsorbent. Based on the value of R_L, the process of adsorption can be unfavorable (R_L >1), linear (R_L =1), favorable (0 < R_L < 1) and irreversible (R_L=0) [199,234]. For the experimental data, the value of R_L varied between 0.324 and 0.986, i.e., 0 < R_L < 1, thereby suggesting favourable adsorption of FLX onto the biochar for initial FLX concentrations varying from 1 to 50 mg/L [199,234]. Also, as the initial FLX concentrations increased from 1 mg/L to 50 mg/L, the highest maximum monolayer adsorption (Q_0 (mg g^{-1})) ranged from 4.38 to 58.51 mg/g, respectively. The observed maximum monolayer adsorption was higher than that obtained for high-surface-area nanoparticles reported previously (40.7 mg/g for $RuFeO_3$ and 15.8 mg/g for $CeFeO_3$) [199].

Table 8.3: Langmuir and Freundlich isotherm model parameters of adsorption of FLX on biochar

	Langmuir Isotherm				**Freundlich Isotherm**		
FLX (mg/L)	**Q_0 (mg/g)**	**b (L/mg)**	**R_L**	**R^2**	**K_F [(mg/g) (L/mg)]$^{1/n}$**	**1/n**	**R^2**
50	58.514	0.003	0.860	0.976	2419.390	0.961	0.975
25	58.140	0.001	0.986	0.991	183.950	0.395	0.959
10	44.723	0.060	0.626	0.997	47.350	0.02	0.735
5	97.371	0.088	0.695	1.000	23.104	0.024	0.967
1	4.382	2.082	0.324	0.999	3.950	0.062	0.940

In addition, the model parameters obtained by data fitting to Freundlich isotherm model (as shown in Table 8.3) further provide insight into the adsorption of FLX onto the surface of the biochar. For instance, the values for $K_F > 1$ indicate strong adsorption capacity, $0 < K_F < 1$ suggests favorable irreversible adsorption, while $K_F = 1$ for linear isotherm. As shown in the table 3, K_F values of 3.95, 23.10, 47.35, 183.95, and 2419.39 were observed for $[FLX]_0$ 1, 5, 10, 25 and 50 mg/L, respectively, which represents that favourable irreversible adsorption. That is, olive-stone derived biochar has a high capacity for adsorbing FLX from its aqueous solution. The heterogeneity factor, 1/n, also suggests favourable adsorption ($0 < 1/n < 1$). Typically, 1/n closer to 0 indicates that the adsorption intensity is higher [238].

8.3.4 Regeneration and reusability tests

To desorb the adsorbed FLX and regenerate the spent biochar, solvents with different polarities were used as eluents and the results are summarized in Figure F6 (a). Since solvent polarity affects the contaminant desorption, a polar protic solvent (Methanol) and a dipolar aprotic solvent (50% ACN) were employed for the study. Deionized water was used to verify desorption at equilibrium. A very low recovery rate of 0.06 ± 0.03 % was observed with water, indicating that the bond strength was sufficient to prevent the establishment of a new equilibrium [234].

Methanol has often been used as a desorption solvent owing to its ability to disrupt polar interactions, such as hydrogen bonding, that may exist between the adsorbate and the surface of the adsorbent. It was also identified as the best desorption solvent for the recovery of FLX from nanofibers, with 100% recovery [237]. However, in the present study, only 21.51± 2.44 % desorption was observed. Similarly, pH-adjusted MeOH (pH 2), under low magnetic stirring at 30 °C, performed best for the desorption of FLX from the chitosan-derived hydrogel beads, thereby achieving >95% desorption [234]. However, in the present study, this solvent could only desorb 19.83 ± 4.78 % after 24 h of stirring at room temperature. This can be explained by the nature of forces acting between FLX and the adsorbent in both studies. The study by Nkana et al., (2024) suggested the physisorption of FLX on active sites of the biosorbent, while in the present study, the adsorption of FLX on biochar is attributed to chemisorption and intra-particle diffusion [234].

Acetonitrile is another solvent popularly used as an eluent. In a recent study by Lago et al., (2024), 50% acetonitrile (% v/v) was found to be the best desorption solvent for FLX from pine- bark-

derived biosorbents with 100% desorption within 48 h [243]. The present study observed 19.02 ± 3.26 % desorption with 50% acetonitrile, indicating a strong interaction, such as pore filling and/or strong π-π stacking, between FLX and the surface of the biochar. This also highlights the need for advanced regeneration methods to recover the porosity of the spent biochar without altering the structural parameters.

Previous studies have suggested the use of solvent-free techniques, such as the Fenton and Fenton-like process with peroxymonosulphate (PMS), to regenerate the spent biochar and subsequent cost reduction [241,242]. However, the use of strong oxidants, such as hydrogen peroxide, can often result in the collapse of pores by introducing oxygen-rich functional groups on the walls and at the entrance of the pores, as observed in the present study [242,296,297]. Despite this loss of porosity, Fe-UlS regenerated biochar retained 38.78 ± 1.59 % removal efficiency for cycle 2 of adsorption with 25 mg/L FLX after 2 h of treatment (as shown in Figure F6 (b)). This decrease in FLX uptake can be attributed to the blocking of pores due to oxidation and loss of potential interaction sites of FLX and biochar. [297] Further, a comparative analysis of TGA curves of unused and regenerated biochar shows an additional weight loss between 200-400 °C, thereby suggesting the presence of residual FLX in the biochar regenerated using solvents. While Fe-UlS regenerated biochar shows higher mass loss than raw biochar, but less than solvent-regenerated biochar. This indicates either more effective desorption of FLX by the synergistic action of Fe-catalysed oxidation and ultrasound. However, in practical application, the dose of the oxidant and the treatment time for regeneration can be optimized to maximize the retention of the porous network, without altering the surface of the adsorbent [297].

8.3.5 Adsorption Mechanism

The exchanges between the adsorbent and the adsorbate, and the subsequent removal by effective adsorption, can occur through one or more of these chemical interactions- (i) Electrostatic attractions between functional groups of the adsorbate and the adsorbent owing to their opposing electrical charges, (ii) Hydrogen bonding or dipole-dipole interactions, (iii) Hydrophobic, (iv) π-π Electron-donor-acceptor (EDA) interactions, and (v) Pore filling [243,298].

The adsorption *via* electrostatic interactions is governed by the surface charge of the adsorbent and the adsorbate, ruled by the pHzc and pKa, respectively. The pHzc of the synthesized biochar was

observed to be around 7, i.e., it has positive and negative charges that balance to give electrically neutral biochar. When the pH of the solution is less than pHzc, the surface of the biochar is positively charged, favouring the adsorption of anionic species [299]. Meanwhile, for pH> pHzc, the negative surface charge of the biochar favours the adsorption of cationic species *via* electrostatic attraction. The pKa of FLX is 9.8, suggesting the presence of FLX as a cationic species at circumneutral pH [233,243]. Therefore, under the conditions of the study (6<pH<7), when the biochar is electrically neutral (with slightly more positive charge) and FLX is positively charged, weak electrostatic forces are expected. For the solution pH <7 (pH=3 and pH=5), where both FLX and biochar surface are positively charged, electrostatic repulsion is expected, while at pH=9 electrostatic attraction is predicted due to the opposite charge of both entities (FLX predominantly positive and negative biochar surface). Since FLX exists predominantly in uncharged form, no electrostatic forces are expected at pH=11.

Therefore, under typical electrostatic considerations, maximum adsorption of FLX is expected at pH 9, where FLX is positively charged while biochar carries a negative charge. However, the observed adsorption order (pH 11> 9 ~ 5 > 6.5 > 3) deviates from the classical electrostatic expectations. In the present study, the maximum adsorption was observed for pH 11 (as shown in Figure 8.4 (a)), where FLX is predominantly neutral and electrostatic attraction is minimal. The findings suggest that there is no significant effect of pH on the adsorption of FLX on biochar (*p* value<0.05) and electrostatic interactions are not the primary forces driving the adsorption.

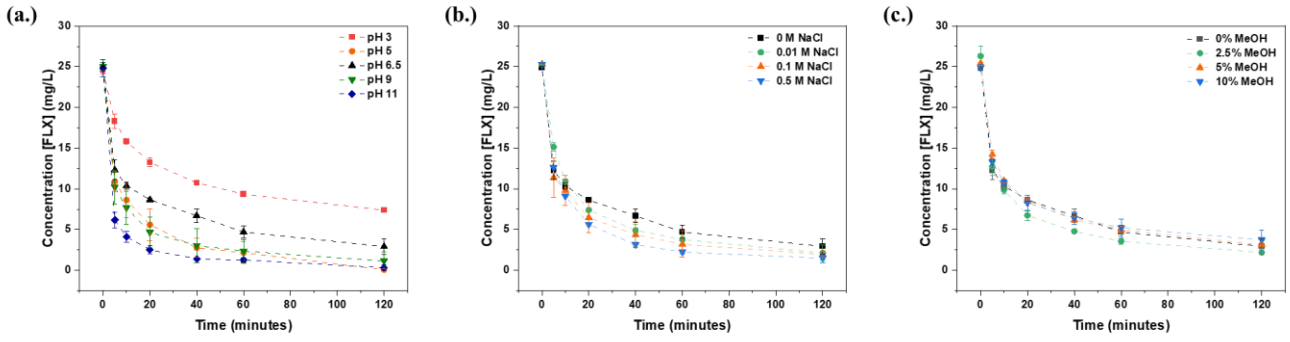

Figure 8.4: Effect of (a) pH, (b) NaCl (ionic strength), and (c.) MeOH (organic solvent) on the adsorption of FLX (C_0 25 mg/L) onto biochar

In addition, no appreciable changes (p value<0.05) in the adsorption of FLX on biochar on varying the concentration of NaCl from 0.01 to 0.1 to 0.5 M (Figure 8.4 (b)) further strengthen that electrostatic forces play only a minor role. Further, the heteroatom-rich, negatively charged surface functional groups, such as -C-O-C-, C=O, -C-O-, -OH, -NH(R), can establish hydrogen bonding with the protonated amine ($-NH_2$) functionality of FLX [240,300].

Besides electrostatic forces and hydrogen bonding, FLX can also base hydrophobic-hydrophobic (van der Waals interaction), attractive interactions, owing to the hydrophobic nature of both- the biochar surface and the target pollutant [298]. The octanol partition coefficient of FLX (K_{ow} of 4.17) indicates the hydrophobic nature of the pharmaceutical compound and its tendency to adsorb on a solid surface rather than remain in the aqueous phase [270,301]. However, co-solvent experiments using methanol (2.5-10% v/v) revealed no appreciable changes in the adsorption (p value<0.05), thereby suggesting hydrophobic interactions do not play a dominant mechanism either (as shown in Figure 8.4 (c)). If hydrophobic interactions were central, the presence of methanol would disrupt the hydrophobic partitioning of FLX into the biochar matrix, thereby affecting the adsorption process.

Moreover, low desorption using solvents, methanol, acidic methanol (pH 2), and 50% ACN, also suggests strong and irreversible adsorption, like pore entrapment, or strong coordination of FLX with the surface functional groups of biochar, rather than electrostatic and hydrophobic forces. The aromatic rings in the structure of FLX can serve as the π-electron acceptors for the carbon-based biochar, which can typically conform as robust π-donors due to the presence of oxygen-rich function groups, such as hydroxyl [235,240,243,298]. In addition, the microporosity of the olive-stone biochar, coupled with high surface area (855 m^2/g), is also expected to greatly contribute to the adsorption of small organic polar molecule, FLX, on the biochar surface [298]. Thereby, for FLX, non-electrostatic and non-hydrophobic interactions, such as pore filling, hydrogen bonding or complexation with functional groups, and π-π EDA forces are expected to play a significant role in adsorption on olive-stone-derived CO_2- activated biochar.

8.4 Conclusion

In the present study, olive stone waste was used as a carbon precursor to produce biochar, which was employed to remove FLX from aqueous solutions. The study of adsorption kinetics demonstrated that the pseudo-second-order kinetic model best described the experimental data

with a regression coefficient of >0.99. The process is also driven by intra-particle diffusion, with a direct correlation between initial FLX concentration and the intra-particle diffusion constant. Further, both Langmuir and Freundlich's isotherm models were in good agreement with the experimental data, with good regression coefficients. Model parameters, including R_L (between 0.324 and 0.986, i.e., $0 < R_L < 1$), and K_F (>1), suggested favourable irreversible adsorption of FLX onto the biochar for initial FLX concentrations varying from 1 to 50 mg/L. Further, the maximum adsorption capacities ranged from 4.82 ± 0.04 mg/g to 146.45 ± 10.55 mg/g, for initial FLX concentrations of 1 mg/L to 50 mg/L, respectively, which exceeds the adsorption capacity of previously reported waste-derived biochar used for FLX removal.

The findings also suggest a significant contribution of pore entrapment, hydrogen bonding, and π-π EDA forces in the adsorption of FLX on olive-stone-derived CO_2-modified biochar, and a minor contribution from the electrostatic attractive and hydrophobic-hydrophobic forces. Overall, the study shows that agri-food waste-derived biosorbents can be a potential alternative to produce high-capacity adsorbents for industrial applications while sustaining the vision of a circular economy and waste valorization.

From the previous study, the optimized biochar was selected, and its adsorption kinetics and mechanism were thoroughly investigated.

For the next study, this optimized biochar was coupled with CuO to form a photocatalytic system for the degradation of FLX under UVC irradiation. For the CuO-biochar mixture, CuO acts as the active photocatalyst, while biochar improves charge separation by effective electron transport, thereby achieving rapid degradation of FLX under UVC.

Chapter 9: Synergistic effect of CuO-biochar composite for efficient UVC photocatalytic treatment of Fluoxetine: Mechanism, Transformation products, and Toxicity assessment

Pratishtha Khurana[a], Ratul Kumar Das[a], Satinder Kaur Brar[a*]

[a] Department of Civil Engineering, Lassonde School of Engineering, York University, Ontario, Canada

*Corresponding author: Satinder Kaur Brar; email: satinder.brar@lassonde.yorku.ca

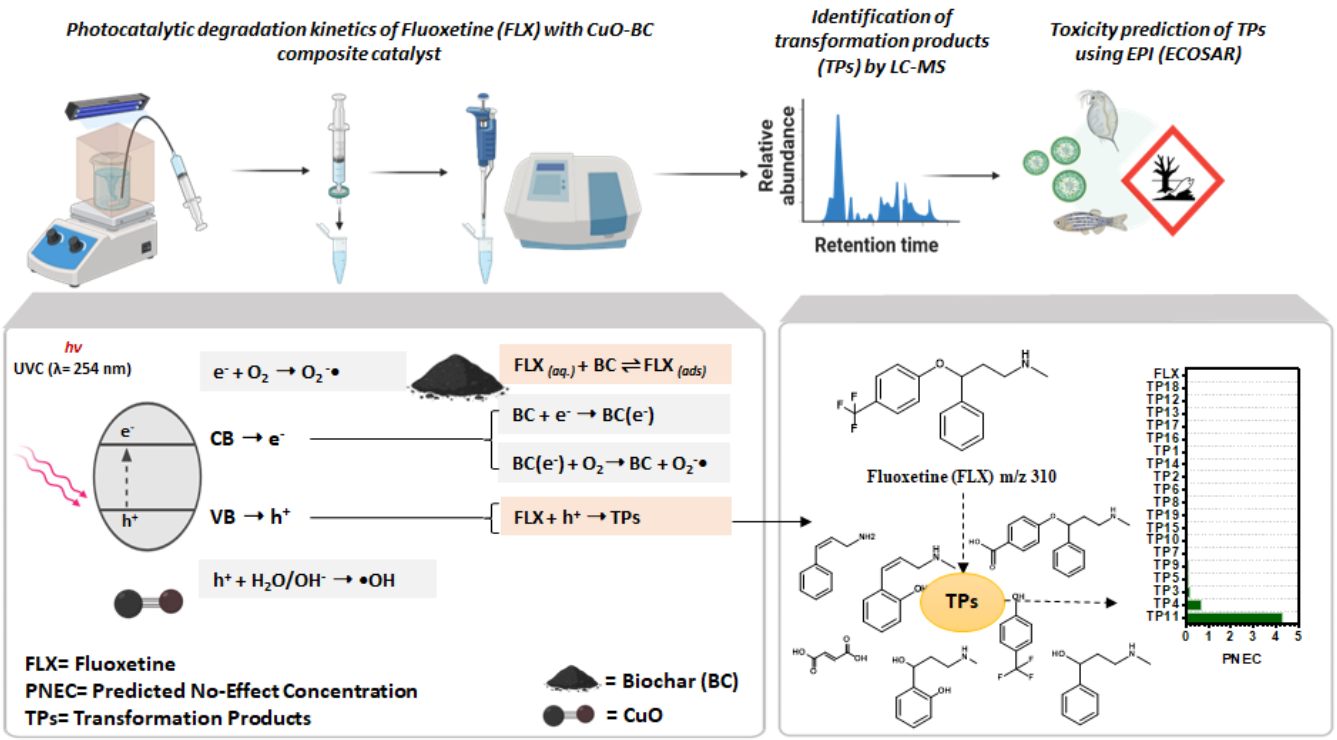

(Submitted)

Abstract

The present work utilizes a mixture of olive-stone-derived physically activated biochar (BC) and cupric oxide (CuO) as a composite photocatalyst under UVC (254 nm) irradiation for the degradation of fluoxetine (FLX). The BC, prepared using a single-step physical activation process with CO2 as the activation agent, showed a high surface area (855 m^2/g) and porosity, a low H/C ratio (0.023), and a high O/C ratio (0.519). Meanwhile, CuO, prepared by co-precipitation, had an energy band gap of 3.32 and 1.34 eV, and exhibits an excellent potential for using it as a photocatalyst for UVC-driven degradation of pollutants. The synergistic effect of BC and CuO under UVC irradiation resulted in the rapid degradation of FLX. Photocatalytic experiments with a catalyst dose of CuO (0.4 g/L) and BC (0.2 g/L) for an initial FLX concentration of 25 mg/L FLX in pure water achieved >95% removal within 2 minutes of UVC irradiation (254 nm, 16 W/m^2). For the same catalyst dose, 46.73 ± 5.68% removal was observed in 2 minutes for 50 mg/L FLX. Mechanistic investigation by scavenging tests (Na_2EDTA, Isopropyl alcohol (IPA), and Furfuryl alcohol (FFA)) indicated that the contribution of each active species follows the order h^+ > $^1O_2$ > •OH, with the degradation rate of 19.58%, 91.70%, and 94.30%, as opposed to 95.76% in the control in 2 minutes of treatment. Photogenerated holes (h^+) were, thereby, identified as the primary active species responsible for the photocatalytic degradation of FLX in the CuO-BC/UVC system, making the treatment apparently faster than the classical •OH-mediated processes. Moreover, the *in-silico* toxicity assessment of the transformation products indicated higher acute and chronic toxicity compared to the parent drug, thereby supporting the importance of this work.

Keywords

Biochar, Composite photocatalyst, Degradation, Fluoxetine, Photocatalysis, Toxicity assessment

9.1 Introduction

Fluoxetine (FLX), a widely prescribed selective serotonin reuptake inhibitor (SSRI), has emerged as a priority contaminant due to its environmental persistence and ecological toxicity. With a high octanol-water partition coefficient (log K_{ow}> 4), FLX exhibits a strong tendency to adsorb, and this property has often been explored as a remediation strategy for FLX-contaminated aqueous systems [238,243,274,302]. For instance, synthetic adsorbents ($RuFeO_3$ and $CeFeO_3$ nanoparticles) synthesized by Narayanan et al. (2021) demonstrated maximum adsorption capacities of 683.5 and 729.6 mg/g [199]. Similarly, a nanocomposite of ZnCoAl layered double hydroxide, supported on activated carbon, achieved a q_{max} of 450.92 mg/g for an initial FLX concentration of 50 µg/mL FLX at pH 10 [240]. Other commercially available adsorbents- activated carbon PBFG4, Granular activated carbon (GAC), and NQ40 were also previously reported to obtain q_{max} of 96.2, 233.5, and 125.24 mg/g for initial FLX concentrations of 10, 5 and 1000 mg/L, respectively [233,235,242].

In addition, waste-derived biosorbents, such as biochar, have also been synthesized and explored for the removal of FLX [238,243,302]. For example, KOH-activated paper sludge (PS800-10KOH) and CO_2-activated olive stone waste biochar have reported maximum adsorption capacities of 191.6 ± 4.8 mg/g and 146.45 mg/g for chemically and physically activated biochar [235,302]. Biochar offers a cost-effective, sustainable, and high-capacity adsorbent while supporting circular economy and zero-waste principles. However, despite their high efficiency (immediate effect, and effective even at low concentrations), adsorption-based removal strategies inevitably generate secondary waste.

In contrast to adsorption, UVC-based advanced oxidation processes (AOPs) have garnered attention for their ability to degrade persistent pharmaceuticals, like FLX. UVC irradiation, particularly at 254 nm, in the presence of a photocatalyst (TiO_2, ZnO, g-C_3N_4, etc.) or oxidant (H_2O_2, persulphate, ozone, etc.), can generate reactive oxygen species (ROS), such as hydroxyl radicals (•OH), which have been highly efficient for the degradation of FLX [247,249,252,260,261]. Unlike adsorption, which merely involves phase transfer of the contaminant, UVC-photocatalysis offers the potential for complete mineralization, eliminating the risk of secondary waste generation. However, UVC comes with its own set of practical limitations. To begin with, in wastewater treatment plants (WWTPs), UVC is rarely employed for the degradation of persistent pharmaceutical residues; its use is primarily limited to microbial disinfection rather than contaminant removal. To achieve disinfection, UVC exposure with water is limited to brief,

instantaneous contact, which is insufficient for any action of ROS on low concentrations of distributed pollutants. Even if UVC is used, its action is limited by the UV dose and kinetics of direct photolysis. In addition, the photolabile fraction for FLX is low, and only minimal degradation has been reported under direct UVC 254 photolysis [258]. The introduction of photocatalysts and oxidants results in kinetic enhancement of FLX degradation under UVC; however, the reaction times remain relatively long for practical implementation in WWTPs. Even the most efficient systems with photocatalyst reported in literature require at least 30 minutes to achieve >95% degradation [261,303].

To improve the kinetics of FLX degradation and shorten the reaction time, a mixture of Copper (II) oxide (CuO) and olive-stone-derived activated biochar (BC) was explored as a composite photocatalyst. CuO is a promising semiconductor photocatalyst due to its optical properties, low cost, and environmental compatibility. In addition to easy preparation from low-cost copper salt precursors, CuO can offer a redox capability [Cu(I)/Cu(II)], high chemical stability, and bactericidal activity [303]. The addition of BC ensures adsorption support and electron transfer in the photocatalytic system [304,305]. Their synergy can lead to a straightforward, practical, scalable, and safer treatment strategy for recalcitrant pharmaceuticals. In this regard, the present study explores the photocatalytic degradation of FLX using a simple CuO-BC composite prepared by physically mixing the two materials. The study evaluates the degradation kinetics under UVC irradiation, explores the role of reactive species by scavenger test, identifies the transformation products (TPs) and predicts their toxicity, and examines the effect of the water matrix by performing degradation in simulated effluent. This comprehensive approach provides insights into both the efficiency and practical applicability of CuO-BC composite for removing recalcitrant pharmaceuticals from water.

9.2 Experimental

9.2.1 Materials and chemicals

Fluoxetine hydrochloride (FLX, 98%) was purchased from Sigma Aldrich (Toronto, Canada). The stock solution for FLX was prepared by dissolving the appropriate amount in water, which was stored in a dark glass vial at 4 °C until further use.

For scavenger studies, EDTA disodium salt dihydrate (99%) was procured from Samchun Pure Chemical Co. Ltd. (China), while Furfuryl alcohol (FFA, 98%) and Isopropyl alcohol (IPA, 70%) were procured from Millipore Sigma and Fisher Scientific, Canada, respectively.

Photocatalytic experiments were performed in a closed cabinet equipped with a disinfectant wand (Crystal Clear Raze 18 W) emitting radiation at a wavelength maximum (λ_{max}) of 254 nm and a fixed irradiance of 16 W/m². The UVC irradiance measurements were performed using Ocean Insight FLAME Miniature spectrometer.

9.2.2 Preparation and characterization of CO_2-activated olive stone biochar (BC) and CuO particles

Biochar was prepared using a single-step physical activation process, employing olive-stone waste as the biomass and CO_2 as the activating agent (CO_2-1000-30-600-1), as previously described [302]. Briefly, olive-stone biomass was carbonized at 600 °C at a heating rate of 10 °C/min, followed by a rest for 60 minutes under N_2 atmosphere (300 N mL/min). The carbonized material was then activated at 1000 °C at a heating rate of 20 °C/min and holding time of 30 min, using CO_2 as the activation agent at a flow rate of 600 N mL/min, and pressure of 1 bar. Detailed physicochemical characterization, including Brunauer-Emmett-Teller (BET) surface area analysis, CHNS elemental analysis, FTIR spectroscopy, Cation Exchange Capacity (CEC), and Scanning Electron Microscopy (SEM), has been described elsewhere[302].

Copper oxide particles (CuO) were synthesized using the co-precipitation method. Briefly, 2 M NaOH was added to 0.2 M $CuSO_4$. $5H_2O$ (aq.) dropwise until a black suspension was observed. This suspension was left overnight for aging, after which it was filtered and rinsed with water to remove unreacted salts. The precipitate was then dried and calcinated at 450-600 °C in a muffle furnace for 6 hours to remove possible impurities and refine the particle size. Finally, the obtained powder was ground using a mortar and pestle before use. The steps involved in the preparation of CuO particles can be presented as [306]:

$$CuSO_4.5H_2O\ (aq.) + 2\ NaOH\ (aq.) \rightarrow Cu\ (OH)_2\ (s) + Na_2SO_4\ (aq.) \ldots \text{(eq. 9.1)}$$

$$Cu\ (OH)_2\ (s) \rightarrow CuO\ (s) + H_2O\ (g) \quad \ldots \text{(eq. 9.2)}$$

The synthesized CuO particles were characterized using X-Ray Diffraction (XRD), BET, Zeta potential, UV-Visible Diffuse Reflectance Spectroscopy (DRS), SEM, and FTIR for their

structural properties, surface area, porosity, optical properties (energy band gap, E_g), morphology, and functional groups. The sample preparation methods and operational parameters for all the techniques are outlined in Text S1 of the supplementary information.

9.2.3 Degradation of FLX and Mechanism of action

The performance of synthesized BC and CuO for FLX degradation was evaluated under UVC irradiation. The UVC-assisted photocatalytic experiments were performed in a closed cabinet equipped with a disinfectant wand (Crystal Clear Raze 18 W) emitting radiation at a wavelength maximum (λ_{max}) of 254 nm and a fixed irradiance of 16 W/m².

The experiments were conducted at room temperature in a 100 mL glass beaker placed on a magnetic stirrer, adjusted to 400 rpm, to ensure uniform suspension of the catalysts. A total volume of 50 mL of an aqueous FLX solution (25 and 50 mg/L) was used. The catalyst system consisted of biochar (BC, 10 mg) and/or CuO particles (20 mg), unless stated otherwise. At predetermined time intervals, aliquots were withdrawn, immediately filtered through 0.22 µm syringe filters to remove the suspended solids, and analyzed for FLX concentrations using UV-visible spectroscopy (at 226 nm) (Genesys 50, ThermoFisher Scientific) [302]. Control experiments were performed in the dark under identical conditions. It is noteworthy that high concentrations of FLX (25 and 50 mg/L) were used in the present study to prevent adsorption-dominated removal at low concentrations and to ensure accurate mechanistic separation of asortion, photolysis, and photocatalysis contributions.

To identify dominant ROS responsible for FLX degradation, radical scavenger tests were performed under identical photocatalytic conditions (50 mL of 25 mg/L FLX, 10 mg BC, 20 mg CuO, UVC 254 nm) in the presence of different scavengers: Na_2EDTA (10 mM), Isopropyl alcohol (IPA, 10 mM), and Furfuryl alcohol (FFA, 0.05 mM) to quench h^+, •OH, and $^1O_2$, respectively[305]. The degradation efficiency in the presence of a scavenger was compared with the control (without any scavenger) to identify the contribution of each reactive species to the degradation of FLX.

All the experiments were performed in duplicates to reduce experimental errors, and the degradation efficiency was calculated as:

$$\text{Degradation } \% = \frac{C_0 - C_t}{C_0} \text{ X } 100 \qquad \ldots \text{(eq. 9.3)}$$

Where C_0 and C_t represent FLX concentrations (mg/L) at time 0 (initial) and at time t.

9.2.4 Identification of transformation products and ecotoxicity prediction

The transformation products from FLX degradation were determined using LC-MS using the Sciex QTOF (Zeno TOF 7600 system) equipped with an electrospray ionization (ESI) in positive ionization mode [302]. The ecotoxicity of the parent compound FLX and identified transformation products to fish (F), daphnids (D), and green algae (GA) was estimated using EPI Web Suite (KOWWIN, WATERNT, and ECOSAR) by USEPA (software version 1.0.2). The software uses QSAR (Quantitative Structure-Activity Relationship) to predict the acute and chronic toxicity of these products to the aquatic organisms, calculate predicted no-effect concentration (PNEC) by dividing the EC50 or LC50 by an uncertainty factor of 1000, and concentration of concern (COC) by dividing the lowest chronic concentrations (ChV) by an uncertainty factor of 10[307].

9.2.5 Matrix effects/ Degradation of FLX in simulated effluent

To evaluate the matrix effects, photocatalytic degradation experiments were performed using a simulated effluent, as shown in Table S1, prepared according to the literature-reported synthetic wastewater composition (excluding copper salts to avoid interference with the CuO catalyst)[308]. The matrix contained a representative concentration of organic carbon, nitrogen, phosphate, carbonate, and major inorganic ions to mimic the conditions of treated municipal wastewater.

FLX was spiked in simulated effluent to achieve an initial concentration of 25 mg/L. Experiments were performed in a 100 mL beaker containing 50 mL of solution under continuous stirring at 400 rpm. The following conditions were tested: effluent + FLX (dark); effluent + FLX + UVC; and effluent + FLX + BC + CuO + UVC (10 mg BC and 20 mg CuO). The UVC irradiation (254 nm) was applied under identical geometric and operational conditions as ultrapure water experiments. Samples were collected at predetermined time intervals, filtered through 0.22 μm syringe filters, and analyzed by UV-Visible spectroscopy.

9.2.6 Catalyst reusability tests

To evaluate the reusability of the catalyst, the CuO-BC mixture was subjected to 5 cycles of UVC-mediated degradation of 25 mg/L FLX. After each cycle, the solution was centrifuged at 4500 rpm for 5 minutes. The supernatant was then collected for FLX analysis and replaced with 50 mL of a 25 mg/L FLX solution for the next degradation cycle.

9.2.7 Statistical analysis

The experiments were performed in duplicates, and analysis of variance (ANOVA) and Tukey test were used to determine their statistical significance with a *p-value* of 0.05 as the level of significance.

9.3 Results and Discussion

9.3.1 Physicochemical characteristics of BC (CO_2-1000-30-600-1) and CuO

The BC (CO_2-1000-30-600-1) exhibited a high surface area (855 m^2/g), low H/C ratio (0.023), and high O/C ratio (0.519) (Table S9.2 and S9.3), indicating a highly condensed aromatic structure with extensive π-conjugation and abundant surface oxygen functionalities. The appearance of peaks at 2400-2250, 1700-1760, 1300-1400, and 1080-1300 cm^{-1} in the FTIR spectra of BC, as shown in Figure S9.1, further confirmed the presence of oxygenated functional groups on the surface of the biochar [302]. In addition to these functionalities, BC also possesses a highly porous structure, as indicated by SEM images (Figure 9.1a) and BET (Table S9.3), which contribute greatly to its adsorption potential [302].

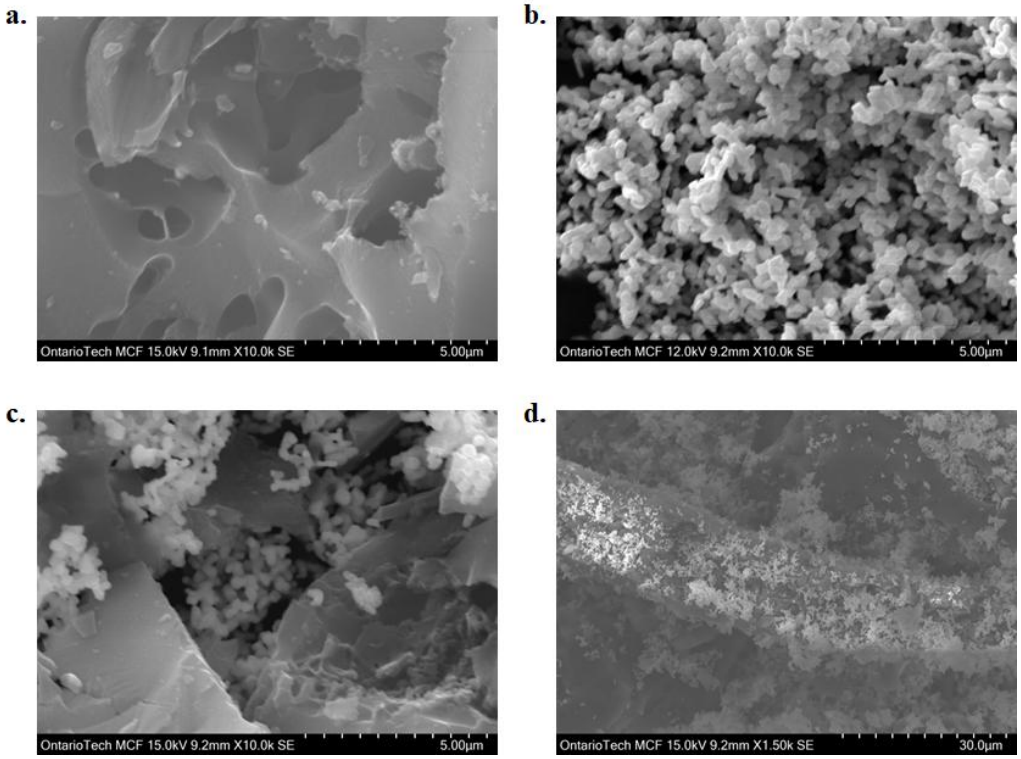

Figure 9.1: SEM images of pristine (a) BC and (b) CuO; and spent CuO + BC (c and d)

On the contrary, the SEM images of CuO particles showed nano-sized, irregular and spherical particles, with a rough, grainy surface (Figure 9.1b). The relatively low zeta potential (-16.83 ± 1.03 mV) (Figure S9.2) indicates weak electrostatic repulsion between CuO particles, resulting in significant particle agglomeration, as confirmed by SEM images. Further, in contrast to the largely amorphous carbon structure of the biochar, the structural analysis of CuO *via* XRD revealed sharp and intense peaks, which are indicative of the excellent crystallinity of the synthesized CuO particles. The diffraction pattern, as shown in Figure 9.2a, with distinct peaks at 2θ values of approximately 32.5°, 35.5°, 38.7°, 48.7°, 53.4°, 58.3°, 61.5°, 65.9°-66.6°, and 67.9°, corresponds to the reflection planes (110), (-111), (111), (-202), (020), (-113), (022), and (220), respectively[303,309]. These identified planes confirm the monoclinic structural phase of the CuO particles, consistent with the COD reference entry 9016105 for tenorite (CuO). A Cu-O stretching band observed in the low wavenumber region of the fingerprint region of the FTIR spectrum (400-600 cm^{-1}) further supported the formation of CuO (Figure S9.1).

The UV-Vis DRS of the synthesized CuO, recorded in the wavelength range of 200-1400 nm (Figure 9.2b), shows increased reflectance intensity at $\lambda > 800$ nm and exhibits low reflectance in the UV and visible regions of the spectrum, further confirming the preparation and semiconductor nature of CuO particles. The optical band gap (E_g) for allowed direct and indirect transitions was determined using the Kubelka-Munk method and the Tauc plot. For this, $(F(R_\infty)\ h\nu)^n$ is plotted against photon energy ($h\nu$), where $F(R_\infty)$ is the Kulbelka-Munk function, given by $F(R_\infty)= (1-R_\infty^2)/2R_\infty$, where R_∞ is $R_{sample}/R_{standard}$ and n depends on the nature of the semiconductor optical transition. For directly allowed transitions, n=2; for directly forbidden transitions, n=3/2; for indirectly allowed transitions, n= 1/2, and for indirectly forbidden transitions, n=3 .[310]
The curves for $(F(R_\infty)\ h\nu)^2$ vs $h\nu$ and $(F(R_\infty)\ h\nu)^{1/2}$ vs $h\nu$ are presented in Figures 9.2c and 9.2d. The extrapolation of the linear regions of these plots yielded optical band gap values of 3.32 (direct) and 1.34 eV (indirect), which are in good agreement with the previously reported band gap values for CuO [303,311]. The E_g values also confirm the excellent potential of using it as a photocatalyst for UVC-driven degradation of pollutants. UVC (254 nm), with energy of 4.88 eV (>3.32 eV), can excite electrons from the valence band (VB) to the conduction band (CB), and generate electron-hole pairs, which are responsible for photocatalytic degradation of contaminants under UVC irradiation.

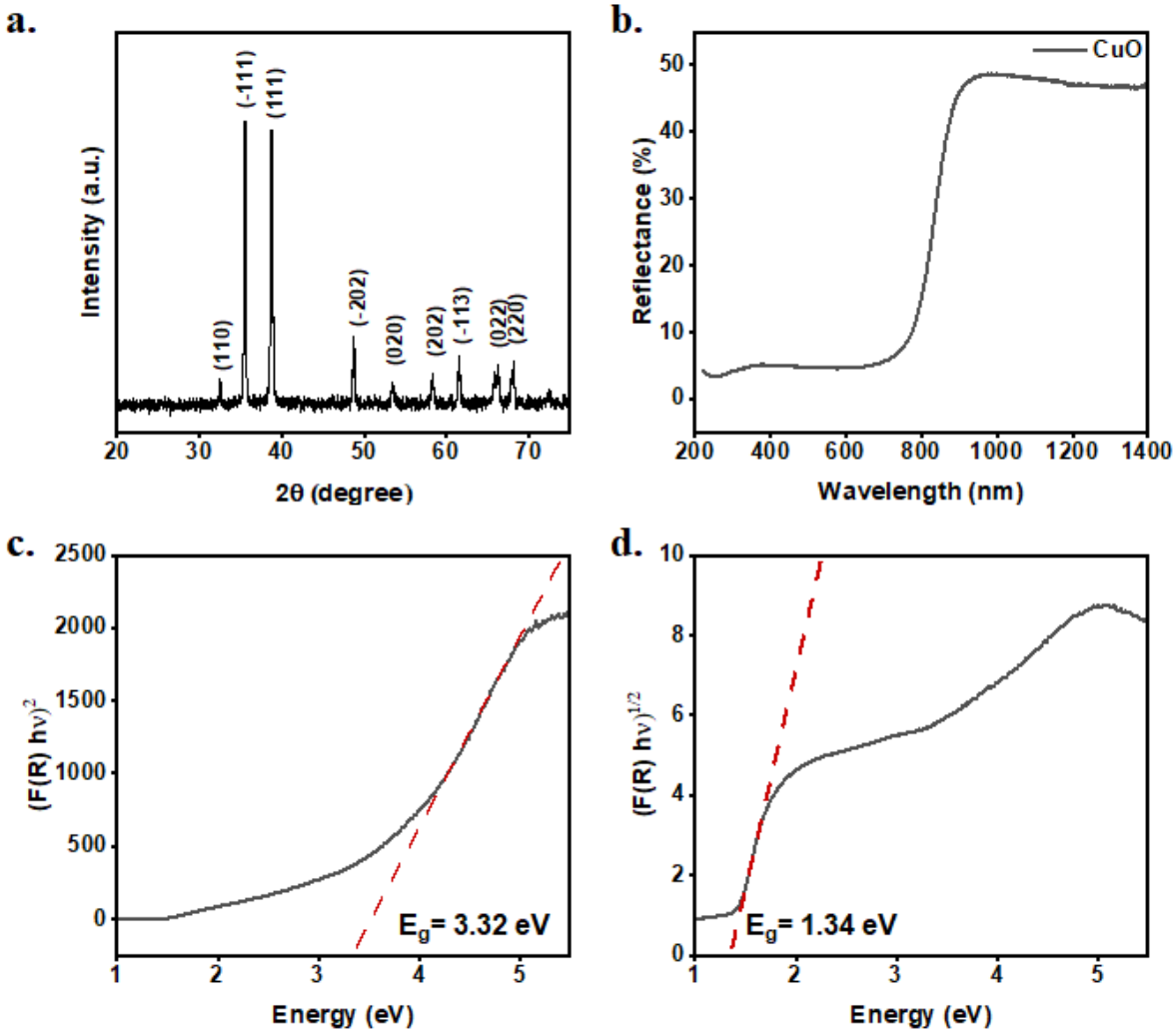

Figure 9.2: (a) XRD of synthesized CuO particles; Variation in (b) reflectance as a function of wavelength, (c) $[F(R)\ h\nu]^2$ and (d) $[F(R)\ h\nu]^{1/2}$ vs the photon energy (eV) for CuO and their extrapolation of the linear portion

9.3.2 Adsorption behaviour of FLX on BC, CuO, and BC-CuO

The adsorption behaviour of BC and CuO towards FLX was evaluated at initial concentrations of 25 and 50 mg/L using pseudo-second order (PSO) kinetic modeling. The results are shown in Figure 9.3(a-d) and the obtained model parameters are summarized in Table 9.1. As shown in table

9.1, the PSO model provided a good correlation for all systems, allowing comparison of adsorption capacity (q_e) and rate constants (k_2). However, the two materials exhibited fundamentally different adsorption characteristics, reflecting their distinct physicochemical properties.

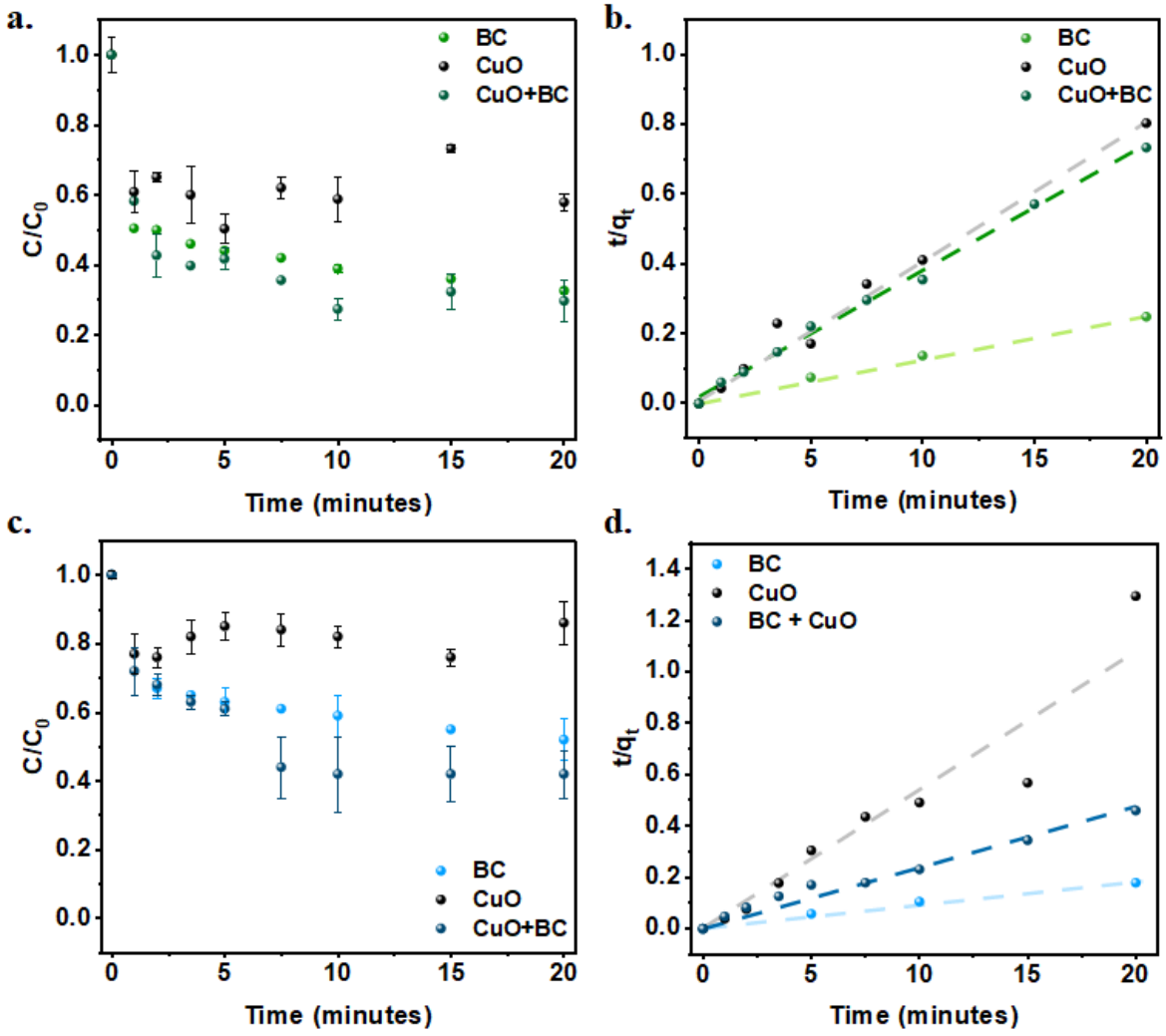

Figure 9.3: Adsorption controls for FLX at initial concentrations of 25 and 50 mg/L shown as normalized concentration (C/C_0) in (a) and (c), respectively. (b) and (d) present the corresponding PSO kinetic model fits. Experimental points represent mean values with error bars indicating standard deviation, while dashed lines represent PSO fitting.

Table 9.1: Rate constants (k_2) and adsorption capacities (q_e) for BC, CuO, and CuO + BC by PSO kinetic model

	BC	CuO	CuO + BC
25 mg/L FLX			
Slope	0.0123	0.0394	0.0359
q_e	81.5661	25.3678	27.8164
Intercept	0.0076	0.0209	0.0191
k_2	0.0197	0.0743	0.0677
R^2	0.9929	0.9788	0.9959
50 mg/L FLX			
Slope	0.0088	0.0565	0.0213
q_e	113.6364	17.6929	46.9704
Intercept	0.0084	0.0259	0.0309
k_2	0.0092	0.1233	0.0147
R^2	0.9819	0.9045	0.9802

The olive-stone-derived activated biochar (CO_2-1000-30-600-1) served as an effective, porous, high-capacity adsorbent for the removal of FLX from aqueous media. At a dose of 10 mg/50 mL for 25 mg/L FLX, the biochar could remove 67.33 ± 1.15 % of FLX within 20 minutes, with an adsorption capacity of 80.59 ± 1.70 mg/g (Figure 9.3a) and its fitting to PSO model is shown in Figure 9.3b. At the same adsorbent dose, for an initial FLX concentration of 50 mg/L, BC exhibited a removal efficiency of 47.58 ± 5.87%, with a q_t of 111.85 ± 10.35 mg/g within 20 minutes of contact (Figure 9.3c).

The BC exhibited a clear concentration-dependent increase in adsorption capacity, thereby indicating efficient utilization of available surface sites at higher solute loading, developed pore structure, and intraparticle diffusion, as explored by a previous mechanistic study [302]. Although the rate constant decreased from 0.0197 to 0.0092 g/mg min with increasing FLX concentration, this

reduction is consistent with site occupation and increasing intraparticular diffusion at higher adsorbate loading. The model fit remained strong ($R^2 \geq 0.98$, Figure 9.3d), suggesting that adsorption is governed primarily by surface interactions rather than physical partitioning.

This also aligns well with the structural properties of BC. The low H/C ratio (0.023) indicates a highly aromatic framework, while the moderate O/C ratio (0.519) suggests the abundance of oxygenated functional groups. These characteristics support multiple interaction mechanisms, such as π-π interactions, surface complexation, electrostatic forces, and hydrogen bonding. High surface area (855 m^2/g), as indicated by BET analysis, and relatively high q_e values, further confirm that BC functions as a true porous adsorbent with significant sorption capacity for FLX.

In contrast, CuO exhibited markedly lower adsorption capacities, which decreased with increasing FLX concentrations. For instance, when FLX concentration increased from 25 to 50 mg/L, the adsorption capacity decreased from 25.37 to 17.69 mg/g (Figures 9.3a and 9.3c). This inverse trend indicates surface-limited adsorption rather than pore-filling behaviour. The PSO rate constant (k_2) increased substantially from 0.0743 to 0.1233 g mg^{-1} min^{-1}, indicating a very rapid adsorption kinetics at a higher concentration gradient. For both the FLX concentrations, CuO exhibited instantaneous partition (<1 minute) with an equilibrium plateau from t = 1 to 20 minutes for both C_0 = 25 and 50 mg/L FLX, with equilibrium concentrations of 14.55 ± 1.64 mg/L and 35.84 ± 1.72 mg/L, respectively. This indicates rapid surface interaction and saturation due to the limited available adsorption sites. The low surface area (~ 7 m^2/g) of CuO further supports its limited adsorption capacity, compared to biochar (855 m^2/g). The negative zeta potential of CuO (-16.83 ± 1.03 mV) and the positive surface charge of FLX (pK_a 9.8) at near-neutral pH (pH = 6.5 ± 0.2) supports that electrostatic forces likely exist between the two entities. Although rapid surface interactions occur, the small number of available active sites results in early saturation, confirming that CuO acts mainly through surface-mediated catalyst for photochemical processes rather than an adsorptive medium.

When BC and CuO were applied simultaneously (10 mg BC + 20 mg CuO), the adsorption capacity was intermediate between the two components and consistently lower than BC alone despite the higher dose of adsorbent used. For instance, at 25 mg/L FLX, the equilibrium capacity of the composite system (27.82 mg/g) was substantially lower than BC alone (81.57 mg/g), but slightly higher than CuO alone (25.37 mg/g). Similarly, for 50 mg/L FLX, the composite exhibited a q_e of 46.97 mg/g, which exceeded CuO (17.69 mg/g) but remained lower than BC (113.64 mg/g).

These results indicate that the incorporation of CuO does not enhance adsorption; instead, it partially suppresses the intrinsic adsorption capacity of BC, possibly due to surface coverage and pore blocking of BC by CuO particles, as reported by previous studies [312,313]. This is further confirmed by the SEM images and specific surface area of the spent catalyst (Figures 9c-d and Table G3). As shown in Figures 9.1c and 9.1d, deposition and agglomeration of CuO particles on the surface of the biochar lead to partial blocking of pores. This reduces the accessible surface area and pores for the adsorption of FLX, thereby decreasing its adsorption capacity, when compared to BC.

9.3.3 Photolytic and photocatalytic degradation of FLX under UVC

The degradation of FLX under UVC irradiation (254 nm) was investigated to distinguish direct photolysis from photocatalytic enhancement in the presence of BC, CuO, and CuO-BC. As shown in the Figure 9.4, FLX undergoes limited direct photolysis under UVC, while significantly enhanced degradation was observed when BC and CuO-containing systems were introduced. Under UVC alone, FLX showed a very slow decline in C/C_0, achieving only 4.70 ± 1.58% and 15.35 ± 0.95 removal in 2 and 20 minutes, respectively (C_0 25 mg/L). For 50 mg/L FLX, removal efficiencies of 2.28 ± 1.14% and 11.77 ± 0.86% were observed after 2 and 20 minutes of UVC irradiation, respectively. This confirms that direct photolysis is not a dominant removal pathway for FLX at the given irradiance.

Following the addition of BC in the presence of UVC (UVC + BC), the removal percentage of 71.40 ± 4.93% and 66.46 ± 1.11% were observed after 20 minutes for 25 and 50 mg/L FLX, respectively. It is noteworthy that the removal efficiency does not differ significantly from the adsorption removal of FLX by BC alone, indicating that the observed effects are dominated by adsorption and not by photochemical processes. However, this slight increase in the removal could be possibly due to the regeneration of the adsorbent in the presence of UVC. Biochar adsorbs fast, boosts low-dose capture, and increases the exposure/contact time for UVC to degrade the adsorbed FLX over time. This can also allow for possible in-situ self-regeneration of the adsorbent media, thereby enhancing the total removal efficiency of FLX. Similarly, the introduction of CuO in presence of UVC did not significantly improve the removal efficiency of FLX (C_0 25 mg/L), when compared to the adsorption control performed with CuO in the dark.

Table 9.2: Comparison of Fluoxetine (FLX) removal efficiency (%) at 2 and 20 minutes under different treatment conditions at initial concentrations of 25 and 50 mg/L

Treatment	Removal in 2 minutes (%)	Removal in 20 minutes (%)
25 mg/L FLX		
BC [a]	49.80 ± 2.39*	67.33 ± 1.15
CuO [ab]	34.91 ± 1.25	42.11 ± 24.06
CuO + BC [a]	57.28 ± 6.07	70.27 ± 5.97
UVC [b]	4.70 ± 1.58	15.35 ± 0.95
UVC + BC [a]	42.06 ± 6.53	71.40 ± 4.93
UVC + CuO [a]	59.59 ± 4.67	54.82 ± 1.45
UVC + BC + CuO [c]	95.76 ± 0.26	100
50 mg/L FLX		
BC [bc]	32.63 ± 1.01*	47.58 ± 5.87
CuO [ab]	23.72 ± 2.82	13.99 ± 6.18
CuO + BC [c]	32.18 ± 2.61	58.12 ± 7.33
UVC [a]	2.28 ± 1.14	11.77 ± 0.86
UVC + BC [c]	27.87 ± 3.26	66.46 ± 1.11
UVC + CuO [c]	54.28 ± 1.15	52.25 ± 4.14
UVC + BC + CuO [c]	46.73 ± 5.68	63.15 ± 8.92

*Estimated from PSO model.
[#] Equal lower letters within same FLX concentration indicate that the treatment do not differ by the Tukey test (p value < 0.05)

However, the simultaneous addition of CuO and BC in presence of UVC significantly improved the removal efficiency of the system. With the introduction of both CuO and BC, >95% of FLX removal (C_0 25 mg/L) was achieved in 2 minutes of treatment, compared to 42.06 ± 6.53% and 59.59 ± 4.67% for BC-UVC and CuO-UVC, respectively (Figure 9.4a). For 50 mg/L FLX, 46.73 ± 5.68% degradation was observed within 2 minutes of treatment (Figure 9.4b). This rapid, unprecedented removal of the parent drug is owed to the synergistic effect of CuO, BC, and the UVC irradiation. CuO, being a direct/indirect gap semiconductor, with the energy band gap of

3.32 and 1.34 eV, serves as an exceptional photocatalyst in the presence of UVC for the degradation of FLX. When CuO is irradiated with UVC, an electron (e^-) gets excited from VB to CB, thereby creating a hole (h^+) in VB and a free e^- in CB (eq. 9.4). These photogenerated charge carriers are highly reactive and can react with H_2O and O_2 to generate ROS like •OH and $O_2^{\bullet-}$, which are highly oxidative and can potentially result in pollutant degradation (eq. 9.5-9.7). However, rapid recombination of e^- and h^+ in CuO limits its photocatalytic activity. The addition of BC aids the faster apparent removal of the drug by reducing electron-hole recombination and improving charge separation, in addition to rapid adsorption. Previous studies have also reported the ability of biochar to separate and transport the photo-generated charge carriers due to its inherent conductivity [305,314,315].

$$CuO + h\nu \rightarrow e^-_{CB} + h^+_{VB} \text{ (photogenerated electron and hole) … (eq. 9.4)}$$

$$h^+ + H_2O/OH^- \rightarrow \bullet OH \text{ (hydroxyl radical) … (eq. 9.5)}$$

$$e^- + O_2 \rightarrow O_2^{\bullet-} \text{ (superoxide radical) … (eq. 9.6)}$$

$$FLX + h^+/\bullet OH/\ e^-/\ O_2^{\bullet-} \rightarrow TPs \text{ … (eq. 9.7)}$$

The olive-stone-activated biochar, in addition to rapid pore filling, which increases local FLX near CuO surface, can act as a green electron transport medium (shuttle) and/or sink *via* the redox action of various carbon structures (such as quinone and phenolic groups) present on its surface. Both high O/C (0.519) and low H/C (0.023) ratios indicate oxygen-rich, highly carbonized, aromatic surface sites, which can participate in electron transfer as an electron shuttle and/or sink (eq. 9.8-9.9).

$$BC + e^- \rightarrow BC\ (e^-) \text{ (electron sink/transfer) … (eq. 9.8)}$$

$$BC\ (e^-) + O_2 \rightarrow BC + O_2^{\bullet-} \text{ … (eq. 9.9)}$$

This separates the charge carriers, suppresses e^- - h^+ recombination, thereby enhancing the lifetime of photogenerated holes for direct oxidation of FLX. This synergy between BC and CuO, therefore, facilitates the rapid adsorption and degradation of FLX by the action of photogenerated holes. This was further confirmed from the findings of the scavenger tests.

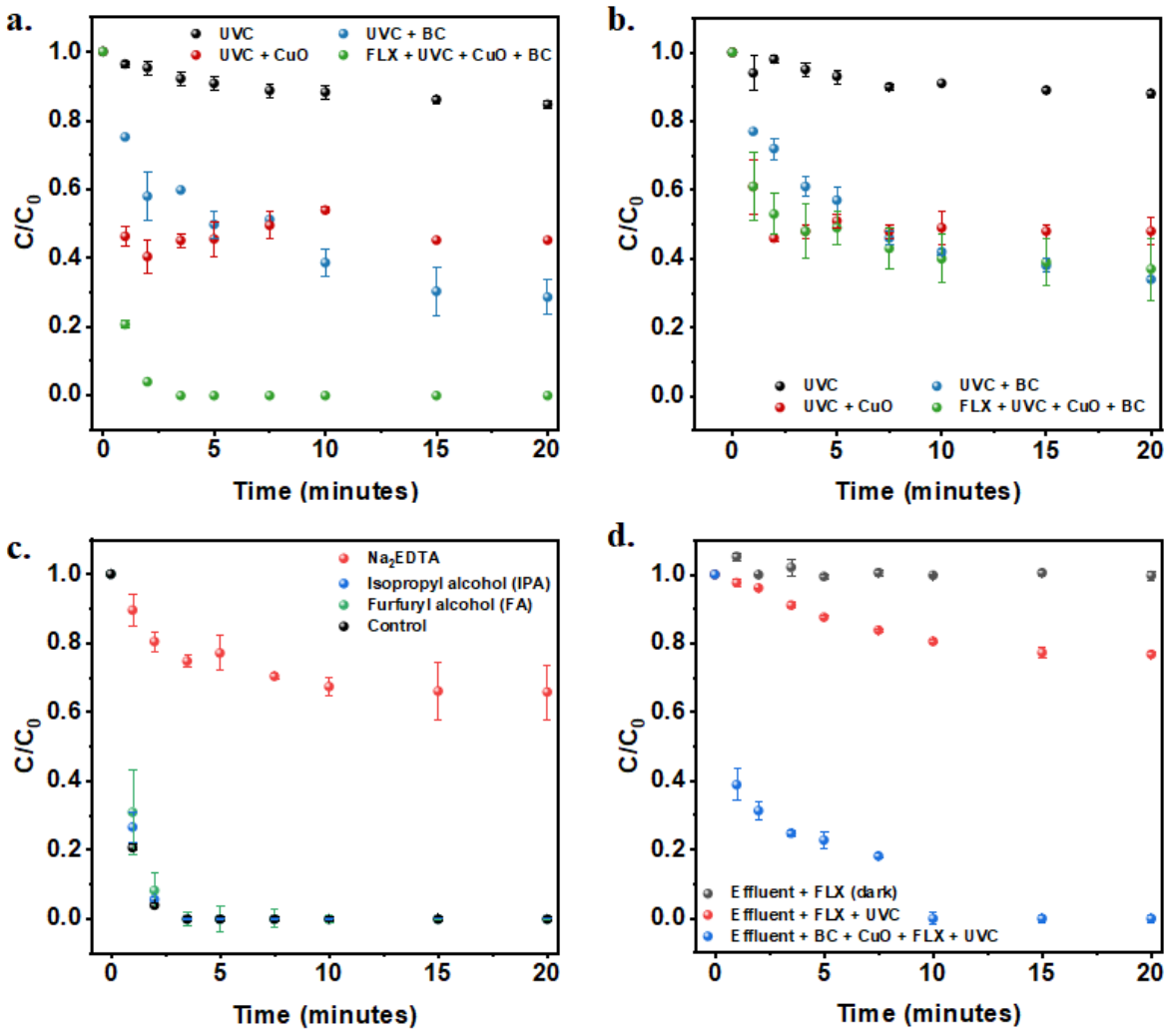

Figure 9.4: Photocatalytic degradation of FLX using BC, CuO, and CuO-BC under UVC irradiation for initial FLX concentrations of (a) 25 mg/L, and (b) 50 mg/L; (c) in presence of scavengers ([FLX_0] = 25 mg/L), and (d) in simulated wastewater effluent ([FLX_0] = 25 mg/L)

To identify the primary ROS responsible for the photocatalytic degradation of FLX, degradation assays in the presence of scavengers, Na_2EDTA (10 mM), IPA (10 mM), and FFA (0.05 mM), were carried out to quench h^+, •OH, and $^1O_2$, respectively, and the results are shown in Figure 4c. The decrease in FLX degradation efficiency reflects the crucial role of these ROS. According to the results illustrated in Figure 4c, the contribution of each active species follows the order $h^+ > {}^1O_2 >$ •OH, with the degradation rate of 19.58%, 91.70%, and 94.30%, as opposed to 95.76% in control in 2 minutes of treatment.

These findings identify the photogenerated hole as the primary active species responsible for the photocatalytic degradation of FLX in the presence of the CuO-BC-UVC system. The C/C_0 remains high even in the presence of a hole scavenger, which supports that the photogenerated holes are critical in the process, and FLX degradation proceeds largely *via* direct hole oxidation. The better fir of PSO also supports surface-controlled electron-transfer interactions, further supporting the involvement of holes as primary oxidative species. Also, since it is not a classical •OH-dominated photocatalysis, which is often an indirect route, to the best of the authors' knowledge, it is the fastest FLX degradation reported in literature so far. To support, a comparison of the photocatalytic responses from recent studies has been summarized in Table 9.3, evidencing the superiority of the CuO + BC system used in the present study for the degradation of FLX. Although CuO is a widely used photocatalyst, its application for FLX degradation is limitedly explored. A targeted literature search using Web of Science displayed only one result where CuO or CuO-based systems were used for the photocatalytic degradation of FLX. This recent study by Becerra et al (2025) reported a 94% removal in 30 minutes using photocatalytic heterostructures CuO/CuWO4 under UVC (254 nm) for an initial FLX concentration of 10 mg/L (10 mL)[303]. Other studies have investigated the use of other photocatalytic systems, such as TiO_2, g-C_3N_4, Fe_3O_4-$BiVO_4$/$Cr_2V_4O_{13}$, as shown in Table 9.3, for the degradation of FLX.

Although the total organic carbon (TOC) was not measured, the changes in pH before and after treatment provide indirect evidence for mineralization. Under UVC irradiation alone (FLX 25 mg/L), the pH decreased from near neutral (pH = 6.5 ± 0.2) to acidic (pH = 4.45 ± 0.1), suggesting formation and accumulation of acidic intermediates. The CuO-BC/UVC system did not show any significant pH change (6.87 ± 0.5) despite complete removal of the parent pharmaceutical drug. This suggests that intermediates were also rapidly degraded, supporting a complete degradation of intermediates and enhanced mineralization, compared to direct photolysis. In addition, potential copper leaching is unlikely under this pH change; however, accounting this in continuous-flow systems can become crucial.

The recyclability studies using CuO-BC showed that the photocatalytic activity decreased from the 1st cycle to the 2nd cycle, which can be attributed to the loss of catalysts during recovery and the adsorption of degradation intermediates onto the catalyst surface (Figure S9.5). After this initial

decline, the removal efficiency of the system remained stable in subsequent cycles, thereby indicating that the catalysts possess good structural stability.

Table 9.3: Comparison of the photocatalytic response of several materials reported in literature for FLX degradation

Photocatalytic treatment	**Dosage and Operating conditions**	**Removal Efficiency**	**Ref.**
Catalytic ozonation with Nano-γ-alumina catalyst	30 mg/L ozone, 1 g/L catalyst	96.14% of 28.56 mg/L FLX in 30 minutes	[261]
Catalytic ozonation	0.11 mM FLX, 60 minutes, pH 11, 0.050 g/L TiO_2	~100% removal in 60 minutes	[250]
FeO/Sulphite (S(IV)) FeO/PMS FeO/PDS		84.4% 56.4% 30.7% in 17.5 minutes	[256]
	Real wastewater	14.4%	
Photocatalysis with TiO_2 P25 and g-C_3N_4 photocatalysts	Ultrapure water (lab); 5 mg/L FLX, 100 mg/L catalyst; I = 500 W/m^2	~100% in 120 minutes using TiO_2 ($t_{1/2}$ =18 minutes) ~91% removal using g-C_3N_4 ($t_{1/2}$ =69 minutes)	[249]
	Real secondary hospital wastewater (pilot scale); 5 mg/L FLX, 100 mg/L catalyst; I = 500 W/m^2	~100% in 120 minutes using TiO_2 ($t_{1/2}$ =34 minutes) ~90% removal using g-C_3N_4 ($t_{1/2}$ =65 minutes)	
Photocatalysis with hybrid heterojunction photocatalyst (Fe_3O_4-$BiVO_4$/$Cr_2V_4O_{13}$ (FBC)	10 mg/L FLX, 30 mg catalyst, 500 W Xe lamp (280 mW cm^2)	~99.2% removal in 60 minutes	[260]

Photocatalysis with Molecularly imprinted catalyst (MI-BiOCl)	Municipal wastewater, 20 mg/L FLX, 20 mg (in V= 50 mL) catalyst; simulated solar irradiation (500 W)	99.3% removal in 150 minutes	[252]
Photocatalysis with $CuO/CuWO_4$ heterostructures	10 mL 10 mg/L FLX	94% in 30 minutes	[303]
Photocatalysis with CuO/BC composite catalyst	50 mL 25 mg/L FLX	>95% in 2 minutes	This work
	50 mL 25 mg/L FLX in simulated wastewater effluent	>95% in 10 minutes	

9.3.4 Effect of water matrix: simulated effluent study

Despite being a promising technique for FLX under laboratory conditions, photocatalysis has often been reported to fail under 'realistic' conditions. Previous studies have seen a significant reduction in the performance of photocatalytic systems when employed for real and simulated wastewater matrices. For instance, a recent study by Chen et al. reported >80% FLX removal in 17.5 minutes under optimal conditions, whereas the performance dropped to 14.4% removal in real wastewater conditions [256]. Similarly, another study (using TiO_2 as photocatalyst; dose 100 mg/L) reported a $t_{1/2}$ of 34 minutes in real secondary hospital wastewater, compared to a $t_{1/2}$ of 18 minutes in ultrapure water (controlled, lab conditions)[249]. This is primarily due to the combined effects of the scavenging action of transformation products and various wastewater constituents, including but not limited to chlorides, NOM, carbonate, and bicarbonate, which consume ROS and reduce degradation rates for the target pollutants [316,317]. In some cases, dissolved organics and turbidity limit the reaction rates by affecting the penetration of UVC irradiation [249,318]. For catalytic systems, these organic and inorganic ions can adsorb on the catalyst surface, limiting the available sites for FLX and deactivating the catalytic surface in some cases [249,256]. For these reasons, photocatalytic systems often show reduced efficiency under real environmental conditions. To evaluate whether similar limitations occur in the present study, the performance of the CuO-BC/UVC system, developed in the present study, was analyzed in simulated wastewater effluent, and the results are shown in Figure 9.4d.

As shown in Figure 9.4d, in the absence of light, the normalized concentration of FLX remained close to 1, indicating negligible adsorption of FLX and no matrix effects on the stability of the drug under the studied conditions. Under UVC irradiation (photolysis control), a gradual decrease in C/C_0 was observed, suggesting limited photolytic degradation of FLX. In contrast, in the presence of CuO-BC under UVC, rapid degradation of FLX was observed, with nearly complete removal within 10 minutes. Despite the presence of scavenging entities such as chloride, bicarbonate, dissolved organic, and inorganic ions, the reaction proceeded rapidly, possibly *via* direct oxidation pathways. Since the reaction proceeds directly *via* photogenerated holes despite indirect •OH photocatalysis, the reaction is fast and unaffected by the wastewater constituents.

9.3.5 Transformation products, and their in-silico toxicity assessment

The photocatalytic transformation products, as identified using LCMS, are shown in Figure 9.5. The identified TPs indicated that the initial oxidation of FLX produces hydroxylated and N-oxide intermediates, followed by defluorination and the formation of multioxygenated species, as seen in previous studies. The transformation of FLX also includes ether bond cleavage to phenolic and side chain fragments, which can culminate in ring oxidation and progressive mineralization [249,250,256,303,319]. The identified TPs, as shown in Figure 9.5, suggest O-dealkylation (amine, phenolic), N-demethylation, hydroxylation, hydrolysis, and defluorination as the primary contributors to the transformation of the parent drug molecule under the synergistic action of CuO-BC/UVC.

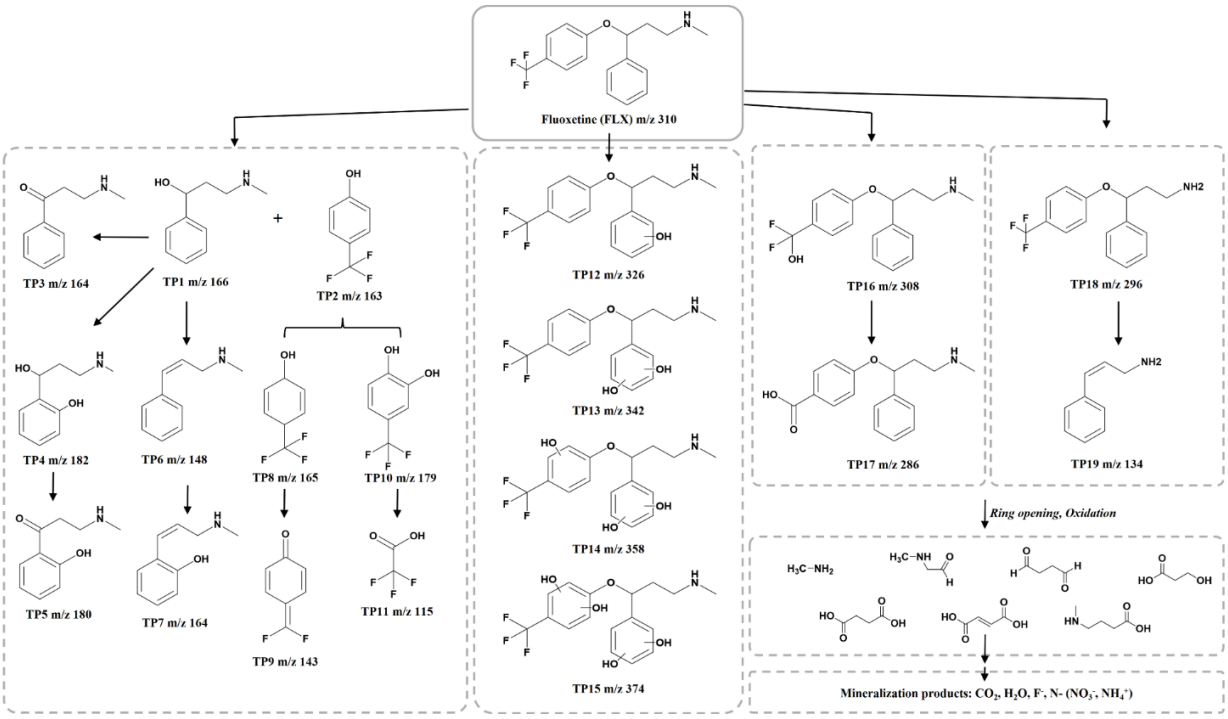

Figure 9.5: Proposed transformation products (TPs) for FLX after photocatalytic treatment with CuO-BC composite catalyst

The physicochemical properties and aquatic toxicity of the identified TPs were assessed using an *in-silico* approach, and the complete dataset is presented in Table G5. From this data, PNEC and COC values were calculated using the most sensitive toxicity endpoint (EC50 or LC50) as ecotoxicity indicators, and the compounds were ranked from highest (red bars) to lowest (green) concern, as presented in Figure 9.6. The data for FLX serves as the reference (gray bar; PNEC = 0.771 µg/L and COC= 13.9 µg/L) for the comparative estimation of the toxicity of the identified TPs. Interestingly, PNEC values for all identified TPs were higher than those of FLX, indicating reduced aquatic toxicity after degradation with the CuO-BC/UVC system. This suggests that the treatment not only removes the parent compound but also lowers the associated ecological risk. However, it is noteworthy that although ecotoxicity parameters estimated using QSAR have been recognized by regulatory agencies as a screening and predictive tool to support risk prioritization and risk assessment frameworks, bioassays and experimental validation are required for definitive confirmation. It is also likely that ECOSAR models can overestimate/underestimate toxicity depending on functional groups.

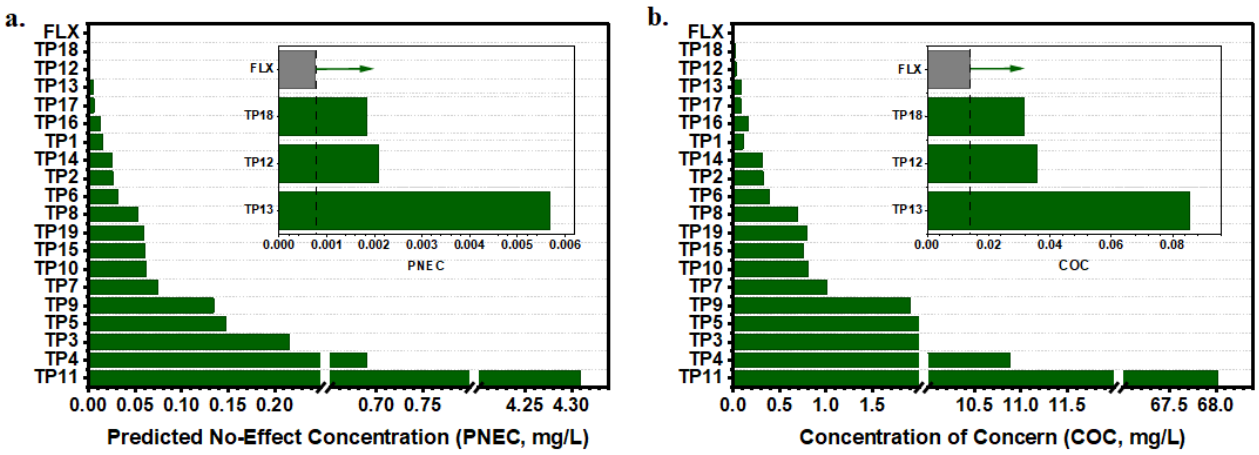

Figure 9.6: Predicted ecotoxicity indicators based on (a) acute values and (b) chronic values for FLX and its TPs generated during the proposed treatment (UVC-CuO/BC)

9.4 Conclusion

In this study, a CuO-BC composite photocatalyst was developed for the efficient and rapid degradation of FLX in pure water and in simulated wastewater effluent under UVC irradiation. For an initial FLX concentration of 25 mg/L in pure water and simulated wastewater effluent, >95% removal was observed within 2 and 10 minutes of UVC irradiation, respectively. Similarly, for 50 mg/L FLX, 46.73 ± 5.68% removal was observed within 2 minutes of irradiation. The photocatalytic degradation in the presence of various scavengers further identified the photogenerated hole as the primary active species responsible for the degradation of FLX in the CuO-BC/UVC system. While CuO serves as an exceptional photocatalyst in the presence of UVC for the degradation of FLX, the presence of BC concentrates FLX for ROS action by rapid adsorption, reduces electron-hole (e^- - h^+) recombination and improves charge separation. Since degradation proceeds primarily *via* direct h^+ oxidation, aided by adsorption on the catalytic surface, it appears to be faster than other reported photocatalytic systems operating *via* indirect •OH-mediated pathways.

The *in-silico* ecotoxicity assessment of TPs revealed a higher PNEC and COC (acute and chronic toxicity indicators) than FLX (PNEC = 0.771 µg/L and COC = 13.9 µg/L), indicating reduced aquatic toxicity (fish, daphnids, and green algae) after the proposed treatment. This reduced toxicity suggests that the CuO-BC/UVC treatment not only removes the parent drug FLX but also lowers the associated ecological risk. Overall, the present work demonstrated the promising performance of CuO-BC/UVC photocatalytic systems for effective degradation of FLX in batch systems; however, further experimental validation on the toxicity and persistence of TPs, the degree of mineralization, and the performance of the composite photocatalytic system in a continuous flow regime is deemed necessary for optimization of conditions (catalyst dose, time of irradiation, flow rate) for application at a larger scale. In addition to this, several operational constraints, including but not limited to continuous flow reactor design, UVC energy demand, catalyst recovery and reusability, potential copper leaching, and its performance under dynamic real wastewater, must also be sought.

Chapter 10: Conclusions and Future Recommendations

10.1 Conclusions

From the results obtained, the following conclusions can be drawn for the two model pharmaceuticals studied as a part of this investigation: Imipenem (IMP) and Fluoxetine (FLX).

- Imipenem: "A Fleeting Threat"

The stability of the antibiotic depends on the presence of light (irradiation), temperature, solvent, humic acids (dissolved organic matter), and metals. The results indicate that under the conditions of the study, the drug was photolabile and thermosensitive and rapidly degraded under visible light and room temperature. Further, the presence of humic acid and metals, such as copper, accelerated the degradation of the antibiotic *via* indirect photochemical pathways. Although the presence of reactive oxygen species was not analyzed for humic acids due to the complexity of the molecule, hydroxyl radicals (OH•) were detected for the IMP-Cu binary system using N, N-dimethyl-4-nitrosoaniline (RNO) as a probe. A notable increase in signal at m/z 316.096 (corresponding to [IMP-O-H+]), a gradual decrease in drug concentration, and discoloration of RNO indicated oxidative degeneration of the antibiotic due to *in vivo* generation of reactive species *via* copper-redox coupling. Copper, owing to its redox cycles of cuprous and cupric copper [Cu (I)/Cu (II)], can produce H_2O_2, and then decompose the generated H_2O_2 to produce OH• *via* a heterogeneous Fenton-like reaction.

In addition to copper, IMP was also observed to interact with other metals, such as Mg (II), Ca (II), Al (III), and Fe (II). For all these metals, a decrease in the free drug concentration, accompanied by the appearance of new signals, indicated facile interaction between the two entities. For instance, signals as m/z 311.08595 and m/z 319.0742 were observed and attributed to $[Mg\ (IMP)_2]^{2+}$ and $[Ca\ (IMP)_2]^{2+}$, respectively. The stoichiometric ratio (M: L = 1: 2) was also confirmed by potentiometric titrations and computational studies using Gaussian. Further, a toxicity assessment of these metal complexes on wastewater model microorganisms (*E. coli* and *B. subtilis*) revealed higher antibacterial activity of IMP-Me complexes, compared to free IMP. This increased toxicity of IMP-Me can be attributed to the electron delocalization over the entire chelated system, which

reduces polarity and increases the lipophilicity of the complexes. This increase in lipophilicity, as also shown from DFT studies, can thereby facilitate stronger interaction between AMCs and the bacterial cell membrane.

Overall, IMP exhibits a potential to form metal complexes, which are more toxic than the parent antibiotic; However, its natural attenuation across multiple pathways in wastewater limits its retention and persistence in the environment.

- Fluoxetine: "Contaminant that stays"

Designed to cross the blood-brain barrier in human hosts, the widely prescribed SSRI, FLX, is resistant to the action of humic acid, metals, and persists in the environment. Its physicochemical properties indicate its high tendency to adsorb on organic matters, such as soil, sediment, and risk the invasion of the food chain by bioaccumulation and magnification in all biomes. Given its persistence, the present study proposed a novel, CuO-biochar-UVC hybrid treatment approach for fast and effective degradation of FLX.

The CO_2-activated biochar, produced using olive stone waste as a carbon precursor, was used for effective removal of FLX by adsorption in batch systems. By optimizing activation parameters (CO_2-1000-30-600-1), this study demonstrates the ability to achieve superior adsorption capacities for FLX. The observed maximum adsorption capacities ranged from 4.82 ± 0.04 mg/g to 146.45 ± 10.55 mg/g, for initial FLX concentrations of 1 mg/L to 50 mg/L, respectively, which exceeds the adsorption capacity of previously reported waste-derived biochar used for FLX removal. The adsorption kinetics follow a pseudo-second-order kinetic model best, and the Langmuir adsorption isotherm, indicating irreversible adsorption of FLX onto the biochar. Non-electrostatic and non-hydrophobic interactions, such as hydrogen bonding, pore filling, and π-π EDA forces, were identified as the primary interactions facilitating FLX adsorption onto the biochar. Overall, the study uses agri-food waste-derived biosorbents as a potential alternative to produce high-capacity adsorbents for industrial applications while sustaining the vision of a circular economy and waste valorization.

The optimized biochar was then coupled with CuO, a photocatalyst, to achieve rapid degradation of the drug under UVC irradiation. While CuO acts as an active photocatalyst, the presence of

biochar improved charge separation by effective electron transport, thereby achieving rapid degradation of FLX. For the initial concentration of 25 mg/L FLX, >95% removal was observed within 2 minutes of treatment, which, *to the best of our knowledge*, is the fastest removal reported to date. Photocatalytic degradation in the presence of different scavengers identified that the photogenerated hole was the primary active species responsible for the degradation of FLX in the presence of the CuO-BC/UVC system. Since it proceeds primarily *via* direct hole oxidation, it is apparently faster than indirect OH•-mediated pathways.

Further, the higher PNEC and COC or reduced predicted ecotoxicity of the identified transformation products support the importance of this work. Overall, the present work demonstrated the promising performance of the CuO-BC-UVC system for effective and rapid degradation of FLX in batch systems.

10.2 A comparative review of Environmental Fate, Toxicity and Treatment implications: IMP vs FLX

As evident from the findings of the study, both IMP and FLX have an environmental impact; however, their behaviour and fate vary greatly. This stark contrast does not imply that one is less of a contaminant than the other; rather, both these contaminants are relevant pollutants, which are undeniably present and pose unique environmental challenges.

Based on the conclusions, a few parallels have been drawn, and a comparative assessment has been presented:

a. Environmental Fate and Persistence

To begin with, IMP's sensitivity to sunlight, temperature, moisture, oxygen, and humidity restricts its environmental presence and persistence, while FLX resists natural attenuation, is highly stable, and can persist in the environment.

Based on the partition coefficients, IMP (with a negative log P value) is hydrophilic in its free form and prefers to occur in the solution phase, while FLX has a positive coefficient, supporting its 'surface' driven effects. For IMP, the degree of hydrophilicity is expected to change on metal complexation; however, the risk of long-term exposure declines sharply due to photodegradation

and hydrolysis. In contrast, FLX displays partitioning to organic matter even in its free form, where it persists, and the impact is drawn out over a long timescale due to its recalcitrance.

b. Toxicity and Biological impacts

This persistence, natural attenuation, combined with partition coefficients, also defines their toxicity and long-term ecological impact. For instance, upon release, IMP can exert antimicrobial pressure, trigger the development and spread of resistance genes in existing bacterial communities. That is, IMP can cause an evolutionary shift in the environmental bacterial microbiome and pose long-term public health implications *via* horizontal gene transfer.

On the other hand, the ecological impact of FLX perturbs various kingdoms of life. The presence of FLX doesn't kill organisms directly, but its ability to cross the blood-brain barrier, along with its high lipophilicity, causes it to both alter neurological signaling and bioaccumulate and magnify across the food chain. Therefore, the acute effects are sub-lethal, but the consequences of chronic exposure to FLX are ecologically significant.

c. Treatment strategies

The distribution of these pharmaceuticals, with their environmental behaviour and persistence, influences the selection of treatment strategies for their effective removal. For example, the use of antibiotic IMP is restricted to hospitals, which would mean that the drug residues appear in hospital wastewater in short bursts. This IMP spike can be mitigated at the point sources through timed innovations such as UV or AOPs, before being released to the WWTPs.

In contrast, the course of FLX spans from a few months to a year, and the discharge is not limited to one type of wastewater effluent. Therefore, to mitigate FLX, round-the-clock removal and degradation approaches are needed. In addition, based on the adsorption potential, adsorption columns and their hybrid systems can be designed and optimized for maximum FLX removal; however, reactor surface area and material affinity must be thoroughly sought.

Overall, the two case studies together provide decisive insights into the prioritization of contaminants and their treatment decisions. IMP is short-lived but toxic, while FLX is stable and persistent. Both are contaminants. Their environmental behaviour, however, influences their prioritization. IMP, owing to its transient yet significant toxicity, should be prioritized for

monitoring over intervention, whereas FLX should be prioritized for treatment. Their physicochemical properties and behaviour also define treatment strategy selection, as one treatment does not fit all the contaminants. Therefore, intervention approaches should shift towards targeted removal strategies.

10.3 Limitations of the study

While the present work demonstrated the promising performance of the CuO-BC-UVC system for effective and rapid degradation of FLX, multiple constraints need to be recognized. These limitations associated with experimental conditions, toxicity assessment, and large-scale applicability provide important directions for future research.

1. **Experimental and Concentration-related constraints**: To begin with, the experiments were conducted (i) at high FLX concentrations, and (ii) in batches in a controlled lab environment, which does not reflect the continuity and spatial variability of real systems. Higher concentrations were necessary to ensure reliable kinetic interpretation and mechanistic exploration of contributing factors- adsorption, photolysis, and photocatalysis. At lower concentrations, rapid adsorption dominated the removal process, limiting accurate evaluation of these contributions. Therefore, future studies should assess system performance at environmentally relevant concentrations under dynamic wastewater conditions in continuous flow systems.
2. **Toxicity assessment of transformation products (TPs):** The ecotoxicity assessment of the TPs was performed using an in-silico prediction model, ECOSAR, by USEPA. While computational tools provide useful preliminary insights, they may not represent the complex biological response under real environmental conditions. Experimental validation of TPs using broader ecological models is therefore recommended.
3. **Scalability and Operational Limitations**: While the rapid degradation observed in batch conditions suggests strong potential for scale-up in continuous flow systems, factors such as reactor design, catalyst dose, flow rate, and UVC energy need to be optimized. In addition to operating parameters, continuous monitoring of copper leaching, the degree of mineralization, catalyst stability, and regeneration can become crucial in extended continuous-flow systems.

10.4 Future Recommendations

Based on the findings of this dissertation, the following recommendations are proposed to explore the feasibility, practicality, and scalability of the proposed treatment approach for FLX:

1. **Scale-up to continuous-flow systems**: The proposed CuO-BC-UVC photocatalytic system showed promising results for FLX degradation in batch mode; however, to evaluate its effectiveness at real wastewater conditions, scaling up to a continuous flow regime is necessary. To maximise surface-area-to-volume ratio and ensure maximum UV penetration, a flat plate photoreactor (FPPR) with a short optical path is suggested. The reactor can be designed with a flat quartz plate on its surface, featuring an immobilized catalyst bed to prevent leaching. The design of the FPPR can be scaled up by parallelization using scalable, modular stacking to cater to the size of the facility and treat varying influent loads. For a compact pilot-scale study, the following parameters are suggested to start with:

    - Light/Energy source: External UVC 254 nm behind quartz windows, or UV-LEDs installed symmetrically to ensure uniform irradiation
    - Flow and residence time: Total working volume of 10-20 L with residence time of about 30 s to 1 minute
    - Pollutant concentration: 1 and 5 mg/L FLX with immobilized catalyst layer (10-500 um)
    - UVC irradiation: 10-20 mW/cm^2
    - Reactor dimensions: 100 cm X 50 cm X 2 mm per channel (V = 1 L)
    - Sampling: Inlet, Outlet
    - Suggested placement: Tertiary treatment + disinfection
    - Performance indicators: Removal efficiency for FLX, Mineralization (TOC removal), catalysts stability and leaching, Cu leaching (mg/L), Fluoride ion concentration

    To reiterate, the optimization of parameters, such as catalyst dose and their ratio, UV dose, and flow rate, is deemed essential for larger-scale applications. In addition, continuous

monitoring of water quality parameters, such as pH (which influences adsorption and potential leaching of copper), fluoride ion concentration and total organic carbon (which indicates the degree of mineralization), is critical.

2. **Evaluation in real wastewater matrices**: The composition of wastewater can greatly influence the efficiency of the proposed treatment approach. To understand the effect of competing ions and organic matter, the performance of the catalytic systems needs to be assessed in real wastewater matrices.

3. **Long-term catalyst stability**: Investigation of the long-term stability, durability, and reusability of the CuO-BC catalyst is required to understand the environmental safety and sustainability of the treatment. Chances of leaching of copper, deposition of copper on biochar, and loss of adsorption potential of biochar must be investigated under long hours of continuous operation.

4. **Identification of TPs and experimental validation of their toxicity**: The present dissertation assessed the in-silico toxicity of TPs and predicted their ecotoxicity in comparison to the parent drug; however, experimental validation of the toxicity and persistence of TPs is necessary to evaluate the safety of the treatment. The models estimate the toxicity of a compound based on its physicochemical properties, which can over- or under-estimate their persistence and long-term risks. It is also important to consider the combined (both additive and synergistic) effects of the TPs, not in isolation, as accounted by these models.

5. **Extension to other fluorinated pharmaceuticals and PFAS**: The proposed photocatalytic system can be extended to other highly persistent and recalcitrant emerging contaminants, such as other fluorinated pharmaceuticals and PFAS, for their potential transformation and/or degradation.

In addition to these recommendations for improving the applicability and efficiency of the proposed degradation approach for FLX in the field, the following recommendations are proposed for contaminant management:

1. **Inclusion of metal interaction in environmental risk assessment**: The co-occurrence and interaction of metals can affect the physicochemical and biological properties of organic contaminants. Consequently, the role of metals in altering contaminant toxicity, mobility, and persistence should be evaluated and included while performing the risk assessment.
2. **Contaminant prioritization (stability v/s transformation)**: Consideration of chemical stability and natural transformation must be accounted for, instead of relying solely on contaminant toxicity and persistence. Contaminant toxicity, along with its stability, determines whether an invention is necessary. For labile compounds like IMP, monitoring should be prioritized, while FLX needs active and targeted removal approaches.
3. **Decision-based treatment strategies**: After establishing priority and risk, the decision for appropriate treatment of persistent, high-risk contaminants must be made to ensure mindful utilization of resources, while ensuring their rapid and targeted removal.

Chapter 11: Bibliography

(1) Ramirez-Mendoza, R. A.; Morales-Menendez, R.; Melchor-Martinez, E. M.; Iqbal, H. M. N.; Parra-Arroyo, L.; Vargas-Martínez, A.; Parra-Saldivar, R. Incorporating the Sustainable Development Goals in Engineering Education. *Int J Interact Des Manuf* **2020**, *14* (3), 739–745. https://doi.org/10.1007/s12008-020-00661-0.

(2) Castillo-Zacarías, C.; Barocio, M. E.; Hidalgo-Vázquez, E.; Sosa-Hernández, J. E.; Parra-Arroyo, L.; López-Pacheco, I. Y.; Barceló, D.; Iqbal, H. N. M.; Parra-Saldívar, R. Antidepressant Drugs as Emerging Contaminants: Occurrence in Urban and Non-Urban Waters and Analytical Methods for Their Detection. *Science of The Total Environment* **2021**, *757*, 143722. https://doi.org/10.1016/j.scitotenv.2020.143722.

(3) Canada, P. H. A. of. *Antimicrobial use: Seasonal update — Canada.ca*. https://health-infobase.canada.ca/carss/amu/results.html?ind=01 (accessed 2025-06-28).

(4) Public Health Agency of Canada. *Canadian Antimicrobial Resistance Surveillance System Report*; Canada.

(5) IQVIA Snapshot. *Trends in the Use of Antidepressants in Canada, 2019–2023*. https://www.iqvia.com/-/media/iqvia/pdfs/canada/fact-sheets/snapshot-antidepressants-2024-en.pdf (accessed 2025-10-04).

(6) García-García, M. L.; Tovilla-Zárate, C. A.; Villar-Soto, M.; Juárez-Rojop, I. E.; González-Castro, T. B.; Genis-Mendoza, A. D.; Ramos-Méndez, M. Á.; López-Nárvaez, M. L.; Saucedo-Osti, A. S.; Ruiz-Quiñones, J. A.; Martinez-Magaña, J. J. Fluoxetine Modulates the Pro-Inflammatory Process of IL-6, IL-1β and TNF-α Levels in Individuals with Depression: A Systematic Review and Meta-Analysis. *Psychiatry Research* **2022**, *307* (Complete). https://doi.org/10.1016/j.psychres.2021.114317.

(7) Pinto, B.; Correia, D.; Conde, T.; Faria, M.; Oliveira, M.; Domingues, M. do R.; Domingues, I. Impact of Chronic Fluoxetine Exposure on Zebrafish: From Fatty Acid Profile to Behaviour. *Chemosphere* **2024**, *357* (Complete). https://doi.org/10.1016/j.chemosphere.2024.142026.

(8) Deodhar, M.; Rihani, S. B. A.; Darakjian, L.; Turgeon, J.; Michaud, V. Assessing the Mechanism of Fluoxetine-Mediated CYP2D6 Inhibition. *Pharmaceutics* **2021**, *13* (2), 148. https://doi.org/10.3390/pharmaceutics13020148.

(9) Sari Erkan, H.; Kaska, D.; Kara, N.; Onkal Engin, G. Fluoxetine Removal by Anodic Oxidation Using Different Anode Materials and Graphite Cathode. *Environmental Technology* **2024**, *0* (0), 1–14. https://doi.org/10.1080/09593330.2024.2304660.

(10) Correia, D.; Domingues, I.; Faria, M.; Oliveira, M. Effects of Fluoxetine on Fish: What Do We Know and Where Should We Focus Our Efforts in the Future? *Science of The Total Environment* **2023**, *857*, 159486. https://doi.org/10.1016/j.scitotenv.2022.159486.

(11) Togunde, O. P.; Oakes, K. D.; Servos, M. R.; Pawliszyn, J. Determination of Pharmaceutical Residues in Fish Bile by Solid-Phase Microextraction Couple with Liquid Chromatography-Tandem Mass Spectrometry (LC/MS/MS). *Environ. Sci. Technol.* **2012**, *46* (10), 5302–5309. https://doi.org/10.1021/es203758n.

(12) Salahinejad, A.; Attaran, A.; Meuthen, D.; Chivers, D. P.; Niyogi, S. Proximate Causes and Ultimate Effects of Common Antidepressants, Fluoxetine and Venlafaxine, on Fish

Behaviour. *Science of The Total Environment* **2022**, *807*, 150846. https://doi.org/10.1016/j.scitotenv.2021.150846.

(13) Pan, C.; Yang, M.; Xu, H.; Xu, B.; Jiang, L.; Wu, M. Tissue Bioconcentration and Effects of Fluoxetine in Zebrafish (*Danio Rerio*) and Red Crucian Cap (*Carassius Auratus*) after Short-Term and Long-Term Exposure. *Chemosphere* **2018**, *205*, 8–14. https://doi.org/10.1016/j.chemosphere.2018.04.082.

(14) de Farias, N. O.; Oliveira, R.; Moretti, P. N. S.; e Pinto, J. M.; Oliveira, A. C.; Santos, V. L.; Rocha, P. S.; Andrade, T. S.; Grisolia, C. K. Fluoxetine Chronic Exposure Affects Growth, Behaviour and Tissue Structure of Zebrafish. *Comparative Biochemistry and Physiology Part C: Toxicology & Pharmacology* **2020**, *237*, 108836. https://doi.org/10.1016/j.cbpc.2020.108836.

(15) Eisenreich, B. R.; Greene, S.; Szalda-Petree, A. Of Fish and Mirrors: Fluoxetine Disrupts Aggression and Learning for Social Rewards. *Physiology & Behaviour* **2017**, *173*, 258–262. https://doi.org/10.1016/j.physbeh.2017.02.021.

(16) Pulicharla, R.; Das, R. K.; Brar, S. K.; Drogui, P.; Sarma, S. J.; Verma, M.; Surampalli, R. Y.; Valero, J. R. Toxicity of Chlortetracycline and Its Metal Complexes to Model Microorganisms in Wastewater Sludge. *Science of The Total Environment* **2015**, *532*, 669–675. https://doi.org/10.1016/j.scitotenv.2015.05.140.

(17) Cuprys, A.; Pulicharla, R.; Lecka, J.; Brar, S. K.; Drogui, P.; Surampalli, R. Y. Ciprofloxacin-Metal Complexes –Stability and Toxicity Tests in the Presence of Humic Substances. *Chemosphere* **2018**, *202*, 549–559. https://doi.org/10.1016/j.chemosphere.2018.03.117.

(18) Guerra, W.; Silva-Caldeira, P. P.; Terenzi, H.; Pereira-Maia, E. C. Impact of Metal Coordination on the Antibiotic and Non-Antibiotic Activities of Tetracycline-Based Drugs. *Coordination Chemistry Reviews* **2016**, *327–328*, 188–199. https://doi.org/10.1016/j.ccr.2016.04.009.

(19) Cuprys, A.; Pulicharla, R.; Brar, S. K.; Drogui, P.; Verma, M.; Surampalli, R. Y. Fluoroquinolones Metal Complexation and Its Environmental Impacts. *Coordination Chemistry Reviews* **2018**, *376*, 46–61. https://doi.org/10.1016/j.ccr.2018.05.019.

(20) Bilal, M.; Ashraf, S. S.; Barceló, D.; Iqbal, H. M. N. Biocatalytic Degradation/Redefining "Removal" Fate of Pharmaceutically Active Compounds and Antibiotics in the Aquatic Environment. *Science of The Total Environment* **2019**, *691*, 1190–1211. https://doi.org/10.1016/j.scitotenv.2019.07.224.

(21) Luo, Y.; Guo, W.; Ngo, H. H.; Nghiem, L. D.; Hai, F. I.; Zhang, J.; Liang, S.; Wang, X. C. A Review on the Occurrence of Micropollutants in the Aquatic Environment and Their Fate and Removal during Wastewater Treatment. *Science of The Total Environment* **2014**, *473–474*, 619–641. https://doi.org/10.1016/j.scitotenv.2013.12.065.

(22) Carlotti, B.; Cesaretti, A.; Elisei, F. Complexes of Tetracyclines with Divalent Metal Cations Investigated by Stationary and Femtosecond-Pulsed Techniques. *Physical Chemistry Chemical Physics* **2012**, *14* (2), 823–834. https://doi.org/10.1039/C1CP22703C.

(23) Kumar, M.; Kaur Sodhi, K.; Singh, P.; Kumar Agrawal, P.; Kumar Singh, D. Synthesis and Characterization of Antibiotic-Metal Complexes [FeCl3(L1)2H2O and Ni(NO3)2(L2)2H2O] and Enhanced Antibacterial Activity. *Environmental Nanotechnology, Monitoring & Management* **2019**, *11*, 100209. https://doi.org/10.1016/j.enmm.2019.100209.

(24) Chen, Y.; Li, H.; Wang, Z.; Tao, T.; Hu, C. Photoproducts of Tetracycline and Oxytetracycline Involving Self-Sensitized Oxidation in Aqueous Solutions: Effects of Ca2+ and Mg2+. *Journal of Environmental Sciences* **2011**, *23* (10), 1634–1639. https://doi.org/10.1016/S1001-0742(10)60625-0.
(25) Girardi, C.; Greve, J.; Lamshöft, M.; Fetzer, I.; Miltner, A.; Schäffer, A.; Kästner, M. Biodegradation of Ciprofloxacin in Water and Soil and Its Effects on the Microbial Communities. *Journal of Hazardous Materials* **2011**, *198*, 22–30. https://doi.org/10.1016/j.jhazmat.2011.10.004.
(26) Poole, K. At the Nexus of Antibiotics and Metals: The Impact of Cu and Zn on Antibiotic Activity and Resistance. *Trends in Microbiology* **2017**, *25* (10), 820–832. https://doi.org/10.1016/j.tim.2017.04.010.
(27) Khurana, P.; Pulicharla, R.; Kaur Brar, S. Antibiotic-Metal Complexes in Wastewaters: Fate and Treatment Trajectory. *Environment International* **2021**, *157*, 106863. https://doi.org/10.1016/j.envint.2021.106863.
(28) Psomas, G.; P. Kessissoglou, D. Quinolones and Non-Steroidal Anti-Inflammatory Drugs Interacting with Copper(Ii), Nickel(Ii), Cobalt(Ii) and Zinc(Ii): Structural Features, Biological Evaluation and Perspectives. *Dalton Transactions* **2013**, *42* (18), 6252–6276. https://doi.org/10.1039/C3DT50268F.
(29) Li, B.; Zhang, T. Biodegradation and Adsorption of Antibiotics in the Activated Sludge Process. *Environ. Sci. Technol.* **2010**, *44* (9), 3468–3473. https://doi.org/10.1021/es903490h.
(30) Gao, P.; He, S.; Huang, S.; Li, K.; Liu, Z.; Xue, G.; Sun, W. Impacts of Coexisting Antibiotics, Antibacterial Residues, and Heavy Metals on the Occurrence of Erythromycin Resistance Genes in Urban Wastewater. *Appl Microbiol Biotechnol* **2015**, *99* (9), 3971–3980. https://doi.org/10.1007/s00253-015-6404-9.
(31) Mao, D.; Yu, S.; Rysz, M.; Luo, Y.; Yang, F.; Li, F.; Hou, J.; Mu, Q.; Alvarez, P. J. J. Prevalence and Proliferation of Antibiotic Resistance Genes in Two Municipal Wastewater Treatment Plants. *Water Research* **2015**, *85*, 458–466. https://doi.org/10.1016/j.watres.2015.09.010.
(32) Ma, Y.; Zhou, Q.; Zhou, S.; Wang, W.; Jin, J.; Xie, J.; Li, A.; Shuang, C. A Bifunctional Adsorbent with High Surface Area and Cation Exchange Property for Synergistic Removal of Tetracycline and Cu2+. *Chemical Engineering Journal* **2014**, *258*, 26–33. https://doi.org/10.1016/j.cej.2014.07.096.
(33) Shao, Y.; Gao, Y.; Yue, Q.; Kong, W.; Gao, B.; Wang, W.; Jiang, W. Degradation of Chlortetracycline with Simultaneous Removal of Copper (II) from Aqueous Solution Using Wheat Straw-Supported Nanoscale Zero-Valent Iron. *Chemical Engineering Journal* **2020**, *379*, 122384. https://doi.org/10.1016/j.cej.2019.122384.
(34) Alekseev, V. G. Acid–Base Properties of Penicillins and Cephalosporins (a Review). *Pharm Chem J* **2010**, *44* (1), 14–24. https://doi.org/10.1007/s11094-010-0389-6.
(35) de Paula, F. C. S.; Carvalho, S.; Duarte, H. A.; Paniago, E. B.; Mangrich, A. S.; Pereira-Maia, E. C. A Physicochemical Study of the Tetracycline Coordination to Oxovanadium(IV). *Journal of Inorganic Biochemistry* **1999**, *76* (3), 221–230. https://doi.org/10.1016/S0162-0134(99)00130-0.
(36) Al-Khodir, F. A. I.; Refat, M. S. Synthesis, Spectroscopic, Thermal and Anticancer Studies of Metal-Antibiotic Chelations: Ca(II), Fe(III), Pd(II) and Au(III) Chloramphenicol

Complexes. *Journal of Molecular Structure* **2016**, *1119*, 157–166. https://doi.org/10.1016/j.molstruc.2016.04.069.
(37) Ames, B. D.; Lee, M.-Y.; Moody, C.; Zhang, W.; Tang, Y.; Tsai, S.-C. Structural and Biochemical Characterization of ZhuI Aromatase/Cyclase from the R1128 Polyketide Pathway. *Biochemistry* **2011**, *50* (39), 8392–8406. https://doi.org/10.1021/bi200593m.
(38) Siddappa, K.; Mane, S. B.; Manikprabhu, D. Spectral Characterization and 3D Molecular Modeling Studies of Metal Complexes Involving the O, N-Donor Environment of Quinazoline-4(3H)-One Schiff Base and Their Biological Studies. *The Scientific World Journal* **2014**, *2014*, e817365. https://doi.org/10.1155/2014/817365.
(39) Uivarosi, V. Metal Complexes of Quinolone Antibiotics and Their Applications: An Update. *Molecules* **2013**, *18* (9), 11153–11197. https://doi.org/10.3390/molecules180911153.
(40) Park, H. R.; Jeong, G. Y.; Lee, H. C.; Lee, J. G.; Baek, G. M. Ionization and Divalent Cation Complexation of Quinolone Antibiotics in Aqueous Solution. *Bulletin of the Korean Chemical Society* **2000**, *21* (9), 849–854. https://doi.org/10.5012/bkcs.2000.21.9.849.
(41) Chapman, D. Electronegativity and the Stability of Metal Complexes. *Nature* **1954**, *174* (4436), 887–888. https://doi.org/10.1038/174887a0.
(42) Irving, H.; Williams, R. J. P. Order of Stability of Metal Complexes. *Nature* **1948**, *162* (4123), 746–747. https://doi.org/10.1038/162746a0.
(43) Irving, H.; Williams, R. J. P. 637. The Stability of Transition-Metal Complexes. *J. Chem. Soc.* **1953**, No. 0, 3192–3210. https://doi.org/10.1039/JR9530003192.
(44) Ghandour, M. A.; Azab, H. A.; Hassan, A.; Ali, A. M. Potentiometric Studies on the Complexes of Tetracycline (TC) and Oxytetracyclin (OTC) with Some Metal Ions. *Monatsh Chem* **1992**, *123* (1), 51–58. https://doi.org/10.1007/BF01045296.
(45) Lipman, B.; Neu, H. C. Imipenem: A New Carbapenem Antibiotic. *Medical Clinics of North America* **1988**, *72* (3), 567–579. https://doi.org/10.1016/S0025-7125(16)30759-3.
(46) Ac, R.; Ej, G.; A, T. Two Decades of Imipenem Therapy. *The Journal of antimicrobial chemotherapy* **2006**, *58* (5). https://doi.org/10.1093/jac/dkl354.
(47) Lyon, J. A. Imipenem/Cilastatin: The First Carbapenem Antibiotic. *Drug Intell Clin Pharm* **1985**, *19* (12), 895–899.
(48) Buckley, M. M.; Brogden, R. N.; Barradell, L. B.; Goa, K. L. Imipenem/Cilastatin. *Drugs* **1992**, *44* (3), 408–444. https://doi.org/10.2165/00003495-199244030-00008.
(49) Scholar, E. Imipenem. In *xPharm: The Comprehensive Pharmacology Reference*; Enna, S. J., Bylund, D. B., Eds.; Elsevier: New York, 2007; pp 1–5. https://doi.org/10.1016/B978-008055232-3.61923-3.
(50) Zhanel, G. G.; Wiebe, R.; Dilay, L.; Thomson, K.; Rubinstein, E.; Hoban, D. J.; Noreddin, A. M.; Karlowsky, J. A. Comparative Review of the Carbapenems. *Drugs* **2007**, *67* (7), 1027–1052. https://doi.org/10.2165/00003495-200767070-00006.
(51) Cheng, S.-F.; Lee, Y.-C.; Kuo, C.-Y.; Wu, T.-N. A Case Study of Antibiotic Wastewater Treatment by Using a Membrane Biological Reactor System. *International Biodeterioration & Biodegradation* **2015**, *102*, 398–401. https://doi.org/10.1016/j.ibiod.2015.04.018.
(52) Szekeres, E.; Baricz, A.; Chiriac, C. M.; Farkas, A.; Opris, O.; Soran, M.-L.; Andrei, A.-S.; Rudi, K.; Balcázar, J. L.; Dragos, N.; Coman, C. Abundance of Antibiotics, Antibiotic Resistance Genes and Bacterial Community Composition in Wastewater Effluents from Different Romanian Hospitals. *Environmental Pollution* **2017**, *225*, 304–315. https://doi.org/10.1016/j.envpol.2017.01.054.

(53) Hrenovic, J.; Ivankovic, T.; Ivekovic, D.; Repec, S.; Stipanicev, D.; Ganjto, M. The Fate of Carbapenem-Resistant Bacteria in a Wastewater Treatment Plant. *Water Research* **2017**, *126*, 232–239. https://doi.org/10.1016/j.watres.2017.09.007.
(54) Shokoohi, R.; Dargahi, A.; Khamutian, R.; Vaziri, Y. Evaluation of the Efficiency of Wastewater Treatment Plants in the Removal of Common Antibiotics from Municipal Wastewater in Hamadan, Iran. *Avicenna J Environ Health Eng* **2017**, *4* (1), 10921–10921. https://doi.org/10.5812/ajehe.10921.
(55) Shokoohi, R.; Leili, M.; Dargahi, A.; Vaziri, Y.; Khamutian, R. Common Antibiotics in Wastewater of Sina and Besat Hospitals, Hamadan, Iran. *Archives of Hygiene Sciences* **2017**, *6* (2), 152–159. https://doi.org/10.29252/ArchHygSci.6.2.152.
(56) Kamatham, S.; Seeralan, M.; Sekar, U.; Kuppusamy, S. Development and Validation of UFLC-MS/MS Analytical Method for the Simultaneous Quantification of Antibiotic Residues in Surface Water, Groundwater, and Pharmaceutical Waste Water Samples from South India. *ACS Omega* **2024**, *9* (11), 12801–12809. https://doi.org/10.1021/acsomega.3c08566.
(57) Wilk, J.; Sowik, P.; Felis, E.; Harnisz, M.; Korzeniewska, E.; Bajkacz, S. Development SPE-LC-MS/MS Method for Determination of WHO AWaRe Reserve Antibiotics in Hospital Wastewater. *Sci Rep* **2025**, *15* (1), 22163. https://doi.org/10.1038/s41598-025-04951-z.
(58) Smith, G. B.; Dezeny, G. C.; Douglas, A. W. Stability and Kinetics of Degradation of Imipenem in Aqueous Solution. *JPharmSci* **1990**, *79* (8), 732–740. https://doi.org/10.1002/jps.2600790816.
(59) MENDEZ, R.; ALEMANY, T.; MARTIN-VILLACORTA, J. Catalytic Effect of Buffers on Degradation of Imipenem (N-Formimidoylthienamycin) in Aqueous Solution. *Chemical & pharmaceutical bulletin* **1991**, *39* (4), 831–835.
(60) Swanson, D. J.; DeAngelis, C.; Smith, I. L.; Schentag, J. J. Degradation Kinetics of Imipenem in Normal Saline and in Human Serum. *Antimicrob Agents Chemother* **1986**, *29* (5), 936–937. https://doi.org/10.1128/aac.29.5.936.
(61) Sornsuvit, C.; Wientong, P.; Uitrakul, S.; Okonogi, S.; Katip, W. Influence of Concentration and Temperature on Stability of Imipenem Focused on Solutions for Extended Infusion. *Dose-Response* **2021**, *19* (4), 15593258211059325. https://doi.org/10.1177/15593258211059325.
(62) de Souza Barbosa, F.; Capra Pezzi, L.; Tsao, M.; Franco de Oliveira, T.; Manoela Dias Macedo, S.; E.S. Schapoval, E.; S.L. Mendez, A. Stability and Degradation Products of Imipenem Applying High-Resolution Mass Spectrometry: An Analytical Study Focused on Solutions for Infusion. *Biomedical Chromatography* **2019**, *33* (4), e4471. https://doi.org/10.1002/bmc.4471.
(63) Zhang, M.; Liu, C.-F.; Chen, X.-Y.; Yang, L.-N.; Zhu, C.-M.; Teng, J.-H.; Wu, H.-X.; Zhang, F.-L. Effect of Oxygen and Water on the Stability of Imipenem and Cilastatin Sodium for Injection. *Pharmaceutical Fronts* **2022**, *04* (02), e78–e88. https://doi.org/10.1055/s-0042-1750043.
(64) Kuti, J. L.; Nicolau, D. P.; Walker, S. E.; Iazzetta, J.; Perks, W.; Law (Response), S. Stability of Ertapenem 100 Mg/mL at Room Temperature. *Canadian Journal of Hospital Pharmacy* **2016**, *69* (3). https://doi.org/10.4212/cjhp.v69i3.1566.

(65) Zając, M.; Cielecka-Piontek, J.; Jelińska, A. Stability of Ertapenem in Aqueous Solutions. *Journal of Pharmaceutical and Biomedical Analysis* **2007**, *43* (2), 445–449. https://doi.org/10.1016/j.jpba.2006.07.021.
(66) Keel, R. A.; Sutherland, C. A.; Crandon, J. L.; Nicolau, D. P. Stability of Doripenem, Imipenem and Meropenem at Elevated Room Temperatures. *International Journal of Antimicrobial Agents* **2011**, *37* (2), 184–185. https://doi.org/10.1016/j.ijantimicag.2010.06.043.
(67) Wei, Y.; Zhang, X.; Dang, L.; Wei, H. Solubility and Pseudopolymorphic Transitions in Mixed Solvent: Meropenem in Methanol–Water Solution. *Fluid Phase Equilibria* **2013**, *349*, 25–30. https://doi.org/10.1016/j.fluid.2013.03.028.
(68) de Souza Barbosa, F.; Cassol, J. P. E.; Batista, L. A. das C.; Cordeiro, E. W. F.; Santos, M. C.; Pohlmann, A. R.; Schapoval, E. E. S.; Garcia, C. V.; Mendez, A. S. L. Stability of Doripenem in Reconstituted Solution – Thermal and Oxidative Decomposition Kinetics and Degradation Products by LC–MS. *Biomedical Chromatography* **2017**, *31* (8), e3940. https://doi.org/10.1002/bmc.3940.
(69) Berthoin, K.; Le Duff, C. S.; Marchand-Brynaert, J.; Carryn, S.; Tulkens, P. M. Stability of Meropenem and Doripenem Solutions for Administration by Continuous Infusion. *Journal of Antimicrobial Chemotherapy* **2010**, *65* (5), 1073–1075. https://doi.org/10.1093/jac/dkq044.
(70) Godini, H.; Sheikhmohammadi, A.; Abbaspour, L.; Heydari, R.; Khorramabadi, G. S.; Sardar, M.; Mahmoudi, Z. Energy Consumption and Photochemical Degradation of Imipenem/Cilastatin Antibiotic by Process of UVC/ Fe2+/ H2O2 through Response Surface Methodology. *Optik* **2019**, *182*, 1194–1203. https://doi.org/10.1016/j.ijleo.2019.01.071.
(71) Furia, F.; Minella, M.; Gosetti, F.; Turci, F.; Sabatino, R.; Di Cesare, A.; Corno, G.; Vione, D. Elimination from Wastewater of Antibiotics Reserved for Hospital Settings, with a Fenton Process Based on Zero-Valent Iron. *Chemosphere* **2021**, *283*, 131170. https://doi.org/10.1016/j.chemosphere.2021.131170.
(72) Reina, A. C.; Martínez-Piernas, A. B.; Bertakis, Y.; Brebou, C.; Xekoukoulotakis, N. P.; Agüera, A.; Sánchez Pérez, J. A. Photochemical Degradation of the Carbapenem Antibiotics Imipenem and Meropenem in Aqueous Solutions under Solar Radiation. *Water Research* **2018**, *128*, 61–70. https://doi.org/10.1016/j.watres.2017.10.047.
(73) Cabrera-Reina, A.; Martínez-Piernas, A. B.; Bertakis, Y.; Xekoukoulotakis, N. P.; Agüera, A.; Sánchez Pérez, J. A. TiO2 Photocatalysis under Natural Solar Radiation for the Degradation of the Carbapenem Antibiotics Imipenem and Meropenem in Aqueous Solutions at Pilot Plant Scale. *Water Research* **2019**, *166*, 115037. https://doi.org/10.1016/j.watres.2019.115037.
(74) Ahmadmoazzam, M.; Akbari, H.; Adibzadeh, A.; Pourfadakari, S.; Akbari, H. Visible-Light-Driven TiO2@Fe2O3/Chitosan Nanocomposite with Promoted Photodegradation of Meropenem and Imipenem Antibiotics by Peroxymonosulfate. *Environmental Technology* **2024**, *45* (17), 3456–3467. https://doi.org/10.1080/09593330.2023.2218042.
(75) Kostyanev, T.; Vilken, T.; Lammens, C.; Timbermont, L.; van't Veen, A.; Goossens, H. Detection and Prevalence of Carbapenem-Resistant Gram-Negative Bacteria among European Laboratories in the COMBACTE Network: A COMBACTE LAB-Net Survey. *International Journal of Antimicrobial Agents* **2019**, *53* (3), 268–274. https://doi.org/10.1016/j.ijantimicag.2018.10.013.

(76) Logan, L. K.; Weinstein, R. A. The Epidemiology of Carbapenem-Resistant Enterobacteriaceae: The Impact and Evolution of a Global Menace. *The Journal of Infectious Diseases* **2017**, *215* (suppl_1), S28–S36. https://doi.org/10.1093/infdis/jiw282.
(77) Puicharla, R.; Mohapatra, D. P.; Brar, S. K.; Drogui, P.; Auger, S.; Surampalli, R. Y. A Persistent Antibiotic Partitioning and Co-Relation with Metals in Wastewater Treatment Plant—Chlortetracycline. *Journal of Environmental Chemical Engineering* **2014**, *2* (3), 1596–1603. https://doi.org/10.1016/j.jece.2014.06.001.
(78) Shamim, S.; Begum, I.; Gul, W.; Quds, T.; Imran, M.; Shah, E.; Jahan, N. Antibacterial, Antifungal and Enzymatic Activities of Azithromycin-Heavy Metal Complexes: Newly Synthesized and Characterized. *Pak J Pharm Sci* **2021**, *34* (3(Supplementary)), 1149–1156.
(79) Sultana, N. Synthesis Characterization and Antimicrobial Activities of Azithromycin Metal Complexes. *Modern Chemistry & Applications* **2014**, *02*. https://doi.org/10.4172/2329-6798.1000133.
(80) Alekseev, V. G. Metal Complexes of Penicillins and Cephalosporins (Review). *Pharm Chem J* **2012**, *45* (11), 679–697. https://doi.org/10.1007/s11094-012-0703-6.
(81) Al-Thubaiti, E. H.; El-Megharbel, S. M.; Albogami, B.; Hamza, R. Z. Synthesis, Spectroscopic, Chemical Characterizations, Anticancer Capacities against HepG-2, Antibacterial and Antioxidant Activities of Cefotaxime Metal Complexes with Ca(II), Cr(III), Zn(II), Cu(II) and Se(IV). *Antibiotics* **2022**, *11* (7), 967. https://doi.org/10.3390/antibiotics11070967.
(82) Anacona, J. R. Synthesis and Antibacterial Activity of Some Metal Complexes of Beta-Lactamic Antibiotics. *Journal of Coordination Chemistry* **2001**, *54* (3–4), 355–365. https://doi.org/10.1080/00958970108022648.
(83) Anacona, J. R.; Figueroa, E. M. Synthesis and Characterization of Metal Complexes with Penicillin. *Journal of Coordination Chemistry* **1999**, *48* (2), 181–189. https://doi.org/10.1080/00958979908027965.
(84) Möhler, J. S.; Kolmar, T.; Synnatschke, K.; Hergert, M.; Wilson, L. A.; Ramu, S.; Elliott, A. G.; Blaskovich, M. A. T.; Sidjabat, H. E.; Paterson, D. L.; Schenk, G.; Cooper, M. A.; Ziora, Z. M. Enhancement of Antibiotic-Activity through Complexation with Metal Ions - Combined ITC, NMR, Enzymatic and Biological Studies. *Journal of Inorganic Biochemistry* **2017**, *167*, 134–141. https://doi.org/10.1016/j.jinorgbio.2016.11.028.
(85) Zabiszak, M.; Frymark, J.; Ogawa, K.; Skrobańska, M.; Nowak, M.; Jastrzab, R.; Kaczmarek, M. T. Complexes of β-Lactam Antibiotics and Their Schiff-Base Derivatives as a Weapon in the Fight against Bacterial Resistance. *Coordination Chemistry Reviews* **2023**, *493*, 215326. https://doi.org/10.1016/j.ccr.2023.215326.
(86) Ratcliffe, R. W.; Wildonger, K. J.; Di Michele, L.; Douglas, A. W.; Hajdu, R.; Goegelman, R. T.; Springer, J. P.; Hirshfield, J. Studies on the Structures of Imipenem, Dehydropeptidase I-Hydrolyzed Imipenem, and Related Analogs. *J. Org. Chem.* **1989**, *54* (3), 653–660. https://doi.org/10.1021/jo00264a028.
(87) Awfa, D.; Ateia, M.; Fujii, M.; Yoshimura, C. Photocatalytic Degradation of Organic Micropollutants: Inhibition Mechanisms by Different Fractions of Natural Organic Matter. *Water Research* **2020**, *174*, 115643. https://doi.org/10.1016/j.watres.2020.115643.
(88) Li, J.; Zhang, X.; Fan, W.-Y.; Yao, M.-C.; Sheng, G.-P. Dissolved Organic Matter Dominating the Photodegradation of Free DNA Bases in Aquatic Environments. *Water Research* **2020**, *179*, 115885. https://doi.org/10.1016/j.watres.2020.115885.

(89) Sunday, M. O.; Takeda, K.; Sakugawa, H. Singlet Oxygen Photogeneration in Coastal Seawater: Prospect of Large-Scale Modeling in Seawater Surface and Its Environmental Significance. *Environ. Sci. Technol.* **2020**, *54* (10), 6125–6133. https://doi.org/10.1021/acs.est.0c00463.

(90) Ahmed, M. B.; Zhou, J. L.; Ngo, H. H.; Guo, W.; Thomaidis, N. S.; Xu, J. Progress in the Biological and Chemical Treatment Technologies for Emerging Contaminant Removal from Wastewater: A Critical Review. *Journal of Hazardous Materials* **2017**, *323*, 274–298. https://doi.org/10.1016/j.jhazmat.2016.04.045.

(91) Richardson, S. D.; Ternes, T. A. Water Analysis: Emerging Contaminants and Current Issues. *Anal. Chem.* **2018**, *90* (1), 398–428. https://doi.org/10.1021/acs.analchem.7b04577.

(92) Di Cesare, A.; Fontaneto, D.; Doppelbauer, J.; Corno, G. Fitness and Recovery of Bacterial Communities and Antibiotic Resistance Genes in Urban Wastewaters Exposed to Classical Disinfection Treatments. *Environ. Sci. Technol.* **2016**, *50* (18), 10153–10161. https://doi.org/10.1021/acs.est.6b02268.

(93) Khurana, P.; Pulicharla, R.; Brar, S. K. Imipenem-Metal Complexes: Computational Analysis and Toxicity Studies with Wastewater Model Microorganisms. *Environmental Research* **2023**, 117275. https://doi.org/10.1016/j.envres.2023.117275.

(94) Pulicharla, R.; Brar, S. K.; Rouissi, T.; Auger, S.; Drogui, P.; Verma, M.; Surampalli, R. Y. Degradation of Chlortetracycline in Wastewater Sludge by Ultrasonication, Fenton Oxidation, and Ferro-Sonication. *Ultrasonics Sonochemistry* **2017**, *34*, 332–342. https://doi.org/10.1016/j.ultsonch.2016.05.042.

(95) Simonsen, M. E.; Muff, J.; Bennedsen, L. R.; Kowalski, K. P.; Søgaard, E. G. Photocatalytic Bleaching of P-Nitrosodimethylaniline and a Comparison to the Performance of Other AOP Technologies. *Journal of Photochemistry and Photobiology A: Chemistry* **2010**, *216* (2), 244–249. https://doi.org/10.1016/j.jphotochem.2010.07.008.

(96) Kraljić, I.; Trumbore, C. N. P-Nitrosodimethylaniline as an OH Radical Scavenger in Radiation Chemistry [1]. *J. Am. Chem. Soc.* **1965**, *87* (12), 2547–2550. https://doi.org/10.1021/ja01090a004.

(97) Khan, S. J.; Osborn, A. M.; Eswara, P. J. Effect of Sunlight on the Efficacy of Commercial Antibiotics Used in Agriculture. *Front Microbiol* **2021**, *12*, 645175. https://doi.org/10.3389/fmicb.2021.645175.

(98) Yu, Y.; Chen, L.; fang, Y.; Jia, X.; Chen, J. High Temperatures Can Effectively Degrade Residual Tetracyclines in Chicken Manure through Composting. *Journal of Hazardous Materials* **2019**, *380*, 120862. https://doi.org/10.1016/j.jhazmat.2019.120862.

(99) Yugatama, A.; Nurmalinda, R.; Rohmani, S.; Ermawati, D. E.; Prihapsara, F. Effect of Temperature and Length of Storage to Chloramphenicol Eye Drop's Concentration. *IOP Conf. Ser.: Mater. Sci. Eng.* **2019**, *578* (1), 012055. https://doi.org/10.1088/1757-899X/578/1/012055.

(100) Uyguner, C. S.; Bekbolet, M. Contribution of Metal Species to the Heterogeneous Photocatalytic Degradation of Natural Organic Matter. *International Journal of Photoenergy* **2007**, *2007* (1), 023156. https://doi.org/10.1155/2007/23156.

(101) Yekrangi, M.; Benvidi, A.; Jahanbani, S.; Zare, H. R.; Banaei, M. Determination of Lead Ions in Fish and Oyster Samples Using a Nano-Adsorbent of Functionalized Magnetic Graphene Oxide Nanosheets-Humic Acid and the Flame Atomic Absorption Technique. *Environ Monit Assess* **2021**, *193* (12), 825. https://doi.org/10.1007/s10661-021-09613-x.

(102) Niu, H.; Yang, H.; Tong, L.; Zhong, S.; Liu, Y. Spectral Study of Humic Substance Extract from Pressurized Oxidizing Slag of Carlin-Typed Gold Deposit. *J. Phys.: Conf. Ser.* **2019**, *1347* (1), 012027. https://doi.org/10.1088/1742-6596/1347/1/012027.
(103) Porras, J.; Bedoya, C.; Silva-Agredo, J.; Santamaría, A.; Fernández, J. J.; Torres-Palma, R. A. Role of Humic Substances in the Degradation Pathways and Residual Antibacterial Activity during the Photodecomposition of the Antibiotic Ciprofloxacin in Water. *Water Research* **2016**, *94*, 1–9. https://doi.org/10.1016/j.watres.2016.02.024.
(104) Vione, D.; Minella, M.; Maurino, V.; Minero, C. Indirect Photochemistry in Sunlit Surface Waters: Photoinduced Production of Reactive Transient Species. *Chemistry – A European Journal* **2014**, *20* (34), 10590–10606. https://doi.org/10.1002/chem.201400413.
(105) Kulikova, N. A.; Solovyova, A. A.; Perminova, I. V. Interaction of Antibiotics and Humic Substances: Environmental Consequences and Remediation Prospects. *Molecules* **2022**, *27* (22), 7754. https://doi.org/10.3390/molecules27227754.
(106) Wenk, J.; von Gunten, U.; Canonica, S. Effect of Dissolved Organic Matter on the Transformation of Contaminants Induced by Excited Triplet States and the Hydroxyl Radical. *Environ. Sci. Technol.* **2011**, *45* (4), 1334–1340. https://doi.org/10.1021/es102212t.
(107) de Melo, B. A. G.; Motta, F. L.; Santana, M. H. A. Humic Acids: Structural Properties and Multiple Functionalities for Novel Technological Developments. *Materials Science and Engineering: C* **2016**, *62*, 967–974. https://doi.org/10.1016/j.msec.2015.12.001.
(108) Shi, Y.; Dai, Y.; Liu, Z.; Nie, X.; Zhao, S.; Zhang, C.; Jia, H. Light-Induced Variation in Environmentally Persistent Free Radicals and the Generation of Reactive Radical Species in Humic Substances. *Front. Environ. Sci. Eng.* **2020**, *14* (6), 106. https://doi.org/10.1007/s11783-020-1285-2.
(109) Zhang, Y.; Yin, M.; Sun, X.; Zhao, J. Implication for Adsorption and Degradation of Dyes by Humic Acid: Light Driven of Environmentally Persistent Free Radicals to Activate Reactive Oxygen Species. *Bioresource Technology* **2020**, *307*, 123183. https://doi.org/10.1016/j.biortech.2020.123183.
(110) Gadhi, T. A.; Mahar, R. B.; Bonelli, B. Actual Mineralization versus Partial Degradation of Wastewater Contaminants. In *Nanomaterials for the Detection and Removal of Wastewater Pollutants*; Elsevier, 2020; pp 331–350. https://doi.org/10.1016/B978-0-12-818489-9.00012-8.
(111) Ramotowska, S.; Wysocka, M.; Brzeski, J.; Chylewska, A.; Makowski, M. A Comprehensive Approach to the Analysis of Antibiotic-Metal Complexes. *TrAC Trends in Analytical Chemistry* **2020**, *123*, 115771. https://doi.org/10.1016/j.trac.2019.115771.
(112) Goodell, B.; Amirbahman, A.; Jellison, J. Electrochemical Study of 2, 3. Dihydroxybenzoic Acid and Its Interaction with Cu (ll) and H 2 0 2 in Aqueous Solutions: Implications for Wood Decay. *Environmental science & technology* **2005**, 175–180.
(113) Jiang, C.; Garg, S.; Waite, T. D. Hydroquinone-Mediated Redox Cycling of Iron and Concomitant Oxidation of Hydroquinone in Oxic Waters under Acidic Conditions: Comparison with Iron–Natural Organic Matter Interactions. *Environ. Sci. Technol.* **2015**, *49* (24), 14076–14084. https://doi.org/10.1021/acs.est.5b03189.
(114) Li, Y.; Trush, M. A. Oxidation of Hydroquinone by Copper: Chemical Mechanism and Biological Effects. *Arch Biochem Biophys* **1993**, *300* (1), 346–355. https://doi.org/10.1006/abbi.1993.1047.

(115) Mandal, S.; Kazmi, N. H.; Sayre, L. M. Ligand Dependence in the Copper-Catalyzed Oxidation of Hydroquinones. *Archives of Biochemistry and Biophysics* **2005**, *435* (1), 21–31. https://doi.org/10.1016/j.abb.2004.11.025.
(116) Zhou, P.; Zhang, J.; Zhang, Y.; Liu, Y.; Liang, J.; Liu, B.; Zhang, W. Generation of Hydrogen Peroxide and Hydroxyl Radical Resulting from Oxygen-Dependent Oxidation of L-Ascorbic Acid *via* Copper Redox-Catalyzed Reactions. *RSC Adv.* **2016**, *6* (45), 38541–38547. https://doi.org/10.1039/C6RA02843H.
(117) Pham, V. L.; Kim, D.-G.; Ko, S.-O. Oxidative Degradation of the Antibiotic Oxytetracycline by Cu@Fe3O4 Core-Shell Nanoparticles. *Science of The Total Environment* **2018**, *631–632*, 608–618. https://doi.org/10.1016/j.scitotenv.2018.03.067.
(118) Huang, W.; Brigante, M.; Wu, F.; Mousty, C.; Hanna, K.; Mailhot, G. Assessment of the Fe(III)–EDDS Complex in Fenton-Like Processes: From the Radical Formation to the Degradation of Bisphenol A. *Environ. Sci. Technol.* **2013**, *47* (4), 1952–1959. https://doi.org/10.1021/es304502y.
(119) Baena-Nogueras, R. M.; González-Mazo, E.; Lara-Martín, P. A. Photolysis of Antibiotics under Simulated Sunlight Irradiation: Identification of Photoproducts by High-Resolution Mass Spectrometry. *Environ. Sci. Technol.* **2017**, *51* (6), 3148–3156. https://doi.org/10.1021/acs.est.6b03038.
(120) Bai, X.; Chen, W.; Wang, B.; Sun, T.; Wu, B.; Wang, Y. Photocatalytic Degradation of Some Typical Antibiotics: Recent Advances and Future Outlooks. *Int J Mol Sci* **2022**, *23* (15), 8130. https://doi.org/10.3390/ijms23158130.
(121) Eikemo, V.; Holmelid, B.; Sydnes, L. K.; Sydnes, M. O. Photodegradable Antimicrobial Agents: Synthesis and Mechanism of Degradation. *J. Org. Chem.* **2022**, *87* (12), 8034–8047. https://doi.org/10.1021/acs.joc.2c00681.
(122) Khan, S. J.; Osborn, A. M.; Eswara, P. J. Effect of Sunlight on the Efficacy of Commercial Antibiotics Used in Agriculture. *Front Microbiol* **2021**, *12*, 645175. https://doi.org/10.3389/fmicb.2021.645175.
(123) Fernandes, R.; Amador, P.; Prudêncio, C. β-Lactams: Chemical Structure, Mode of Action and Mechanisms of Resistance. *Reviews and Research in Medical Microbiology* **2013**, *24* (1), 7. https://doi.org/10.1097/MRM.0b013e3283587727.
(124) Lima, L. M.; Silva, B. N. M. da; Barbosa, G.; Barreiro, E. J. β-Lactam Antibiotics: An Overview from a Medicinal Chemistry Perspective. *European Journal of Medicinal Chemistry* **2020**, *208*, 112829. https://doi.org/10.1016/j.ejmech.2020.112829.
(125) Ory, J.; Bricheux, G.; Robin, F.; Togola, A.; Forestier, C.; Traore, O. Biofilms in Hospital Effluents as a Potential Crossroads for Carbapenemase-Encoding Strains. *Science of the Total Environment* **2019**, *657*, 7–15.
(126) Abou-Melha, K. S.; Al-Hazmi, G. A.; Althagafi, I.; Alharbi, A.; Shaaban, F.; El-Metwaly, N. M.; El-Bindary, A. A.; El-Bindary, M. A. Synthesis, Characterization, DFT Calculation, DNA Binding and Antimicrobial Activities of Metal Complexes of Dimedone Arylhydrazone. *Journal of Molecular Liquids* **2021**, *334*, 116498. https://doi.org/10.1016/j.molliq.2021.116498.
(127) Claudel, M.; Schwarte, J. V.; Fromm, K. M. New Antimicrobial Strategies Based on Metal Complexes. *Chemistry* **2020**, *2* (4), 849–899. https://doi.org/10.3390/chemistry2040056.
(128) El-Bindary, M. A.; El-Desouky, M. G.; El-Bindary, A. A. Metal–Organic Frameworks Encapsulated with an Anticancer Compound as Drug Delivery System: Synthesis, Characterization, Antioxidant, Anticancer, Antibacterial, and Molecular Docking

Investigation. *Applied Organometallic Chemistry* **2022**, *36* (5), e6660. https://doi.org/10.1002/aoc.6660.
(129) El-Gammal, O. A.; El-Bindary, A. A.; Sh. Mohamed, F.; Rezk, G. N.; El-Bindary, M. A. Synthesis, Characterization, Design, Molecular Docking, Anti COVID-19 Activity, DFT Calculations of Novel Schiff Base with Some Transition Metal Complexes. *Journal of Molecular Liquids* **2022**, *346*, 117850. https://doi.org/10.1016/j.molliq.2021.117850.
(130) El-Gammal, O. A.; Mohamed, F. Sh.; Rezk, G. N.; El-Bindary, A. A. Structural Characterization and Biological Activity of a New Metal Complexes Based of Schiff Base. *Journal of Molecular Liquids* **2021**, *330*, 115522. https://doi.org/10.1016/j.molliq.2021.115522.
(131) Frei, A. Metal Complexes, an Untapped Source of Antibiotic Potential? *Antibiotics (Basel)* **2020**, *9* (2), 90. https://doi.org/10.3390/antibiotics9020090.
(132) Frei, A.; Zuegg, J.; G. Elliott, A.; Baker, M.; Braese, S.; Brown, C.; Chen, F.; Dowson, C. G.; Dujardin, G.; Jung, N.; Paden King, A.; M. Mansour, A.; Massi, M.; Moat, J.; A. Mohamed, H.; K. Renfrew, A.; J. Rutledge, P.; J. Sadler, P.; H. Todd, M.; E. Willans, C.; J. Wilson, J.; A. Cooper, M.; T. Blaskovich, M. A. Metal Complexes as a Promising Source for New Antibiotics. *Chemical Science* **2020**, *11* (10), 2627–2639. https://doi.org/10.1039/C9SC06460E.
(133) Kiwaan, H. A.; El-Mowafy, A. S.; El-Bindary, A. A. Synthesis, Spectral Characterization, DNA Binding, Catalytic and in Vitro Cytotoxicity of Some Metal Complexes. *Journal of Molecular Liquids* **2021**, *326*, 115381. https://doi.org/10.1016/j.molliq.2021.115381.
(134) Graouer-Bacart, M.; Sayen, S.; Guillon, E. Adsorption of Enrofloxacin in Presence of Zn(II) on a Calcareous Soil. *Ecotoxicology and Environmental Safety* **2015**, *122*, 470–476. https://doi.org/10.1016/j.ecoenv.2015.09.019.
(135) Serna-Galvis, E. A.; Martínez-Mena, Y. L.; Porras, J.; Ávila-Torres, Y.; Silva-Agredo, J.; Torres-Palma, R. A. Understanding the Role of Complexation of Fluoroquinolone and β-Lactam Antibiotics with Iron (III) on the Photodegradation under Solar Light and UVC Light. *Water* **2021**, *13* (18), 2603. https://doi.org/10.3390/w13182603.
(136) Sultana, N.; Arayne, M. S.; Rizvi, S. B. S.; Haroon, U.; Mesaik, M. A. Synthesis, Spectroscopic, and Biological Evaluation of Some Levofloxacin Metal Complexes. *Med Chem Res* **2013**, *22* (3), 1371–1377. https://doi.org/10.1007/s00044-012-0132-9.
(137) Zhao, Y.; Geng, J.; Wang, X.; Gu, X.; Gao, S. Adsorption of Tetracycline onto Goethite in the Presence of Metal Cations and Humic Substances. *Journal of Colloid and Interface Science* **2011**, *361* (1), 247–251. https://doi.org/10.1016/j.jcis.2011.05.051.
(138) Cuprys, A.; Lecka, J.; Brar, S. K.; Rouissi, T.; Drogui, P. Influence of Metal Speciation in Wastewater Sludge on Antibiotic Distribution. *Journal of Hazardous, Toxic, and Radioactive Waste* **2021**, *25* (2), 04020078. https://doi.org/10.1061/(ASCE)HZ.2153-5515.0000592.
(139) Klamt, A.; Moya, C.; Palomar, J. A Comprehensive Comparison of the IEFPCM and SS(V)PE Continuum Solvation Methods with the COSMO Approach. *J. Chem. Theory Comput.* **2015**, *11* (9), 4220–4225. https://doi.org/10.1021/acs.jctc.5b00601.
(140) Prakash, S.; Banu, S.; Mishra, A. K. The Structure and Stability of Faecal Pigment-Zinc(II) Complexes. *Journal of Molecular Structure* **2021**, *1238*, 130440. https://doi.org/10.1016/j.molstruc.2021.130440.

(141) Shamuyarira, K. K.; Gumbo, J. R. Assessment of Heavy Metals in Municipal Sewage Sludge: A Case Study of Limpopo Province, South Africa. *Int J Environ Res Public Health* **2014**, *11* (3), 2569–2579. https://doi.org/10.3390/ijerph110302569.
(142) Morrison, G.; Fatoki, O. S.; Linder, S.; Lundehn, C. Determination of Heavy Metal Concentrations and Metal Fingerprints of Sewage Sludge from Eastern Cape Province, South Africa by Inductively Coupled Plasma – Mass Spectrometry (ICP-MS) and Laser Ablation-Inductively Coupled Plasma-Mass Spectrometry (LA-ICP-MS). *Water, Air, & Soil Pollution* **2004**, *152* (1), 111–127. https://doi.org/10.1023/B:WATE.0000015353.16815.b9.
(143) Agoro, M. A.; Adeniji, A. O.; Adefisoye, M. A.; Okoh, O. O. Heavy Metals in Wastewater and Sewage Sludge from Selected Municipal Treatment Plants in Eastern Cape Province, South Africa. *Water* **2020**, *12* (10), 2746. https://doi.org/10.3390/w12102746.
(144) Silhavy, T. J.; Kahne, D.; Walker, S. The Bacterial Cell Envelope. *Cold Spring Harb Perspect Biol* **2010**, *2* (5), a000414. https://doi.org/10.1101/cshperspect.a000414.
(145) Breijyeh, Z.; Jubeh, B.; Karaman, R. Resistance of Gram-Negative Bacteria to Current Antibacterial Agents and Approaches to Resolve It. *Molecules* **2020**, *25* (6), 1340. https://doi.org/10.3390/molecules25061340.
(146) Moore, C. M.; Helmann, J. D. Metal Ion Homeostasis in Bacillus Subtilis. *Current Opinion in Microbiology* **2005**, *8* (2), 188–195. https://doi.org/10.1016/j.mib.2005.02.007.
(147) Porcheron, G.; Garenaux, A.; Proulx, J.; Sabri, M.; Dozois, C. Iron, Copper, Zinc, and Manganese Transport and Regulation in Pathogenic Enterobacteria: Correlations between Strains, Site of Infection and the Relative Importance of the Different Metal Transport Systems for Virulence. *Frontiers in Cellular and Infection Microbiology* **2013**, *3*.
(148) Lusk, J. E.; Williams, R. J. P.; Kennedy, E. P. Magnesium and the Growth of Escherichia Coli. *Journal of Biological Chemistry* **1968**, *243* (10), 2618–2624. https://doi.org/10.1016/S0021-9258(18)93417-4.
(149) Martins, A.; Machado, L.; Costa, S.; Cerca, P.; Spengler, G.; Viveiros, M.; Amaral, L. Role of Calcium in the Efflux System of Escherichia Coli. *International Journal of Antimicrobial Agents* **2011**, *37* (5), 410–414. https://doi.org/10.1016/j.ijantimicag.2011.01.010.
(150) Beveridge, T. J.; Murray, R. G. Uptake and Retention of Metals by Cell Walls of Bacillus Subtilis. *J Bacteriol* **1976**, *127* (3), 1502–1518.
(151) Ehrström, M.; Eriksson, L. E. G.; Israelachvili, J.; Ehrenberg, A. The Effects of Some Cations and Anions on Spin Labeled Cytoplasmic Membranes of Bacillus Subtilis. *Biochemical and Biophysical Research Communications* **1973**, *55* (2), 396–402. https://doi.org/10.1016/0006-291X(73)91100-5.
(152) Macdonald, T. L.; Bruce Martin, R. Aluminum Ion in Biological Systems. *Trends in Biochemical Sciences* **1988**, *13* (1), 15–19. https://doi.org/10.1016/0968-0004(88)90012-6.
(153) Pi□a, R. G.; Cervantes, C. Microbial Interactions with Aluminium. *Biometals* **1996**, *9* (3), 311–316. https://doi.org/10.1007/BF00817932.
(154) Wong, D. T.; Perry, K. W.; Bymaster, F. P. The Discovery of Fluoxetine Hydrochloride (Prozac). *Nat Rev Drug Discov* **2005**, *4* (9), 764–774. https://doi.org/10.1038/nrd1821.
(155) Diaz-Camal, N.; Cardoso-Vera, J. D.; Islas-Flores, H.; Gómez-Oliván, L. M.; Mejía-García, A. Consumption and Ocurrence of Antidepressants (SSRIs) in Pre- and Post-COVID-19 Pandemic, Their Environmental Impact and Innovative Removal Methods: A Review. *Science of The Total Environment* **2022**, *829*, 154656. https://doi.org/10.1016/j.scitotenv.2022.154656.

(156) Chen, Y.; Kelton, C. M. L.; Jing, Y.; Guo, J. J.; Li, X.; Patel, N. C. Utilization, Price, and Spending Trends for Antidepressants in the US Medicaid Program. *Research in Social and Administrative Pharmacy* **2008**, *4* (3), 244–257. https://doi.org/10.1016/j.sapharm.2007.06.019.
(157) Daneshmand, R.; Acharya, S.; Zelek, B.; Cotterill, M.; Wood, B. Changes in Children and Youth's Mental Health Presentations during COVID-19: A Study of Primary Care Practices in Northern Ontario, Canada. *International Journal of Environmental Research and Public Health* **2023**, *20* (16), 6588. https://doi.org/10.3390/ijerph20166588.
(158) Khan, S.; Siddique, R.; Li, H.; Ali, A.; Shereen, M. A.; Bashir, N.; Xue, M. Impact of Coronavirus Outbreak on Psychological Health. *Journal of Global Health* **2020**, *10* (1), 010331. https://doi.org/10.7189/jogh.10.010331.
(159) Lewer, D.; O'Reilly, C.; Mojtabai, R.; Evans-Lacko, S. Antidepressant Use in 27 European Countries: Associations with Sociodemographic, Cultural and Economic Factors. *The British Journal of Psychiatry* **2015**, *207* (3), 221–226. https://doi.org/10.1192/bjp.bp.114.156786.
(160) Soleymani, F.; Taheri, F.; Roughead, E.; Nikfar, S.; Abdollahi, M. Pattern of Antidepressant Utilization and Cost in Iran from 2006 to 2013 in Comparison with Other Countries. *J Epidemiol Glob Health* **2018**, *8* (3), 213–219. https://doi.org/10.2991/j.jegh.2018.06.101.
(161) *OECD Data Explorer • Pharmaceutical consumption*. https://data-explorer.oecd.org/vis?lc=en&pg=0&fs[0]=Topic%2C1%7CHealth%23HEA%23%7CPharmaceutical%20market%23HEA_PHM%23&fc=Topic&bp=true&snb=4&vw=tb&df[ds]=dsDisseminateFinalDMZ&df[id]=HEALTH_PHMC%40DF_PHMC_CONSUM&df[ag]=OECD.ELS.HD&df[vs]=1.1&dq=....N06A&pd=2010%2C&to[TIME_PERIOD]=false (accessed 2025-08-31).
(162) BCPS, S. P. K., PharmD. *ClinCalc DrugStats 2021 Update – The Most Commonly Prescribed Drugs in the United States - ClinCalc.com*. https://clincalc.com/blog/2021/09/clincalc-drugstats-2021-update-the-most-commonly-prescribed-drugs-in-the-united-states/ (accessed 2024-10-10).
(163) Medstat.dk. *Sundhedsdatastyrelsen - Statistikker*. https://www.medstat.dk/da/viewDataTables/medicalTreatments/%7B%22year%22:[%222024%22,%222023%22,%222022%22,%222021%22,%222020%22],%22region%22:[%220%22],%22gender%22:[%22A%22],%22ageGroup%22:[%22A%22],%22searchVariable%22:[%22people_count_1000%22],%22errorMessages%22:[],%22treatmentGroup%22:[%22SSRI%22]%7D (accessed 2025-08-31).
(164) *Observatorio de uso de medicamentos*. Agencia Española de Medicamentos y Productos Sanitarios. https://www.aemps.gob.es/medicamentos-de-uso-humano/observatorio-de-uso-de-medicamentos/?lang=en (accessed 2025-08-31).
(165) Evans, S. E.; Davies, P.; Lubben, A.; Kasprzyk-Hordern, B. Determination of Chiral Pharmaceuticals and Illicit Drugs in Wastewater and Sludge Using Microwave Assisted Extraction, Solid-Phase Extraction and Chiral Liquid Chromatography Coupled with Tandem Mass Spectrometry. *Analytica Chimica Acta* **2015**, *882*, 112–126. https://doi.org/10.1016/j.aca.2015.03.039.
(166) Paíga, P.; Correia, M.; Fernandes, M. J.; Silva, A.; Carvalho, M.; Vieira, J.; Jorge, S.; Silva, J. G.; Freire, C.; Delerue-Matos, C. Assessment of 83 Pharmaceuticals in WWTP Influent and Effluent Samples by UHPLC-MS/MS: Hourly Variation. *Science of The Total Environment* **2019**, *648*, 582–600. https://doi.org/10.1016/j.scitotenv.2018.08.129.

(167) Vaudreuil, M.-A.; Vo Duy, S.; Munoz, G.; Sauvé, S. Pharmaceutical Pollution of Hospital Effluents and Municipal Wastewaters of Eastern Canada. *Science of The Total Environment* **2022**, *846*, 157353. https://doi.org/10.1016/j.scitotenv.2022.157353.
(168) Boogaerts, T.; Degreef, M.; Covaci, A.; van Nuijs, A. L. N. Development and Validation of an Analytical Procedure to Detect Spatio-Temporal Differences in Antidepressant Use through a Wastewater-Based Approach. *Talanta* **2019**, *200*, 340–349. https://doi.org/10.1016/j.talanta.2019.03.052.
(169) Costa Junior, I. L.; Machado, C. S.; Pletsch, A. L.; Torres, Y. R. Simultaneous HPLC-PDA Determination of Commonly Prescribed Antidepressants and Caffeine in Sludge from Sewage Treatment Plants and River Sediments in the Itaipu Reservoir Region, Paraná, Brazil. *International Journal of Environmental Analytical Chemistry* **2020**, *100* (9), 1004–1020. https://doi.org/10.1080/03067319.2019.1646738.
(170) Langford, K. H.; Reid, M.; Thomas, K. V. Multi-Residue Screening of Prioritised Human Pharmaceuticals, Illicit Drugs and Bactericides in Sediments and Sludge. *J. Environ. Monit.* **2011**, *13* (8), 2284–2291. https://doi.org/10.1039/C1EM10260E.
(171) Whitlock, S. E.; Pereira, M. G.; Shore, R. F.; Lane, J.; Arnold, K. E. Environmentally Relevant Exposure to an Antidepressant Alters Courtship Behaviours in a Songbird. *Chemosphere* **2018**, *211*, 17–24. https://doi.org/10.1016/j.chemosphere.2018.07.074.
(172) Liu, Y.; Lv, J.; Guo, C.; Jin, X.; Zuo, D.; Xu, J. Environmental Behaviour, Risks, and Management of Antidepressants in the Aquatic Environment. **2025**. https://doi.org/10.1039/D4EM00793J.
(173) Orozco-Hernández, J. M.; Gómez-Oliván, L. M.; Elizalde-Velázquez, G. A.; Rosales-Pérez, K. E.; Cardoso-Vera, J. D.; Heredia-García, G.; Islas-Flores, H.; García-Medina, S.; Galar-Martínez, M. Fluoxetine-Induced Neurotoxicity at Environmentally Relevant Concentrations in Adult Zebrafish *Danio Rerio*. *NeuroToxicology* **2022**, *90*, 121–129. https://doi.org/10.1016/j.neuro.2022.03.007.
(174) Yamindago, A.; Lee, N.; Lee, N.; Jo, Y.; Woo, S.; Yum, S. Fluoxetine in the Environment May Interfere with the Neurotransmission or Endocrine Systems of Aquatic Animals. *Ecotoxicology and Environmental Safety* **2021**, *227*, 112931. https://doi.org/10.1016/j.ecoenv.2021.112931.
(175) Ja, P.; Ds, R.; Pn, A.; Kf, H. Stability of Fluoxetine Hydrochloride in Fluoxetine Solution Diluted with Common Pharmaceutical Diluents. *American journal of hospital pharmacy* **1994**, *51* (10).
(176) Kwon, J.-W.; Armbrust, K. L. Laboratory Persistence and Fate of Fluoxetine in Aquatic Environments. *Environmental Toxicology and Chemistry* **2006**, *25* (10), 2561–2568. https://doi.org/10.1897/05-613R.1.
(177) Souza, L. P.; Carneiro, J. G. M.; Lastre-Acosta, A. M.; Ramos, B.; Teixeira, A. C. S. C. Environmental Persistence of the Antidepressant Fluoxetine and Its Pharmaceutical Alternative: Kinetics of Oxidation and Mathematical Simulations. *Water* **2022**, *14* (21), 3536. https://doi.org/10.3390/w14213536.
(178) Madureira, T. V.; Rocha, M. J.; Cass, Q. B.; Tiritan, M. E. Development and Optimization of a HPLC-DAD Method for the Determination of Diverse Pharmaceuticals in Estuarine Surface Waters. *Journal of Chromatographic Science* **2010**, *48* (3), 176–182. https://doi.org/10.1093/chromsci/48.3.176.

(179) Langford, K. H.; Reid, M.; Thomas, K. V. Multi-Residue Screening of Prioritised Human Pharmaceuticals, Illicit Drugs and Bactericides in Sediments and Sludge. *J. Environ. Monit.* **2011**, *13* (8), 2284–2291. https://doi.org/10.1039/C1EM10260E.
(180) Lajeunesse, A.; Smyth, S. A.; Barclay, K.; Sauvé, S.; Gagnon, C. Distribution of Antidepressant Residues in Wastewater and Biosolids Following Different Treatment Processes by Municipal Wastewater Treatment Plants in Canada. *Water Research* **2012**, *46* (17), 5600–5612. https://doi.org/10.1016/j.watres.2012.07.042.
(181) Verlicchi, P.; Al Aukidy, M.; Zambello, E. Occurrence of Pharmaceutical Compounds in Urban Wastewater: Removal, Mass Load and Environmental Risk after a Secondary Treatment—A Review. *Science of The Total Environment* **2012**, *429*, 123–155. https://doi.org/10.1016/j.scitotenv.2012.04.028.
(182) Baker, D. R.; Kasprzyk-Hordern, B. Spatial and Temporal Occurrence of Pharmaceuticals and Illicit Drugs in the Aqueous Environment and during Wastewater Treatment: New Developments. *Science of The Total Environment* **2013**, *454–455*, 442–456. https://doi.org/10.1016/j.scitotenv.2013.03.043.
(183) Petrie, B.; Proctor, K.; Youdan, J.; Barden, R.; Kasprzyk-Hordern, B. Critical Evaluation of Monitoring Strategy for the Multi-Residue Determination of 90 Chiral and Achiral Micropollutants in Effluent Wastewater. *Science of The Total Environment* **2017**, *579*, 569–578. https://doi.org/10.1016/j.scitotenv.2016.11.059.
(184) Afonso-Olivares, C.; Sosa-Ferrera, Z.; Santana-Rodríguez, J. J. Occurrence and Environmental Impact of Pharmaceutical Residues from Conventional and Natural Wastewater Treatment Plants in Gran Canaria (Spain). *Science of The Total Environment* **2017**, *599–600*, 934–943. https://doi.org/10.1016/j.scitotenv.2017.05.058.
(185) Ng, K. T.; Rapp-Wright, H.; Egli, M.; Hartmann, A.; Steele, J. C.; Sosa-Hernández, J. E.; Melchor-Martínez, E. M.; Jacobs, M.; White, B.; Regan, F.; Parra-Saldivar, R.; Couchman, L.; Halden, R. U.; Barron, L. P. High-Throughput Multi-Residue Quantification of Contaminants of Emerging Concern in Wastewaters Enabled Using Direct Injection Liquid Chromatography-Tandem Mass Spectrometry. *Journal of Hazardous Materials* **2020**, *398*, 122933. https://doi.org/10.1016/j.jhazmat.2020.122933.
(186) Sagristà, E.; Cortés, J. M.; Larsson, E.; Salvadó, V.; Hidalgo, M.; Jönsson, J. Å. Comparison of Two Extraction Methods for the Determination of Selective Serotonin Reuptake Inhibitors in Sewage Sludge by Hollow Fiber Liquid-Phase Microextraction. *Journal of Separation Science* **2012**, *35* (18), 2460–2468. https://doi.org/10.1002/jssc.201200257.
(187) Velázquez, Y. F.; Nacheva, P. M. Biodegradability of Fluoxetine, Mefenamic Acid, and Metoprolol Using Different Microbial Consortiums. *Environ Sci Pollut Res* **2017**, *24* (7), 6779–6793. https://doi.org/10.1007/s11356-017-8413-y.
(188) Palma, T.; Valentine, J.; Gomes, V.; Faleiro, M.; Costa, M. Batch Studies on the Biodegradation Potential of Paracetamol, Fluoxetine and 17α-Ethinylestradiol by the Micrococcus Yunnanensis Strain TJPT4 Recovered from Marine Organisms. *Water* **2022**, *14* (21), 3365. https://doi.org/10.3390/w14213365.
(189) Luz Palma, T.; Shylova, A.; Dias Carlier, J.; Costa, M. C. An Autochthonous Aerobic Bacterial Community and Its Cultivable Isolates Capable of Degrading Fluoxetine. *Journal of Chemical Technology & Biotechnology* **2021**, *96* (10), 2813–2826. https://doi.org/10.1002/jctb.6829.

(190) Palma, T. L.; Costa, M. C. Anaerobic Biodegradation of Fluoxetine Using a High-Performance Bacterial Community. *Anaerobe* **2021**, *68*, 102356. https://doi.org/10.1016/j.anaerobe.2021.102356.
(191) Wackett, L. P.; Robinson, S. L. A Prescription for Engineering PFAS Biodegradation. *Biochemical Journal* **2024**.
(192) Wackett, L. P. Nothing Lasts Forever: Understanding Microbial Biodegradation of Polyfluorinated Compounds and Perfluorinated Alkyl Substances. *Microbial Biotechnology* **2022**, *15* (3), 773–792. https://doi.org/10.1111/1751-7915.13928.
(193) Wackett, L. P. Confronting PFAS Persistence: Enzymes Catalyzing C–F Bond Cleavage. *Trends in Biochemical Sciences* **2025**, *50* (1), 71–83. https://doi.org/10.1016/j.tibs.2024.11.001.
(194) Marquis, R. E.; Clock, S. A.; Mota-Meira, M. Fluoride and Organic Weak Acids as Modulators of Microbial Physiology. *FEMS Microbiology Reviews* **2003**, *26* (5), 493–510. https://doi.org/10.1016/S0168-6445(02)00143-2.
(195) Andrés-Costa, M. J.; Proctor, K.; Sabatini, M. T.; Gee, A. P.; Lewis, S. E.; Pico, Y.; Kasprzyk-Hordern, B. Enantioselective Transformation of Fluoxetine in Water and Its Ecotoxicological Relevance. *Sci Rep* **2017**, *7*, 15777. https://doi.org/10.1038/s41598-017-15585-1.
(196) Cârcu-Dobrin, M.; Budău, M.; Hancu, G.; Gagyi, L.; Rusu, A.; Kelemen, H. Enantioselective Analysis of Fluoxetine in Pharmaceutical Formulations by Capillary Zone Electrophoresis. *Saudi Pharmaceutical Journal* **2017**, *25* (3), 397–403. https://doi.org/10.1016/j.jsps.2016.09.007.
(197) Moreira, I. S.; Ribeiro, A. R.; Afonso, C. M.; Tiritan, M. E.; Castro, P. M. L. Enantioselective Biodegradation of Fluoxetine by the Bacterial Strain *Labrys Portucalensis* F11. *Chemosphere* **2014**, *111*, 103–111. https://doi.org/10.1016/j.chemosphere.2014.03.022.
(198) Ternes, T.; Joss, A. *Human Pharmaceuticals, Hormones and Fragrances - The Challenge of Micropollutants in Urban Water Management*; IWA Publishing, 2006. https://doi.org/10.2166/9781780402468.
(199) Narayanan, J.; Hernández, J. G.; Padilla-Martínez, I. I.; Thangarasu, P.; Santos Garay, S. E.; Palacios Cabrera, C. B.; Santiago Cuevas, A. J. Geometry Influenced Adsorption of Fluoxetine over the Surface of RuFeO3 and CeFeO3 Nanoparticles: Kinetics and Thermodynamic Studies. *Ceramics International* **2021**, *47* (14), 20544–20561. https://doi.org/10.1016/j.ceramint.2021.04.064.
(200) Mekureyaw, M. F.; Junker, A. L.; Bai, L.; Zhang, Y.; Wei, Z.; Guo, Z. Laccase Based Per- and Polyfluoroalkyl Substances Degradation: Status and Future Perspectives. *Water Research* **2025**, *271*, 122888. https://doi.org/10.1016/j.watres.2024.122888.
(201) O'Hagan, D. Understanding Organofluorine Chemistry. An Introduction to the C–F Bond. https://doi.org/10.1039/B711844A.
(202) Lam, M. W.; Young, C. J.; Mabury, S. A. Aqueous Photochemical Reaction Kinetics and Transformations of Fluoxetine. *Environ. Sci. Technol.* **2005**, *39* (2), 513–522. https://doi.org/10.1021/es0494757.
(203) Risley, D. S.; Bopp, R. J. Fluoxetine. In *Analytical Profiles of Drug Substances*; Florey, K., Ed.; Academic Press, 1990; Vol. 19, pp 193–219. https://doi.org/10.1016/S0099-5428(08)60368-8.

(204) Souter, R. W.; Dinner, A. GLC Determination of Degradation of Two Related Amine Uptake Inhibitors. *Journal of Pharmaceutical Sciences* **1976**, *65* (3), 457–459. https://doi.org/10.1002/jps.2600650341.
(205) Rogers, H. R. Sources, Behaviour and Fate of Organic Contaminants during Sewage Treatment and in Sewage Sludges. *Science of The Total Environment* **1996**, *185* (1), 3–26. https://doi.org/10.1016/0048-9697(96)05039-5.
(206) Joss, A.; Keller, E.; Alder, A. C.; Göbel, A.; McArdell, C. S.; Ternes, T.; Siegrist, H. Removal of Pharmaceuticals and Fragrances in Biological Wastewater Treatment. *Water Research* **2005**, *39* (14), 3139–3152. https://doi.org/10.1016/j.watres.2005.05.031.
(207) Kibbey, T. C. G.; Paruchuri, R.; Sabatini, D. A.; Chen, L. Adsorption of Beta Blockers to Environmental Surfaces. *Environ. Sci. Technol.* **2007**, *41* (15), 5349–5356. https://doi.org/10.1021/es070152v.
(208) Monteiro, S. C.; Boxall, A. B. A. Occurrence and Fate of Human Pharmaceuticals in the Environment. *Rev Environ Contam Toxicol* **2010**, *202*, 53–154. https://doi.org/10.1007/978-1-4419-1157-5_2.
(209) OECD. *Test No. 315: Bioaccumulation in Sediment-Dwelling Benthic Oligochaetes*; Organisation for Economic Co-operation and Development: Paris, 2008.
(210) Yan, Z.; Lu, G.; Sun, H.; Bao, X.; Jiang, R.; Liu, J.; Ji, Y. Comparison of the Accumulation and Metabolite of Fluoxetine in Zebrafish Larva under Different Environmental Conditions with or without Carbon Nanotubes. *Ecotoxicology and Environmental Safety* **2019**, *172*, 240–245. https://doi.org/10.1016/j.ecoenv.2019.01.089.
(211) Redshaw, C. H.; Cooke, M. P.; Talbot, H. M.; McGrath, S.; Rowland, S. J. Low Biodegradability of Fluoxetine HCl, Diazepam and Their Human Metabolites in Sewage Sludge-Amended Soil. *J Soils Sediments* **2008**, *8* (4), 217–230. https://doi.org/10.1007/s11368-008-0024-2.
(212) Carter, L. J.; Ryan, J. J.; Boxall, A. B. A. Effects of Soil Properties on the Uptake of Pharmaceuticals into Earthworms. *Environmental Pollution* **2016**, *213*, 922–931. https://doi.org/10.1016/j.envpol.2016.03.044.
(213) Redshaw, C. H.; Wootton, V. G.; Rowland, S. J. Uptake of the Pharmaceutical Fluoxetine Hydrochloride from Growth Medium by *Brassicaceae*. *Phytochemistry* **2008**, *69* (13), 2510–2516. https://doi.org/10.1016/j.phytochem.2008.06.018.
(214) Bedner, M.; MacCrehan, W. A. Reactions of the Amine-Containing Drugs Fluoxetine and Metoprolol during Chlorination and Dechlorination Processes Used in Wastewater Treatment. *Chemosphere* **2006**, *65* (11), 2130–2137. https://doi.org/10.1016/j.chemosphere.2006.06.016.
(215) Nałęcz-Jawecki, G.; Wawryniuk, M.; Giebułtowicz, J.; Olkowski, A.; Drobniewska, A. Influence of Selected Antidepressants on the Ciliated Protozoan Spirostomum Ambiguum: Toxicity, Bioaccumulation, and Biotransformation Products. *Molecules* **2020**, *25* (7), 1476. https://doi.org/10.3390/molecules25071476.
(216) Serna-Galvis, E. A.; Silva-Agredo, J.; Giraldo-Aguirre, A. L.; Torres-Palma, R. A. Sonochemical Degradation of the Pharmaceutical Fluoxetine: Effect of Parameters, Organic and Inorganic Additives and Combination with a Biological System. *Science of The Total Environment* **2015**, *524–525*, 354–360. https://doi.org/10.1016/j.scitotenv.2015.04.053.
(217) Ding, J.; Zou, H.; Liu, Q.; Zhang, S.; Mamitiana Razanajatovo, R. Bioconcentration of the Antidepressant Fluoxetine and Its Effects on the Physiological and Biochemical Status in

Daphnia Magna. *Ecotoxicology and Environmental Safety* **2017**, *142*, 102–109. https://doi.org/10.1016/j.ecoenv.2017.03.042.
(218) Howard, P. H.; Muir, D. C. G. Identifying New Persistent and Bioaccumulative Organics Among Chemicals in Commerce II: Pharmaceuticals. *Environ. Sci. Technol.* **2011**, *45* (16), 6938–6946. https://doi.org/10.1021/es201196x.
(219) Oakes, K. D.; Coors, A.; Escher, B. I.; Fenner, K.; Garric, J.; Gust, M.; Knacker, T.; Küster, A.; Kussatz, C.; Metcalfe, C. D.; Monteiro, S.; Moon, T. W.; Mennigen, J. A.; Parrott, J.; Péry, A. R.; Ramil, M.; Roennefahrt, I.; Tarazona, J. V.; Sánchez-Argüello, P.; Ternes, T. A.; Trudeau, V. L.; Boucard, T.; Van Der Kraak, G. J.; Servos, M. R. Environmental Risk Assessment for the Serotonin Re-Uptake Inhibitor Fluoxetine: Case Study Using the European Risk Assessment Framework. *Integrated Environmental Assessment and Management* **2010**, *6* (S1), 524–539. https://doi.org/10.1002/ieam.77.
(220) Silva, L. J. G.; Martins, M. C.; Pereira, A. M. P. T.; Meisel, L. M.; Gonzalez-Rey, M.; Bebianno, M. J.; Lino, C. M.; Pena, A. Uptake, Accumulation and Metabolization of the Antidepressant Fluoxetine by *Mytilus Galloprovincialis*. *Environmental Pollution* **2016**, *213*, 432–437. https://doi.org/10.1016/j.envpol.2016.02.022.
(221) Atli, G.; Sevgiler, Y. Binary Effects of Fluoxetine and Zinc on the Biomarker Responses of the Non-Target Model Organism Daphnia Magna. *Environ Sci Pollut Res* **2024**, *31* (19), 27988–28006. https://doi.org/10.1007/s11356-024-32846-5.
(222) Karine de Sousa, A.; Rocha, J. E.; Gonçalves de Souza, T.; Sampaio de Freitas, T.; Ribeiro-Filho, J.; Melo Coutinho, H. D. New Roles of Fluoxetine in Pharmacology: Antibacterial Effect and Modulation of Antibiotic Activity. *Microbial Pathogenesis* **2018**, *123*, 368–371. https://doi.org/10.1016/j.micpath.2018.07.040.
(223) Ramírez-Morales, D.; Rojas-Jiménez, K.; Castro-Gutiérrez, V.; Rodríguez-Saravia, S.; Vaglio-Garro, A.; Araya-Valverde, E.; Rodríguez-Rodríguez, C. E. Ecotoxicological Effects of Ketoprofen and Fluoxetine and Their Mixture in an Aquatic Microcosm. *Aquatic Toxicology* **2024**, *271*, 106924. https://doi.org/10.1016/j.aquatox.2024.106924.
(224) Vasantha Raman, N.; Gebreyohanes Belay, B. M.; South, J.; Botha, T. L.; Pegg, J.; Khosa, D.; Mofu, L.; Walsh, G.; Jordaan, M. S.; Koelmans, A. A.; Teurlincx, S.; Helmsing, N. R.; de Jong, N.; van Donk, E.; Lürling, M.; Wepener, V.; Fernandes, T. V.; de Senerpont Domis, L. N. Effect of an Antidepressant on Aquatic Ecosystems in the Presence of Microplastics: A Mesocosm Study. *Environmental Pollution* **2024**, *357*, 124439. https://doi.org/10.1016/j.envpol.2024.124439.
(225) Xie, Z.; Li, P.; Lei, X.; Tang, Q.; Zhao, X.; Tang, J.; He, X. Unraveling the Combined Toxicity and Removal Mechanisms of Fluoxetine and Sertraline Co-Contaminants by the Freshwater Microalga *Chlorella Pyrenoidosa*. *Chemosphere* **2023**, *343*, 140217. https://doi.org/10.1016/j.chemosphere.2023.140217.
(226) Charles, E.; Hammadi, M.; Kischel, P.; Delcroix, V.; Demaurex, N.; Castelbout, C.; Vacher, A.-M.; Devin, A.; Ducret, T.; Nunes, P.; Vacher, P. The Antidepressant Fluoxetine Induces Necrosis by Energy Depletion and Mitochondrial Calcium Overload. *Oncotarget* **2016**, *8* (2), 3181–3196. https://doi.org/10.18632/oncotarget.13689.
(227) Kang, Y.; Xu, L.; Dong, J.; Huang, Y.; Yuan, X.; Li, R.; Chen, L.; Wang, Z.; Ji, X. Calcium-Based Nanotechnology for Cancer Therapy. *Coordination Chemistry Reviews* **2023**, *481*, 215050. https://doi.org/10.1016/j.ccr.2023.215050.
(228) Tang, K.-Y.; Lu, T.; Chang, C.-H.; Lo, Y.-K.; Cheng, J.-S.; Wang, J.-L.; Chang, H.-T.; Jan, C.-R. Effect of Fluoxetine on Intracellular Ca2+levels in Bladder Female Transitional

Carcinoma (BFTC) Cells. *Pharmacological Research* **2001**, *43* (5), 503–507. https://doi.org/10.1006/phrs.2001.0810.
(229) Vasconcelos, L. L.; Cabral, V. P. de F.; Ferreira, T. L.; Ferreira, T. L.; Coutinho, T. do N. P.; Barbosa, L. B.; Gomes, A. O. C. V.; Barroso, F. D. D.; Sá, L. G. do A. V.; Silva, C. R. da; Júnior, H. V. N.; Neto, J. B. de A. Antimicrobial Activity of Selective Serotonin Reuptake Inhibitors in Bacteria and Fungi: A Systematic Review. *Journal of Health & Biological Sciences* **2022**, *10* (1), 1–12. https://doi.org/10.12662/2317-3076jhbs.v10i1.4241.p1-12.2022.
(230) Orozco-Hernández, J. M.; Hernández-Varela, J. D.; Gómez-Oliván, L. M.; Chanona-Pérez, J. J.; Hernández-Díaz, M.; Juan-Reyes, N. S.; Rosales-Pérez, K. E.; Juan-Reyes, S. S. Toxic Interactions between Fluoxetine and Microplastics in Zebrafish Embryonic Development. *Science of The Total Environment* **2025**, *970*, 179040. https://doi.org/10.1016/j.scitotenv.2025.179040.
(231) Yan, Z.; Zhao, H.; Zhu, P.; Wang, Y.; Hou, J.; Lu, G.; He, C. Polystyrene Microplastics Alter the Trophic Transfer and Biotoxicity of Fluoxetine in an Aquatic Food Chain. *Journal of Hazardous Materials* **2024**, *470*, 134179. https://doi.org/10.1016/j.jhazmat.2024.134179.
(232) Gu, W.; Guo, D.; Zhang, L.; Xu, D.; Sun, S. The Synergistic Effect of Azoles and Fluoxetine against Resistant Candida Albicans Strains Is Attributed to Attenuating Fungal Virulence. *Antimicrob Agents Chemother* **2016**, *60* (10), 6179–6188. https://doi.org/10.1128/AAC.03046-15.
(233) Silva, B.; Martins, M.; Rosca, M.; Rocha, V.; Lago, A.; Neves, I. C.; Tavares, T. Waste-Based Biosorbents as Cost-Effective Alternatives to Commercial Adsorbents for the Retention of Fluoxetine from Water. *Separation and Purification Technology* **2020**, *235*, 116139. https://doi.org/10.1016/j.seppur.2019.116139.
(234) Nkana, G. R. N.; Lajeunesse, A.; Chabot, B.; Nguyen-Tri, P. Design of Porous Spherical Biomaterials from Carboxymethyl Chitosan for Removal of Fluoxetine in Aqueous Medium. *Journal of Environmental Chemical Engineering* **2024**, *12* (2), 112228. https://doi.org/10.1016/j.jece.2024.112228.
(235) Jaria, G.; Calisto, V.; Gil, M. V.; Otero, M.; Esteves, V. I. Removal of Fluoxetine from Water by Adsorbent Materials Produced from Paper Mill Sludge. *Journal of Colloid and Interface Science* **2015**, *448*, 32–40. https://doi.org/10.1016/j.jcis.2015.02.002.
(236) Farghal, H. H.; Nebsen, M.; El-Sayed, M. M. H. Eco-Friendly Biopolymer/Activated Charcoal Magnetic Nanocomposites with Enhanced Stability and Adsorption Properties for Water Treatment Applications. *J Polym Environ* **2023**, *31* (12), 5338–5354. https://doi.org/10.1007/s10924-023-02959-y.
(237) Camiré, A.; Espinasse, J.; Chabot, B.; Lajeunesse, A. Development of Electrospun Lignin Nanofibers for the Adsorption of Pharmaceutical Contaminants in Wastewater. *Environ Sci Pollut Res* **2020**, *27* (4), 3560–3573. https://doi.org/10.1007/s11356-018-3333-z.
(238) Fernandes, M. J.; Moreira, M. M.; Paíga, P.; Dias, D.; Bernardo, M.; Carvalho, M.; Lapa, N.; Fonseca, I.; Morais, S.; Figueiredo, S.; Delerue-Matos, C. Evaluation of the Adsorption Potential of Biochars Prepared from Forest and Agri-Food Wastes for the Removal of Fluoxetine. *Bioresource Technology* **2019**, *292*, 121973. https://doi.org/10.1016/j.biortech.2019.121973.
(239) Piccirillo, C.; Moreira, I. S.; Novais, R. M.; Fernandes, A. J. S.; Pullar, R. C.; Castro, P. M. L. Biphasic Apatite-Carbon Materials Derived from Pyrolysed Fish Bones for Effective

Adsorption of Persistent Pollutants and Heavy Metals. *Journal of Environmental Chemical Engineering* **2017**, *5* (5), 4884–4894. https://doi.org/10.1016/j.jece.2017.09.010.
(240) Mahgoub, S. M.; Essam, D.; Eldin, Z. E.; Moaty, S. A. A.; Shehata, M. R.; Farghali, A.; Abdalla, S. E. B.; Othman, S. I.; Allam, A. A.; El-Ela, F. I. A.; Mahmoud, R. Carbon Supported Ternary Layered Double Hydroxide Nanocomposite for Fluoxetine Removal and Subsequent Utilization of Spent Adsorbent as Antidepressant. *Sci Rep* **2024**, *14* (1), 3990. https://doi.org/10.1038/s41598-024-53781-y.
(241) Escudero-Curiel, S.; Penelas, U.; Sanromán, M. Á.; Pazos, M. An Approach towards Zero-Waste Wastewater Technology: Fluoxetine Adsorption on Biochar and Removal by the Sulfate Radical. *Chemosphere* **2021**, *268*, 129318. https://doi.org/10.1016/j.chemosphere.2020.129318.
(242) Escudero-Curiel, S.; Pazos, M.; Sanromán, A. Sustainable Regeneration of a Honeycomb Carbon Aerogel Used as a High-Capacity Adsorbent for Fluoxetine Removal. *Journal of Molecular Liquids* **2022**, *357*, 119079. https://doi.org/10.1016/j.molliq.2022.119079.
(243) Lago, A.; Silva, B.; Tavares, T. Biowaste Valorization on Pharmaceuticals and Pesticides Abatement in Aqueous Environments. *Sustainable Materials and Technologies* **2024**, *39*, e00792. https://doi.org/10.1016/j.susmat.2023.e00792.
(244) Escudero-Curiel, S.; Pazos, M.; Sanromán, A. Facile One-Step Synthesis of a Versatile Nitrogen-Doped Hydrochar from Olive Oil Production Waste, "Alperujo", for Removing Pharmaceuticals from Wastewater. *Environmental Pollution* **2023**, *330*, 121751. https://doi.org/10.1016/j.envpol.2023.121751.
(245) Dalbosco, T.; Cadore, J. S.; Pezzini, A.; Bandeira, N. M. G.; Giubel, G. O. M.; Lazzari, T.; Barbizan, L. D.; Novello, D. T.; Brião, V. B. Removal of Fluoxetine from Water by Nanofiltration and Reverse Osmosis. *Rev. ambiente água* **2023**, *18*, 1–10. https://doi.org/10.4136/ambi-agua.2885.
(246) Rad, L. R.; Irani, M.; Anbia, M. Membrane Filtration and Adsorption of Doxorubicin Hydrochloride and Fluoxetine Hydrochloride from Water Using Polysulfone/MIL-125-NH2 (Ti) Nanofibrous Membranes. *Journal of Molecular Liquids* **2024**, *408*, 125429. https://doi.org/10.1016/j.molliq.2024.125429.
(247) Aghaeinejad-Meybodi, A.; Ebadi, A.; Shafiei, S.; Khataee, A. R.; Rostampour, M. Modeling and Optimization of Antidepressant Drug Fluoxetine Removal in Aqueous Media by Ozone/H2O2 Process: Comparison of Central Composite Design and Artificial Neural Network Approaches. *Journal of the Taiwan Institute of Chemical Engineers* **2015**, *48*, 40–48. https://doi.org/10.1016/j.jtice.2014.10.022.
(248) Chedeville, O.; Di Giusto, A.; Delpeux, S.; Cagnon, B. Oxidation of Pharmaceutical Compounds by Ozonation and Ozone/Activated Carbon Coupling: A Kinetic Approach. *Desalination and Water Treatment* **2016**, *57* (40), 18956–18963. https://doi.org/10.1080/19443994.2015.1093552.
(249) Fotiou, D.; Lykos, C.; Konstantinou, I. Photocatalytic Removal of the Antidepressant Fluoxetine from Aqueous Media Using TiO2 P25 and G-C3N4 Catalysts. *Journal of Environmental Chemical Engineering* **2024**, *12* (1), 111677. https://doi.org/10.1016/j.jece.2023.111677.
(250) Méndez-Arriaga, F.; Otsu, T.; Oyama, T.; Gimenez, J.; Esplugas, S.; Hidaka, H.; Serpone, N. Photooxidation of the Antidepressant Drug Fluoxetine (Prozac®) in Aqueous Media by Hybrid Catalytic/Ozonation Processes. *Water Research* **2011**, *45* (9), 2782–2794. https://doi.org/10.1016/j.watres.2011.02.030.

(251) Perini, J. A. de L.; Silva, B. C. e.; Tonetti, A. L.; Nogueira, R. F. P. Photo-Fenton Degradation of the Pharmaceuticals Ciprofloxacin and Fluoxetine after Anaerobic Pre-Treatment of Hospital Effluent. *Environ Sci Pollut Res* **2017**, *24* (7), 6233–6240. https://doi.org/10.1007/s11356-016-7416-4.
(252) Liu, L.; Zhi, S.; Chen, R.; Yang, Y.; Luo, C.; Liang, P.; Liu, Y.; Zhu, G. Highly Selective and Rapid Sequential Degradation of Venlafaxine-Class Antidepressants Using a Novel BiOCl-Based Two-Dimensional Molecularly Imprinted Photocatalyst. *Separation and Purification Technology* **2025**, *362*, 131777. https://doi.org/10.1016/j.seppur.2025.131777.
(253) Bhat, A. P.; Mundhenke, T. F.; Whiting, Q. T.; Peterson, A. A.; Pomerantz, W. C. K.; Arnold, W. A. Tracking Fluorine during Aqueous Photolysis and Advanced UV Treatment of Fluorinated Phenols and Pharmaceuticals Using a Combined 19F-NMR, Chromatography, and Mass Spectrometry Approach. *ACS Environ. Au* **2022**, *2* (3), 242–252. https://doi.org/10.1021/acsenvironau.1c00057.
(254) Shao, H.; Wu, M.; Deng, F.; Xu, G.; Liu, N.; Li, X.; Tang, L. Electron Beam Irradiation Induced Degradation of Antidepressant Drug Fluoxetine in Water Matrices. *Chemosphere* **2018**, *190*, 184–190. https://doi.org/10.1016/j.chemosphere.2017.09.133.
(255) García-Galán, M. J.; Anfruns, A.; Gonzalez-Olmos, R.; Rodríguez-Mozaz, S.; Comas, J. UV/H2O2degradation of the Antidepressants Venlafaxine and *O*-Desmethylvenlafaxine: Elucidation of Their Transformation Pathway and Environmental Fate. *Journal of Hazardous Materials* **2016**, *311*, 70–80. https://doi.org/10.1016/j.jhazmat.2016.02.070.
(256) Chen, Y.; Zeng, B.; Lai, L.; Luo, L.; Xie, P.; Shao, Q.; Liu, Z.; Ma, J. Sulfite Activation Using FeO as a Source of Ferrous Ions for Fluoxetine Degradation: A Collaborated Experimental and DFT Study. *Chemical Engineering Journal* **2022**, *441*, 135960. https://doi.org/10.1016/j.cej.2022.135960.
(257) Zhao, Y.; Yu, G.; Chen, S.; Zhang, S.; Wang, B.; Huang, J.; Deng, S.; Wang, Y. Ozonation of Antidepressant Fluoxetine and Its Metabolite Product Norfluoxetine: Kinetics, Intermediates and Toxicity. *Chemical Engineering Journal* **2017**, *316*, 951–963. https://doi.org/10.1016/j.cej.2017.02.032.
(258) Yu, H.-W.; Anumol, T.; Park, M.; Pepper, I.; Scheideler, J.; Snyder, S. A. On-Line Sensor Monitoring for Chemical Contaminant Attenuation during UV/H2O2 Advanced Oxidation Process. *Water Research* **2015**, *81*, 250–260. https://doi.org/10.1016/j.watres.2015.05.064.
(259) Aghaeinejad-Meybodi, A.; Ebadi, A.; Shafiei, S.; Khataee, A.; Rostampour, M. Degradation of Antidepressant Drug Fluoxetine in Aqueous Media by Ozone/H2O2 System: Process Optimization Using Central Composite Design. *Environmental Technology* **2015**, *36* (12), 1477–1488. https://doi.org/10.1080/09593330.2014.994041.
(260) Sharma, S. K.; Kumar, A.; Sharma, G.; Naushad, Mu.; Vo, D.-V. N.; Alam, M.; Stadler, F. J. Fe3O4 Mediated Z-Scheme BiVO4/Cr2V4O13 Strongly Coupled Nano-Heterojunction for Rapid Degradation of Fluoxetine under Visible Light. *Materials Letters* **2020**, *281*, 128650. https://doi.org/10.1016/j.matlet.2020.128650.
(261) Aghaeinejad-Meybodi, A.; Ebadi, A.; Shafiei, S.; Khataee, A.; Kiadehi, A. D. Degradation of Fluoxetine Using Catalytic Ozonation in Aqueous Media in the Presence of Nano-γ-Alumina Catalyst: Experimental, Modeling and Optimization Study. *Separation and Purification Technology* **2019**, *211*, 551–563. https://doi.org/10.1016/j.seppur.2018.10.020.
(262) Pan, C.; Zhu, F.; Wu, M.; Jiang, L.; Zhao, X.; Yang, M. Degradation and Toxicity of the Antidepressant Fluoxetine in an Aqueous System by UV Irradiation. *Chemosphere* **2022**, *287*, 132434. https://doi.org/10.1016/j.chemosphere.2021.132434.

(263) Salazar, C.; Ridruejo, C.; Brillas, E.; Yáñez, J.; Mansilla, H. D.; Sirés, I. Abatement of the Fluorinated Antidepressant Fluoxetine (Prozac) and Its Reaction by-Products by Electrochemical Advanced Methods. *Applied Catalysis B: Environmental* **2017**, *203*, 189–198. https://doi.org/10.1016/j.apcatb.2016.10.026.
(264) Ye, Z.; Padilla, J. A.; Xuriguera, E.; Beltran, J. L.; Alcaide, F.; Brillas, E.; Sirés, I. A Highly Stable Metal–Organic Framework-Engineered FeS2/C Nanocatalyst for Heterogeneous Electro-Fenton Treatment: Validation in Wastewater at Mild pH. *Environ. Sci. Technol.* **2020**, *54* (7), 4664–4674. https://doi.org/10.1021/acs.est.9b07604.
(265) *Fluoxetine Wastewater Treatment System | Fluoxetine Removal Water*. https://arviatechnology.com/pollutants/fluoxetine-removal-from-water/ (accessed 2025-09-08).
(266) Gojkovic, Z.; Lindberg, R. H.; Tysklind, M.; Funk, C. Northern Green Algae Have the Capacity to Remove Active Pharmaceutical Ingredients. *Ecotoxicology and Environmental Safety* **2019**, *170*, 644–656. https://doi.org/10.1016/j.ecoenv.2018.12.032.
(267) Xie, P.; Chen, C.; Zhang, C.; Su, G.; Ren, N.; Ho, S.-H. Revealing the Role of Adsorption in Ciprofloxacin and Sulfadiazine Elimination Routes in Microalgae. *Water Research* **2020**, *172*, 115475. https://doi.org/10.1016/j.watres.2020.115475.
(268) Xie, Z.; Wang, X.; Gan, Y.; Cheng, H.; Fan, S.; Li, X.; Tang, J. Ecotoxicological Effects of the Antidepressant Fluoxetine and Its Removal by the Typical Freshwater Microalgae *Chlorella Pyrenoidosa*. *Ecotoxicology and Environmental Safety* **2022**, *244*, 114045. https://doi.org/10.1016/j.ecoenv.2022.114045.
(269) Xiong, Q.; Hu, L.-X.; Liu, Y.-S.; Zhao, J.-L.; He, L.-Y.; Ying, G.-G. Microalgae-Based Technology for Antibiotics Removal: From Mechanisms to Application of Innovational Hybrid Systems. *Environment International* **2021**, *155*, 106594. https://doi.org/10.1016/j.envint.2021.106594.
(270) Silva, A. D. M.; Fernandes, D. F.; Figueiredo, S. A.; Freitas, O. M.; Delerue-Matos, C. Fluoxetine and Nutrients Removal from Aqueous Solutions by Phycoremediation. *International Journal of Environmental Research and Public Health* **2022**, *19* (10), 6081. https://doi.org/10.3390/ijerph19106081.
(271) Khan, M. F.; Murphy, C. Bacterial Degradation of the Anti-Depressant Drug Fluoxetine Produces Trifluoroacetic Acid and Fluoride Ion. *Applied Microbiology and Biotechnology* **2021**, *105*. https://doi.org/10.1007/s00253-021-11675-3.
(272) Moreira, I. S.; Amorim, C. L.; Ribeiro, A. R.; Mesquita, R. B. R.; Rangel, A. O. S. S.; van Loosdrecht, M. C. M.; Tiritan, M. E.; Castro, P. M. L. Removal of Fluoxetine and Its Effects in the Performance of an Aerobic Granular Sludge Sequential Batch Reactor. *Journal of Hazardous Materials* **2015**, *287*, 93–101. https://doi.org/10.1016/j.jhazmat.2015.01.020.
(273) Mantovani, M.; Rossi, S.; Ficara, E.; Collina, E.; Marazzi, F.; Lasagni, M.; Mezzanotte, V. Removal of Pharmaceutical Compounds from the Liquid Phase of Anaerobic Sludge in a Pilot-Scale High-Rate Algae-Bacteria Pond. *Science of The Total Environment* **2024**, *908*, 167881. https://doi.org/10.1016/j.scitotenv.2023.167881.
(274) Silva, A. D. M.; Sousa, J.; Hultberg, M.; Figueiredo, S. A.; Freitas, O. M.; Delerue-Matos, C. Fluoxetine Removal from Aqueous Solutions Using a Lignocellulosic Substrate Colonized by the White-Rot Fungus Pleurotus Ostreatus. *International Journal of Environmental Research and Public Health* **2022**, *19* (5), 2672. https://doi.org/10.3390/ijerph19052672.

(275) Rodarte-Morales, A. I.; Feijoo, G.; Moreira, M. T.; Lema, J. M. Degradation of Selected Pharmaceutical and Personal Care Products (PPCPs) by White-Rot Fungi. *World J Microbiol Biotechnol* **2011**, *27* (8), 1839–1846. https://doi.org/10.1007/s11274-010-0642-x.
(276) Minguez, L.; Pedelucq, J.; Farcy, E.; Ballandonne, C.; Budzinski, H.; Halm-Lemeille, M.-P. Toxicities of 48 Pharmaceuticals and Their Freshwater and Marine Environmental Assessment in Northwestern France. *Environ Sci Pollut Res* **2016**, *23* (6), 4992–5001. https://doi.org/10.1007/s11356-014-3662-5.
(277) Alneyadi, A. H.; Rauf, M. A.; Ashraf, S. S. Oxidoreductases for the Remediation of Organic Pollutants in Water – a Critical Review. *Critical Reviews in Biotechnology* **2018**, *38* (7), 971–988. https://doi.org/10.1080/07388551.2017.1423275.
(278) Espina, G.; Atalah, J.; Blamey, J. M. Extremophilic Oxidoreductases for the Industry: Five Successful Examples With Promising Projections. *Front Bioeng Biotechnol* **2021**, *9*, 710035. https://doi.org/10.3389/fbioe.2021.710035.
(279) Torres, E.; Bustos-Jaimes, I.; Le Borgne, S. Potential Use of Oxidative Enzymes for the Detoxification of Organic Pollutants. *Applied Catalysis B: Environmental* **2003**, *46* (1), 1–15. https://doi.org/10.1016/S0926-3373(03)00228-5.
(280) Steffens, S. D.; Antell, E. H.; Cook, E. K.; Rao, G.; Britt, R. D.; Sedlak, D. L.; Alvarez-Cohen, L. An Artifact of Perfluoroalkyl Acid (PFAA) Removal Attributed to Sorption Processes in a Laccase Mediator System. *Environ. Sci. Technol. Lett.* **2023**, *10* (4), 337–342. https://doi.org/10.1021/acs.estlett.3c00173.
(281) Leung, S. C. E.; Shukla, P.; Chen, D.; Eftekhari, E.; An, H.; Zare, F.; Ghasemi, N.; Zhang, D.; Nguyen, N.-T.; Li, Q. Emerging Technologies for PFOS/PFOA Degradation and Removal: A Review. *Science of The Total Environment* **2022**, *827*, 153669. https://doi.org/10.1016/j.scitotenv.2022.153669.
(282) Verma, S.; Lee, T.; Sahle-Demessie, E.; Ateia, M.; Nadagouda, M. N. Recent Advances on PFAS Degradation *via* Thermal and Nonthermal Methods. *Chemical Engineering Journal Advances* **2023**, *13*, 100421. https://doi.org/10.1016/j.ceja.2022.100421.
(283) Brauer, R.; Alfageh, B.; Blais, J. E.; Chan, E. W.; Chui, C. S. L.; Hayes, J. F.; Man, K. K. C.; Lau, W. C. Y.; Yan, V. K. C.; Beykloo, M. Y.; Wang, Z.; Wei, L.; Wong, I. C. K. Psychotropic Medicine Consumption in 65 Countries and Regions, 2008-19: A Longitudinal Study. *Lancet Psychiatry* **2021**, *8* (12), 1071–1082. https://doi.org/10.1016/S2215-0366(21)00292-3.
(284) Orozco-Hernández, J. M.; Elizalde-Velázquez, G. A.; Gómez-Oliván, L. M.; Santamaría-González, G. O.; Rosales-Pérez, K. E.; García-Medina, S.; Galar-Martínez, M.; Juan-Reyes, N. S. Acute Exposure to Fluoxetine Leads to Oxidative Stress and Hematological Disorder in Danio Rerio Adults. *Science of The Total Environment* **2023**, *905* (Complete). https://doi.org/10.1016/j.scitotenv.2023.167391.
(285) Richmond, E. K.; Rosi, E. J.; Reisinger, A. J.; Hanrahan, B. R.; Thompson, R. M.; Grace, M. R. Influences of the Antidepressant Fluoxetine on Stream Ecosystem Function and Aquatic Insect Emergence at Environmentally Realistic Concentrations. *Journal of Freshwater Ecology* **2019**, *34* (1), 513–531. https://doi.org/10.1080/02705060.2019.1629546.
(286) Correia, D.; Domingues, I.; Faria, M.; Oliveira, M. Chronic Effects of Fluoxetine on Danio Rerio: A Biochemical and Behavioural Perspective. *Applied Sciences* **2022**, *12* (4), 2256. https://doi.org/10.3390/app12042256.

(287) OECD. *Pharmaceutical Residues in Freshwater: Hazards and Policy Responses*; Organisation for Economic Co-operation and Development: Paris, 2019.
(288) Puig-Gamero, M.; Esteban-Arranz, A.; Sanchez-Silva, L.; Sánchez, P. Obtaining Activated Biochar from Olive Stone Using a Bench Scale High-Pressure Thermobalance. *Journal of Environmental Chemical Engineering* **2021**, *9* (4). https://doi.org/10.1016/j.jece.2021.105374.
(289) Sajjadi, B.; Chen, W.-Y.; Egiebor, N. O. A Comprehensive Review on Physical Activation of Biochar for Energy and Environmental Applications. *Reviews in Chemical Engineering* **2019**, *35* (6), 735–776. https://doi.org/10.1515/revce-2017-0113.
(290) Mathew, J.; Bhardwaj, G.; Pulicharla, R.; Rezai, P.; Brar, S. K. Innovating Ferro-Sonication Approach for Extracting Microplastics from Wastewater. *Science of The Total Environment* **2024**, *951*, 175595. https://doi.org/10.1016/j.scitotenv.2024.175595.
(291) *Biochar for Environmental Management: Science and Technology*; Lehmann, J., Joseph, S., Eds.; Earthscan: London ; Sterling, VA, 2009.
(292) Hiew, B. Y. Z.; Lee, L. Y.; Lee, X. J.; Gan, S.; Thangalazhy-Gopakumar, S.; Lim, S. S.; Pan, G.-T.; Yang, T. C.-K. Adsorptive Removal of Diclofenac by Graphene Oxide: Optimization, Equilibrium, Kinetic and Thermodynamic Studies. *Journal of the Taiwan Institute of Chemical Engineers* **2019**, *98*, 150–162. https://doi.org/10.1016/j.jtice.2018.07.034.
(293) Puga, A.; Pazos, M.; Rosales, E.; Sanromán, M. A. Electro-Reversible Adsorption as a Versatile Tool for the Removal of Diclofenac from Wastewater. *Chemosphere* **2021**, *280*, 130778. https://doi.org/10.1016/j.chemosphere.2021.130778.
(294) Nassar, M. M. Intraparticle Diffusion of Basic Red and Basic Yellow Dyes on Palm Fruit Bunch. *Water Science and Technology* **1999**, *40* (7), 133–139. https://doi.org/10.1016/S0273-1223(99)00592-2.
(295) Guo, X.; Wang, J. Comparison of Linearization Methods for Modeling the Langmuir Adsorption Isotherm. *Journal of Molecular Liquids* **2019**, *296*, 111850. https://doi.org/10.1016/j.molliq.2019.111850.
(296) Moreno-castilla, C.; Carrasco-marín, F.; Maldonado-hódar, F. J.; Rivera-utrilla, J. Effects of Non-Oxidant and Oxidant Acid Treatments on the Surface Properties of an Activated Carbon with Very Low Ash Content. *Carbon* **1998**, *36* (1), 145–151. https://doi.org/10.1016/S0008-6223(97)00171-1.
(297) Chen, Q.; Liu, H.; Yang, Z.; Tan, D. Regeneration Performance of Spent Granular Activated Carbon for Tertiary Treatment of Dyeing Wastewater by Fenton Reagent and Hydrogen Peroxide. *J Mater Cycles Waste Manag* **2017**, *19* (1), 256–264. https://doi.org/10.1007/s10163-015-0410-y.
(298) Jeirani, Z.; Niu, C. H.; Soltan, J. Adsorption of Emerging Pollutants on Activated Carbon. *Reviews in Chemical Engineering* **2017**, *33* (5), 491–522. https://doi.org/10.1515/revce-2016-0027.
(299) Maia, L. S.; da Silva, A. I. C.; Carneiro, E. S.; Monticelli, F. M.; Pinhati, F. R.; Mulinari, D. R. Activated Carbon From Palm Fibres Used as an Adsorbent for Methylene Blue Removal. *J Polym Environ* **2021**, *29* (4), 1162–1175. https://doi.org/10.1007/s10924-020-01951-0.
(300) Brás, I.; Teixeira Lemos, L.; Alves, A.; Fernando R. Pereira, M. Application of Pine Bark as a Sorbent for Organic Pollutants in Effluents. *Management of Environmental Quality: An International Journal* **2004**, *15* (5), 491–501. https://doi.org/10.1108/14777830410553933.

(301) Aghababaei, A.; Borugadda, V. B.; Dalai, A.; Niu, C. H. An Investigation on Adsorption of Carbamazepine with Adsorbents Developed from Flax Shives: Kinetics, Mechanisms, and Desorption. *Chemical Engineering Research and Design* **2023**, *189*, 138–155. https://doi.org/10.1016/j.cherd.2022.11.008.
(302) Khurana, P.; Sran, S.; Kumar Das, R.; Sanchez-Silva, L.; Kaur Brar, S. High-Capacity Adsorption of Fluoxetine Using Olive-Stone Derived Activated Biochar: Insights into Efficiency and Mechanism. *RSC Adv.* **2025**, *15* (25), 20330–20340. https://doi.org/10.1039/D5RA01258A.
(303) Becerra, L. C. I. F.; Malafatti, J. O. D.; Paris, E. C.; Joya, M. R.; Moreira, A. J.; Reis, R. Y. N.; Lima, J. B.; Vargas, C. A. P.; Páez, A. M. R. Photocatalytic Degradation of Fluoxetine Mediated by CuO/CuWO4 Nanostructures. *Journal of the Taiwan Institute of Chemical Engineers* **2025**, *174*, 106215. https://doi.org/10.1016/j.jtice.2025.106215.
(304) Lalmalsawmdawngliani; Lalhriatpuia, C.; Ralte, L.; Dihingia, H.; Tiwari, D. Novel Biochar Supported Heterojunction of RH-BC (Fe0/Au0) Catalyst: A Highly Efficient Catalyst in the Degradation of Micro-Pollutants. *Journal of Environmental Chemical Engineering* **2023**, *11* (5), 110945. https://doi.org/10.1016/j.jece.2023.110945.
(305) Chen, X.; Zhang, M.; Qin, H.; Zhou, J.; Shen, Q.; Wang, K.; Chen, W.; Liu, M.; Li, N. Synergy Effect between Adsorption and Heterogeneous Photo-Fenton-like Catalysis on LaFeO3/Lignin-Biochar Composites for High Efficiency Degradation of Ofloxacin under Visible Light. *Separation and Purification Technology* **2022**, *280*, 119751. https://doi.org/10.1016/j.seppur.2021.119751.
(306) Khan, W. U.; Khan, S. U.; Khan, S. U.; Gul, A.; Zaman, H.; Khan, W. U.; Ali, N.; Aziz, A.; Khan, M. I.; Khan, D.; Gouda, M. M. Carboxymethyl-Cellulose/Starch/Copper-Oxide Nanocomposite Hydrogel Green Synthesis for Organic Pollutants Photocatalytic Degradation That Supports Health Applications. *Colloids and Surfaces A: Physicochemical and Engineering Aspects* **2025**, *718*, 136919. https://doi.org/10.1016/j.colsurfa.2025.136919.
(307) Klanovicz, N.; Khurana, P.; Ramos, B.; Treichel, H.; Brar, S. K.; Teixeira, A. C. S. C. Efficient Degradation of Carbamazepine in Continuous and Batch Modes by Laccase-Photo-Fenton-Intensified Hybrid Treatment. *ACS EST Water* **2025**, *5* (12), 7253–7266. https://doi.org/10.1021/acsestwater.5c00676.
(308) Pulicharla, R.; Zolfaghari, M.; Brar, S. K.; Drogui, P.; Auger, S.; Verma, M.; Surampalli, R. Y. Acute Impact of Chlortetracycline on Nitrifying and Denitrifying Processes. *Water Environment Research* **2018**, *90* (7), 604–614. https://doi.org/10.2175/106143017X15131012153095.
(309) Jeevarathinam, M.; Asharani, I. V. Synthesis of CuO, ZnO Nanoparticles, and CuO-ZnO Nanocomposite for Enhanced Photocatalytic Degradation of Rhodamine B: A Comparative Study. *Scientific Reports* **2024**, *14* (1), 9718. https://doi.org/10.1038/s41598-024-60008-7.
(310) Makuła, P.; Pacia, M.; Macyk, W. How To Correctly Determine the Band Gap Energy of Modified Semiconductor Photocatalysts Based on UV–Vis Spectra. *J. Phys. Chem. Lett.* **2018**, *9* (23), 6814–6817. https://doi.org/10.1021/acs.jpclett.8b02892.
(311) Korell, L.; Lauterbach, S.; Timm, J.; Wang, L.; Mellin, M.; Kundmann, A.; Wu, Q.; Tian, C.; Marschall, R.; Hofmann, J. P.; Osterloh, F. E.; Einert, M. On the Structural Evolution of Nanoporous Optically Transparent CuO Photocathodes upon Calcination for Photoelectrochemical Applications. https://doi.org/10.1039/D4NA00199K.

(312) Y, L.; L, W.; C, L.; J, M.; X, O.; L, W.; Y, C.; Y, L. Enhanced Cadmium Removal by Biochar and Iron Oxides Composite: Material Interactions and Pore Structure. *PubMed* **2023**.
(313) Liang, H.; Wang, W.; Liu, H.; Deng, X.; Zhang, D.; Zou, Y.; Ruan, X. Porous MgO-Modified Biochar Adsorbents Fabricated by the Activation of Mg(NO3)2 for Phosphate Removal: Synergistic Enhancement of Porosity and Active Sites. *Chemosphere* **2023**, *324*, 138320. https://doi.org/10.1016/j.chemosphere.2023.138320.
(314) Wei, Q.; Yi, B.; Hua, Z.; Sun, Z.; Guo, F. Biochar-Mediated Carbon Nitride and Covalent Organic Framework Photocatalyst for Enhanced Tetracycline Degradation. https://doi.org/10.1039/D5RA01986A.
(315) Guo, X.; Zhou, T.; Wang, G.; Liu, K.; Zhang, Y.; Wang, C.; Wu, J.; Liu, B.; Gao, H.; Hu, X.; Jiang, K.; Wu, D. Synergistic Enhancement of Biochar in TiO2/g-C3N4 Z-Scheme Heterojunction Photocatalysts: Mechanistic Insights into the Degradation Pathways of Sulfonamide Antibiotics. *Biochar* **2026**, *8* (1), 36. https://doi.org/10.1007/s42773-025-00552-1.
(316) Brame, J.; Long, M.; Li, Q.; Alvarez, P. Inhibitory Effect of Natural Organic Matter or Other Background Constituents on Photocatalytic Advanced Oxidation Processes: Mechanistic Model Development and Validation. *Water Research* **2015**, *84*, 362–371. https://doi.org/10.1016/j.watres.2015.07.044.
(317) Zhou, Y.; Wu, Y.; Lei, Y.; Pan, Y.; Cheng, S.; Ouyang, G.; Yang, X. Redox-Active Moieties in Dissolved Organic Matter Accelerate the Degradation of Nitroimidazoles in SO4•−-Based Oxidation. *Environ. Sci. Technol.* **2021**, *55* (21), 14844–14853. https://doi.org/10.1021/acs.est.1c04238.
(318) Wang, L.; Zhang, Q.; Chen, B.; Bu, Y.; Chen, Y.; Ma, J.; Rosario-Ortiz, F. L.; Zhu, R. Some Issues Limiting Photo(Cata)Lysis Application in Water Pollutant Control: A Critical Review from Chemistry Perspectives. *Water Research* **2020**, *174*, 115605. https://doi.org/10.1016/j.watres.2020.115605.
(319) Silva, V. H. O.; dos Santos Batista, A. P.; Silva Costa Teixeira, A. C.; Borrely, S. I. Degradation and Acute Toxicity Removal of the Antidepressant Fluoxetine (Prozac®) in Aqueous Systems by Electron Beam Irradiation. *Environmental Science and Pollution Research* **2016**, *23* (12), 11927–11936. https://doi.org/10.1007/s11356-016-6410-1.
(320) Fuller, R. W.; Beasley, C. M. Fluoxetine Mechanism of Action. *Journal of the American Academy of Child & Adolescent Psychiatry* **1991**, *30* (5), 849. https://doi.org/10.1016/S0890-8567(10)80032-2.
(321) Mandrioli, R.; Forti, G.; Raggi, M. Fluoxetine Metabolism and Pharmacological Interactions: The Role of Cytochrome P450. *CDM* **2006**, *7* (2), 127–133. https://doi.org/10.2174/138920006775541561.
(322) Deodhar, M.; Rihani, S. B. A.; Darakjian, L.; Turgeon, J.; Michaud, V. Assessing the Mechanism of Fluoxetine-Mediated CYP2D6 Inhibition. *Pharmaceutics* **2021**, *13* (2), 148. https://doi.org/10.3390/pharmaceutics13020148.
(323) Trindade, C. M. B.; Silva, M. K. L.; Cesarino, I. Copper Nanostructures Anchored on Renewable Carbon as Electrochemical Platform for the Detection of Dopamine, Fluoxetine and Escitalopram. *Sensors and Actuators Reports* **2022**, *4*, 100107. https://doi.org/10.1016/j.snr.2022.100107.

(324) Ammar, R. A.; Al-Qahtani, S. D. Potentiometric Studies of Ternary Complexes Involving Palladium(II) with Fluoxetine Drug and Some Bio-Ligands. *J Solution Chem* **2017**, *46* (4), 957–965. https://doi.org/10.1007/s10953-017-0611-1.
(325) Fleming, G. D.; Ortiz, Ú. M.; León, F. Z.; Koch, R. USING MOLECULAR ELECTROSTATIC POTENTIALS AND FRONTIER ORBITALS FOR THE SURFACE-ENHANCED RAMAN INTERPRETATION OF FLUOXETINE. *Journal of the Chilean Chemical Society* **2019**, *64* (4), 4627–4632.
(326) Lotfi, A.; Manzoori, J. L. Determination of Fluoxetine in Pharmaceutical and Biological Samples Based on the Silver Nanoparticle Enhanced Fluorescence of Fluoxetine–Terbium Complex. *Luminescence* **2016**, *31* (7), 1349–1357. https://doi.org/10.1002/bio.3114.
(327) Katrahalli, U.; Jaldappagari, S.; Kalanur, S. S. Probing the Binding of Fluoxetine Hydrochloride to Human Serum Albumin by Multispectroscopic Techniques. *Spectrochimica Acta Part A: Molecular and Biomolecular Spectroscopy* **2010**, *75* (1), 314–319. https://doi.org/10.1016/j.saa.2009.10.031.
(328) Khan, M. S.; Shahwan, M.; Shamsi, A.; Alhumaydhi, F. A.; Alsagaby, S. A.; Al Abdulmonem, W.; Abdullaev, B.; Yadav, D. K. Elucidating the Interactions of Fluoxetine with Human Transferrin Employing Spectroscopic, Calorimetric, and In Silico Approaches: Implications of a Potent Alzheimer's Drug. *ACS Omega* **2022**, *7* (10), 9015–9023. https://doi.org/10.1021/acsomega.2c00182.
(329) Shishkina, G. T.; Dygalo, N. N.; Yudina, A. M.; Kalinina, T. S.; Tolstikova, T. G.; Sorokina, I. V.; Kovalenko, I. L.; Anikina, L. V. The Effects of Fluoxetine and Its Complexes with Glycerrhizic Acid on Behaviour in Rats and Brain Monoamine Levels. *Neurosci Behav Physiol* **2006**, *36* (4), 329–333. https://doi.org/10.1007/s11055-006-0021-0.
(330) Gillman, G. P.; Sumpter, E. A. Modification to the Compulsive Exchange Method for Measuring Exchange Characteristics of Soils. *Soil Res.* **1986**, *24* (1), 61–66. https://doi.org/10.1071/sr9860061.
(331) Shen, Z.; Jin, F.; Wang, F.; McMillan, O.; Al-Tabbaa, A. Sorption of Lead by Salisbury Biochar Produced from British Broadleaf Hardwood. *Bioresource Technology* **2015**, *193*, 553–556. https://doi.org/10.1016/j.biortech.2015.06.111.
(332) Belhachemi, M.; Belala, Z.; Lahcene, D.; Addoun, F. Adsorption of Phenol and Dye from Aqueous Solution Using Chemically Modified Date Pits Activated Carbons. *Desalination and Water Treatment* **2009**, *7* (1), 182–190. https://doi.org/10.5004/dwt.2009.729.
(333) Ezzati, R. Derivation of Pseudo-First-Order, Pseudo-Second-Order and Modified Pseudo-First-Order Rate Equations from Langmuir and Freundlich Isotherms for Adsorption. *Chemical Engineering Journal* **2020**, *392*, 123705. https://doi.org/10.1016/j.cej.2019.123705.

Appendices

Appendix A: Supplementary information for Chapter 4

List of Tables:

A1	Rate constants for degradation of Imipenem (IMP= 25-250 mg/L) under different conditions of light and temperature

List of Figures:

A1	Spectral irradiance profile showing the distribution of irradiance ($\mu W/cm^2$) across wavelengths for the ambient light conditions used in the study
A2	Mass spectra for: (a and b) humic acid; and (c and d) Humic acid -Imipenem mixture.
A3	Overlapped chromatogram and mass spectrum for Imipenem (blue) and Imipenem-Al (III) solution (pink) (M: L = 2: 1)
A4	Mass spectrum of the identified Imipenem-Mg (II) complex $[Mg\ (IMP)_2]^{2+}$ (m/z 311.08595)
A5	Change in % peak area for m/z 300.1012 $[IMP\text{-}H]^+$ and m/z 316.0960 $[IMP\text{-}O\text{-}H]^+$
A6	Time-dependent mass spectra of IMP-Cu system (IMP= 33 μM; Cu(II)= 66 μM) at RT: 0.1-0.2 min
A7	Time-dependent mass spectra of IMP-Cu system (IMP= 33 μM; Cu(II)= 66 μM) at RT: 0.2-0.4 min
A8	Proposed pathway for bleaching of the dye and oxidation of Imipenem by copper redox coupling
A9	Mass spectra for: (a) Aqueous Imipenem solution at zero-hour, (b) Imipenem spiked in wastewater at zero hour, and (c) Imipenem spiked in wastewater after 5 hours of natural solar exposure

Table A1: Rate constants for degradation of Imipenem (IMP= 25-250 mg/L) under different conditions of light and temperature

Concentration (ppm)	Dark/RT	Light/RT	Light/Cold
25	7.14797E-4 ± 9.00343E-5	8.37505E-4 ± 8.39714E-5	4.62445E-4 ± 7.13623E-5
50	0.0014 ± 7.66232E-5	0.00316 ± 1.65134E-4	6.05345E-4 ± 6.04115E-5
100	0.00415 ± 8.93126E-5	0.014640413 ± 1.25867E-3	0.00229 ± 1.54225E-4
125	0.00341 ± 6.11294E-5	0.020449342 ± 1.66855E-3	0.00336 ± 7.53442E-5
150	0.00497 ± 1.0379E-4	0.024614287 ± 2.70341E-3	0.004532 ± 5.012536E-4
200	0.00763 ± 1.26764E-4	0.026207433 ± 3.15681E-3	0.00605 ± 2.48481E-4
250	0.00965 ± 2.93634E-4	0.025963957 ± 3.13374E-3	0.00735 ± 2.80363E-4

Zero order (k, ppm/h) First order (k, h^{-1}) **ppm= parts per million (mg/L); RT= Room temperature*

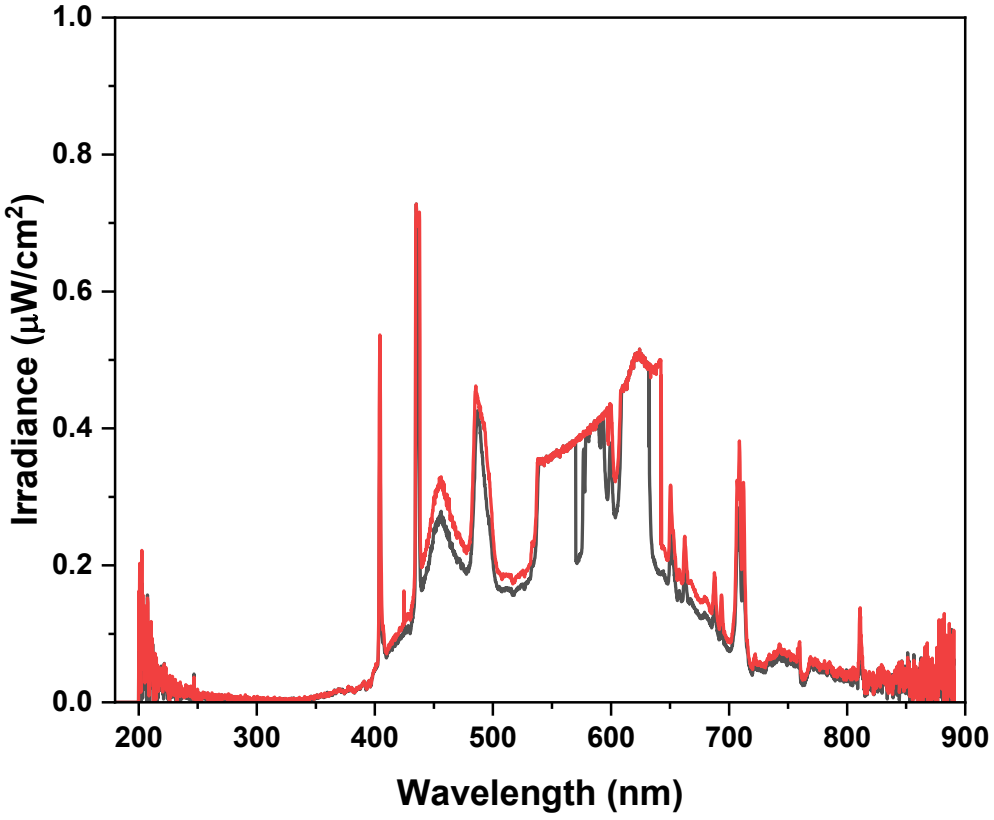

Figure A1: Spectral irradiance profile showing the distribution of irradiance (μW/cm^2) across wavelengths for the ambient light conditions used in the study. The dominant emissions between 400-700 nm confirm visible light conditions. For light protected samples, amber glass vials, which block UV light and visible light (blue and violet), was used.
(Two overlapping curves, red and black spectral profiles, represent the duplicate measurements)

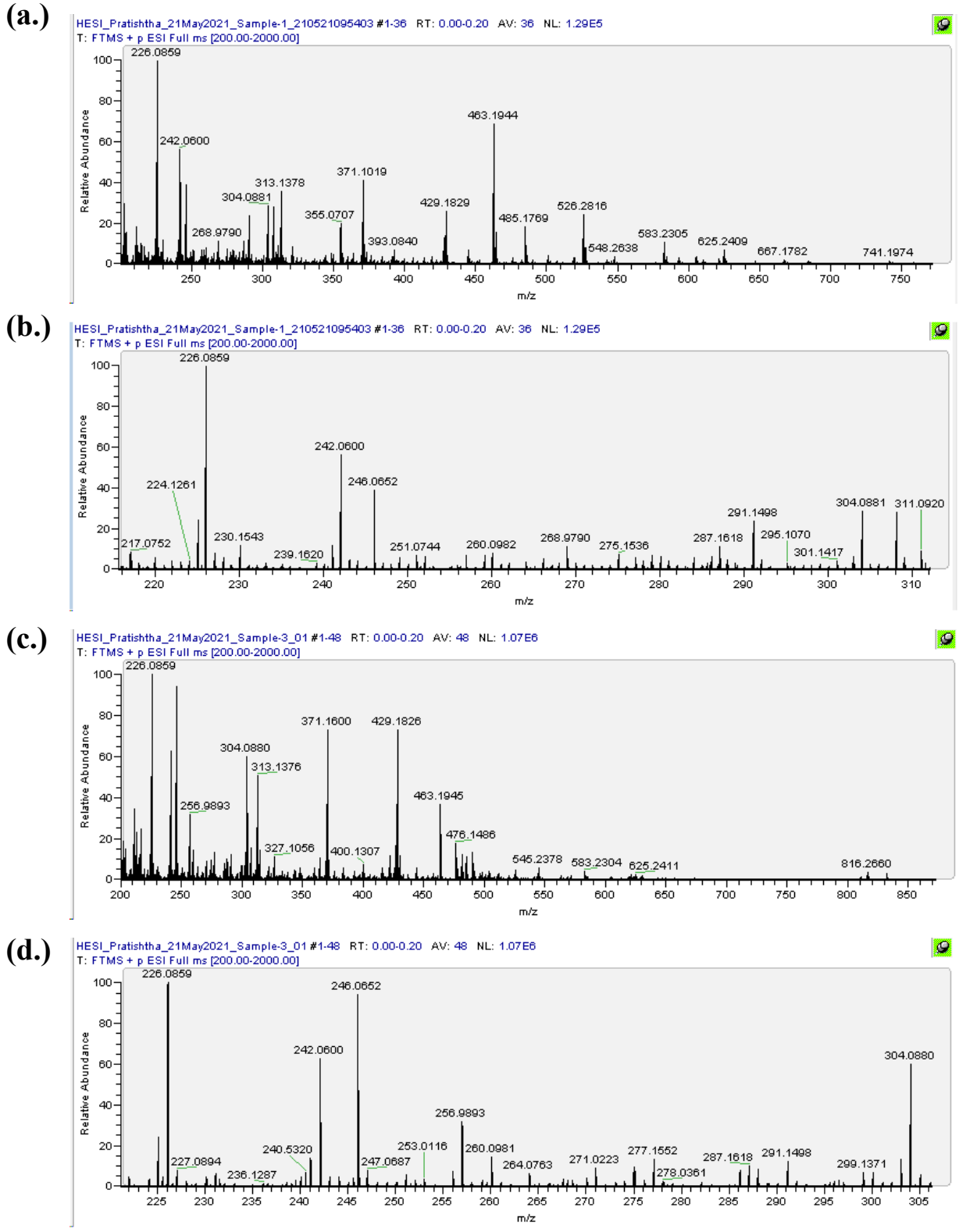

Figure A2: Mass spectra for: (a and b) humic acid; and (c and d) Humic acid-Imipenem mixture.

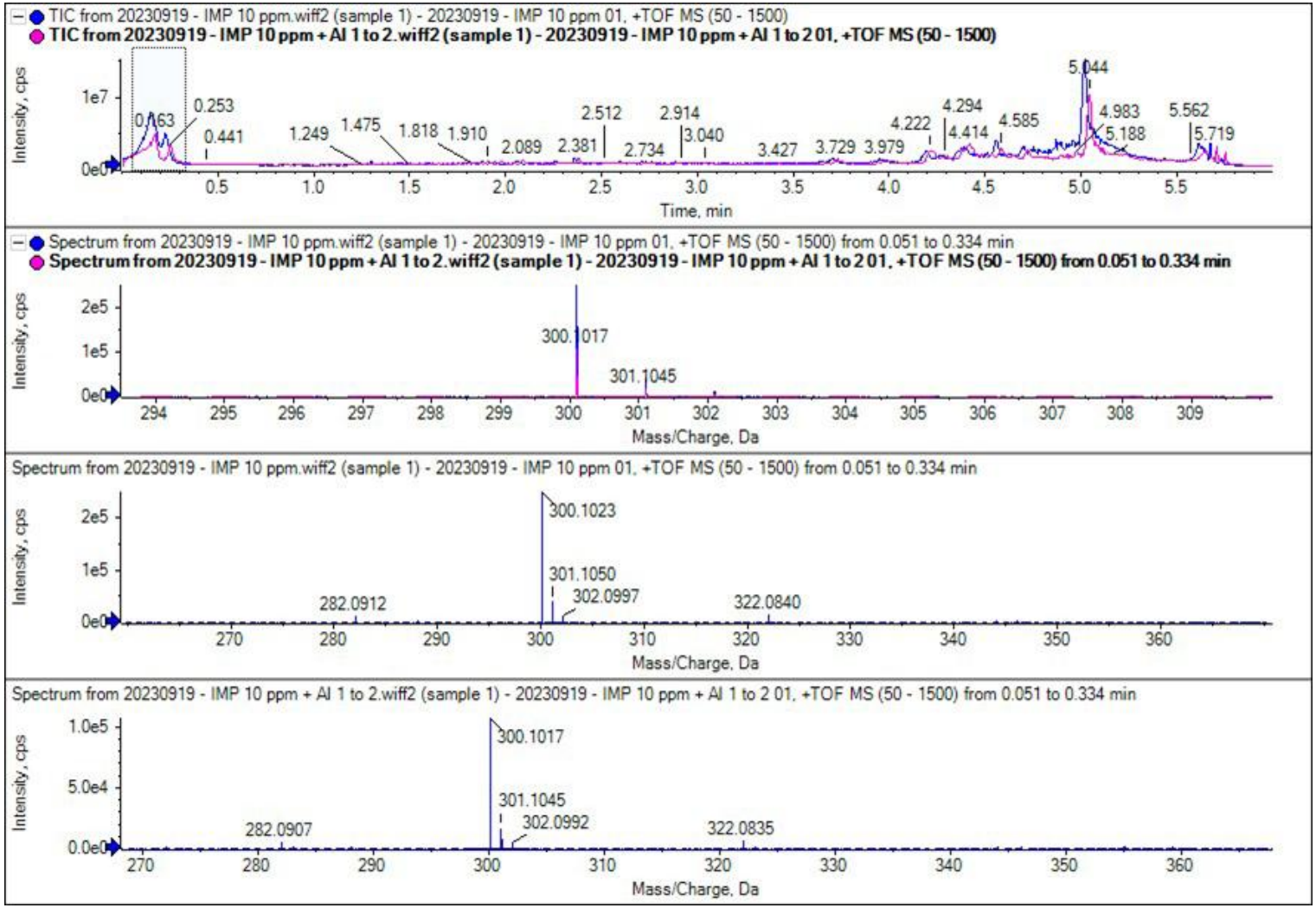

Figure A3: Overlapped chromatogram and mass spectrum for Imipenem (blue) and Imipenem-Al (III) solution (pink) (M: L = 2: 1)

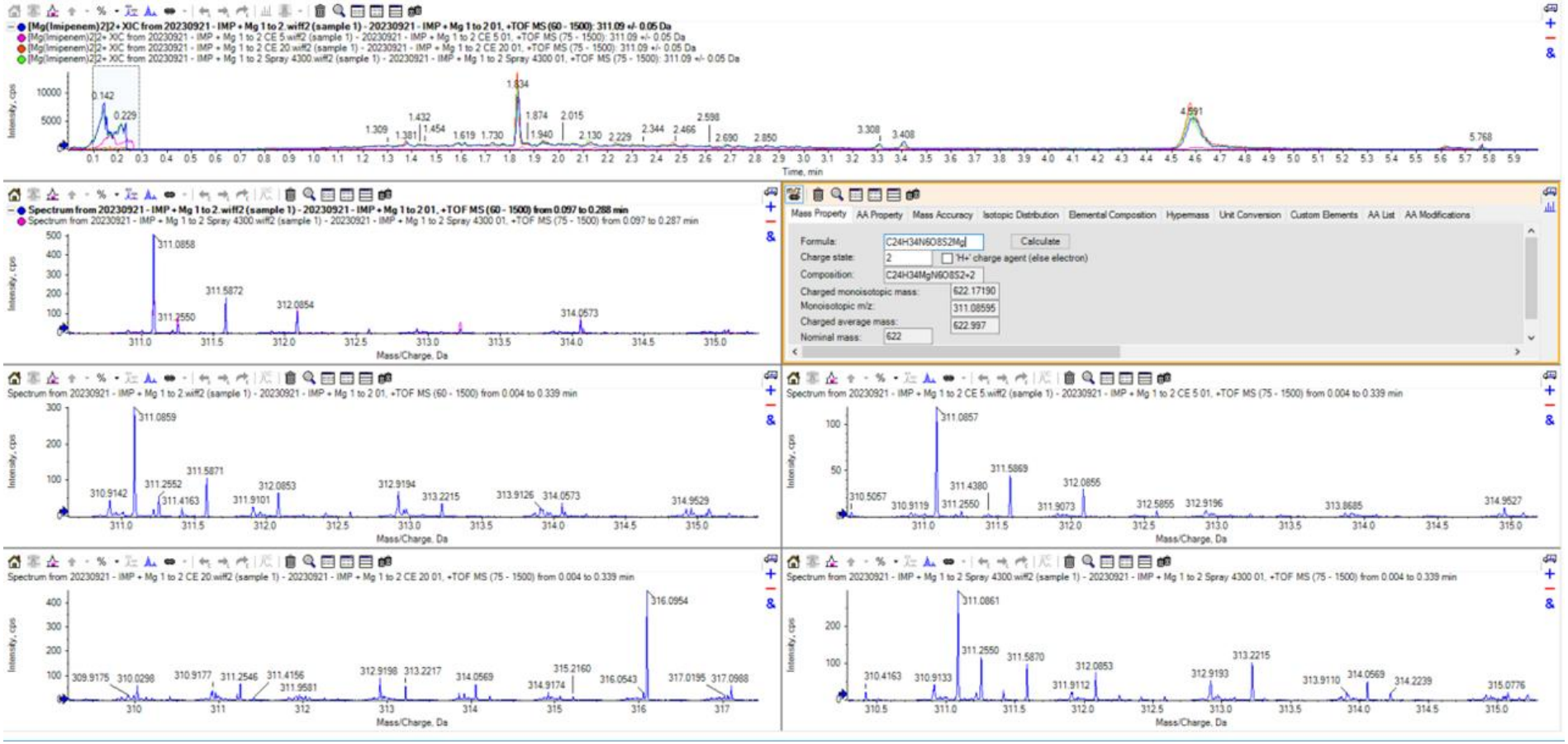

Figure A4: Mass spectrum of the identified Imipenem-Mg (II) complex $[Mg\ (IMP)_2]^{2+}$ (m/z 311.08595)

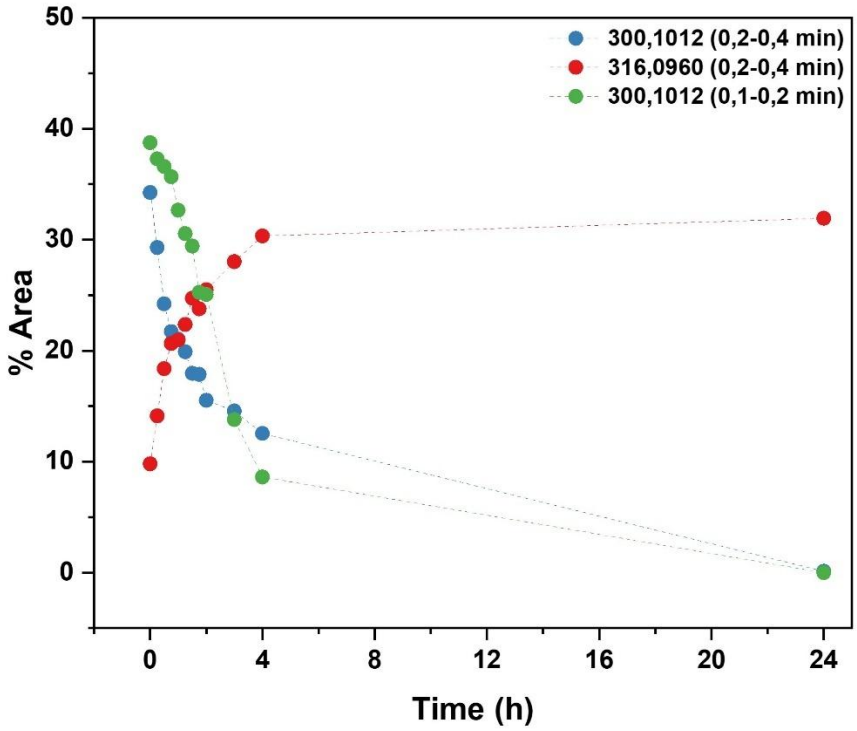

Figure A5: Change in % peak area for m/z 300.1012 $[IMP-H]^+$ and m/z 316.0960 $[IMP-O-H]^+$

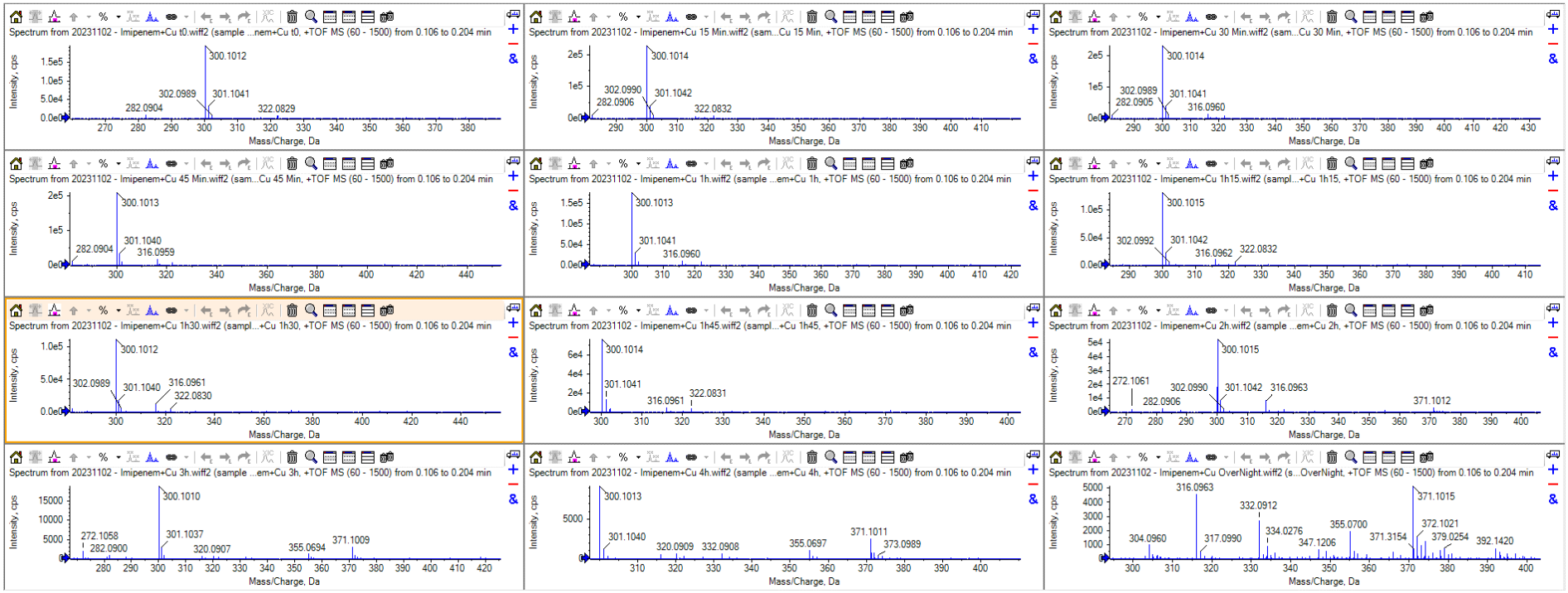

Figure A6: Time-dependent mass spectra of IMP-Cu system (IMP= 33 µM; Cu(II)= 66 µM) at RT: 0.1-0.2 min

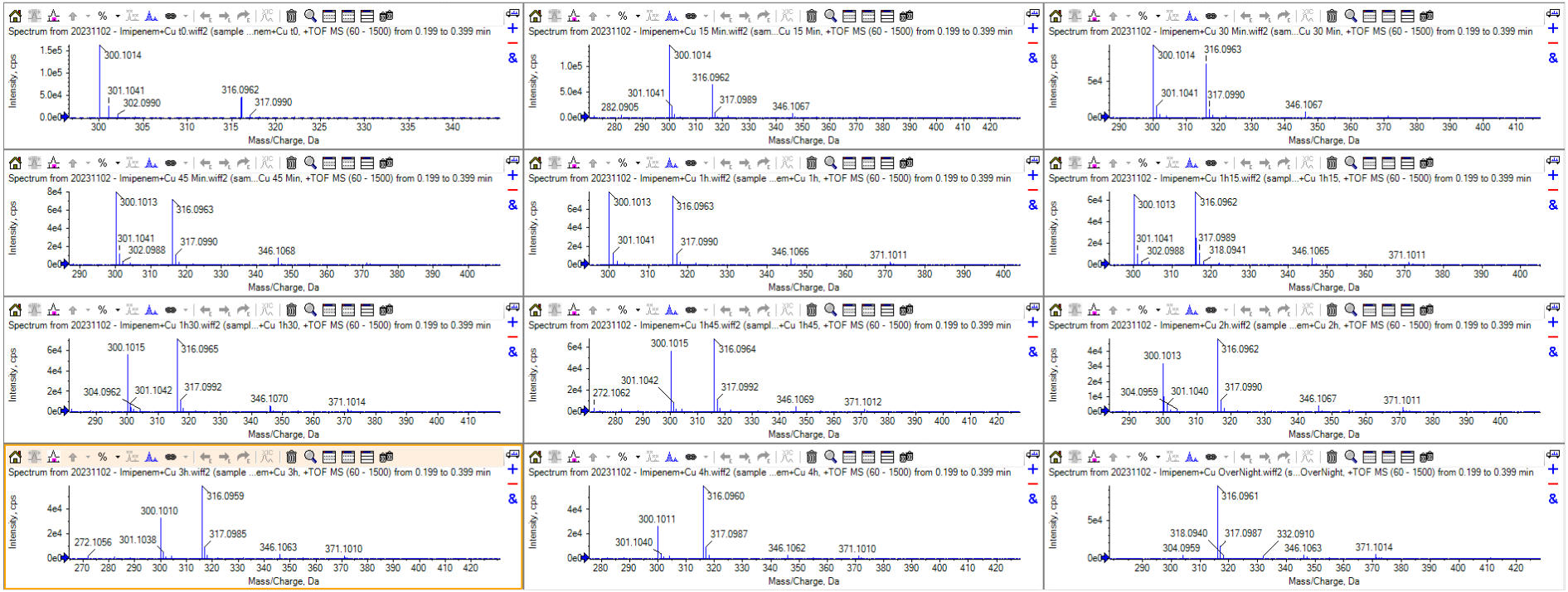

Figure A7: Time-dependent mass spectra of IMP-Cu system (IMP= 33 µM; Cu(II)= 66 µM) at RT: 0.2-0.4 min

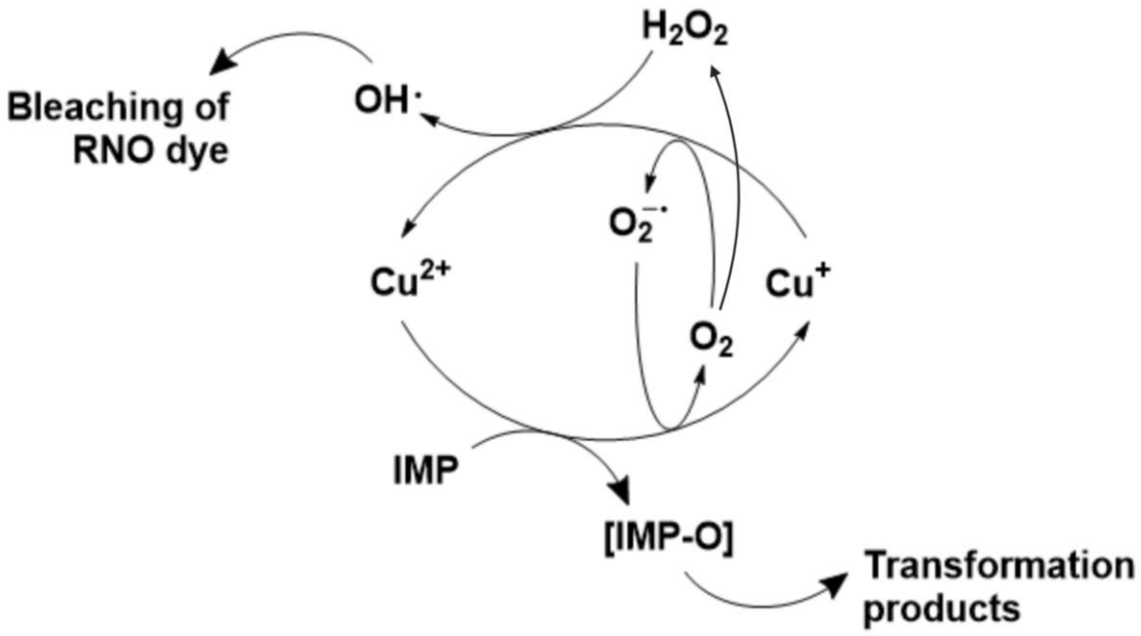

Figure A8: Proposed pathway for bleaching of the dye and oxidation of Imipenem by copper redox coupling

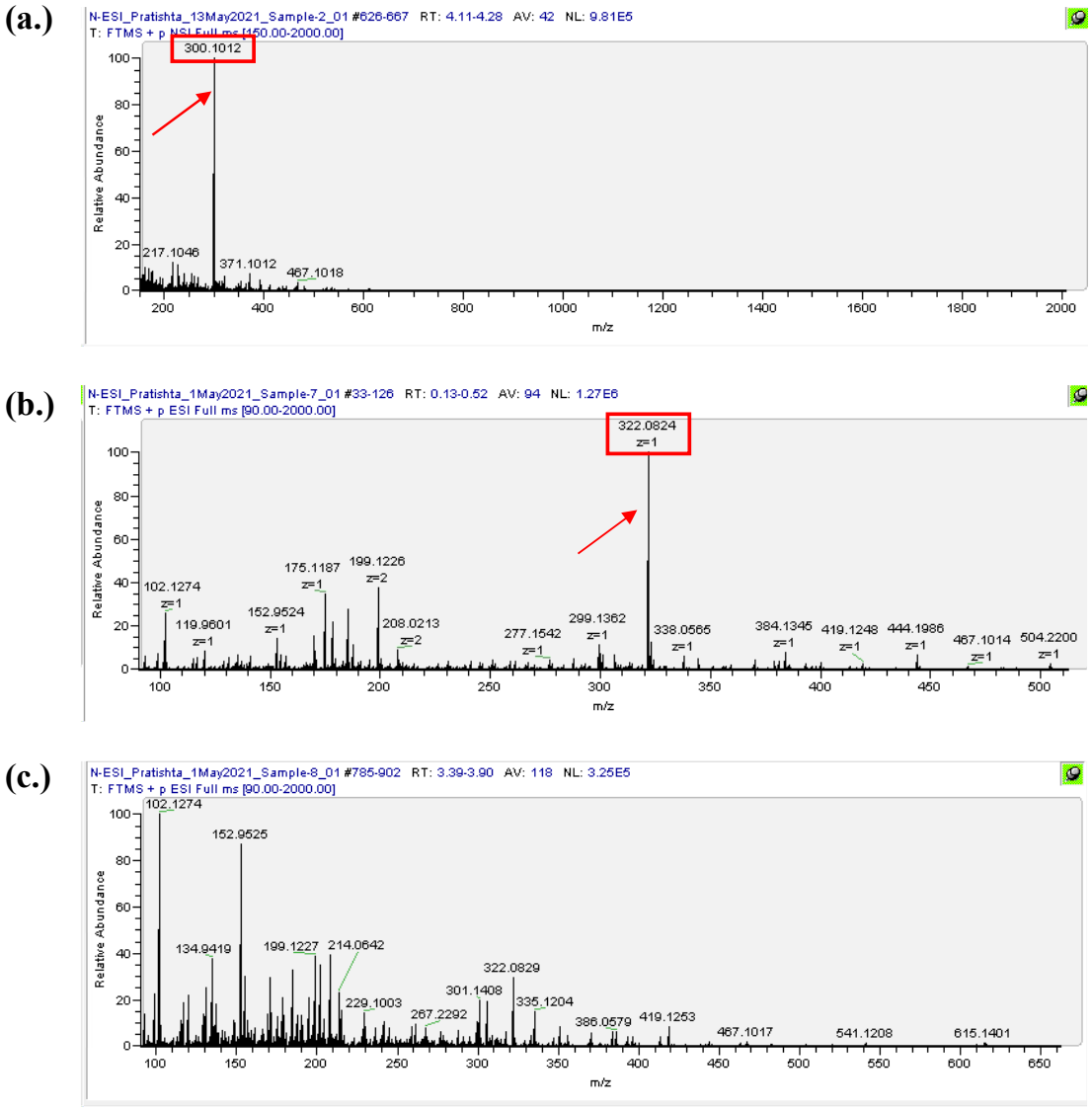

Figure A9: Mass spectra for: (a) Aqueous Imipenem solution at zero-hour, (b) Imipenem spiked in wastewater at zero hour, and (c) Imipenem spiked in wastewater after 5 hours of natural solar exposure.

Appendix B: Supplementary information for Chapter 5

List of Tables:

B1	Concentrations of metals in collected municipal wastewater and wastewater sludge samples by ICP-OES
B2	Concentrations of metals in collected municipal wastewater and wastewater sludge samples by ICP-OES

List of Figures:

B1	Overlapped chromatogram and mass spectrum for Imipenem (blue) and Imipenem-M solution (M= Mg (II) and Ca (II)) (M: L = 2: 1)
B2	Mass spectrum of the identified Imipenem-Ca (II) complex $[Ca\ (IMP)_2]^{2+}$ (m/z 319.0742)
B3	Mass spectrum of the identified Imipenem-Mg (II) complex $[Mg\ (IMP)_2]^{2+}$ (m/z 311.08595)
B4	Overlapped chromatogram and mass spectrum for Imipenem (blue) and Imipenem-Fe (II) and Cu (II) solution (M: L = 2: 1)
B5	Overlapped chromatogram and mass spectrum for Imipenem (blue) and Imipenem-Al (III) solution (pink) (M: L = 2: 1)
B6	Proposed hypothetical structures for (a) IMP-M (2: 1) complex (M= Mg (II) or Ca (II)); and (b) IMP-Al complex (3: 2)
B7	(a) Growth curve for B. subtilis at different concentrations of Imipenem; (b) Average normalized CFU; and (c) Average %inhibition of B. subtilis in presence of Imipenem
B8	(a) Growth curve for E. coli at different concentrations of Imipenem; (b) Average normalized CFU; and (c) Average %inhibition of E. coli in the presence of Imipenem

Table B1: Concentrations of metals in collected municipal wastewater (mg/L) and wastewater sludge (mg/kg) samples by ICP-OES

*(RS- Return activated sludge, and TS- Thickened sludge)

Metal	**Al**	**As**	**B**	**Ba**	**Ca**	**Cd**	**Co**	**Cr**	**Cu**	**Fe**	**K**	**Mg**	**Mn**
	mg/L	mg/L	mg/L	mg/L	mg/L	mg/L	mg/L	mg/L	mg/L	mg/L	mg/L	mg/L	mg/L
LOD	**0.005**	**0.04**	**0.01**	**0.0005**	**0.01**	**0.0007**	**0.004**	**0.005**	**0.007**	**0.004**	**0.1**	**0.02**	**0.0008**
WW1	0.509	< 0.04	0.12	0.067	82.3	0.0013	< 0.004	0.006	0.64	0.95	15.6	13.8	0.123
WW2	38.6	< 0.04	0.18	0.206	92.6	< 0.0007	< 0.004	0.012	0.35	4.00	21	15.6	0.971
WW3	0.188	< 0.04	0.18	0.031	77.3	< 0.0007	< 0.004	< 0.005	0.021	0.015	21	13	0.005
WW4	0.048	< 0.04	0.18	0.030	79.4	< 0.0007	< 0.004	< 0.005	0.015	0.020	14.5	12.9	0.0069
WW5	0.048	< 0.04	0.18	0.031	79.2	< 0.0007	< 0.004	< 0.005	0.018	0.014	14.2	12.9	0.007
RS raw	107	< 0.04	0.20	0.505	117	< 0.0007	< 0.004	0.035	0.944	11.2	35	20	2.47
RS liq	0.637	< 0.04	0.16	0.022	83.7	< 0.0007	< 0.004	< 0.005	0.015	1.38	31	15	1.42
TS liq	14.5	< 0.04	0.19	0.075	124	0.0010	< 0.004	< 0.005	0.133	5.16	72	24.8	3.12
TS raw	808	< 0.04	0.54	3.70	325	0.0045	0.031	0.29	7.3	61.8	89	55	11.3
	mg/kg	mg/kg	mg/kg	mg/kg	mg/kg	mg/kg	mg/kg	mg/kg	mg/kg	mg/kg	mg/kg	mg/kg	mg/kg
RS dry	33840	< 2	48	157	27620	0.21	1.56	13.2	299	1895	7946	4612	632
TS dry	38840	< 2	24	176	15710	0.27	1.63	15.5	354	1973	4360	2622	538

Table B2: Concentrations of metals in collected municipal wastewater and wastewater sludge samples by ICP-OES

*(RS- Return activated sludge, and TS- Thickened sludge)

Metal	**Mo**	**Na**	**Ni**	**P**	**Pb**	**S**	**Sb**	**Se**	**Sr**	**Ti**	**V**	**Zn**	**Hg**
	mg/L	mg/L	mg/L	mg/L	mg/L	mg/L	mg/L	mg/L	mg/L	mg/L	mg/L	mg/L	ug/L
LOD	**0.006**	**0.1**	**0.03**	**0.4**	**0.02**	**0.014**	**0.05**	**0.03**	**0.00022**	**0.004**	**0.003**	**0.003**	**1.0**
WW1	< 0.006	106	< 0.03	7.2	0.02	12.9	< 0.05	< 0.03	0.29	0.013	< 0.003	0.474	1.4
WW2	< 0.006	111	< 0.03	29	< 0.02	31.9	< 0.05	< 0.03	0.329	0.028	< 0.003	0.368	1.4
WW3	< 0.006	109	< 0.03	< 0.4	< 0.02	28.1	< 0.05	< 0.03	0.262	< 0.004	< 0.003	0.064	1.3
WW4	< 0.006	111	< 0.03	< 0.4	< 0.02	32.2	< 0.05	< 0.03	0.261	< 0.004	< 0.003	0.057	2.3
WW5	< 0.006	112	< 0.03	< 0.4	< 0.02	31.5	< 0.05	< 0.03	0.264	< 0.004	< 0.003	0.068	< 1.0
RS raw	0.006	110	< 0.03	77.6	0.03	31.9	< 0.05	< 0.03	0.446	0.077	0.003	0.943	3.0
RS liq	< 0.006	104	< 0.03	2.4	< 0.02	9.7	< 0.05	< 0.03	0.244	< 0.004	< 0.003	0.023	2.8
TS liq	< 0.006	111	< 0.03	12.5	< 0.02	15.9	< 0.05	< 0.03	0.35	< 0.004	< 0.003	0.111	1.6
TS raw	0.061	114	0.14	556	0.29	164	< 0.05	0.07	1.69	0.148	0.055	6.5	2.8
	mg/kg	mg/kg	mg/kg	mg/kg	mg/kg	mg/kg	mg/kg	mg/kg	mg/kg	mg/kg	mg/kg	mg/kg	ug/kg
RS dry	2.3	23900	7.0	22370	6.0	8523	< 3	3	115	0.7	2.4	276	237
TS dry	2.8	5744	7.0	25650	5.0	7875	< 3	4	80.7	1.14	2.9	317	204

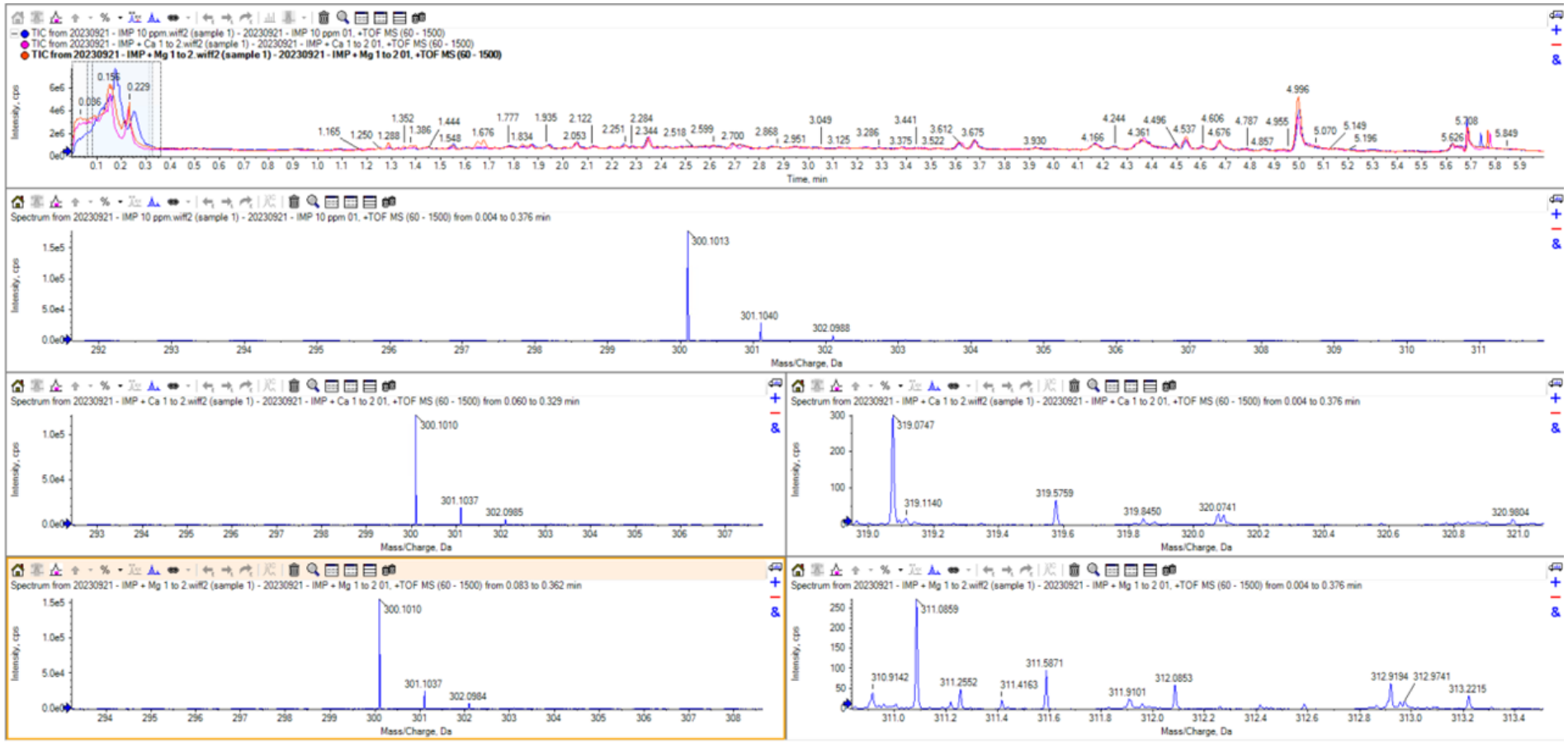

Figure B1: Overlapped chromatogram and mass spectrum for Imipenem (blue) and Imipenem-M solution (M= Mg (II) and Ca (II)) (M: L = 2: 1)

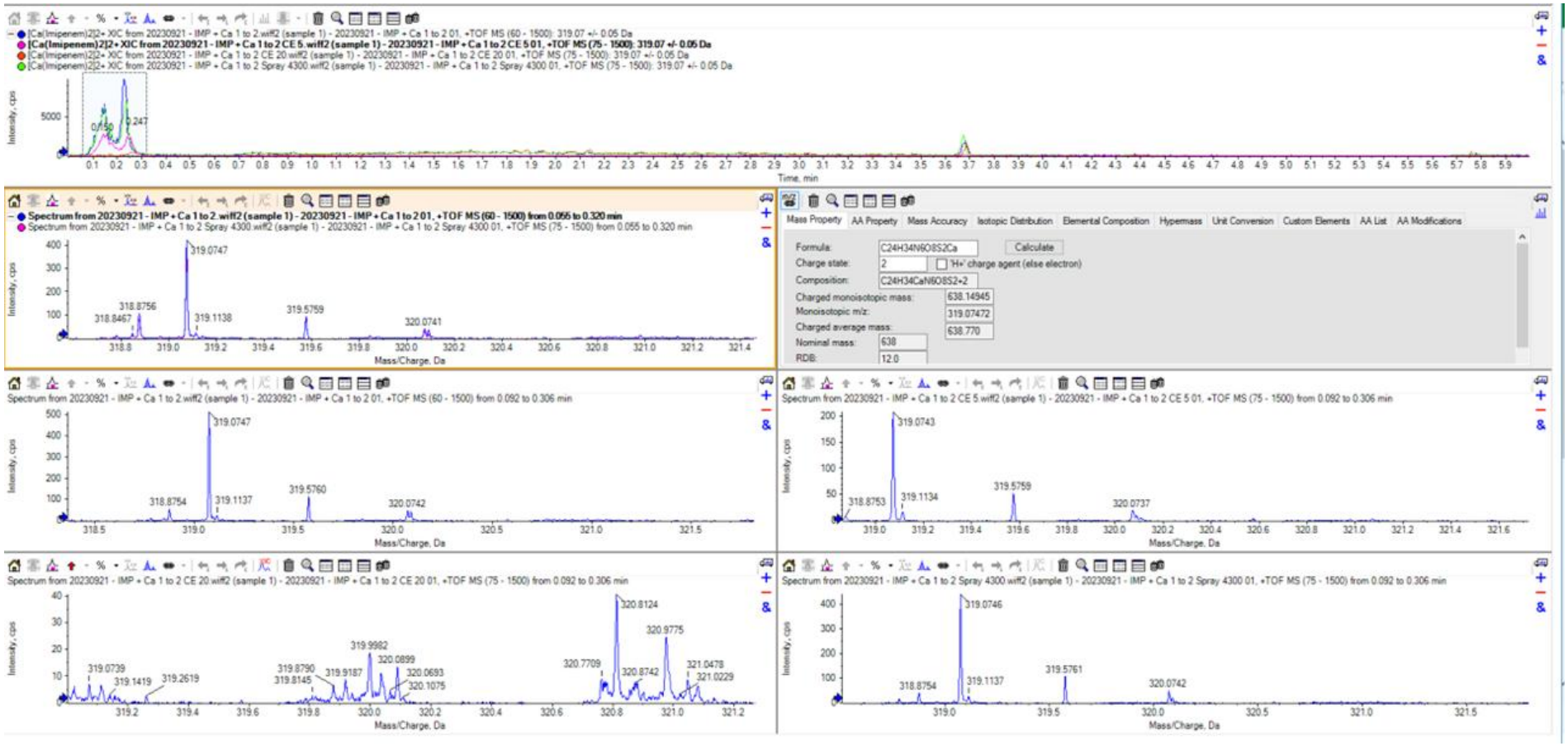

Figure B2: Mass spectrum of the identified Imipenem-Ca (II) complex $[Ca\ (IMP)_2]^{2+}$ (m/z 319.0742)

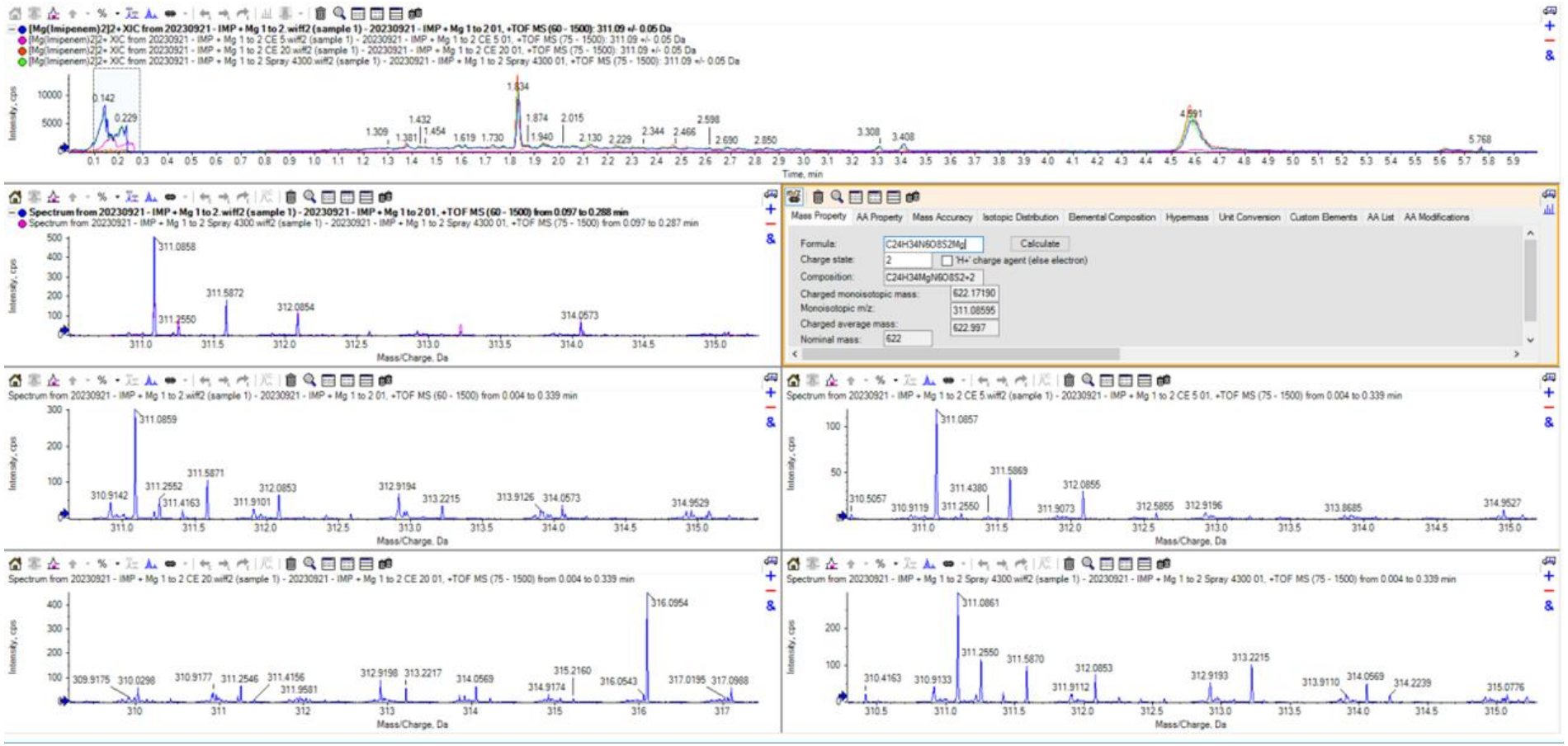

Figure B3: Mass spectrum of the identified Imipenem-Mg (II) complex $[Mg\ (IMP)_2]^{2+}$ (m/z 311.08595)

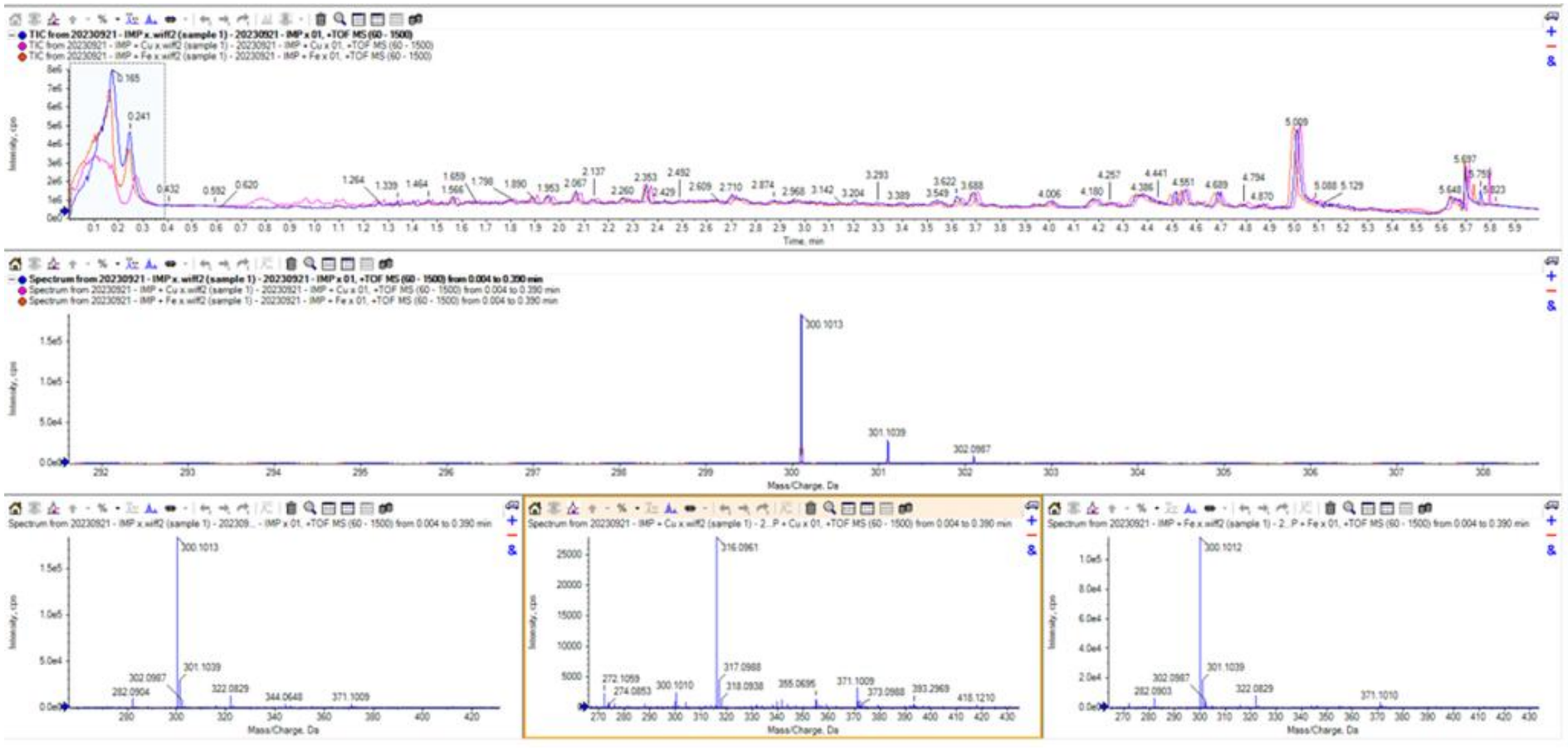

Figure B4: Overlapped chromatogram and mass spectrum for Imipenem (blue) and Imipenem-Fe (II) (orange) and Cu (II) (pink) solution (M: L = 2: 1)

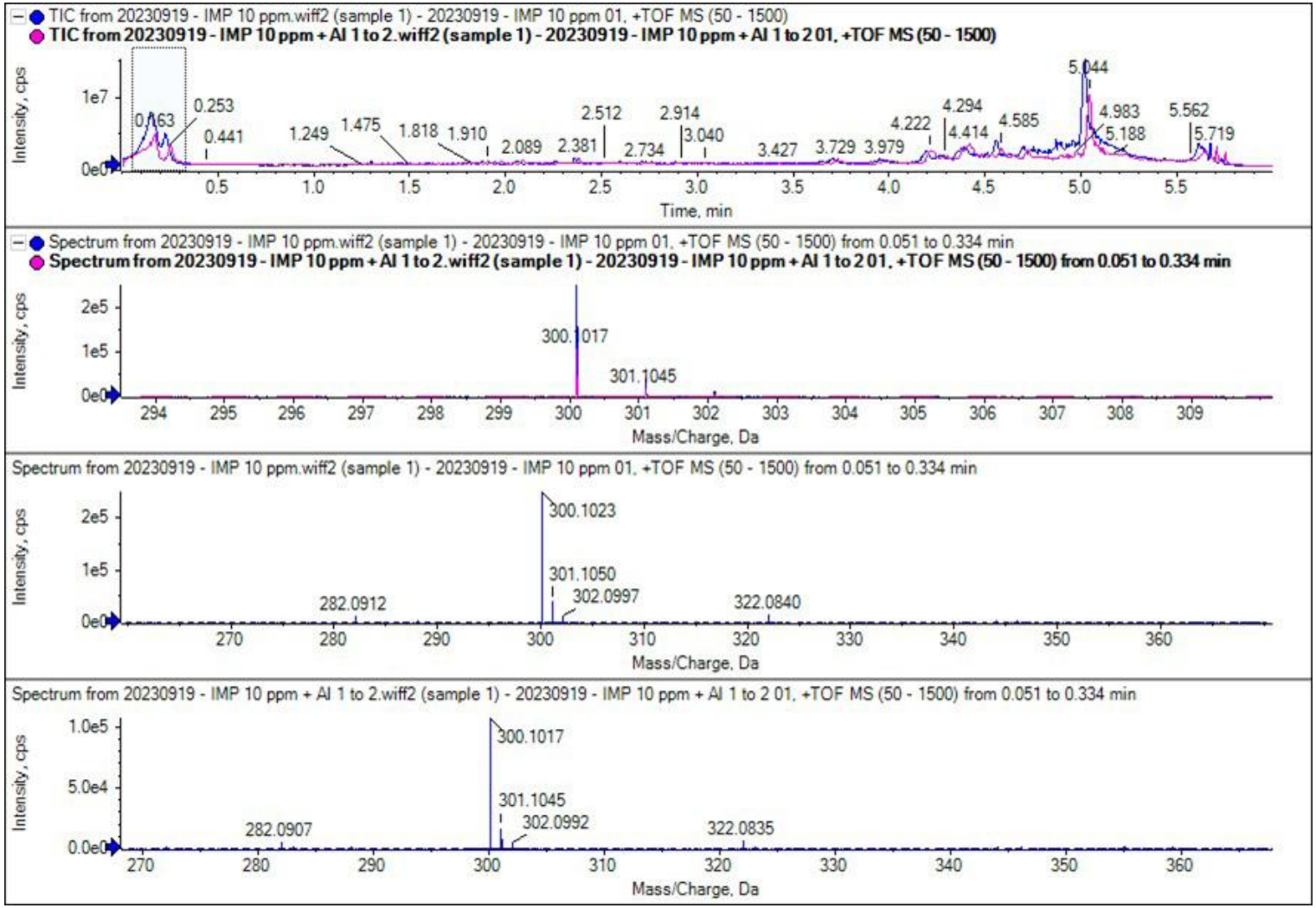

Figure B5: Overlapped chromatogram and mass spectrum for Imipenem (blue) and Imipenem-Al (III) solution (pink) (M: L = 2: 1)

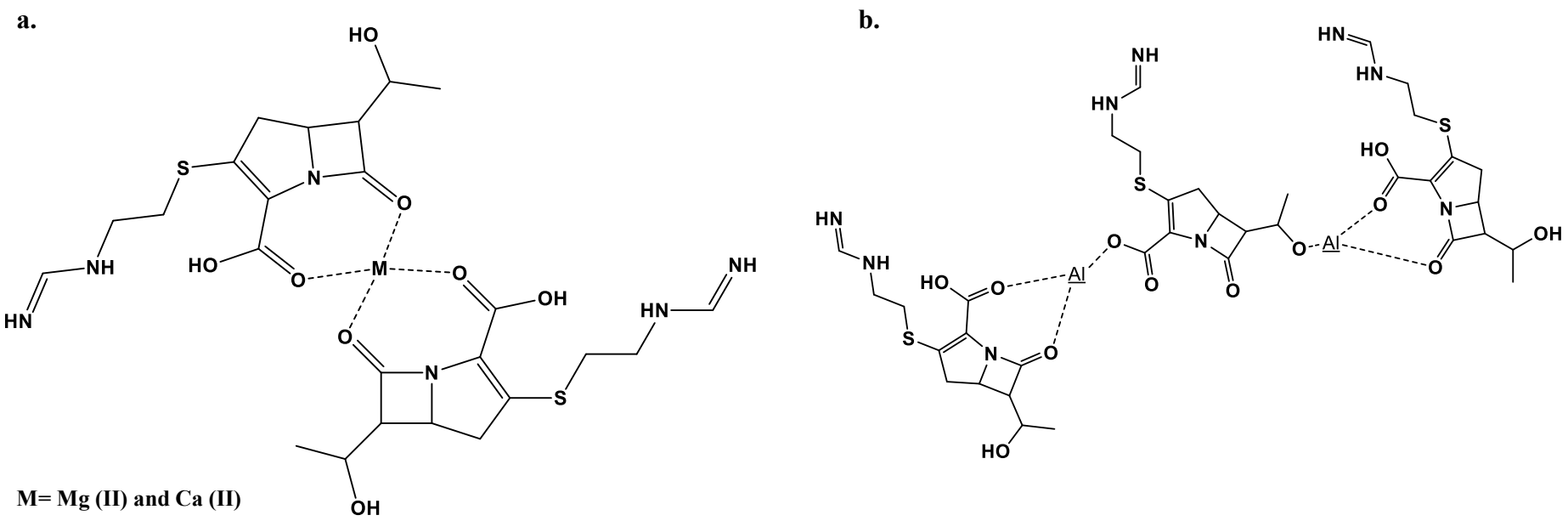

Figure B6: Proposed hypothetical structures for (a) IMP-M (2: 1) complex (M= Mg (II) or Ca (II)); and (b) IMP-Al complex (3: 2)

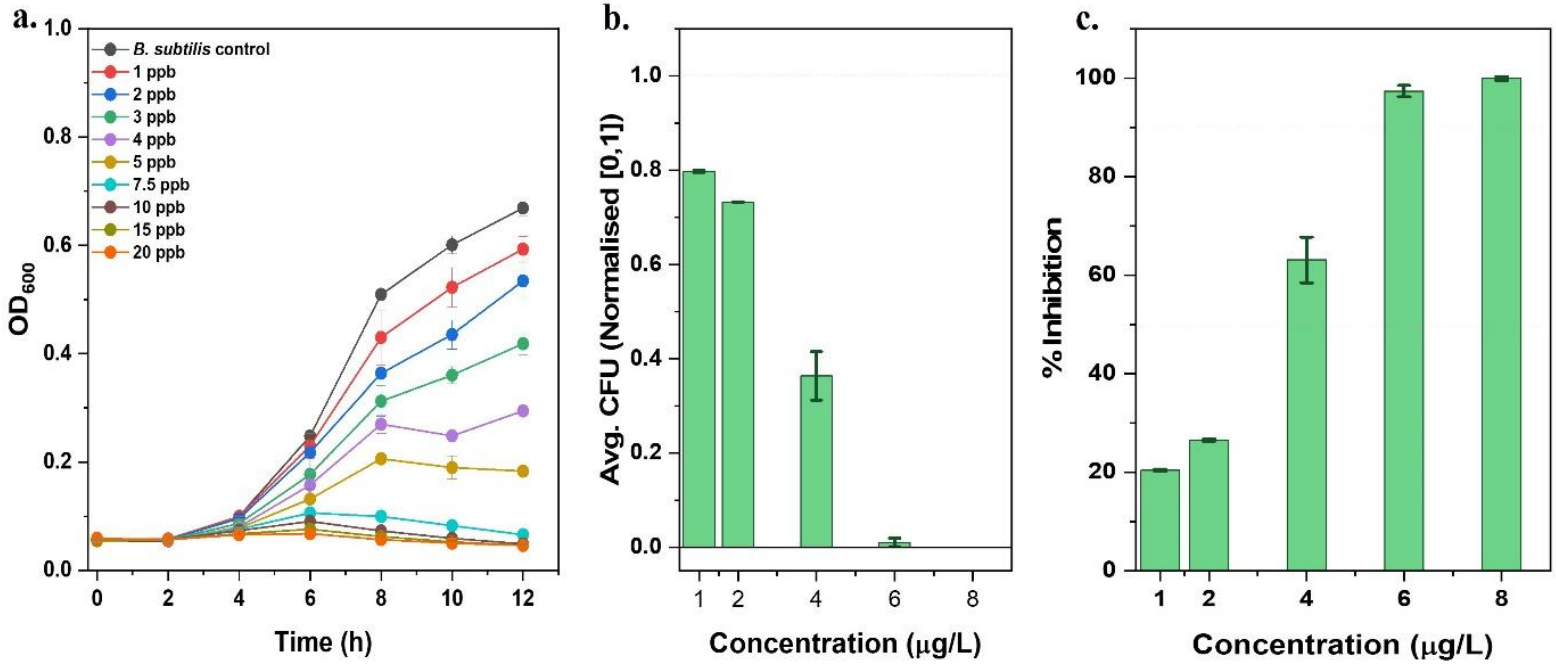

Figure B7: (a) Growth curve for B. subtilis at different concentrations of Imipenem; (b) Average normalized CFU; and (c) Average %inhibition of B. subtilis in presence of Imipenem

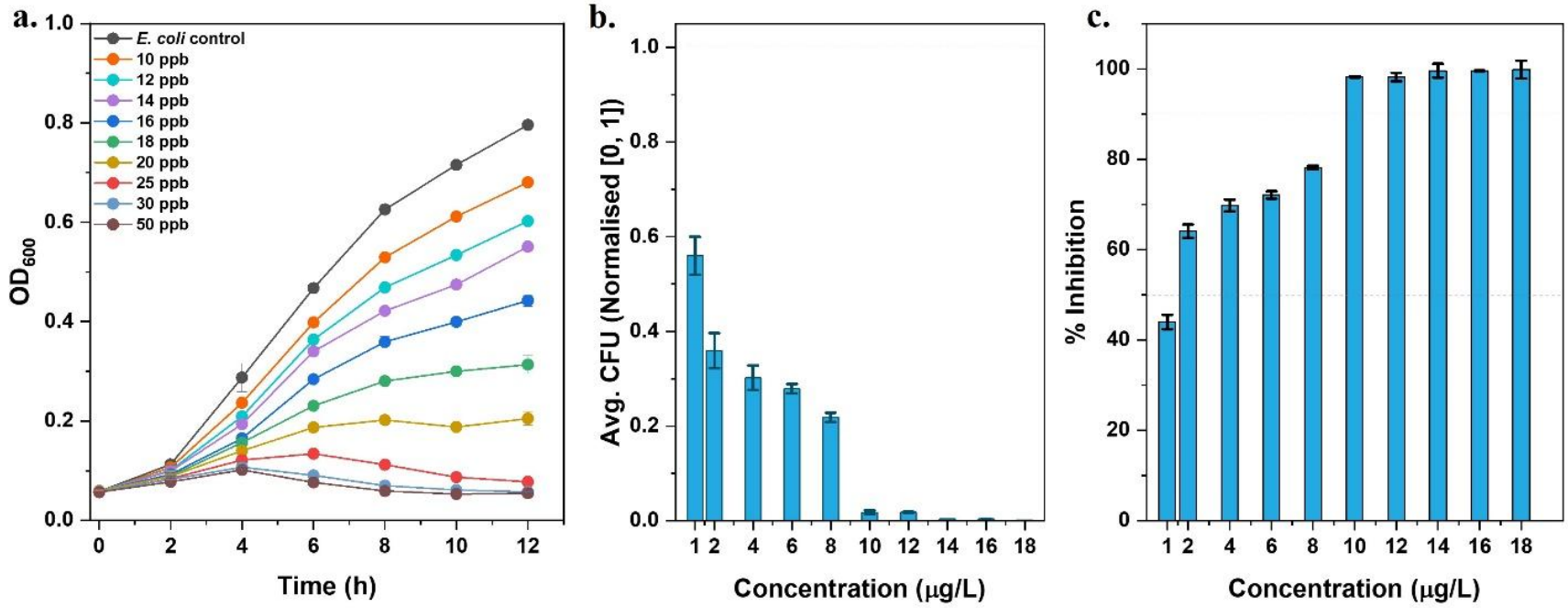

Figure B8: (a) Growth curve for E. coli at different concentrations of Imipenem; (b) Average normalized CFU; and (c) Average %inhibition of E. coli in the presence of Imipenem

Appendix C: Mechanism of action and Metabolites of FLX

List of Figures:

C1	Mechanism of action of Fluoxetine (FLX)
C2	ADME (Absorption, Distribution, Metabolism, Excretion) of FLX in human body

Text 1:

Fluoxetine (FLX) is a selective serotonin reuptake inhibitor (SSRI), i.e., acts on the central nervous system and inhibits the uptake of neurotransmitter serotonin (5-hydroxytryptamine or 5-HT) by the presynaptic neuron by blocking the serotonin transporters (or SERT) in the neural membrane. This prevents the re-uptake or serotonin, increasing its concentration in the synaptic cleft. This further increases the activation of pre- and post-synaptic receptors and increased neurotransmission, resulting in an anxiolytic effect [10,155,320] (as shown in Figure C1).

In body, FLX is extensively metabolized in the liver by cytochrome P450 enzymes, resulting in an N-demethylated product known as Norfluoxetine. The elimination half-life of fluoxetine is 1-4 days, while that of Norfluoxetine is 7-15 days [321]. In addition to this, fluoxetine also undergoes glucuronidation, yielding fluoxetine glucuronide. Oxidative O-dealkylation of fluoxetine, facilitated by enzymes CYP2C19 and possibly CYP3A4, produces p-trifluoromethyl phenol (TFMP), which on further transformation results in hippuric acid, a glycine conjugate [321,322] (Figure C2).

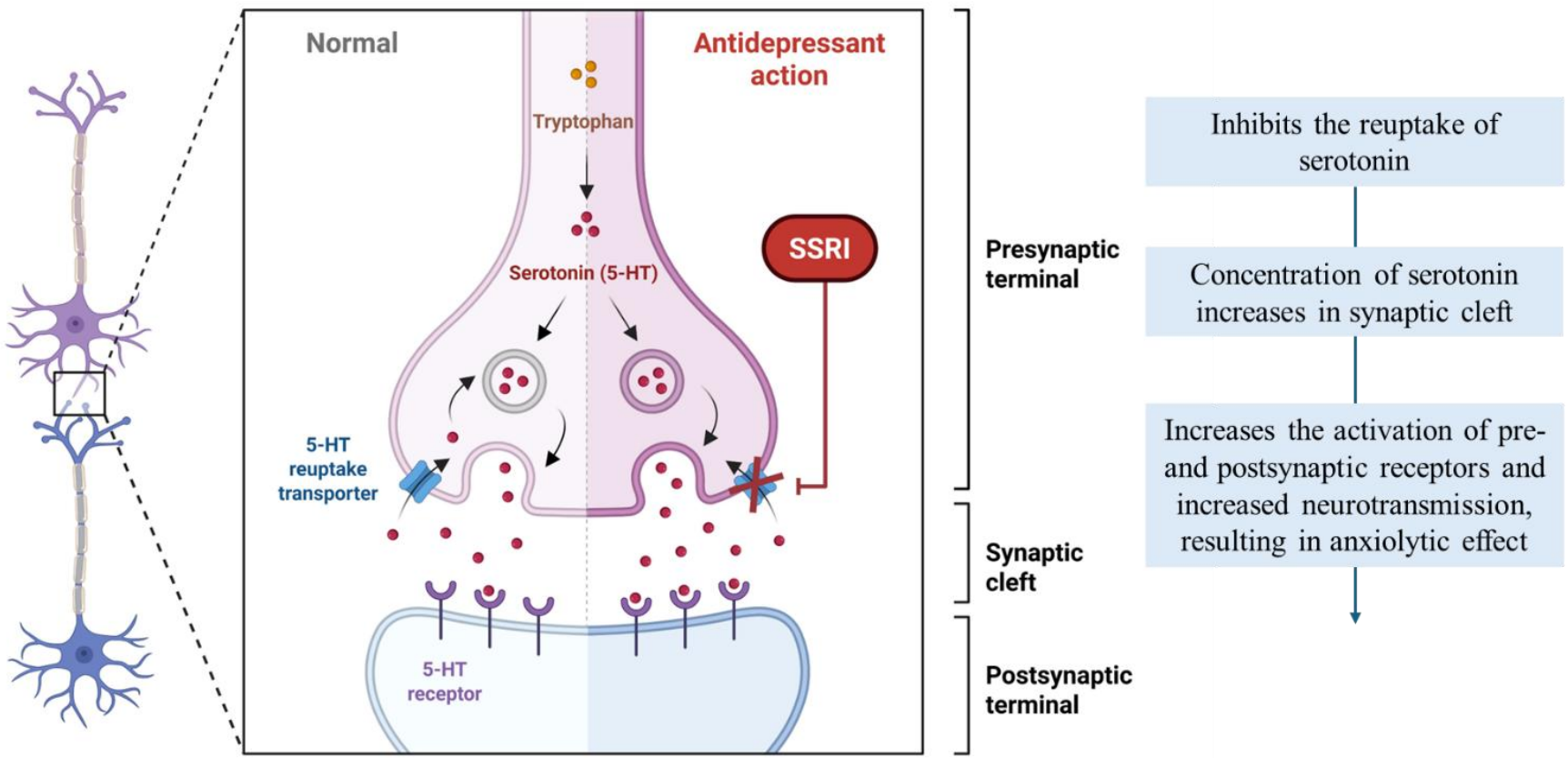

Figure C1: Mechanism of action of Fluoxetine (FLX)

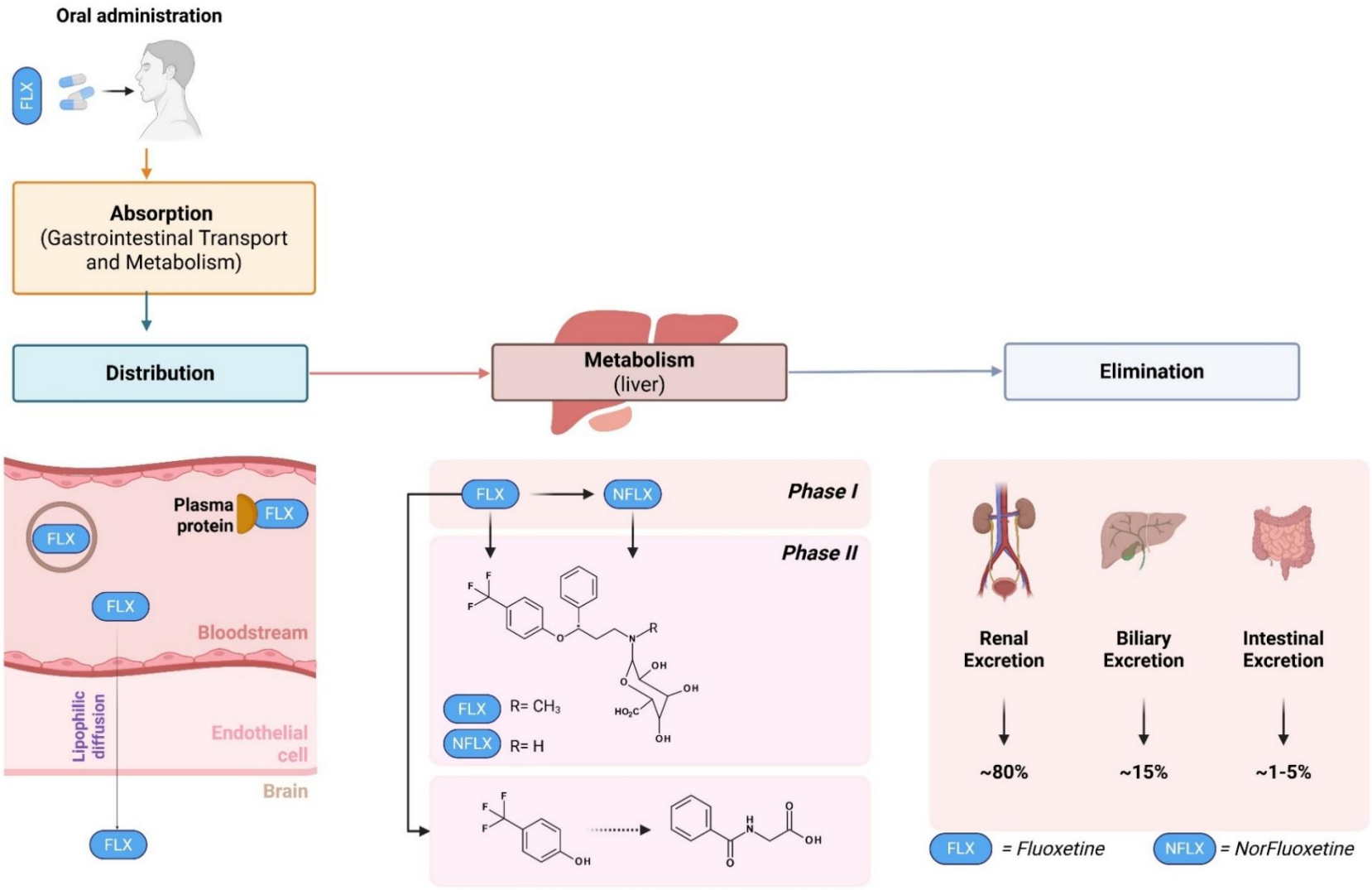

Figure C2: ADME (Absorption, Distribution, Metabolism, Excretion) of FLX in human body

Appendix D: Extraction and Detection of Fluoxetine from Wastewater and Wastewater sludge

List of Figures:

D1	Sample preparation for extractions of FLX from wastewater (WW) and wastewater sludge (WWS)
D2	Solid Phase Extraction (SPE) for Fluoxetine from WW
D3	Microwave-assisted extraction (MAE) of FLX from WWS
D4	Recovery efficiency (%) for the extraction methods of FLX from WW and WWS

Text 1: Wastewater Sample collection, preparation, and extraction of Fluoxetine (FLX)

Grab samples were collected in stainless steel containers from the Ashbridges Bay Wastewater Treatment Plant (WWTP), Toronto, Canada, in May 2023 and stored at 4 °C till further use. The facility has a capacity of 818 ML/day, with an average daily flow rate of 570.4 ML/day and serves a population of about 1,393,845 inhabitants. The treatment train includes preliminary treatment (grit and screening removal), primary clarification tanks, and secondary treatment through a biomass-activated sludge process in aeration tanks, followed by disinfection with sodium hypochlorite. The primary and waste-activated sludge (WAS) is further treated by anaerobic digestion, dewatering, and then hauled and pelletized. Samples were collected for influent (after primary screening), secondary effluent and secondary sludge.

For wastewater (WW) samples (influent and effluent), extraction of FLX was performed by solid phase extraction (SPE), while microwave-assisted extraction (MAE) was employed to extract the analyte from wastewater sludge (WWS) (Figure D.1).

Extraction of FLX from WW: For this, a small volume of wastewater was filtered through a Whatman filter paper (0.45um) to remove the suspended solids. After filtration, the samples were acidified to pH 2 with 0.1% formic acid, followed by SPE using an Oasis HLB cartridge (6 cc, 200 mg) (Figure D2). In brief, the cartridge was first conditioned and activated with 5 mL methanol, followed by 5 mL water. Then, the acidified samples were loaded at a flow rate of 2 mL/min, before washing with 5 mL of 70% methanol in 2% ammonium acetate to remove the interferences. Finally, the analyte was eluted with 5 mL 70% methanol-acid (2% acetic acid) and analyzed using LC-MS. MilliQ water spiked with known concentration of FLX (5 µg/L) was used as a control to determine the efficiency of the process.

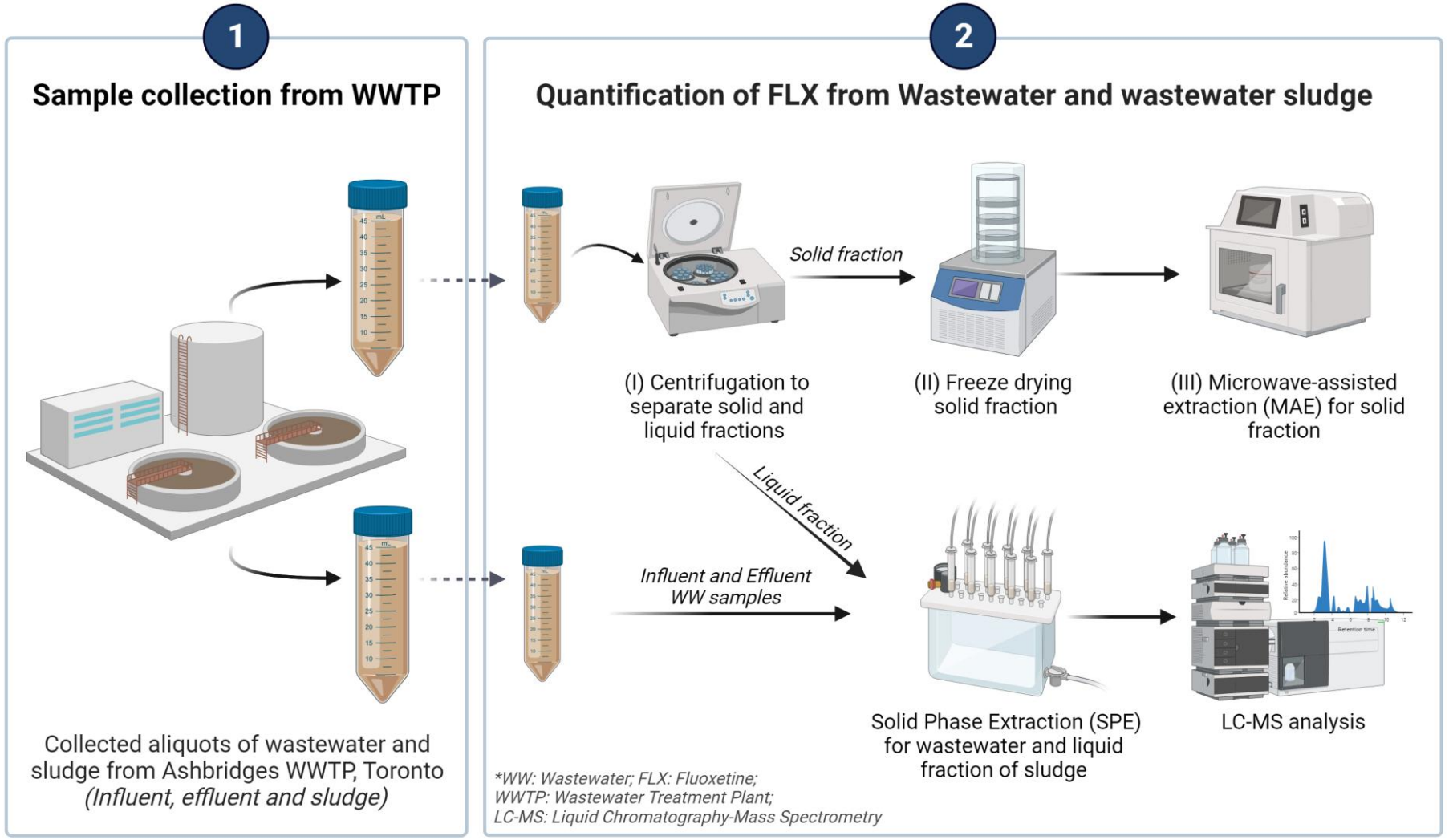

Figure D1: Sample preparation for extractions of FLX from wastewater (WW) and wastewater sludge (WWS)

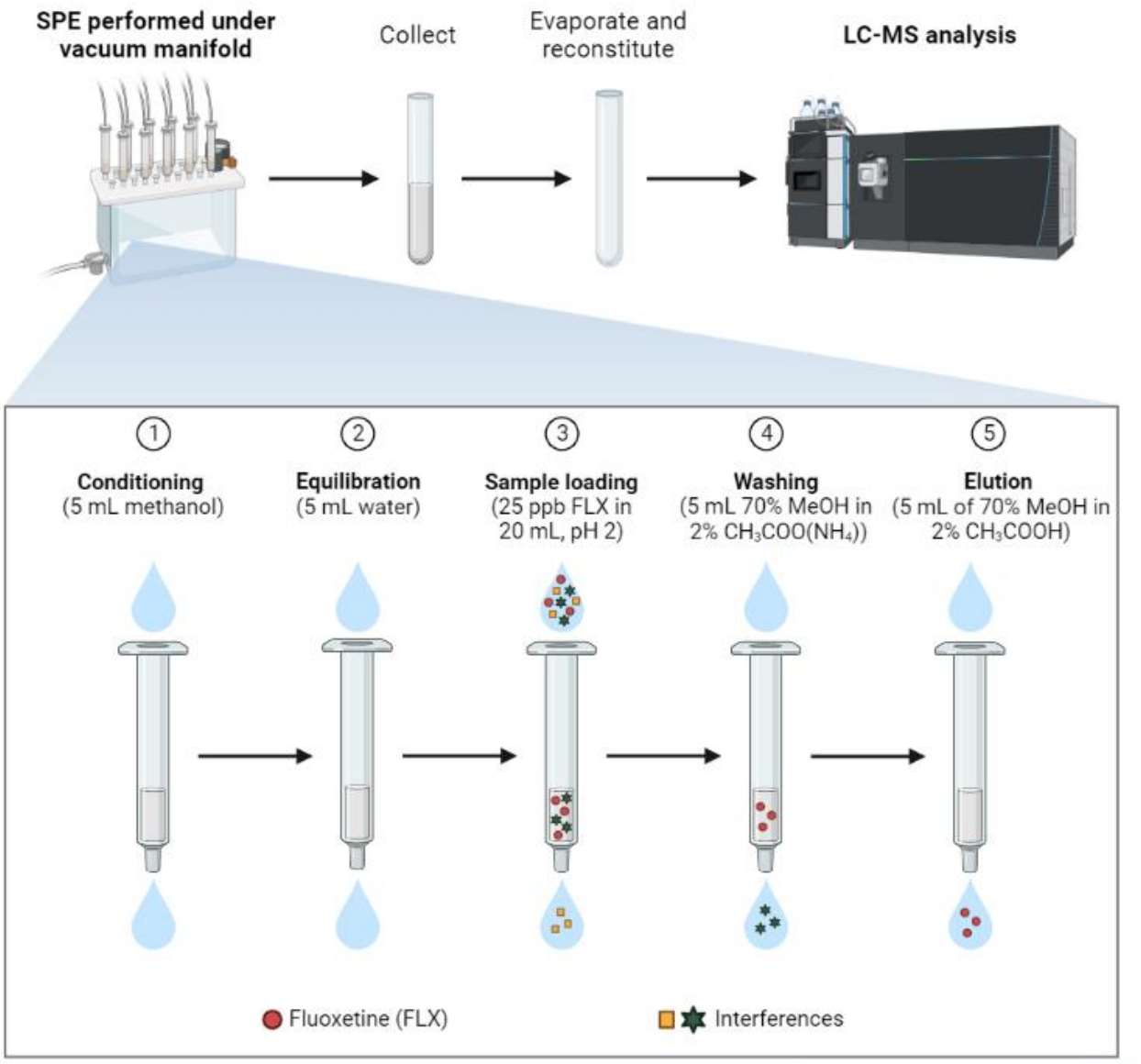

Figure D2: Solid Phase Extraction (SPE) for Fluoxetine from WW

Extraction of FLX from WWS: The sludge was centrifuged at 4000 rpm for 20 minutes to separate the sludge cake and water. The sludge cake was freeze-dried (-20 °C), followed by grinding and sieving to obtain homogeneity. Then, 1 g sludge was mixed with 60 mL solvent [methanol: water (1:3 v/v; 15 and 45 mL, respectively), vortexed for 30 s, and placed in the microwave for 30 min at a controlled ramp to 120 °C. After 30 minutes, the samples were allowed to cool to room temperature before centrifugation at 4800 rpm for 1 minutes and decantation to collect the solvent. The solvent (20 mL) was then diluted with 30 mL water and SPE was performed with an elution volume of 5 mL. Here, solvent (15 mL methanol + 45 mL milliQ water) spiked with known concentration of FLX (125 µg/L) was used as a control to determine the efficiency of the process. All the extractions were performed in duplicates and the results indicated are the average of the duplicates and error bars represent the standard deviation of the results.

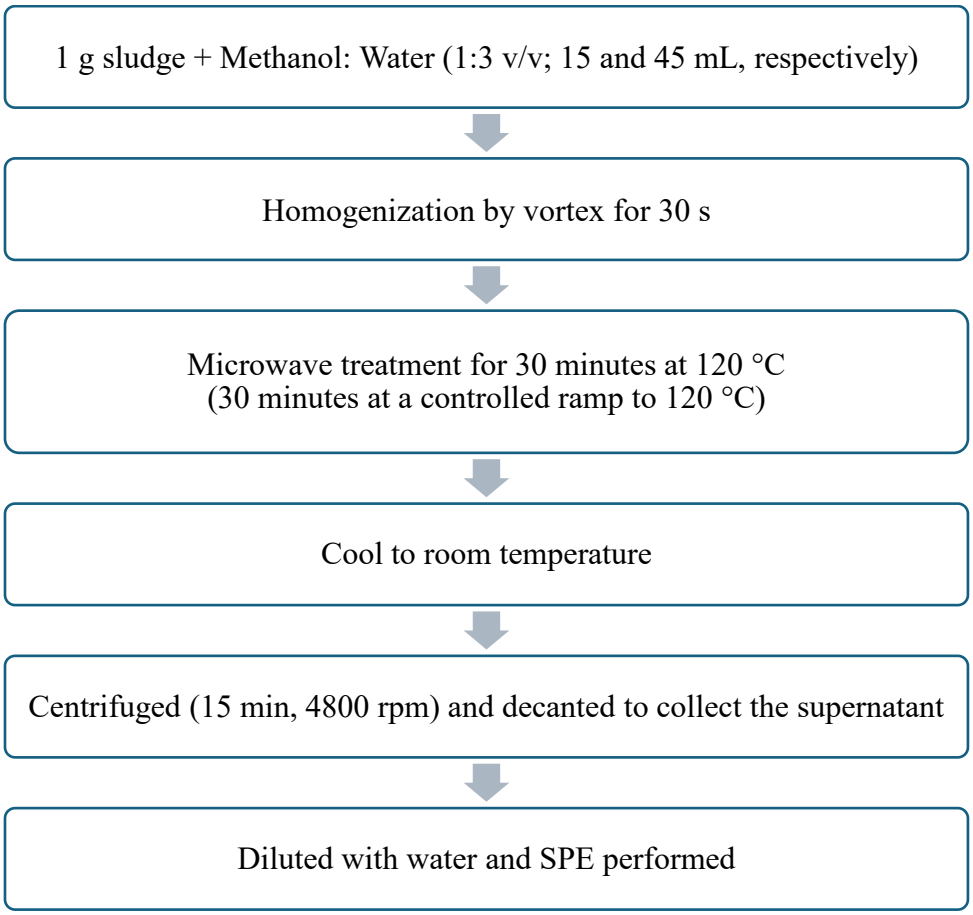

Figure D3: Microwave-assisted extraction (MAE) of FLX from WWS

Text 2: Recovery efficiency and Concentration of FLX in WW and WWS

The efficiency of the extraction process by SPE in clean water and spiked wastewater was observed to be 89.53 ± 8.57% and 93.42 ± 0.72 %, respectively (Figure D4). Similarly, an extraction efficiency of 67.03 ± 15.29 % was achieved for the extraction of FLX from wastewater sludge using MAE. Using these extraction techniques, the concentration of FLX in WW influent and effluent was found to be 0.422 ± 0.0179 and 1.057 ± 0.121 µg/L, respectively. For the liquid and solid fractions of sludge, 1.089+ 0.037 µg/L and 1.64 ± 0.196 µg/kg were observed.

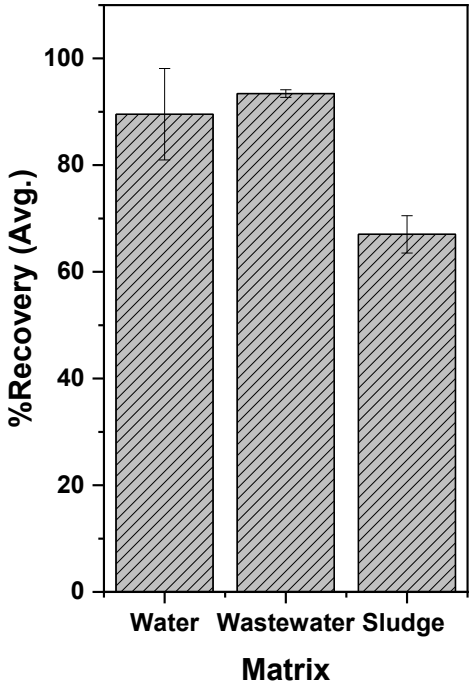

Figure D4: Recovery efficiency (%) for the extraction methods of FLX from WW and WWS

Appendix E: Fluoxetine and metals: A Case of Complex Formation?

List of Figures:

E1	Results for the titration of 100 µM FLX in 100 mM MES buffer (pH 6.5) using 20 injections with metals (a.) Mg (II) and (b.) Ca (II). The upper panel shows the heat response given by each injection and the lower panel shows the integrated heat curve normalized per mole of injectant as a function of molar ratio.
E2	Results for the titration of 100 µM FLX in 100 mM MES buffer (pH 6.5) using 20 injections with metals (a.) Cu (II), (b.) Fe (II), and (c.) Al (III). The upper panel shows the heat response given by each injection and the lower panel shows the integrated heat curve normalized per mole of injectant as a function of molar ratio.
E3	Comparison of the proton shifts (1H NMR) of FLX with different molar ratios of Fe (II)
E4	Comparison of the proton shifts (1H NMR) of FLX with different molar ratios of Al (III)
E5	Residual FLX concentrations in WW after equilibration with metals for 24 h

Text 1:

The SSRI of interest, Fluoxetine (FLX), has been reported to induce indirect effects in the presence of metals, such as Zn (II), Ca (II), and Cu (II) [221,226,323]. Although the studies reporting metal complexation of FLX are limited [324–326], FLX has been reported to coordinate with glycyrrhizic acid (GA), human serum albumin (HSA), and transferrin due to its high lipophilicity [327–329].

However, the structure of the antidepressant also possesses a secondary amine (-NH), ether oxygen (-OCH_2-) and aromatic π-system, which can serve as potential sites for metal coordination. For instance, a recent study suggested the coordination of FLX to Terbium (Tb^{3+}) *via* secondary amine and ether oxygen to form the Tb (III)-FLX complex [326]. The presence of metal cations can also facilitate the transfer of electrons from HOMO (localized on the secondary amine of FLX) to LUMO (the aromatic rings) *via* metal charge transfer [325].

Therefore, interactions between FLX and metals are probable but have not been explored in an environmental context. In this sense, the potential of the formation of FLX-metal complexes (Metals= Mg (II), Ca (II), Cu (II), Fe (II), and Al (III)) were investigated using Isothermal Titration Calorimetry (ITC), Nuclear Magnetic Resonance (NMR), and Mass Spectrometry (MS).

1. Isothermal Titration Calorimetry

The potential of metal complexation of Fluoxetine (Metals= Mg (II), Ca (II), Cu (II), Fe (II), and Al (III)) was investigated by ITC performed using MicroCal ITC200, Malvern Panalytical and the data was analyzed using OriginPro software. The measurements were carried out at 298 K under the atmosphere of nitrogen, with a stirring speed of 350 rpm and a reference power of 11 µcal/sec. The reference cell was filled with ultrapure water (250 µL), sample cell with 100 µM FLX (250 µL) in 100 mM MES buffer at pH 6.5, and the syringe with respective metal chloride solutions (5 mM) in 100 mM MES (pH 6.5), prepared gravimetrically. The titration setup consisted of 20 injections of 2 µL each with a spacing of 180 sec between injections to allow full return to baseline signal. The controls were performed by titrating each metal ion into buffer, and buffer into FLX cell for reference.

The results for the titration of 100 µM FLX in 100 mM MES buffer (pH 6.5) using 20 injections with metals are shown in Figure E1. For alkaline earth metals, Mg(II) and Ca (II), the titration of

FLX exhibited the same heat at every injection, indicating no interaction between the metals and the SSRI at pH 6.5 (Figure E1 (a-b)).

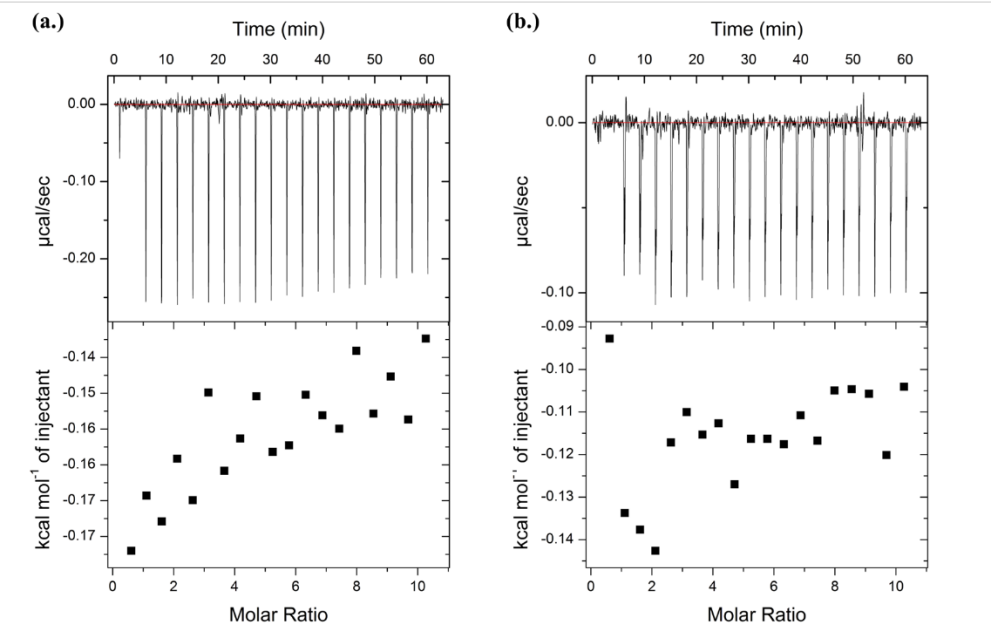

Figure E1: Results for the titration of 100 µM FLX in 100 mM MES buffer (pH 6.5) using 20 injections with metals (a.) Mg (II) and (b.) Ca (II). The upper panel shows the heat response given by each injection and the lower panel shows the integrated heat curve normalized per mole of injectant as a function of molar ratio.

Likewise, no interactions were discerned during the titration of $CuCl_2$ with FLX (Figure E2 (a)). Unlike other metals, the titration of Fe (II) with FLX was associated with the heat change, as shown in Figure E (b). Data fitting with a one-site model revealed the stoichiometry ratio (n, Metal: FLX) to be 0.5, that is, 1: 2, with negative enthalpy of interaction (exothermic). However, this peak intensity is similar to the intensity of the heat produced by the dissolution of $FeCl_2$ into buffer (that is, control). This indicates that the heat of dissolution of Fe (II) overpowers the potential heat of binding to FLX, or no FLX interactions were observed with Fe (II) solution.

On the contrary, the titration of Al (III) with FLX exhibited very strong absorption of heat (endothermic) upon each addition; however, no FLX-Al (III) interactions were observed (Figure E2(c)). To corroborate the results obtained by ITC, NMR studies were performed for FLX-Fe (II) and FLX-Al (III) binary systems.

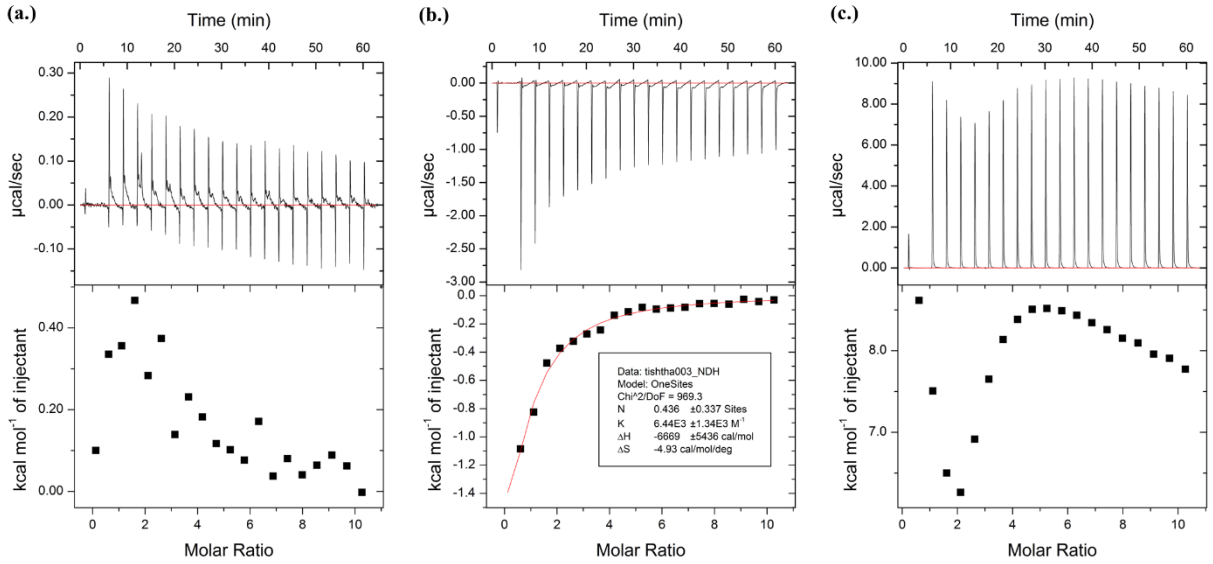

Figure E2: Results for the titration of 100 µM FLX in 100 mM MES buffer (pH 6.5) using 20 injections with metals (a.) Cu (II), (b.) Fe (II), and (c.) Al (III). The upper panel shows the heat response given by each injection and the lower panel shows the integrated heat curve normalized per mole of injectant as a function of molar ratio.

2. NMR studies

The interactions between FLX and metal ions (Fe (II) and Al (III)) were investigated using ^{1}H NMR spectroscopy with a Bruker Avance III 700 MHz instrument. Initially, the ^{1}H NMR spectrum of 100 µM FLX (600 µL in D_2O) was recorded. FLX was then titrated with small aliquots of the metal solutions prepared in D_2O, and NMR spectra were recorded to study different molar ratios for FLX to metal. The ^{1}H NMR spectrum of the free ligand (FLX) was compared with that of the FLX-metal mixture to analyze the binding sites of the metal ions to FLX.

The results for NMR measurements are shown in Figures D3 and D4. As shown in the figures, no prominent change was observed in the 1H NMR spectrum of FLX with the addition of metals Fe (II) and Al (III). The NMR experiments, thereby, showed no interaction of FLX- with the metal entities.

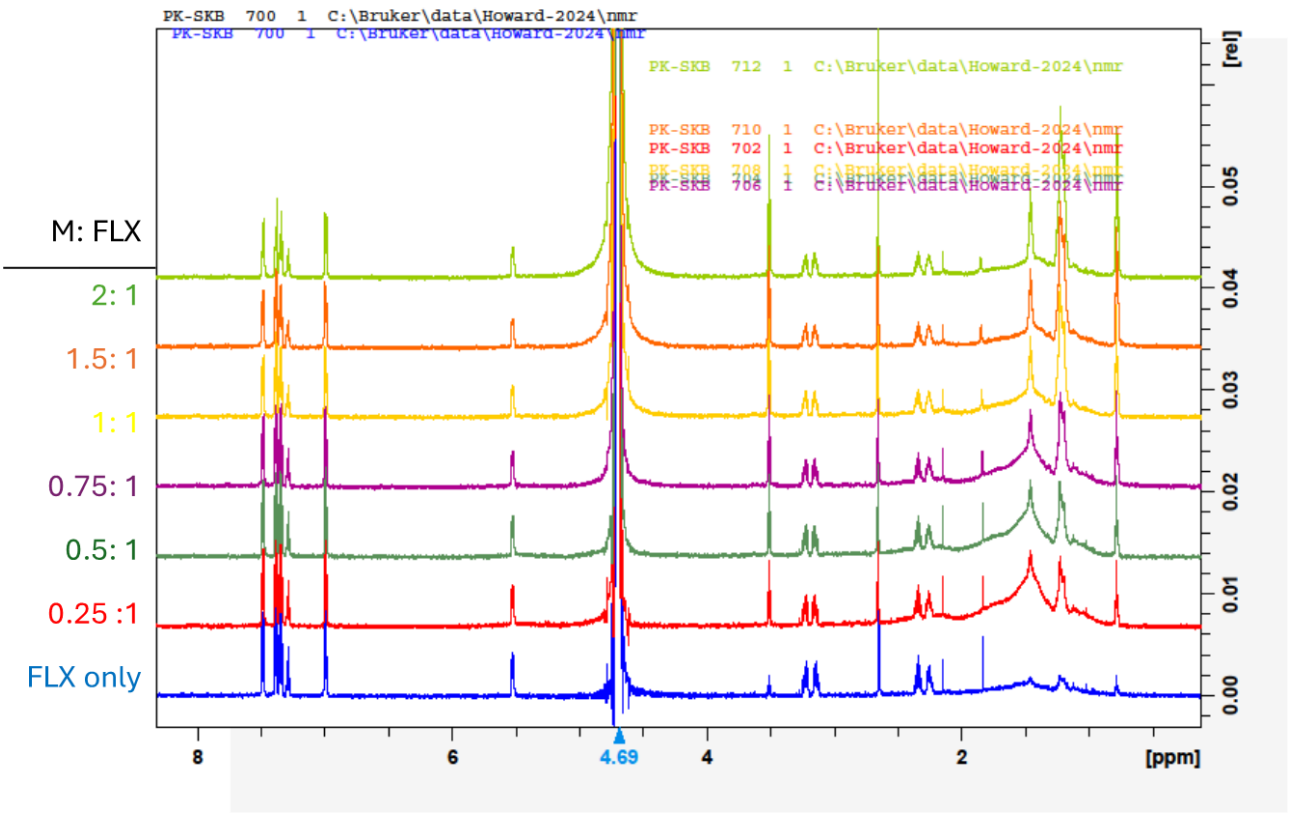

Figure E3: Comparison of the proton shifts (^{1}H NMR) of FLX with different molar ratios of Fe (II)

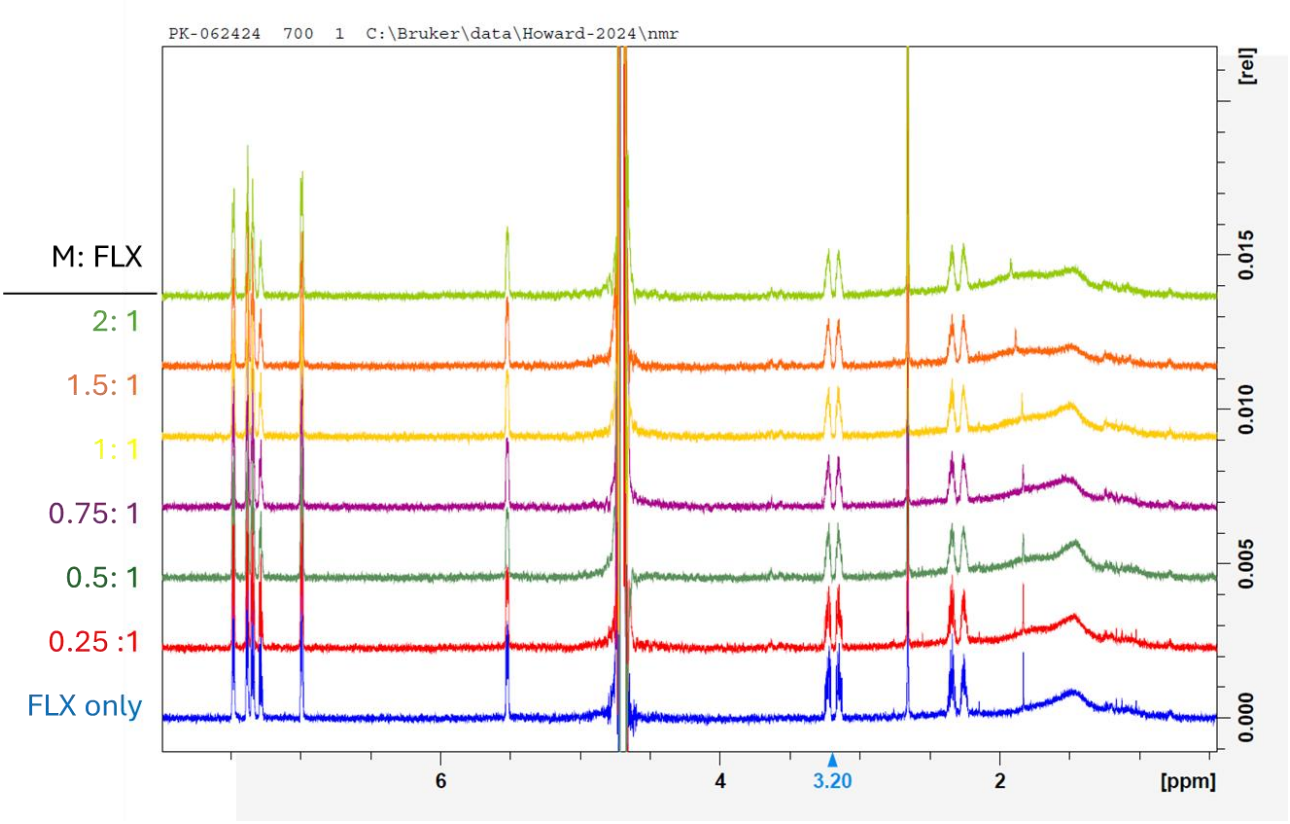

Figure E4: Comparison of the proton shifts (^{1}H NMR) of FLX with different molar ratios of Al (III)

3. Direct MS analysis

Unlike a clean matrix like water, WW is a complex matrix where different parameters, such as ionic strength and the presence of promoters and inhibitors, play a crucial role in determining the behaviour of drugs towards metals. Therefore, in addition to ITC and NMR performed in the clean matrix, MS was used to study the formation of FLX-metal complex in wastewater collected from WWTP. For this, 100 ug/L (~1.62 µM) was spiked in collected filtered secondary wastewater, along with metals in a molar stoichiometric ratio of 1: 10 FLX: Metal. The metal: FLX ratio was deliberately maintained high to mimic real wastewater conditions and to enable accurate quantification using direct MS injection. The FLX-metal mixture was equilibrated for 24 h at room temperature, followed by MS analysis.

The results from MS analysis showed similar results. The concentrations of FLX after equilibration in WW spiked with metals (10 times the molar concentration of FLX) and were found to be similar to the control, where no metals were added (Figure E5). Further, a targeted analysis with expected FLX-metal complexes for different stoichiometric ratios yielded no results. Therefore, with ITC, NMR, and MS, it was confirmed that the formation of FLX-metal complex does not occur in both clean matrix like water or complex matrix like WW.

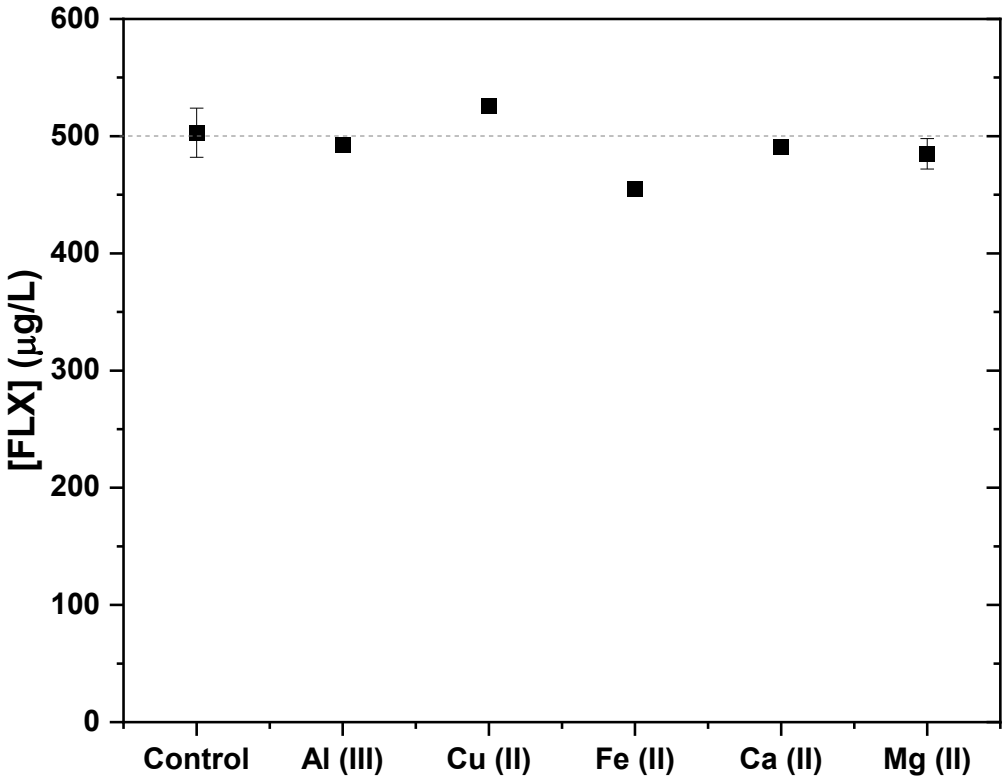

Figure E5: Residual FLX concentrations in WW after equilibration with metals for 24 h

Appendix F: Supplementary Information for Chapter 8

List of Tables:

F1	Operating conditions for the steam- and CO2-activated biochar
F2	Surface area, pore radius, elemental analyses and mineral composition of the synthesized biochar
F3	FTIR spectral features for the selected biochar (CO_2-1000-30-600-1)

List of Figures:

F1	Removal efficiency of (a.) Steam-activated (1-5), and (b.) CO_2-activated biochar (6-10) for FLX concentrations of 0.5, 5, and 50 mg/L after 24 h
F2	(a.) Comparison of kinetics of biochar 4 and 7 with 50 mg/L FLX for 24 h; (b) pHzc and (c) FTIR spectrum of selected biochar 7
F3	Pore size distribution of biochar 7 (CO_2-1000-30-600-1)
F4	Adsorption kinetic models for FLX adsorption onto biochar (a) Pseudo-first order (PFO) kinetic model, (b) Pseudo-second order (PSO) kinetic model, and (c) Intra-particle diffusion model
F5	Adsorption isotherm models for FLX adsorption onto biochar (a) Langmuir isotherm model, and (b) Freundlich isotherm model
F6	(a) % Desorption by various solvents, (b) % Removal and adsorption capacity of the regenerated biochar for subsequent adsorption cycles with 25 mg/L FLX after 2 h, and (c) TGA of raw and regenerated biochar

Text 1: Sample preparation for Biochar characterization

a. Surface area analysis: The biochar samples were analyzed for their surface area with BET using surface area analyzer (NOVA 1200e) at Materials Characterization facility (MCF), Ontario Tech University, Canada. The sample preparation included degassing in a vacuum at 200 °C for 3 h before N_2 gas physisorption analysis at 77 K. The P/P_0 range of >0.15 was chosen for the DFT method to calculate the pore volume distribution. However, the samples, due to their low density, were too volatile and did not sit well at the bottom of the tube during analysis. The samples spread on the walls and gave a negative intercept on the BET plot. Therefore, the BET results were utilized only for optimization and comparison purposes.

b. Elemental contents: The samples were prepared by the method mentioned elsewhere (McGrath and Cunliffe, 1985). Briefly, 1 mg of biochar sample was acid-digested with 6 mL HCl and 2 mL HNO_3 at 110 °C for 60 minutes. The mixture was cooled to room temperature before the second acid digestion with 10 mL 1.2% HNO_3 at 80 °C for 30 minutes. After the digestion, the samples were cooled again, volume made up to 20 mL with milliQ water, filtered and analyzed with ICP-OES Thermo Flash 2000 elemental analyzer.

c. Cation Exchange Capacity (CEC): A compulsive exchange method with slight modifications was used to determine the cation exchange capacity (CEC) [330,331]. A solution of 1 mg biochar was agitated at 200 rpm for 2 h with 5 mL 0.5 M $BaCl_2$ solution, followed by filtration using a 0.45 µm syringe filter. The concentration of exchangeable bases (Mg, Na, Ca, Al, Mn, and Fe) was analyzed using ICP-AES Agilent 5110 Dual View.

d. Zeta (ζ) potential measurements: The zeta potential for the biochar samples were recorded with Zetasizer Nano Malvern, using 0.1 M NaCl as solvent. Briefly, 1 mg of biochar was bath sonicated in 0.1 M NaCl (5 mL) for 2 h to disperse the material. The suspension was then left undisturbed for 24 h, prior to the analysis.

e. Point of zero charge (pH_{zc}): The drift method, as reported elsewhere, with slight modification, was used to determine the pHzc for selected biochar sample (Liu et al., 2015; Xie et al., 2016). Briefly, 1 mg of biochar was added to 2 mL 0.1 M NaCl, initial pH values adjusted from 2-11 with 0.1 M NaOH or HCl. The difference between final and initial values of pH (pH_{final} - $pH_{initial}$) was noted and plotted as a function of $pH_{initial}$. The pH_{zc} is the point where $pH_{final} = pH_{initial}$, or ΔpH ($pH_{final}$ - $pH_{initial}$) is zero.

f. Surface functional groups: FTIR analysis for the selected biochar was performed using a KBr pellet Bruker Alpha-P, for wavelength 400-4000 cm^{-1} with a resolution of 2 cm^{-1} and number of scans 250.

g. Scanning electron microscopy (SEM): The biochar samples were imaged using a Quanta FEG ESEM, operating at 20kV without gold coating to observe their superficial morphology. The samples were mounted on double-sided conductive carbon tape. EDS data were collected in high vacuum mode, while some higher magnification images were obtained in environmental (low vacuum) mode at 0.8 mB water vapour. The EDS data were acquired using an Oxford Inca system.

Text 2: Adsorption Isotherm and Kinetic Models

Langmuir isotherm theory assumes ideal, irreversible, monolayer adsorption on a homogenous surface, and is characterized by the equation [295]:

$$\frac{C_e}{q_e} = \frac{1}{Q_0 b} + \frac{C_e}{Q_0} \quad \text{… equation (F1)}$$

where C_e is the equilibrium concentration of FLX (mg L^{-1}), q_e is the amount of FLX adsorbed per unit mass of adsorbent at equilibrium (mg g^{-1}), b (L mg^{-1}) is a constant related to the energy of adsorption (Langmuir constant), and Q_0 (mg g^{-1}) is the maximum monolayer adsorption capacity. These parameters are determined from the slope and intercept of the linear plot of C_e/q_e *vs* C_e. While Freundlich isotherm accommodates non-ideal adsorption behaviour and describes multilayer adsorption on heterogeneous surfaces. The Freundlich parameters are characterized by the following linearized empirical equation [199]:

$$ln\, q_e = ln\, K_F + \frac{1}{n}\, ln\, C_e \quad \text{… equation (F2)}$$

where K_F (mg g^{-1} (L g^{-1}) $^{1/n}$) is the Freundlich coefficient and n is the Freundlich exponent, representing adsorption capacity and strength, respectively, calculated from the linear plot of $ln\, q_e$ *vs* $ln\, C_e$.

To further understand the kinetics of the adsorption, the experimental data was fit into the PFO, PSO, and IP models. The PFO kinetic model or Lagergren model for the adsorption of FLX onto biochar is described by [199,332]:

$$ln(q_e - q_t) = ln\, q_e - k_1 t \quad \text{… equation (F3)}$$

where q_t and q_e are the adsorbed FLX onto biochar at time t and at equilibrium (mg/g), and k_1 is the rate constant (min^{-1}). A plot of $ln\,(q_e - q_t)$ *vs* t for different initial concentrations of FLX (1, 5,

10, 25, and 50 mg/L) was used to determine the rate constant for the adsorption. According to the PSO model, the rate of adsorption of analyte is proportional to the sites available on the adsorbent, and is given by equations [199,332,333]:

$$\frac{t}{q_t} = \frac{1}{k_2\, q_e^2} + \frac{t}{q_e} \quad \text{… equation (F4)}$$

The parameters k_2 (g/mg. min) and q_e (mg/g) were determined from the slope and intercept of the linear plot of t/q_t *vs* t.

To determine diffusion and rate limiting step during adsorption, the experimental data was fit to IP diffusion model. Based on the presumption that adsorption of solute in a solution involves mass transfer of adsorbate (film or external diffusion), surface diffusion, and pore diffusion, the model is expressed by Weber-Morris equation [332]:

$$q_t = K_p\sqrt{t} + C \quad \text{… equation (F5)}$$

K_p is the intraparticle diffusion rate constant (mg/g. $\text{min}^{0.5}$) and C (mg/g) is the boundary layer thickness, which determines the boundary layer effect- higher values, the greater the effect. If C=0 (i.e., the plot passes through origin), IP diffusion controls the adsorption process; and if $C \neq 0$ with multiple linear sections, these sections in the plot correspond to different mechanisms that control the adsorption process [199]. The model parameters- C (mg/g) and rate constant (K_p), as determined from the intercept and slope of the linear plot of q_t *vs* $\sqrt{t}$, respectively.

Text 3: Quantification of FLX using LC-MS

The LCMS system comprised of Waters M-class UHPLC and a Sciex ZenoToF 7600. The chromatographic separation was achieved with Kinetex 2.6 µm XB-C18 100 Å, 50 X 0.3 mm column, maintained at a temperature of 50 °C, using gradient mobile phase (ultrapure water with 0.1% v/v formic acid to Acetonitrile with 0.1% v/v formic acid). The other parameters were maintained as: positive ionization mode, flow rate 20 µL/min, injection volume 5 µL, curtain gas 35 psi, CAD gas 7 psi, and spray voltage of 5500 V.

Table F1: Operating conditions for the steam- and CO_2-activated biochar

Biochar ID	Activation agent	Flow (ml/min)	P (bar)	Activation temperature (°C)	Activation time (min)	
1	Steam	0.3	1	700	60	H_2O-700-60-0.3-1
2	Steam	0.3	1	800	60	H_2O-800-60-0.3-1
3	Steam	0.15	1	900	30	H_2O-900-30-0.15-1
4	Steam	0.07	1	900	30	H_2O-900-30-0.07-1
5	Steam	0.15	1	800	60	H_2O-800-60-0.15-1
6	CO_2	300	1	900	30	CO_2-900-30-300-1
7	CO_2	600	1	1000	30	CO_2-1000-30-600-1
8	CO_2	600	>1	1000	30	CO_2-1000-30-600-1
9	CO_2	600	1	800	30	CO_2-800-30-600-1
10	CO_2	300	1	1000	15	CO_2-1000-15-300-1

Table F2: Surface area, pore radius, elemental analyses and mineral composition of the synthesized biochar

	Biochar ID									
Parameters	**1**	**2**	**3**	**4**	**5**	**6**	**7**	**8**	**9**	**10**
Multipoint BET surf. area (m^2/g)	449	828	902	836	678	236	855	775	382	557
Single point (P/Po= 0.3) BET surf. area (m^2/g)	458	829	907	830	692	221	804	721	377	549
DFT surface area (m^2/g)	457	803	577	741	642	233	681	605	407	524
DA pore radius (Å)	6.1	6.8	7.4	7.8	7.2	8.2	6.6	6.3	7.1	6.5
Ca (mg/L)	2.20	1.96	3.10	2.20	2.10	1.92	2.30	2.60	1.71	2.30
K (mg/L)	3.90	5.50	13.0	5.90	7.00	5.60	8.50	10.1	3.40	4.50
Mg (mg/L)	0.310	0.360	0.470	0.370	0.340	0.390	0.370	0.380	0.300	0.340
Mn (mg/L)	0.003	0.005	0.010	0.004	0.004	0.003	0.005	0.005	0.003	0.003
Na (mg/L)	4.60	5.30	4.50	4.60	4.70	5.70	4.60	4.80	4.70	4.70
N %	0.72	0.28	0.25	0.29	0.39	0.41	2.42	0.47	0.42	0.54
C %	83.5	76.1	69.6	73.5	74.9	76.3	63.3	70.6	81.5	75.5
H %	1.79	2.09	2.60	2.00	2.02	1.36	1.44	2.17	1.42	1.54
S %	0.0	0.0	0.0	0.0	0.0	0.0	0.0	0.0	0.0	0.0
O%	13.94	21.58	27.51	24.22	22.73	21.96	32.83	26.73	16.64	22.47
O/C	0.167	0.284	0.395	0.33	0.304	0.288	0.519	0.378	0.204	0.298
H/C	0.021	0.027	0.037	0.027	0.027	0.018	0.023	0.031	0.017	0.02
(O+N)/C	0.176	0.287	0.399	0.334	0.309	0.293	0.557	0.385	0.209	0.305

163 **Table F3: FTIR spectral features for the selected biochar (CO_2-1000-30-600-1)**

Wavenumber (cm^{-1})	**Vibration and Functional groups**
3100-3800	O-H stretching
2800-3000	Aliphatic C-H stretching (alkane/alkyl groups)
2400-2250	C=O stretching for carbonyl functionalities
1700-1760	C=O stretching (aldehyde, ketone, esters, and carboxylic acid)
1500-1600	Aromatic C=C stretching
1300-1400	O-H bending in phenols; C-O stretching from C-O-C groups, aryl ether
1080-1300	Bending of phenolic C-O associated with lignin
550-830	Aromatic C-H out-of-plane bending

164

165

Figures:

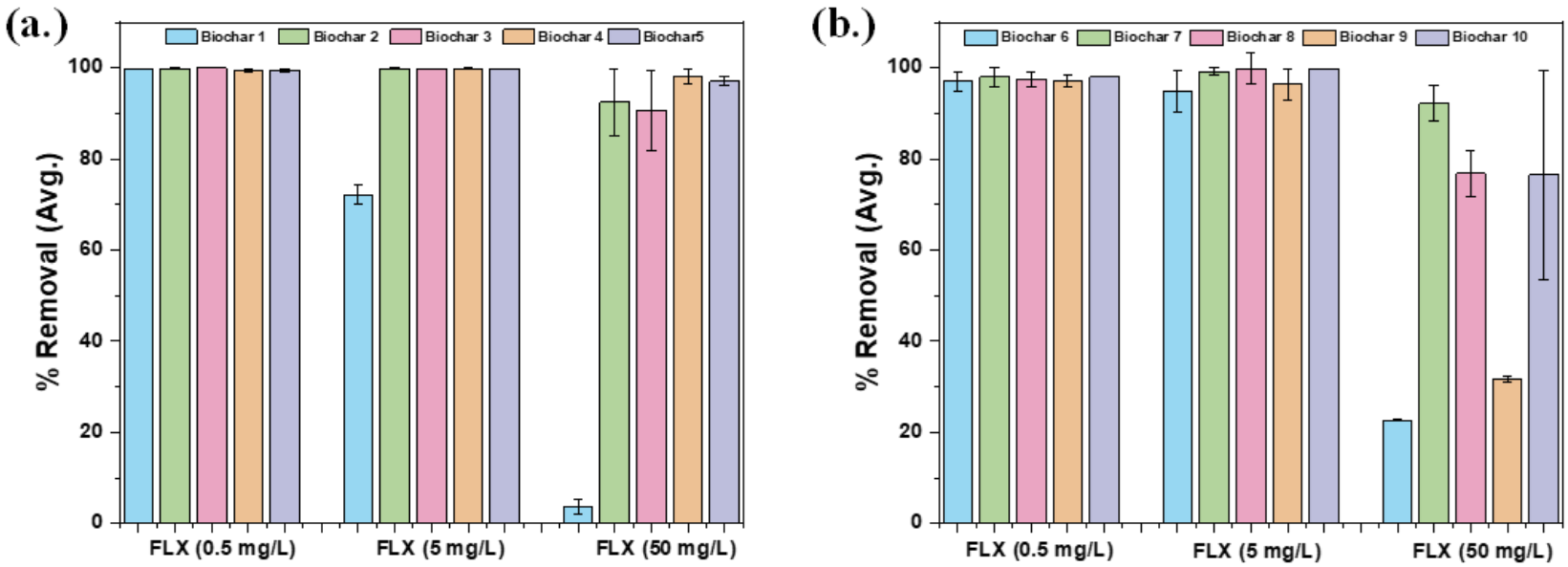

Figure F8: Removal efficiency of (a.) Steam-activated (1-5), and (b.) CO_2-activated biochar (6-10) for FLX concentrations of 0.5, 5, and 50 mg/L after 24 h

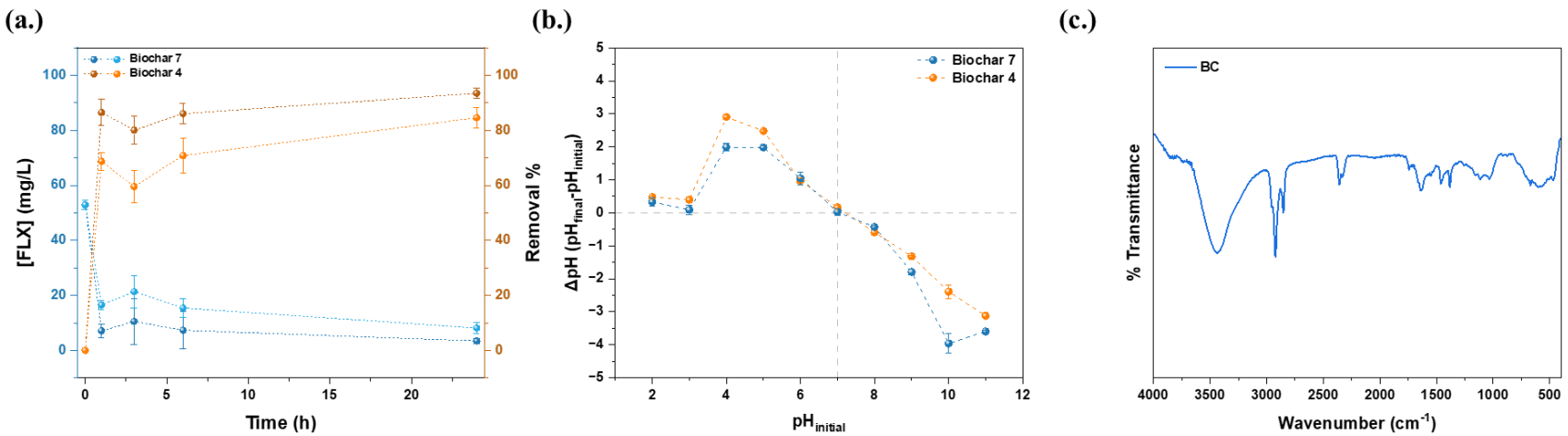

Figure F2: (a.) Comparison of biochar 4 and 7 kinetics with 50 mg/L FLX for 24 h; (b) pHzc and (c) FTIR spectrum of selected biochar 7

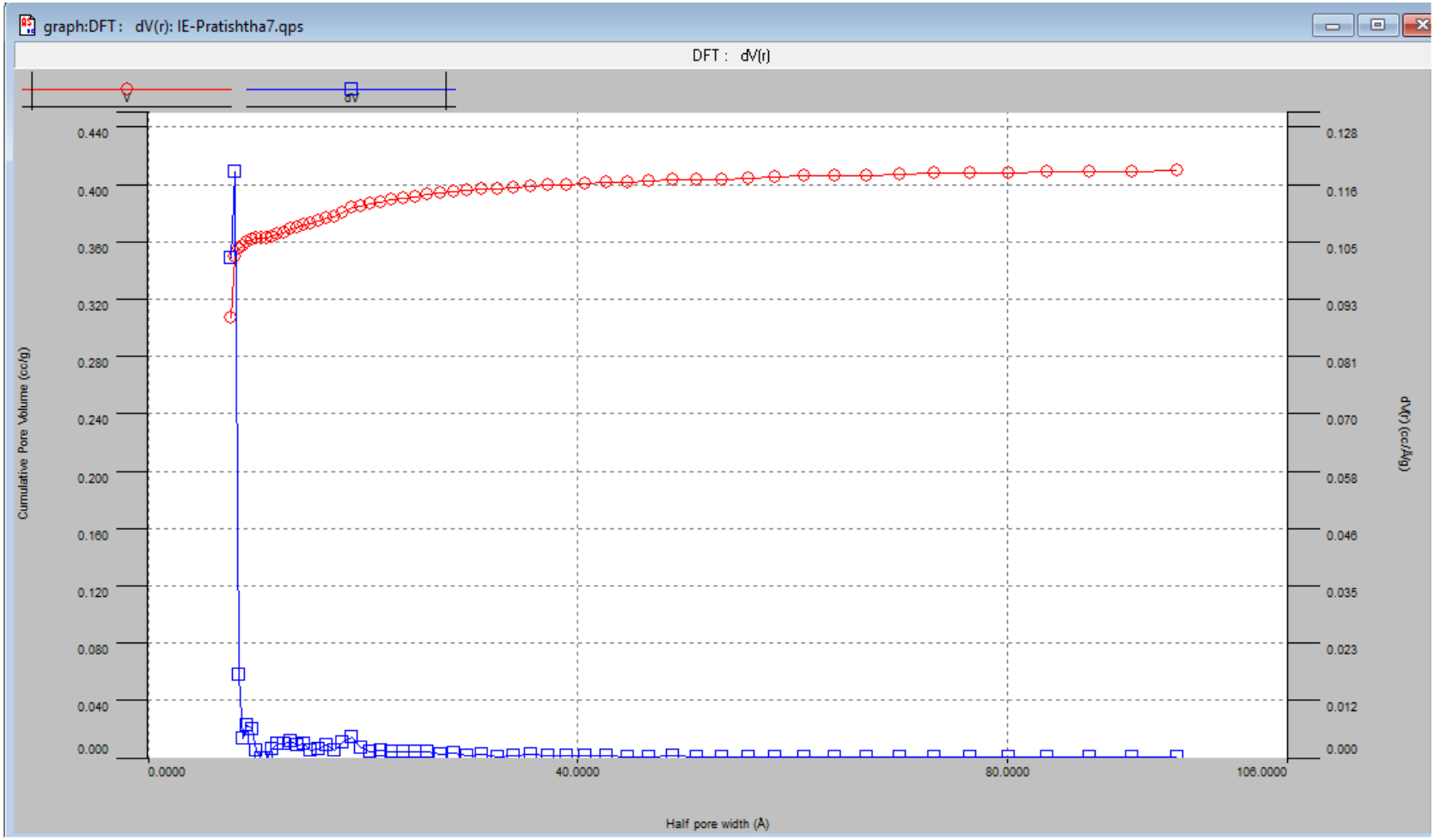

Figure F3: Pore size distribution of biochar 7 (CO_2-1000-30-600-1)

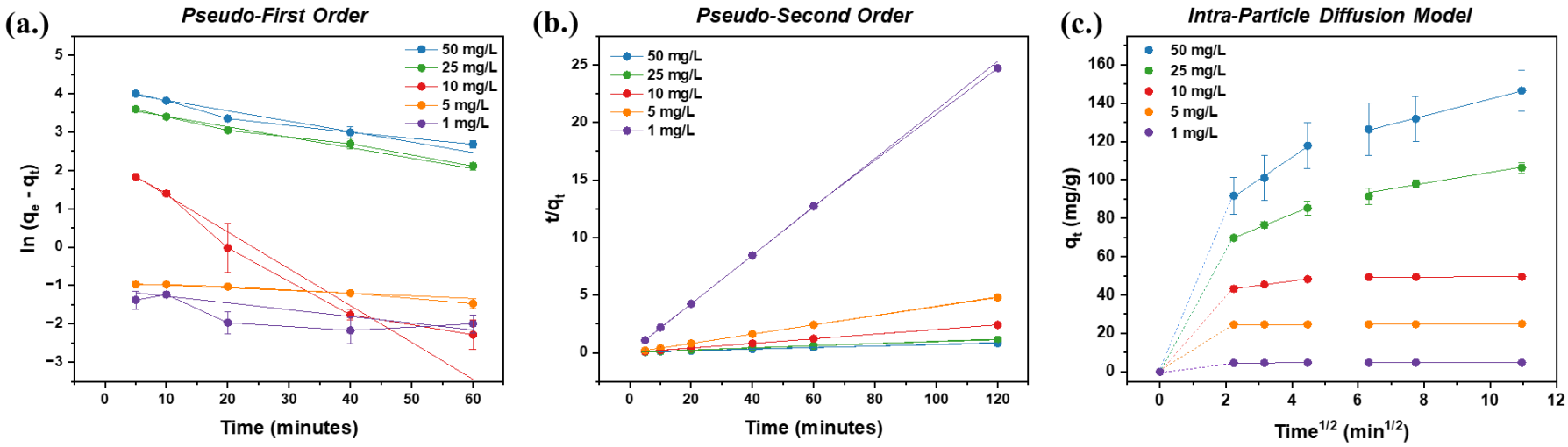

Figure F4: Adsorption kinetic models for FLX adsorption onto biochar (a) Pseudo-first order (PFO) kinetic model, (b) Pseudo-second order (PSO) kinetic model, and (c) Intra-particle diffusion model.

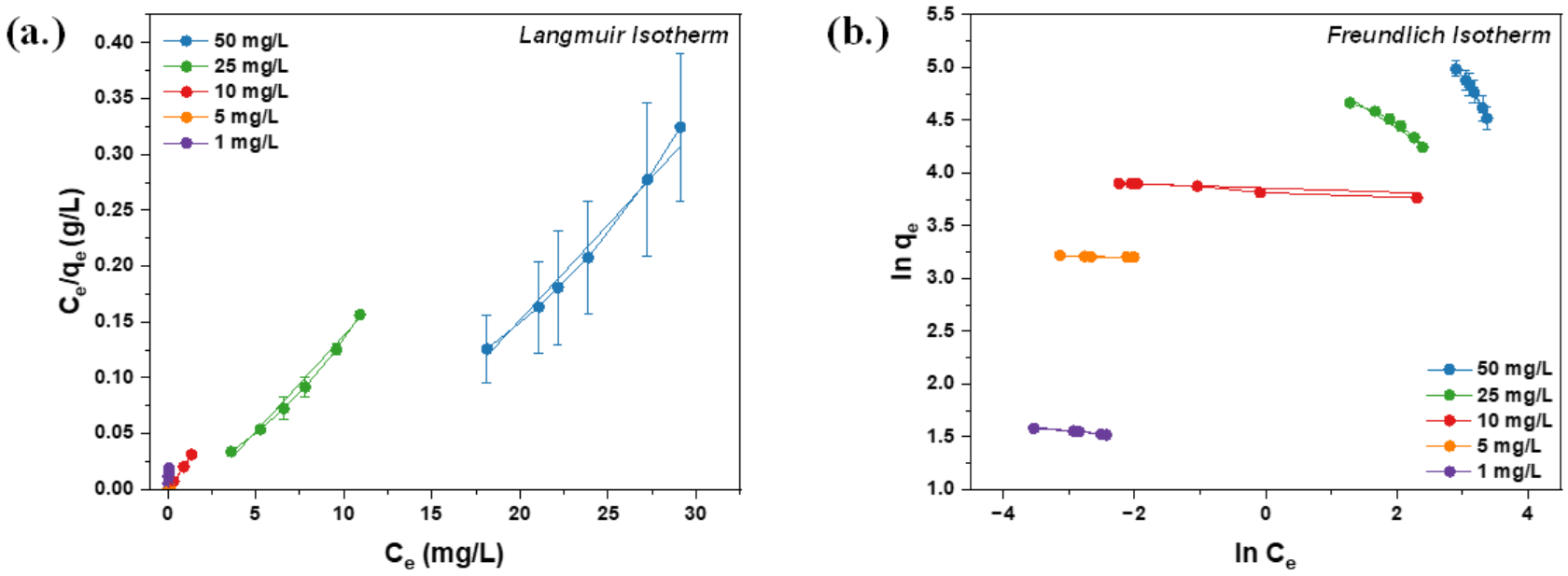

Figure F5: Adsorption isotherm models for FLX adsorption onto biochar (a) Langmuir isotherm model, and (b) Freundlich isotherm model.

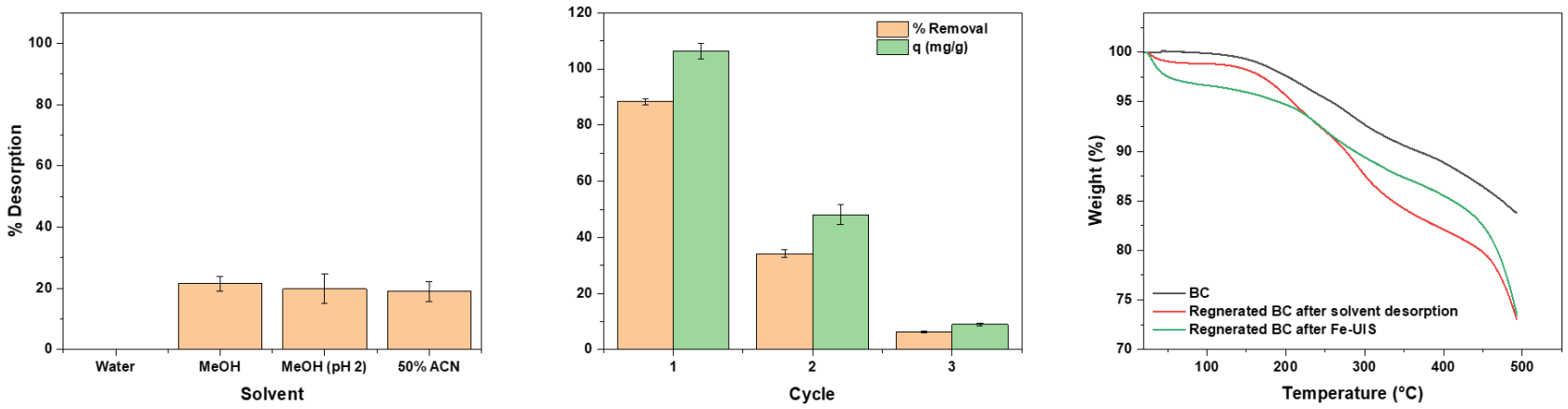

Figure F6: (a) % Desorption by various solvents, (b) % Removal and adsorption capacity of the regenerated biochar for subsequent adsorption cycles with 25 mg/L FLX after 2 h, and (c) TGA of raw and regenerated biochar

Appendix G: Supplementary Information for Chapter 9

List of Tables:

G1	Composition of simulated wastewater effluent
G2	Elemental analysis of CO_2-activated olive stone biochar (CO_2-1000-30-600-1)
G3	Superficial parameters obtained from N_2 adsorption and desorption of CO_2-activated olive stone biochar (BC) and CuO before and after treatment
G4	FTIR spectral features for BC and CuO
G5	Characteristics of TPs and their predicted lethal (LC50), effective (EC50), and chronic doses (ChV) for fish (F), Daphnid (D) and green algae (GA) using EPI Suite

List of Figures:

G1	FTIR spectra for biochar (BC) and synthesized CuO particles
G2	Zeta Potential of synthesized CuO particles
G3	UVC irradiance versus distance from the source
G4	Calibration curve for Fluoxetine (FLX) using UV-Visible spectroscopy (λ = 226 nm)
G5	Removal efficiency for FLX (25 mg/L, 50 mL) for five cycles of catalysts reuse
G6	MS spectra of transformation products (TPs) formed during photocatalytic treatment at reaction times of 30 s, 2 min, and 5 min

Text 1: Sample Preparation for Biochar and CuO characterization

a. Surface area analysis**:** Biochar and CuO particles were analyzed for their surface area and pore size distribution with BET analysis using NOVA 1200e surface area analyzer (Materials Characterization Facility, Ontario Tech. University, Canada). The samples were degassed in vacuum for 3 h at 200 °C, followed by N_2 gas physisorption analysis at 77 K using a static volumetric method. That is, the amount of N_2 that adsorbs on the surface was measured at varying relative pressures and the surface area was calculated using the linear plot of $1/[(W(P_0/P -1))]$ vs P/P_0 (also called the BET plot), with P/P_0 varying from 0.05 to 0.3. The specific surface area was calculated from the BET plot sample surface, cross sectional area of the adsorbed gas (16.2 $Å^2$ for N_2), and the mass of the analyte powder (BC and CuO). For pore size distribution using DFT, $P/P_0 > 0.15$ was chosen.
b. Elemental contents: The CHNS analysis of BC was performed using ICP-OES Thermo Flash 2000 elemental analyzer. For this, BC was acid-digested with HCl and HNO_3 at 110 °C for 1 h, followed by second acid digestion with 1.2% HNO_3 at 80 °C for 30 minutes and colling to room temperature.
c. Surface functional groups: FTIR analysis for both BC and CuO was performed using KBr pellet with Bruker Alpha-P, for a wavenumber range 400-4000 cm-1, resolution of 2 cm^{-1}, and number of scans 250.
d. X-Ray Diffraction (XRD): The XRD for CuO powder was recorded at room temperature (25 °C) with Bruker D8 eco Advance equipped with a source delivering Cu Kα radiation (λ = 1.54056 Å) with a step size of 0.02 and 2θ range of 20-75°.
e. UV-Visible Diffuse Reflectance Spectroscopy (DRS): The DRS measurements were performed with Shimazdu UV-2600 Spectrophotometer DRS *via* two-detector integrating sphere with the wavelength ranging from 200 to 1400 nm. The baseline ($R_{standard}$) was measured using a reference $BaSO_4$.
f. Zeta potential: The zeta potential of synthesized CuO particles was measured with Zetasizer Nano Malvern using milliQ water as the dispersant.
g. Scanning electron microscopy (SEM): The samples (BC and CuO) were mounted on a conductive copper tape and imaged without gold coating using Hitachi FlexSEM 1000 II.

Text 2: Data fitting suing Pseudo-Second Order (PSO) kinetic model

For data fitting, the data was fit to the PSO model using the following equation:

$$\frac{t}{q_t} = \frac{1}{k_2\, q_e^2} + \frac{t}{q_e} \qquad \ldots \text{(equation G1)}$$

Where k_2 (g/mg. min) is the rate constant, t (min) is time, and q_t and q_e (mg/g) is the adsorption capacity at time t and at equilibrium, respectively. The k_2 and q_e were determined from the slope and the intercept of the linear plot of t/q_t *vs* t.

Figures:

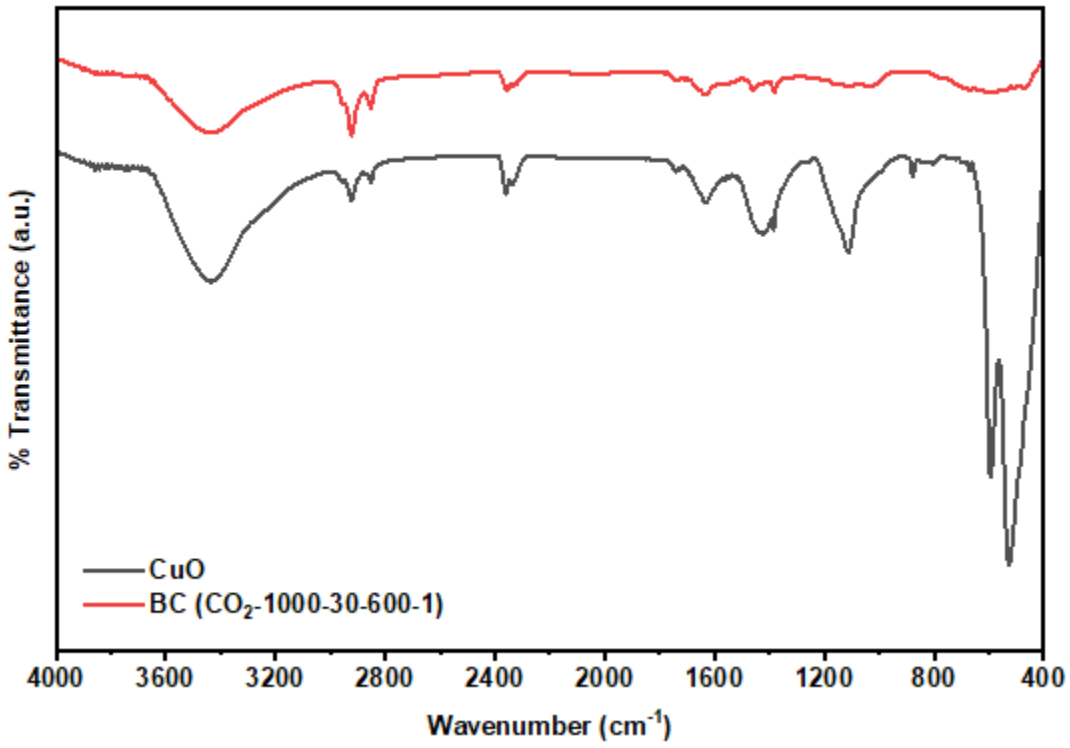

Figure G1: FTIR spectra for biochar (BC) and synthesized CuO particles

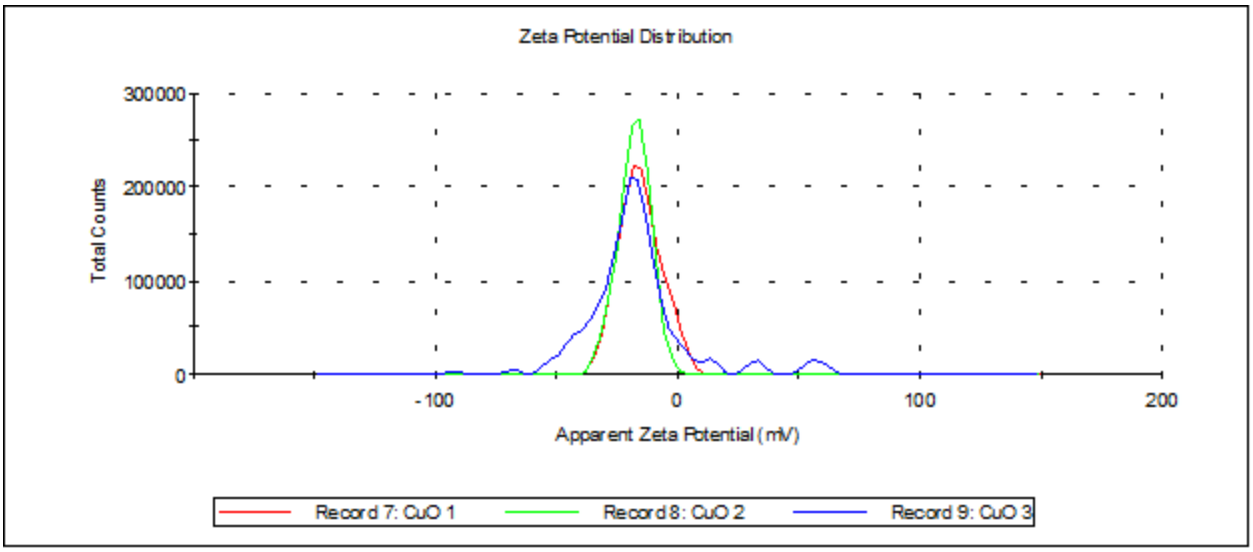

Figure G2: Zeta Potential of synthesized CuO particles

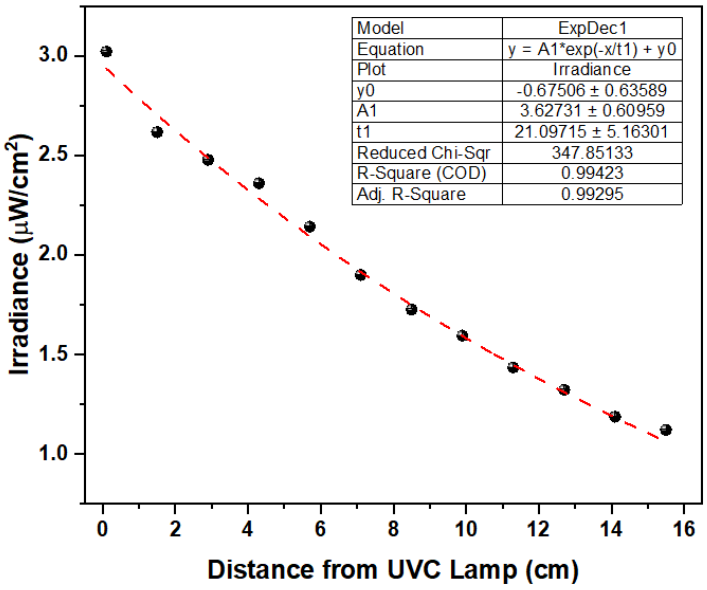

Figure G3: UVC irradiance versus distance from the source

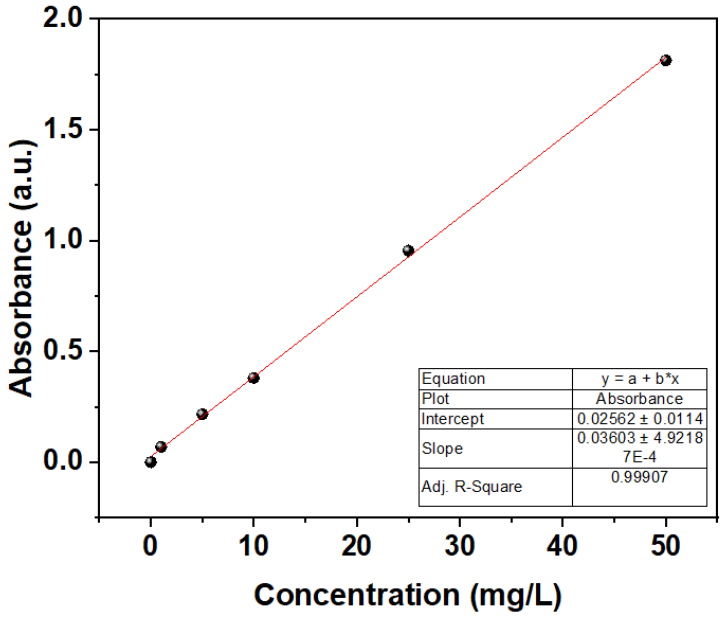

Figure G4: Calibration curve for Fluoxetine (FLX) using UV-Visible spectroscopy (λ = 226 nm)

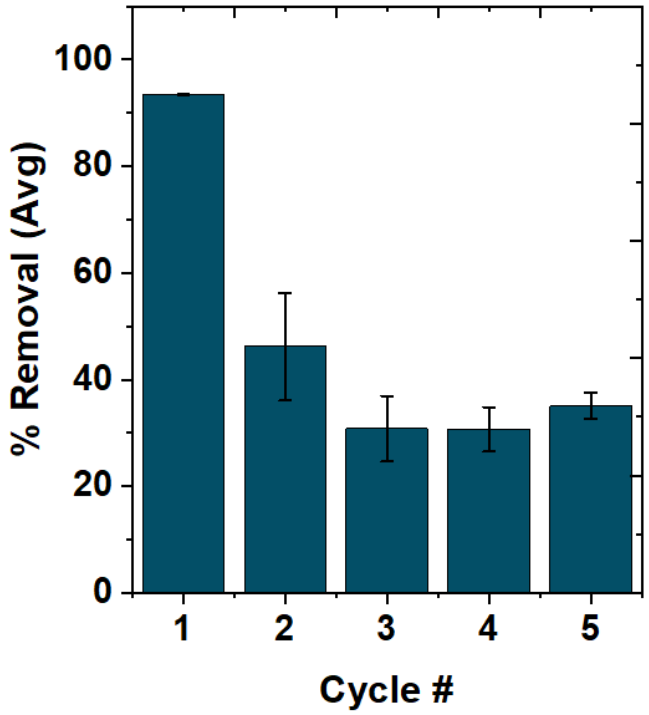

Figure G5: Removal efficiency for FLX (25 mg/L, 50 mL) for five cycles of catalysts reuse

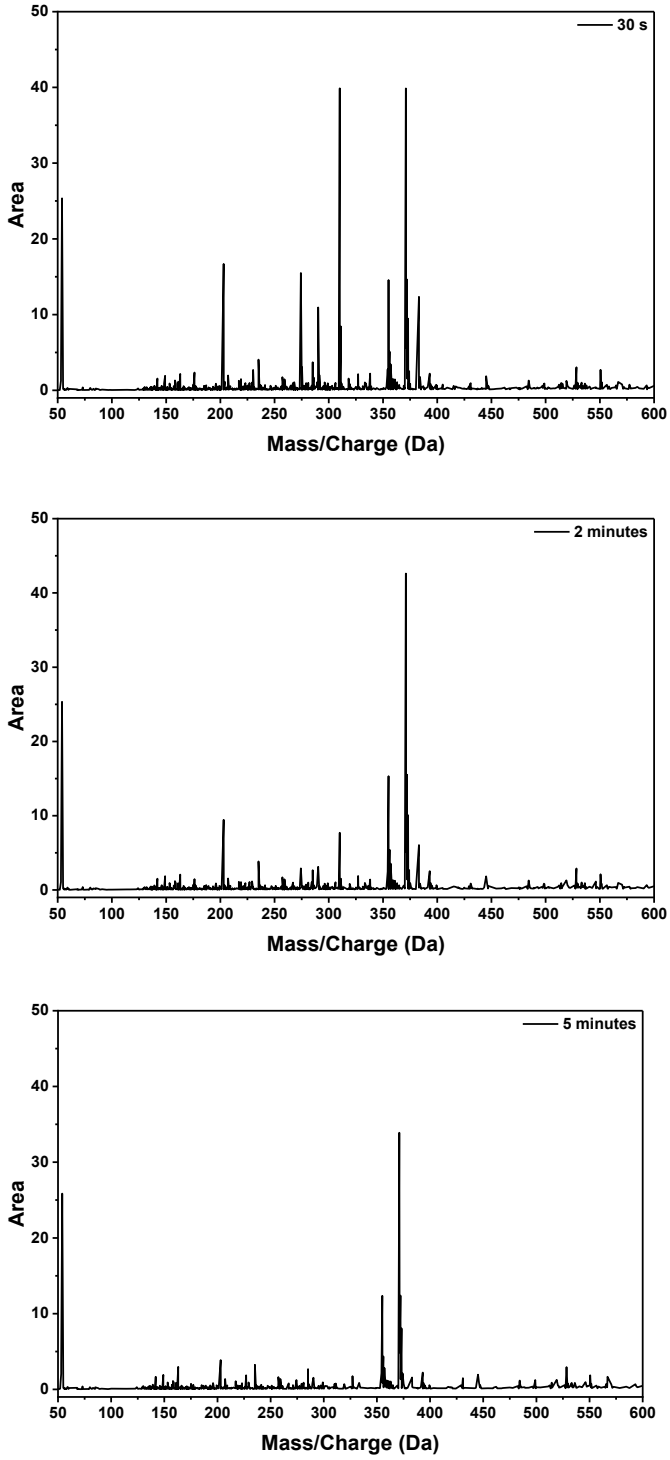

Figure G6: MS spectra of transformation products (TPs) formed during photocatalytic treatment at reaction times of 30 s, 2 min, and 5 min

Tables:

Table G1: Composition of simulated wastewater effluent

Composition	**Concentration (mg/L)**
Glucose	1000 ± 7.43
$(NH_4)_2SO_4$	235.7 ± 3.65
KH_2PO_4	61.463 ± 1.5
$MgSO_4$	23.12 ± 0.56
$CaCl_2•2H_2O$	14.67 ± 0.6
$FeCl_3$	7.76 ± 0.82
Na_2CO_3	285.74 ± 3.5
$CoSO_4· 7H_2O$	0.32 ± 0.03
$Na_2MoO_4•2H_2O$	0.07 ± 0.08
$MnSO_4•H_2O$	0.08 ± 0.001
$ZnCl_2$	0.15 ± 0.05
pH	6.6 ± 0.2

Table G2: Elemental analysis of CO_2-activated olive stone biochar (CO_2-1000-30-600-1)

Material	Parameter	Value
Biochar (CO_2-1000-30-600-1)	C %	63.3
	N %	2.42
	H%	1.44
	S %	0
	O %	32.83
	O/C	0.519
	H/C	0.023
	(O+N)/C	0.557

Table G3: Superficial parameters obtained from N_2 adsorption and desorption of CO_2-activated olive stone biochar (BC) and CuO before and after treatment

Material	Multipoint BET Surface area (m^2/g)		DA pore radius (Å)	
	Before treatment	After treatment	Before treatment	After treatment
BC	855	154.5	6.6	11.5
CuO	7.0	23.2	15.6	15.9
BC + CuO	210.8	149.0	9.3	13.6

Table G4: FTIR spectral features for BC and CuO

Material	Wavenumber (cm^{-1})	Vibration and Functional groups
Biochar (CO_2-1000-30-600-1)	3100-3800	O-H stretching
	2800-3000	Aliphatic C-H stretching (alkane/alkyl groups)
	2400-2250	C=O stretching for carbonyl functionalities
	1700-1760	C=O stretching (aldehyde, ketone, esters, and carboxylic acid)
	1500-1600	Aromatic C=C stretching
	1300-1400	O-H bending in phenols; C-O stretching from C-O-C groups, aryl ether
	1080-1300	Bending of phenolic C-O associated with lignin
	550-830	Aromatic C-H out-of-plane bending
CuO	3400-3500	O-H stretching
	2800-2900	Aliphatic C-H stretching
	1380-1430	C-H bending; carboxylate groups
	400-600	Cu-O

Table G5: Characteristics of TPs and their predicted lethal (LC50), effective (EC50), and chronic doses (ChV) for fish (F), Daphnid (D) and green algae (GA) using EPI Suite

Compound	m/z	Chemical formula	SMILES code	Chemical and physical properties*			Acute toxicity*		Chronic toxicity*
				Molecular weight (g mol^{-1})	Water solubility (mg L^{-1})	Log K_{ow}	LC_{50}	EC_{50}	ChV
FLX	310	$C_{17}H_{18}F_3NO$	CNCCC(C1=CC=CC=C1)OC2=CC=C(C=C2)C(F)(F)F	309.33	60.28	4.65	F_{96h} = 1.06 D_{48h} = 0.771	GA_{96h} = 1.578	F = 0.139 D = 0.148 GA = 0.712
TP1	166	$C_{10}H_{15}NO$	OC(CCNC)C1=CC=CC=C1	165.24	9.62 e+004	0.98	F_{96h} = 148.71 D_{48h} = 15.743	GA_{96h} = 16.427	F =12.432 D =1.152 GA =5.006
TP2	163	$C_7H_5F_3O$	OC1=CC=C(C(F)(F)F)C=C1	162.11	993.9	2.48	F_{96h} = 49.785 D_{48h} = 29.538	GA_{96h} = 26.386	F = 5.125 D = 3.255 GA = 7.620
TP3	164	$C_{10}H_{13}NO$	O=C(CCNC)C1=CC=CC=C1	163.22	6.89 e+004	1.16	F_{96h} = 762.324 D_{48h} = 400.534	GA_{96h} = 216.472	F = 67.997 D = 31.474 GA = 47.693
TP4	182	$C_{10}H_{15}NO_2$	OC1=C(C(O)CCNC)C=CC=C1	181.24	7.885 e+005	0.50	F_{96h} = 3318.819 D_{48h} = 1640.550	GA_{96h} = 688.981	F = 275.475 D = 108.784 GA = 132.513
TP5	180	$C_{10}H_{13}NO_2$	OC1=C(C(CCNC)=O)C=CC=C1	179.22	1.227 e+005	1.46	F_{96h} = 453.101	GA_{96h} = 148.104	F = 41.743 D = 20.751 GA = 34.684

							D_{48h} =244.679		
TP6	148	$C_{10}H_{13}N$	CNC/C=C\C1=CC=CC=C1	147.22	8589	2.30	F_{96h} = 64.712 D_{48h} = 37.784	GA_{96h} = 31.590	F = 6.537 D = 3.983 GA = 8.803
TP7	164	$C_{10}H_{13}NO$	OC1=C(/C=C\CNC)C=CC=C1	163.22	7.118 e+004	1.82	F_{96h} = 193.668 D_{48h} = 108.175	GA_{96h} = 75.292	F = 18.567 D = 10.078 GA = 19.010
TP8	165	$C_7H_7F_3O$	OC1C=CC(C(F)(F)F)C=C1	164.13	3834	2.04	F_{96h} = 123.971 D_{48h} = 70.656	GA_{96h} = 53.454	F = 12.171 D = 6.963 GA = 14.116
TP9	143	$C_7H_4F_2O$	O=C(C=C/1)C=CC1=C(F)/F	142.11	5552	1.37	F_{96h} = 429.907 D_{48h} = 230.301	GA_{96h} = 134.857	F = 39.233 D = 19.100 GA = 31.023
TP10	179	$C_7H_5F_3O_2$	OC1=C(O)C=C(C(F)(F)F)C=C1	178.11	4225	2.00	F_{96h} = 147.654 D_{48h} = 83.805	GA_{96h} = 62.322	F = 14.426 D = 8.164 GA = 16.306
TP11	115	$C_2HF_3O_2$	OC(C(F)(F)F)=O	114.02	9.745 e+004	0.50	F_{96h} = 20725.350 D_{48h} = 10248.305	GA_{96h} = 4309.894	F = 1720.957 D = 680.191 GA = 829.545
TP12	326	$C_{17}H_{18}F_3NO_2$	CNCCC(OC1=CC=C(C(F)(F)F)C=C1)C2=C(O)C=CC=C2	325.33	92.97	4.17	F_{96h} = 3.018 D_{48h} = 2.094	GA_{96h} = 3.568	F = 0.374 D = 0.356 GA = 1.459

TP13	342	$C_{17}H_{18}F_3NO_3$	CNCCC(OC1=CC=C(C(F)(F)F)C=C1)C2=C(O)C=C(O)C=C2	341.33	191.8	3.69	F_{96h} = 8.548 D_{48h} = 5.672	GA_{96h} = 8.048	F = 1.004 D = 0.854 GA = 2.982
TP14	358	$C_{17}H_{18}F_3NO_4$	CNCCC(OC1=C(O)C=C(C(F)(F)F)C=C1)C2=C(O)C=C(O)C=C2	357.33	653	2.95	F_{96h} = 41.016 D_{48h} = 25.428	GA_{96h} = 27.240	F = 4.447 D = 3.167 GA = 8.675
TP15	374	$C_{17}H_{18}F_3NO_5$	CNCCC(OC1=C(O)C=C(C(F)(F)F)C=C1O)C2=C(O)C=C(O)C=C2	373.33	1341	2.47	F_{96h} = 115.675 D_{48h} = 68.604	GA_{96h} = 61.182	F = 11.903 D = 7.552 GA = 17.653
TP16	308	$C_{17}H_{19}F_2NO_2$	CNCCC(OC1=CC=C(C(F)(F)O)C=C1)C2=CC=CC=C2	307.34	192.7	3.24	F_{96h} = 19.323 D_{48h} = 12.306	GA_{96h} = 14.732	F = 2.162 D = 1.652 GA = 4.981
TP17	286	$C_{17}H_{19}NO_3$	O=C(O)C(C=C1)=CC=C1OC(CCNC)C2=CC=CC=C2	285.35	13.43	3.57	F_{96h} = 9.182 D_{48h} = 6.025	GA_{96h} = 8.162	F = 1.064 D = 0.879 GA = 2.950
TP18	296	$C_{16}H_{16}F_3NO$	FC(F)(F)C1=CC=C(OC(CCN)C2=CC=CC=C2)C=C1	295.31	35.7	4.18	F_{96h} = 2.660 D_{48h} = 1.847	GA_{96h} = 3.166	F = 0.330 D = 0.316 GA = 1.299
TP19	134	$C_9H_{11}N$	NC/C=C\C1=CC=CC=C1	133.19	2.457 e+004	1.84	F_{96h} = 153.436 D_{48h} = 85.816	GA_{96h} = 60.057	F = 14.733 D = 8.025 GA = 15.208

* Estimated by ECOSAR software ; Log Kow = Octanol-water partition coefficient; LC50 = lethal concentration of a substance that can cause death in 50% of a test group; EC50 = expected concentration of a substance that can cause a specific adverse effect in 50% of a test group; ChV = chronic values; NES = no effects at saturation, reported when the effect level exceeds water solubility.